

1988

Aspects Of Sims Matrix Effects In Aluminum-gallium - Arsenide

William Harvey Robinson

Follow this and additional works at: <https://ir.lib.uwo.ca/digitizedtheses>

Recommended Citation

Robinson, William Harvey, "Aspects Of Sims Matrix Effects In Aluminum-gallium - Arsenide" (1988). *Digitized Theses*. 1712.
<https://ir.lib.uwo.ca/digitizedtheses/1712>

This Dissertation is brought to you for free and open access by the Digitized Special Collections at Scholarship@Western. It has been accepted for inclusion in Digitized Theses by an authorized administrator of Scholarship@Western. For more information, please contact tadam@uwo.ca, wlsadmin@uwo.ca.



National Library
of Canada

Bibliothèque nationale
du Canada

Canadian Theses Service

Service des thèses canadiennes

Ottawa, Canada
K1A 0N4

NOTICE

The quality of this microform is heavily dependent upon the quality of the original thesis submitted for microfilming. Every effort has been made to ensure the highest quality of reproduction possible.

If pages are missing, contact the university which granted the degree.

Some pages may have indistinct print especially if the original pages were typed with a poor typewriter ribbon or if the university sent us an inferior photocopy.

Previously copyrighted materials (journal articles, published tests, etc.) are not filmed.

Reproduction in full or in part of this microform is governed by the Canadian Copyright Act, R.S.C. 1970, c. C-30.

AVIS

La qualité de cette microforme dépend grandement de la qualité de la thèse soumise au microfilmage. Nous avons tout fait pour assurer une qualité supérieure de reproduction.

S'il manque des pages, veuillez communiquer avec l'université qui a conféré le grade.

La qualité d'impression de certaines pages peut laisser à désirer, surtout si les pages originales ont été dactylographiées à l'aide d'un ruban usé ou si l'université nous a fait parvenir une photocopie de qualité inférieure.

Les documents qui font déjà l'objet d'un droit d'auteur (articles de revue, tests publiés, etc.) ne sont pas microfilmés.

La reproduction, même partielle, de cette microforme est soumise à la Loi canadienne sur le droit d'auteur, SRC 1970, c. C-30.

ASPECTS OF SIMS MATRIX EFFECTS IN
ALUMINUM GALLIUM ARSENIDE

by

William H. Robinson

Faculty of Engineering Science

Submitted in partial fulfillment
of the requirements for the degree of
Doctor of Philosophy

Faculty of Graduate Studies
The University of Western Ontario
London, Ontario
December, 1987

© William H. Robinson 1987

Permission has been granted to the National Library of Canada to microfilm this thesis and to lend or sell copies of the film.

The author (copyright owner) has reserved other publication rights, and neither the thesis nor extensive extracts from it may be printed or otherwise reproduced without his/her written permission.

L'autorisation a été accordée à la Bibliothèque nationale du Canada de microfilmer cette thèse et de prêter ou de vendre des exemplaires du film.

L'auteur (titulaire du droit d'auteur) se réserve les autres droits de publication; ni la thèse ni de longs extraits de celle-ci ne doivent être imprimés ou autrement reproduits sans son autorisation écrite.

ISBN 0-315-40790-5.

ABSTRACT

In secondary ion mass spectrometry (SIMS) the detected ion count rate must be corrected for differences in matrix when depth profiling semiconductor samples with layered structures of different composition. Few published studies of the matrix effect exist and those that have studied the matrices give widely differing factors. The situation is further complicated by secondary ion molecular interferences which can completely mask the ion signal of interest. These problems are examined in this thesis.

The depth distribution of ion implanted samples of ^{28}Si and ^{52}Cr in $\text{Al}_x\text{Ga}_{1-x}\text{As}$ with x equal to 0, 0.066, 0.21 and 0.40 for energies of 25, 50, 100 and 125 keV and doses of 3×10^{13} , 1×10^{14} and 1×10^{15} atoms cm^{-2} have been measured. Primary ion beams of $^{16}\text{O}_2^+$ with a net energy of 8.0 keV and $^{133}\text{Cs}^+$ with a net energy of 14.5 keV were used in this study and both positive and negative secondary ion intensities were measured.

This study found that while the ^{52}Cr implant profile in $\text{Al}_x\text{Ga}_{1-x}\text{As}$ could be obtained by using the simple technique of voltage offset to discriminate against low energy molecular interferences, the same technique was ineffective with interferences to the ^{28}Si species. In order to obtain depth distributions of ^{28}Si , new computer software for the

Cameca IMS-3f SIMS was developed with several innovations for high mass resolution depth profiling. Profiles with good dynamic range for ^{28}Si were then obtained.

The negative and positive practical ion yields and sputter yields were observed to vary linearly with aluminum concentration. Negative practical ion yields with Cs^+ bombardment gave the smallest overall matrix effect for the species studied. The measured sputter yield for $^{16}\text{O}_2^+$ bombardment is close to predicted values and those of a previous study. The positive practical ion yields measured in this study differ from past studies which were performed without experimental conditions to limit molecular interferences. The measured projected range for ^{28}Si implants agreed with theoretical calculations while those of ^{52}Cr will provide the basis for comparison with theoretical predictions.

ACKNOWLEDGEMENTS

I wish to express my sincere appreciation for the encouragement, guidance and understanding shown by Professor J.D. Brown in serving as my Chief Advisor.

I also wish to thank Dr. N.S. McIntyre of Surface Science Western for his assistance, Dr. F.R. Shepherd of Bell-Northern Research for supplying semiconductor samples and Mrs. D.D. Johnston of Surface Science Western for her contributions in revising computer software. These people, their staff and colleagues inspired and unselfishly assisted my work.

Farsighted individuals at The University of Western Ontario, in Canadian corporations and in the Natural Sciences and Engineering Research Council were responsible for the establishment and funding of Surface Science Western. The economic success of this laboratory and its growing scientific reputation are proof that surface microanalysis is an important, emerging, interdisciplinary field. I am indebted to everyone who has been involved in the creation and operation of this facility.

Friends provided much moral support and encouragement. But most of all, my wife Suzanne has been a warm light of confidence in times of dark despair. My sons Jacob and Christopher have lost the race to complete their formal education before I could complete mine.

In the ignorance that implies impression
that knits knowledge that finds the nameform
that whets the wits that convey contacts
that sweeten sensation that drives desire
that adheres to attachment that dogs death....

James Joyce - Finnegans Wake

TABLE OF CONTENTS

	Page
CERTIFICATE OF EXAMINATION.....	ii
ABSTRACT.....	iii
ACKNOWLEDGEMENTS.....	v
TABLE OF CONTENTS.....	vii
LIST OF TABLES.....	viii
LIST OF FIGURES.....	ix
NOMENCLATURE.....	xix
CHAPTER 1 - A GENERAL REVIEW.....	1
1.1 Introduction.....	1
1.2 Early Contributions.....	8
1.3 The SIMS Technique.....	11
1.4 Analytical Considerations.....	20
1.5 Sputtering.....	36
1.6 Ionization.....	46
1.7 Matrix Effects.....	67
1.8 Matrix Effects in the $Al_xGa_{1-x}As$ System.....	86
CHAPTER 2 - THE ION MICROSCOPE.....	105
2.1 Introduction.....	105
2.2 Computer Software.....	113
2.3 Sample Preparation.....	122
2.4 Analysis Conditions and Procedures.....	123
2.5 Statistical Errors.....	125
CHAPTER 3 - EXPERIMENTAL RESULTS.....	127
3.1 Implant Profiles.....	127
CHAPTER 4 - DISCUSSION OF RESULTS.....	177
4.1 Depth Distributions.....	177
4.2 Sputter Yields.....	194
4.3 Practical Ion Yields.....	197
CHAPTER 5 - CONCLUSIONS.....	206
REFERENCES.....	209
VITA.....	219

LIST OF TABLES

Table	Description	Page
1	Secondary ion yield as related to surface condition (after Klaus (106)).....	47
2	Relative ionization coefficients (after Blaise and Nourtier (123)).....	78
3	Heat of Formation and Bond Energy (151,156)	85
4	Element-oxygen diatomic bond energies.....	100
5	Projected range of implants.....	191
6	Ionization potential and electron affinity.	203

LIST OF FIGURES

Figure	Description	Page
1	Relative sensitivity factor for boron in silicon, showing linearity of $^{11}\text{B}^+$ signal ratioed to the silicon matrix signal $^{28}\text{Si}^{++}$ with respect to concentration (36).....	6
2	Schematic representation of a secondary ion mass spectrometer.....	12
3	Three-dimensional representation of ion trajectories.....	15
4	Angular distributions of various secondary ions. The ordinate axis is count rate (61) a) normal primary beam incidence, $\theta_S = 0^\circ$ b) $\theta_S = 60^\circ$	14
5	Energy distributions of $^{27}\text{Al}^+$ and $^{27}\text{Al}^{16}\text{O}^+$ secondary ions.....	16
6	Mass resolution.....	19
7	Profile of sodium in silica glass using $^{16}\text{O}^-$ bombardment (72).....	26
8	Profile of sodium in silica glass using $^{16}\text{O}^+$ bombardment (72).....	27
9	Predicted depth distribution of momentum (90).....	32
10	Predicted tracer profiles of sputtered atoms for square-shaped tracers positioned originally at different depths (90).....	34

Figure	Description	Page
11	Measured decay lengths for implants in silicon (94).....	35
12	Physical sputtering regimes, a) the single knock-on, b) the linear cascade, and c) the spike regime.....	39
13	Sputtering and evaporation regions defined by ion energy and thermal energy (99).....	40
14	Experimental sputter yield data for Al (100).....	41
15	Sputter yield of Cu with 45 keV ions of atomic number Z_1 (99).....	43
16	Sputter yields of Cu as a function of primary ion beam angle, θ_S (100).....	45
17	Ion emission from a metallic surface. a) prior to emission, b) barrier becomes finite during emission, c) decreased opportunity of neutralization, d) increased opportunity.....	53
18	Relative ion intensities of pure elements bombarded with $^{16}O^-$	56
19	Probability of neutralization of a sputtered positive ion (127). a) Al, Si and Ti with O^- bombardment, b) In, Ta and Sn With O^- bombardment, c) Au with O^- bombardment, d) electron emission.....	57

Figure	Description	Page
20	Energy relationships for surface ionization (132).....	63
21	Electron transitions (137). a) Core electron emission, b) Auger electron emission.....	66
22a	Uncorrected depth distribution profile of PtGe ₂ on Ge.....	68
22b	Corrected depth distribution profile of PtGe ₂ on Ge.....	68
23	Plot of $\log(I_i^+ M_i^{1/2} Z_i^0 / C_i Z_i^+)$ versus first ionization potential for glasses a) Q33 (21% Si, 20% Li and 55% oxygen), b) K1012 (18% Si, 8% Al, 4% Ca and 61% oxygen) (141). —	70
24	Plot of $\log(I_i^+ M_i^{3/2} Z_i^0 / C_i Z_i^+)$ versus first ionization potential for GaAs (142).....	71
25	Integrated positive ion counts versus the reciprocal of the matrix sputter rate (109)	73
26	Secondary ion yield as a function of the reciprocal of the erosion rate a), and re-plotted b). The reciprocal substrate emission rate per unit area $(n_o \dot{x})^{-1}$ is shown in c). (110).....	75
27	Relative ionization coefficient for Fe and Ni (123).....	79

Figure	Description	Page
28	Ni $2p_{3/2}$ photoemission spectra of Cr-Ni alloys after steady-state bombardment with 15 keV O_2^+ (151).....	82
29	Normalized ionization probabilities of Cr^+ and Ni^+ for O_2^+ bombardment (151).....	83
30	Secondary ion count of $AlGa^+$ as a function of Al concentration in $Al_xGa_{1-x}As$ with Ar^+ bombardment (153).....	87
31	Secondary ion count of Al^+ as a function of Al concentration in $Al_xGa_{1-x}As$ with Ar^+ bombardment (153).....	87
32	Relative ion yield of dopants and matrix species in $Al_xGa_{1-x}As$ (154).....	90
33	Sputter yield versus oxygen surface concentration.....	91
34	Ion count rate versus reciprocal sputter yield.....	92
35	Surface concentration of $Al_xGa_{1-x}As$ determined by Auger electron spectroscopy versus bulk Al fraction (154).....	94
36	Depth distribution of $^{11}B^+$ in GaAs. The Al concentration is inferred from the $^{75}As^+$ signal (155).....	95
37	Relative ion yields versus bulk Al fraction	98
38	Relative ion yields versus modified bond energies (145).....	101

Figure	Description	Page
39	Relative ion yields versus literature values of bond energies.....	102
40	Relative ion yields of Meyer et al. (154), and Galuska and Morrison (145) versus literature values of bond energies.....	103
41	Schematic representation of the Cameca IMS 3f TM (trade mark).....	107
42	Mass spectrum showing molecular interferences.....	118
43	Mass spectrum with magnetic field parameter displayed.....	120
44	Secondary Ion Count Distributions of Cr in GaAs.....	128
45	Secondary Ion Count Distributions of Cr in Al _{0.21} Ga _{0.79} As.....	129
46	Secondary Ion Count Distributions of Cr in Al _{0.40} Ga _{0.60} As.....	130
47	Secondary Ion Count Distributions of Cr in GaAs.....	131
48	Secondary Ion Count Distributions of Cr in Al _{0.21} Ga _{0.79} As.....	132
49	Secondary Ion Count Distributions of Cr in Al _{0.40} Ga _{0.60} As.....	133
50	Secondary Ion Count Distributions of Cr in GaAs.....	134

Figure	Description	Page
51	Secondary Ion Count Distributions of Cr in Al _{.21} Ga _{.79} As.....	135
52	Secondary Ion Count Distributions of Cr in Al _{.40} Ga _{.60} As.....	136
53	Secondary Ion Count Distributions of Cr in GaAs.....	137
54	Secondary Ion Count Distributions of Cr in Al _{.21} Ga _{.79} As.....	138
55	Secondary Ion Count Distributions of Cr in Al _{.40} Ga _{.60} As.....	139
56	Secondary Ion Count Distributions of Cr in GaAs.....	140
57	Secondary Ion Count Distributions of Cr in Al _{.21} Ga _{.79} As.....	141
58	Secondary Ion Count Distributions of Cr in Al _{.40} Ga _{.60} As.....	142
59	Secondary Ion Count Distribution of Cr in GaAs.....	143
60	Secondary Ion Count Distributions of Cr in Al _{.21} Ga _{.79} As.....	144
61	Secondary Ion Count Distributions of Cr in Al _{.40} Ga _{.60} As.....	145
62	Secondary Ion Count Distributions of Si in GaAs.....	146

Figure	Description	Page
63	Secondary Ion Count Distributions of Si in Al _{.21} Ga _{.79} As.....	147
64	Secondary Ion Count Distributions of Si in Al _{.40} Ga _{.60} As.....	148
65	Secondary Ion Count Distributions of Si in GaAs.....	149
66	Secondary Ion Count Distributions of Si in Al _{.21} Ga _{.79} As.....	150
67	Secondary Ion Count Distributions of Si in Al _{.40} Ga _{.60} As.....	151
68	Secondary Ion Count Distributions of Si in GaAs.....	152
69	Secondary Ion Count Distributions of Si in Al _{.21} Ga _{.79} As.....	153
70	Secondary Ion Count Distributions of Si in Al _{.40} Ga _{.60} As.....	154
71	Secondary Ion Count Distributions of Si in GaAs.....	155
72	Secondary Ion Count Distributions of Si in Al _{.21} Ga _{.79} As.....	156
73	Secondary Ion Count Distributions of Si in Al _{.40} Ga _{.60} As.....	157
74	Secondary Ion Count Distributions of Cr in GaAs.....	158

Figure	Description	Page
75	Secondary Ion Count Distributions of Cr in GaAs.....	159
76	Secondary Ion Count Distributions of Si in GaAs.....	160
77	Secondary Ion Count Distributions of Si in GaAs.....	161
78	Secondary Ion Count Distributions of Cr in GaAs.....	164
79	Secondary Ion Count Distributions of Cr in $Al_{.40}Ga_{.60}As$	165
80	Secondary Ion Count Distributions of Si in $Al_{.40}Ga_{.60}As$	166
81	Secondary Ion Count Distributions of Si in $Al_{.40}Ga_{.60}As$	167
82	Secondary Ion Count Distributions of Si in $Al_{.40}Ga_{.60}As$	168
83	Mass spectrum of Si and AlH.....	169
84	Secondary Ion Count Distributions of Cr in $Al_{.40}Ga_{.60}As$	176
85	Concentration profile of Cr in GaAs profiled with O_2	178
86	Concentration profile of Cr in $Al_{.21}Ga_{.79}As$ profiled with O_2	179
87	Concentration profile of Cr in $Al_{.40}Ga_{.60}As$ profiled with O_2	180

Figure	Description	Page
88	Concentration profile of Cr in GaAs profiled with Cs.....	181
89	Concentration profile Cr in Al _{.21} Ga _{.79} As profiled with Cs.....	182
90	Concentration profile of Cr in Al _{.40} Ga _{.60} As profiled with Cs.....	183
91	Concentration profile of Si in GaAs pro- filed with O ₂	184
92	Concentration profile of Si in Al _{.21} Ga _{.79} As profiled with O ₂	185
93	Concentration profile of Si in Al _{.40} Ga _{.60} As profiled with O ₂	186
94	Concentration profile of Si in GaAs pro- filed with Cs.....	187
95	Concentration profile of Si in Al _{.21} Ga _{.79} As profiled with Cs.....	188
96	Concentration profile of Si in Al _{.40} Ga _{.60} As profiled with Cs.....	189
97	Projected range as a function of energy...	193
98	Measured versus displayed primary ion current.....	195
99	Sputter yield variation with aluminum concentration.....	196

Figure	Description	Page
100	Positive practical ion yield relative to GaAs as a function of Al concentration with O_2 primary ion species.....	198
101	Negative practical ion yield relative to GaAs as a function of Al concentration with Cs primary ion species.....	199
102	Positive relative ion yields of Meyer et al. (154), Galuska and Morrison (155) and this work.....	200
103	Local thermal equilibrium analysis showing $\log(I_{i+} M_i^{3/2} z_{i0} / c_i z_{i+})$ versus first ionization potential.....	202
104	Local thermal equilibrium analysis showing $\log(I_{i-} M_i^{3/2} / c_i)$ versus electron affinity...	205

NOMENCLATURE

I_M	measured secondary ion count rate of element m
C_M	concentration of element m
\bar{C}_M	average concentration of element m
J	primary ion beam flux density
Y_M	sputter yield of element m
A	sputtered area
τ_m	practical ion yield
B_M	the probability of ionization
η_M	instrument transmission efficiency
θ_S	angle between the primary ion beam and the surface normal
ψ_S	angle between the secondary ion optics and the surface normal
E_k	kinetic energy
ω_S	azimuth angle
ΔE	energy bandpass
R_M	mass resolution
ΔM	width of the peak at 10% of maximum
m/e	mass to charge ratio
E_1	primary ion energy
E_2	energy transfer to particle 2
θ_2	angle between the centre of the mass and the velocity vector of recoil particle

$F_p(x)$	the depth distribution of momentum
λ	decay length
$I_m(z)$	count rate of mass m at depth z
\bar{I}	the count rate at reference place located at \bar{z}
\bar{z}	from the surface
\bar{z}	the reference plane
$d\lambda/dE$	the rate at which λ changes with energy
Y	total sputter yield
Y_i	the partial sputtering yield of element i
Y_M^C	the component sputter yield
C_M^S	the atomic concentration of element m at the surface
M_1, M_2	mass
Z	the atomic number
δ_2	the nuclear stopping power of the specimen
N_p	the atomic density
E_S	the surface binding energy
ΔH_{at}	the heat of atomization
ΔH_f	the heat of formation
ΔH_s	the heat of sublimation
n_b	the number of atoms per molecule
ϕ	the work function
ϕ_B	the surface barrier height
I_1	the first ionization potential
k_B	Boltzmann's constant
T	the absolute temperature

Q	the transition rate
x	the distance of the atom or ion from the surface
K	the equilibrium constant
h	Plank's constant
Z	the internal partition function
R_m^+	the positive ionization probability
R_m^-	the negative ionization probability
ϕ_m	the effective Fermi energy
T_m	the effective temperature
I_m	the ionization potential
A_m	the electron affinity
E_k	the kinetic energy of ejected particles
V_{ak}	the transfer integral
μ_F	the Fermi level
I	the ionization energy of the sputtered atom
$\epsilon_a(x)$	the valence energy of the sputtered atom
D(x)	the width of the valence energy level
γ_a	a parameter characterizing the spatial dependence of $\epsilon_a(x)$
P^+	the probability of ionization
Z_c	the critical distance for energy level crossings
Δ	level-width function
V_{\perp}	the velocity of the sputtered ion perpendicular to the surface
r	the reference element
\bar{C}_p^S	the surface concentration of the primary ion species

Y_L	the linear sputtering rate in $\text{\AA}/\text{sec}$
n_p^S	the steady-state surface number density of primary ions
ξ	the primary ion accommodation coefficient
β_{NM}^M	the secondary ion yield of M^+ in alloy NM
ρ_{MN}^M	the relative ionization coefficient
K_N^M	the non-linear ionization coefficient
ΔH_f°	the heat of formation -
f_m	the isotopic abundance
$\bar{\Omega}$	the bond energy
Ω_i^O	the bond energy-diatomic, between i and oxygen
σ	the standard deviation
N	the total number of counts, measured secondary ion count
N_T	actual true secondary ion count
N_B	the background secondary ion count
V_D	digital output voltage
I_D	ion count at V_D
V_C	digital voltage corresponding to the centroid

The author of this thesis has granted The University of Western Ontario a non-exclusive license to reproduce and distribute copies of this thesis to users of Western Libraries. Copyright remains with the author.

Electronic theses and dissertations available in The University of Western Ontario's institutional repository (Scholarship@Western) are solely for the purpose of private study and research. They may not be copied or reproduced, except as permitted by copyright laws, without written authority of the copyright owner. Any commercial use or publication is strictly prohibited.

The original copyright license attesting to these terms and signed by the author of this thesis may be found in the original print version of the thesis, held by Western Libraries.

The thesis approval page signed by the examining committee may also be found in the original print version of the thesis held in Western Libraries.

Please contact Western Libraries for further information:

E-mail: libadmin@uwo.ca

Telephone: (519) 661-2111 Ext. 84796


Web site: <http://www.lib.uwo.ca/>

CHAPTER 1
A GENERAL REVIEW

1.1 INTRODUCTION

The microanalysis of the solid surface and near surface region is key to the exploitation and understanding of many phenomena, as well as the exploitation of a multitude of new technologies. Analyses are performed by scientists and engineers seeking to characterize the chemical, structural, and functional properties of materials and processes. A staggering number of techniques have been used to investigate surfaces (1-3), many of which are new and novel, while others were well known in the last century. The analysis of a small volume of material is necessary when the feature under investigation is small. This is often the case in microelectronic, metallurgical, geological and biological samples.

Solid surfaces are frequently analyzed with techniques which bombard with radiation in the form of particles or waves and detect radiation which is emitted or scattered. Secondary ion mass spectrometry (SIMS) is a microanalytical technique in which the specimen is bombarded with ions (typically O_2^+ , O^- , Cs^+ or Ar^+) and ions which are ejected from the sample are detected. SIMS has been widely used



(4;5); alone or in conjunction with complementary analysis techniques, for the characterization of solid surfaces because of its excellent sensitivity. Concentrations of impurities in the part per million range (6,7) can quickly be measured and all elements and isotopes can be detected. Indeed, the count rate of a matrix element is typically in the order of 10^7 counts per second (cps) while the background noise of the detection and counting system is about 0.1 cps. The lateral resolution in favourable circumstances can be 20 to 90 nm (8) and is usually less than 0.5 μm (9). Good depth resolution, 10 to 20 nm per decade (10) of signal during erosion of the sample surface provides information in the third dimension when depth profiling to several microns.

Less fortunate attributes also accompany the SIMS technique. The sensitivity may vary by several orders of magnitude, depending on the ions being monitored (11). Sensitivity also varies with matrix composition, structure and adsorbed surface species (12-16). Along with the emission of elemental ions, molecular ions are ejected. Their presence is one of the factors which limits the sensitivity of the technique (17). The spatial resolution of SIMS is poorer than most electron microscopy techniques and is degraded by mixing and segregation effects induced by the bombarding primary ion beam (18-20). The analysis is destructive and interpretation of the chemical state of the surface is difficult (21,22). Due to the complexity of collision, ejection

and ionization processes the goal of successful quantification from first principles has ~~not been~~ attained.

The word analysis is derived from the Greek root "to loosen"--each of the basic constituents. This is an especially apt description in the case of SIMS analysis. Projectile or primary ions strike a solid with a selectable energy, of the order of 100 eV to 30 keV. A primary ion may be backscattered from the surface or undergo elastic and inelastic collisions, giving up energy until it either escapes from or becomes implanted in the solid. The atoms to which energy has been transferred may be ejected from the surface if they have sufficient energy to overcome surface binding forces. Ejected particles include atoms, either single or as clusters, ions, either monatomic or molecular and electrons. As well, electromagnetic radiation is emitted from the region of bombardment. Most of the sputtered material is uncharged and has an energy of less than 10 eV but a small fraction is charged and may have much higher energy (23,24). This is discussed in more detail in later sections.

The aim of SIMS quantitative analysis is to relate the measured secondary ion count rate I_M , to the concentration C_M of element M in the sample. Actually C_M , the average concentration through the probed volume, is determined in routine analysis (25). The performance of a quantitative procedure is influenced by the presence of measured "random

uncertainties" (i.e. systematic errors, accuracy) (26). The relationship between ion count rate and concentration is defined (60) as

$$I_M = J C_M Y A \tau_M \quad (1)$$

where J is the primary ion beam flux, Y is the sputter yield; A is the sputtered area and τ_M is the practical ion yield, i.e. the ratio of the detected ions of M to the number of atoms of M sputtered from the specimen. This equation applies to a given isotopic ion (e.g. M^+ or M^- or MO^+ etc.). The practical ion yield can also be defined as the product of the probability of ionization and the instrument transmission efficiency, β_M and η_M respectively. Equation 1 becomes

$$I_M = J C_M Y A \beta_M \eta_M \quad (2)$$

The probability of ionization is often called the secondary ion yield by many authors. Lack of knowledge of the factors Y , β_M and η_M hampers the accurate determination of the concentration, C_M .

Empirical approaches to SIMS analysis have shown some success, as have efforts classified as being either first principle or semi-theoretical. Empirical methods include the creation of a calibration curve and the relative sensitivity factor, RSF. A calibration curve is developed by measuring standards of known composition over an applicable concentration

range which for SIMS is usually several orders of magnitude. The element of interest is usually dilute (<1%) and matrix dependent factors are assumed to be constant. Instrument factors must be constant and reproducible. In practice, both long term and short term instrument instabilities limit the usefulness of calibration curves. To overcome these limitations, RSFs make use of an "internal standard", usually the ion count rate of a matrix element (Figure 1). Improved precision is observed if RSFs are selected as an empirical analysis methodology compared to calibration curves.

Empirical methods are satisfactory when a large number of samples of similar composition need to be analyzed on a routine basis. This justifies the meticulous care and dedication required to prepare and characterize standards. Enormous expenses may be encountered in the task of confirming the composition of such standards by other, frequently time consuming, techniques. These difficulties would be overcome by a quantification approach based on first principle calculations.

Simple models of secondary ion emission have been proposed by a number of authors (28-32). Some models, such as the local thermodynamic equilibrium model (28) can be applied to a broad range of complex matrices, are based on much criticized assumptions and yet have a surprisingly good accuracy of between 25% and a factor of 2 (26). Other models, such

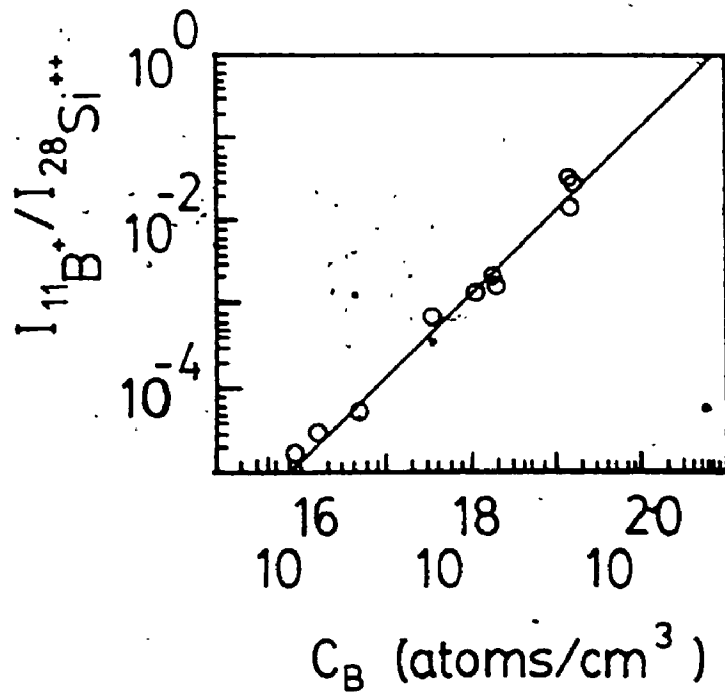


FIGURE 1 Relative sensitivity factor for boron in silicon, showing linearity of $^{11}B^+$ signal ratioed to the silicon matrix signal $^{28}Si^{++}$ with respect to concentration (36)

as those dealing with autoionization (29) or local bond breaking (21,30) tend to give some insight into a particular ionization process, but can not be readily applied to a broad base of analysis situations which are of practical interest.

The importance of SIMS analysis for semiconductor process and device development was recognized by early workers (33-38). Indeed, the reliable measurement of ion implanted semiconductor material was so successful, in agreement with theoretically predicted and electrically measured concentration profiles, that it has been adopted as a method for providing analytical standards. To be classified as a SIMS standard, a specimen must fulfill a number of criteria; a) it should be laterally homogeneous on a submicron scale, b) be chemically stable over an extended time frame, c) have had independent assessment by other analysis techniques, and d) should have the capability of providing samples over a large composition range (39). In addition to these requirements, ion implantation has the advantage that it can be applied to many element/matrix combinations. By using ion implanted standards, the SIMS detection limit for many elements has been shown to lie in the range of 10^{16} to 10^{17} atoms/cm³ with a value as low as 10^{13} atoms/cm³ for some elements (40). The detection limit depends not only on the implant species but on the semiconductor matrix as well.

Many analytical situations are encountered where matrices

of significantly different composition are sputtered in succession when characterizing the feature of interest. An example of this in the semiconductor industry is the aluminum gallium arsenide ($\text{Al}_x\text{Ga}_{1-x}\text{As}$) system. A variety of semiconductor devices are fabricated with four or more layers of $\text{Al}_x\text{Ga}_{1-x}\text{As}$ with x varying from 0.01 to 0.6. These layers in turn are intentionally doped or contain undesired impurities. SIMS quantitative analysis of the major elements and dopants in these structures relies upon the exact understanding of and compensation for the matrix effect. The work described in this thesis is an evaluation of the SIMS matrix effect in the $\text{Al}_x\text{Ga}_{1-x}\text{As}$ system.

1.2 EARLY CONTRIBUTIONS

The emission of "secondary rays", a small fraction of which carried a positive charge as a result of bombarding a metal with ions, was reported by J.J. Thomson (41) in 1910. By the 1930s, secondary ion formation studies had gained wider interest. Sawyer (42) observed and Woodcock (43) and Thompson (44) correctly identified negative secondary ions. Arnot and Milligan (45), in the course of determining whether Hg^- was stable--and if stable the value of its electron affinity--proposed the occurrence of electron exchange between a tungsten surface and a beam of Hg^+ producing Hg^- . Later studies by Arnot (46,47) and with Becket (48) led to the observation of the negative ions C^- , O^- and COH^- from absorbed

gas species. During the same period, similar experiments were carried out by Sloane and Press (49) who constructed an apparatus to mass analyze the primary ion species Hg^+ before it interacted with the metal surface. They failed to observe Hg^- but did observe C_3H^- and CO^- . These early workers did not mention whether they observed metal ions from the tungsten surfaces which were bombarded. It may be that the available apparatus did not have the sensitivity to detect these ions. Sloane and Press did recognize that the interaction of a beam of particles with a solid is a sputtering process.

The analysis of secondary ions experienced a dormant period during the Second World War but attracted new interest in the 1950s when Honig (50) adopted it to study the sputtering process. At that time he stated, ". . .there has been considerable speculation but very little experimental evidence concerning the charge and state of aggregation of sputtered particles". Honig went on to cite Herzog and Viehböck's (51) short letter to Physical Review in 1949 describing in general terms work that had begun in generating positive secondary ions by a sputtering process. Honig also outlined the requirements for an ideal sputtering experiment and many of these conditions are of concern in SIMS experiments today. They include: a) knowledge of the crystallinity of the specimen and its orientation, b) provisions to heat or cool the specimen, c) mass analysis of primary ions with arrangements for knowing and varying their energy and

angle of incidence, d) a stable ion source capable of generating current densities of several mA/cm^2 , e) determination of the mass of the sputtered ions as well as their kinetic energy distribution, angular distribution and yield, and f) determination of residual gases in the specimen region. Despite the knowledge of these requirements, early researchers were unable to satisfy them. Ions sputtered from the target were observed by Honig, who tried to relate the observed secondary ion count rate from a Ge/11% Si crystal to its composition. The estimated Si content varied by a factor of 2 with changes in the primary ion energy (100 to 400 eV). His detailed examination of this specimen qualifies this as the first reported attempt of SIMS quantitative analysis. Later, Bradley (52) found the count rate of Ca^+ secondary ions from Ca present as a trace impurity in a Pt sample, to be comparable to the Pt^+ count rate. This was attributed to the difference in ionization potentials of the two species.

Examination and refinement of the SIMS technique continues today, with application to a broad range of analytical problems. Major contributions have been made by Andersen and Hinthorne (53) in an early model of secondary ion emission which served as a catalyst for later models; by Castaing and Slodzian (54) in their development of the ion microscope and by Liebl (55) and coworkers for advances in the design of ion microprobes.

1.3 THE SIMS TECHNIQUE

A secondary ion mass spectrometer is an instrument for generating primary ions, directing them at a specimen and analyzing the sputtered secondary ions (Figure 2). Commonly used primary ion sources include the duoplasmatron (56,57), the liquid metal ion source (58) and the surface ionization source (59). The primary ion beam is mass analyzed to remove source impurities and undesired charge states (60). Ion optics focus and direct the primary ion beam. Neutral components in the primary beam may be removed by deflecting the beam with an electric or magnetic field prior to impact with the specimen. The primary beam hits the sample at an angle, θ_S , with respect to the surface normal. Secondary ions sputtered from the specimen are accelerated by an electric field and collected by secondary ion optics which are at an angle, ψ_S , to the surface normal. The secondary ions are energy and mass analyzed before detection.

Secondary ions are sputtered from the specimen with a kinetic energy E_k , and a direction defined by the emergence angle ψ_S with respect to the specimen normal and ω_S , the azimuth angle with respect to the plane containing the incident beam direction and specimen normal (Figure 3). The angular distributions of secondary ions for various targets (61) are shown in Figure 4. The function cosine ψ is plotted for comparison. Typical kinetic energy distributions are

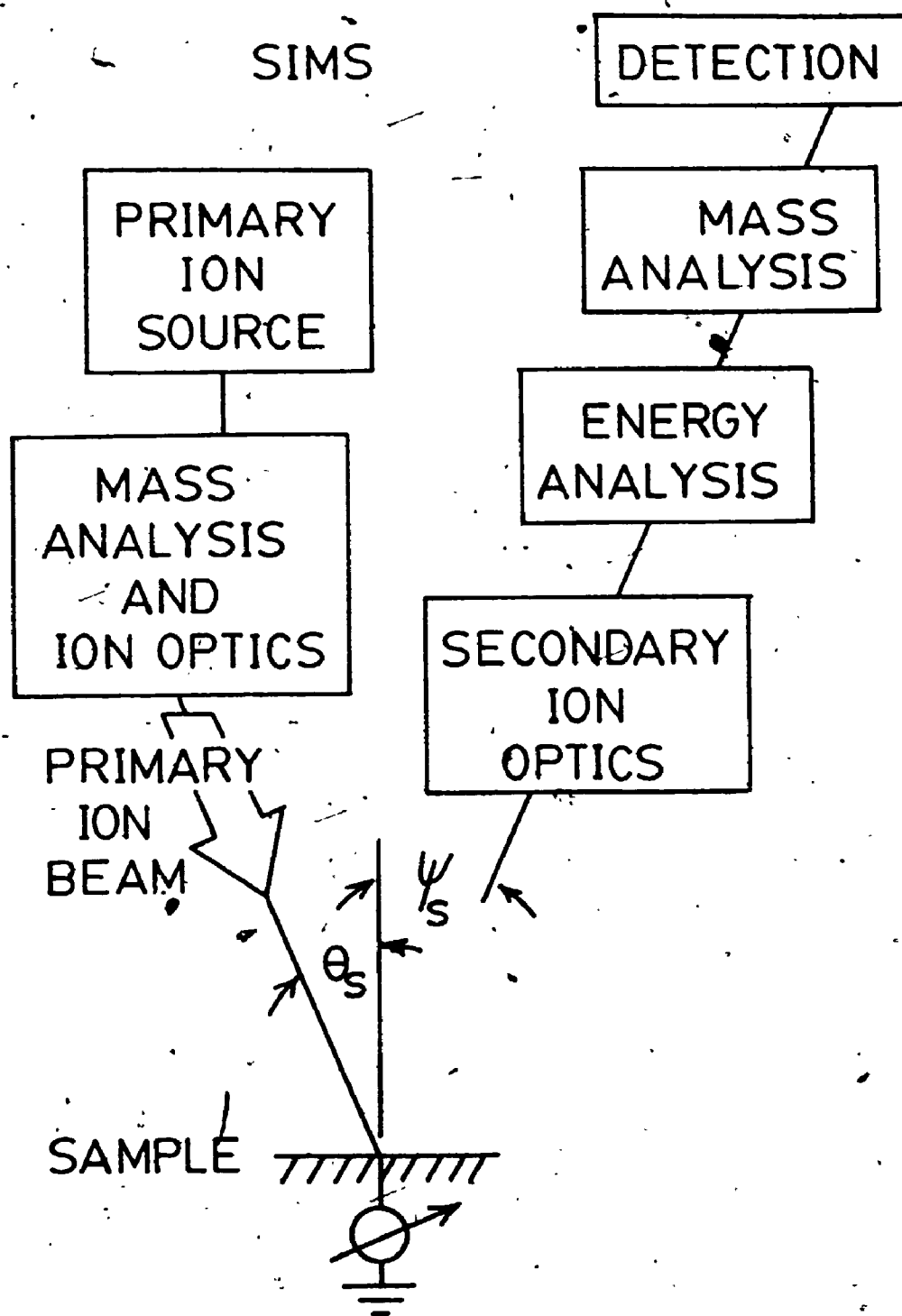


FIGURE 2 Schematic representation of a secondary ion mass spectrometer

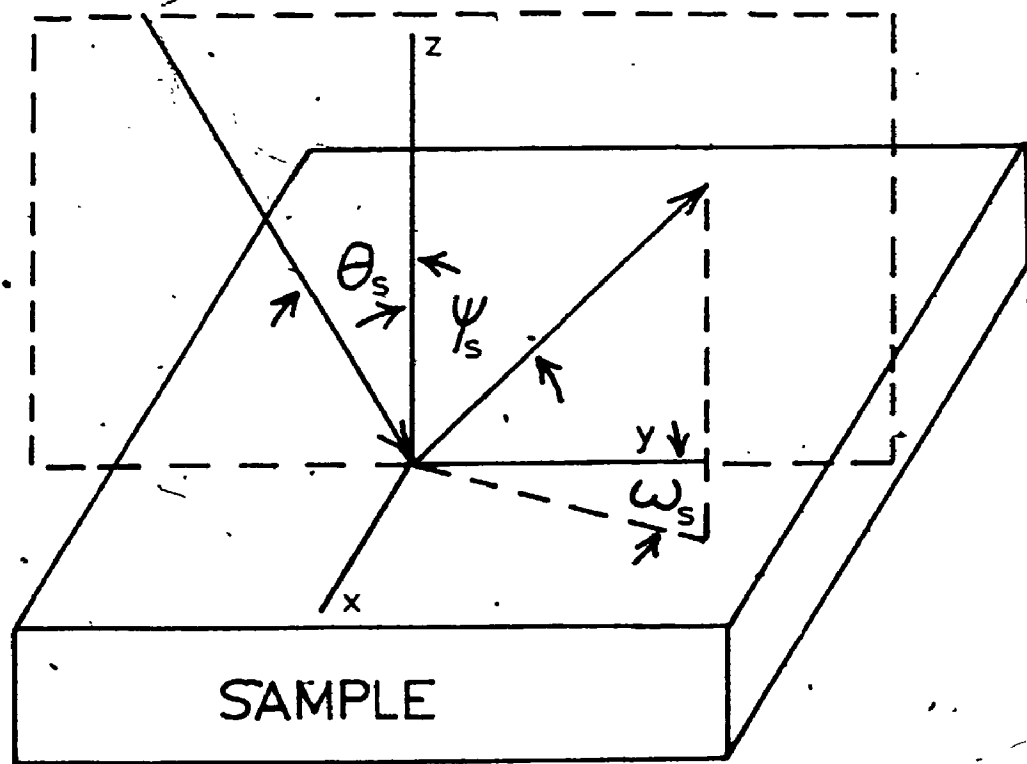


FIGURE 3 Three-dimensional representation of ion trajectories

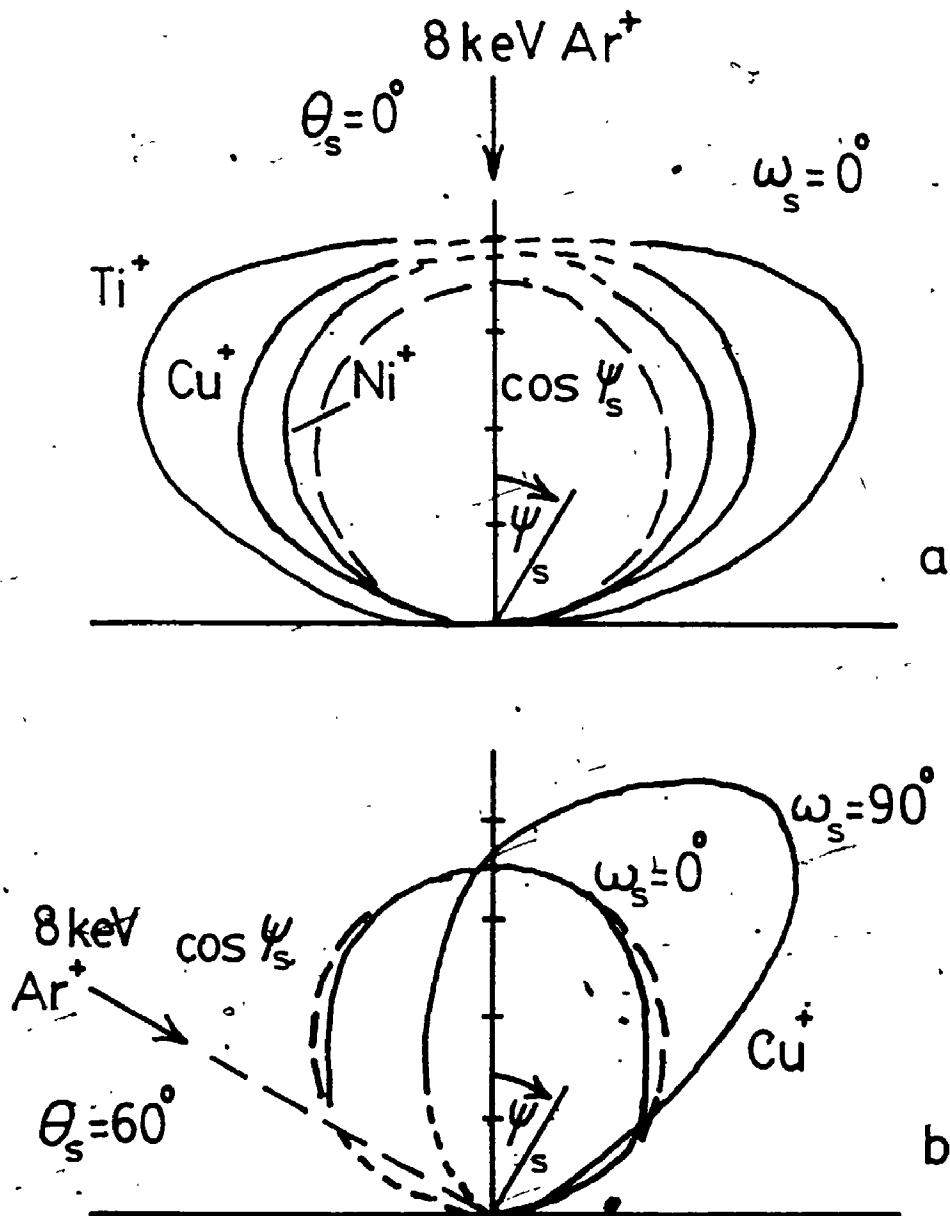


FIGURE 4 Angular distributions of various secondary ions. The ordinate axis is count rate (61).
 a) normal primary beam incidence, $\theta_s = 0^\circ$
 b) $\theta_s = 60^\circ$

plotted in Figure 5. The kinetic energy distribution increases rapidly from low energies to peak at a few electron volts. The distribution then decreases. The rate of this decrease is much greater for molecular ions than for monatomic ions. The distributions are uncorrected for energy filtering by the collection optics. A typical SIMS instrument allows only a fraction of the ions, with a given energy band pass ΔE , to be transmitted through the energy analyzer. Ions created in the region between the specimen and the accelerating ion optics account for the ions shown as having energies less than zero.

Instrument design is diverse and the technique has evolved in a number of distinct directions. The terminology *static* SIMS denotes the SIMS technique utilizing low primary ion current densities (less than 10 nA/cm^2). This results in a specimen erosion rate of less than 10^{-2} atomic layers per second. Molecular ions characteristic of absorbed gases on metals have been investigated and other studies have dealt with the emission of organic molecules from polymer systems. Static SIMS provides information about fundamental processes of secondary ion formation and radiation damage, especially for organic molecules. In addition, there are applications such as surface reaction studies of catalysts (62). Ultra high vacuum conditions (10^{-7} to 10^{-10} Pa) are necessary to reduce residual gas adsorption and a large area (about 0.1 cm^2) is bombarded in order to obtain greater sensitivity. In contrast, *dynamic* SIMS employs high primary ion current

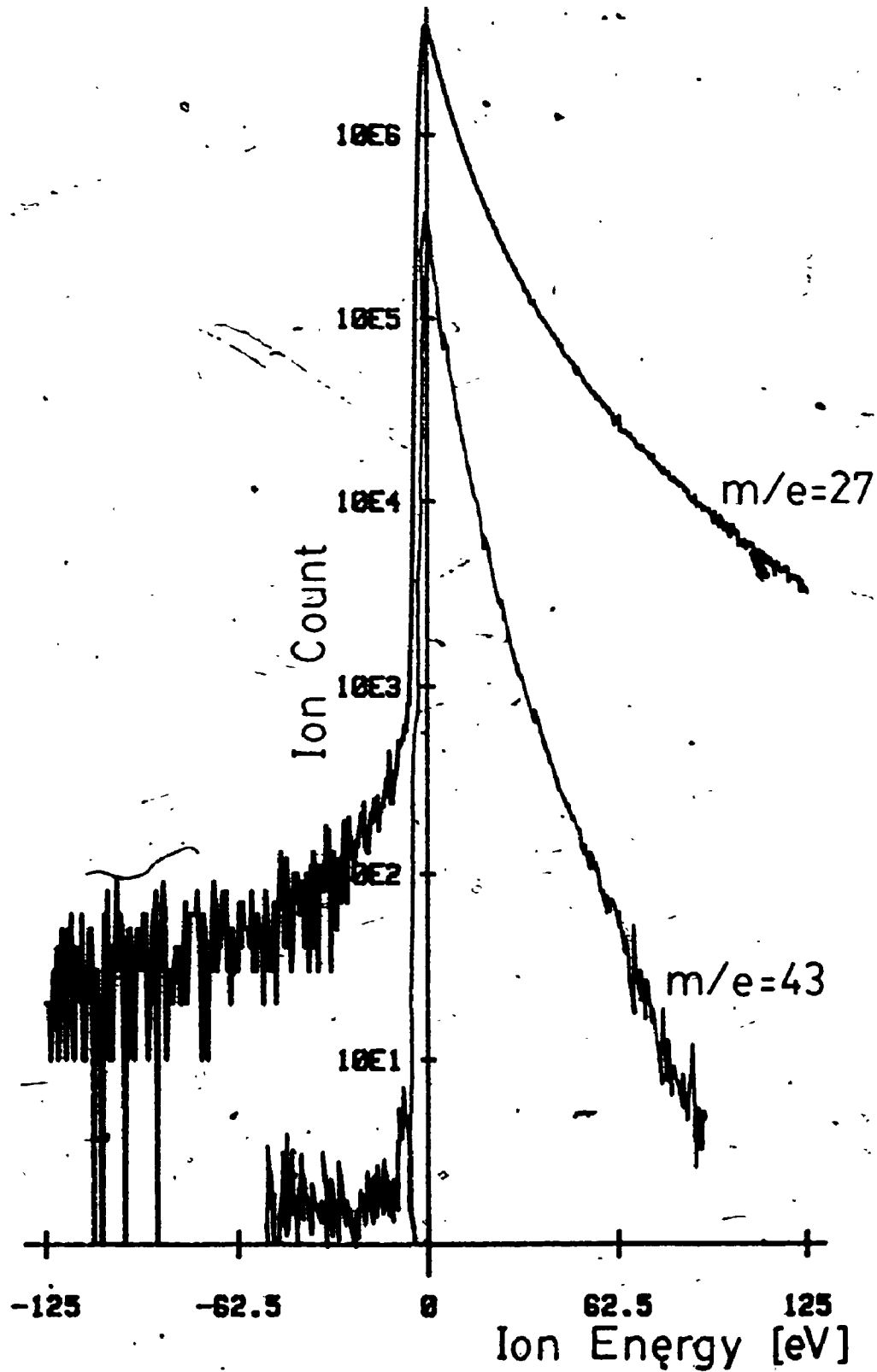


FIGURE 5 Energy distributions of $^{27}\text{Al}^+$ and $^{27}\text{Al}^{16}\text{O}^+$ secondary ions

densities (larger than 10 nA cm^{-2}) which results in erosion rates of greater than 10^{-2} atomic layers per second. As a result, vacuum requirements are less stringent and the analysis area is smaller (250 to $25,000 \text{ } \mu\text{m}^2$).

In classifying SIMS instrumentation a distinction is made between an ion microscope and an ion microprobe. A direct imaging ion microscope is analogous to the light microscope and has ion optics which ensure (if correctly designed and maintained) that secondary ions emitted from the specimen maintain their spatial relationships when projected on an image plane. The spatial resolution of such a secondary ion image is dependent on the secondary ion optics and is independent of the primary ion beam. Secondary ions are converted to a visible image by way of an ion to electron converter, most often a microchannel plate. This array of 10^4 to 10^7 miniature electron multipliers is composed of small glass channels, about $50 \text{ } \mu\text{m}$ in diameter. Ions strike the walls of these channels giving rise to secondary electrons which produce additional electrons on collision with the walls of the microchannel before striking a fluorescent screen or resistive anode encoder (63).

An ion microprobe is analogous to a scanning electron microscope. The imaging system is composed of a cathode ray tube (CRT) which is rastered in unison with the primary ion beam. The intensity of the CRT is controlled by the intensity

of the secondary ion signal. The spatial resolution of an ion microprobe depends critically upon the size of the primary ion beam striking the sample.

Ion microscopes have a magnetic sector mass spectrometer (MS) in the secondary ion detection section, while ion microprobes may have either a magnetic sector MS or a quadrupole MS. The performance of a MS can be characterized by its a) mass resolution, R_M , b) energy bandpass, ΔE and c) transmission efficiency, η_M . The mass resolution is defined as the ratio of the mass, M , analyzed to the width of that mass, ΔM , measured at a percentage of the peak count rate (typically 50% or 10%) as illustrated in Figure 6, where ion count is plotted versus mass to charge ratio, M/e so that

$$R_M = \frac{M}{\Delta M} \quad (3)$$

The variables R_M , ΔE and η_M are all interdependent. To obtain high mass resolution both the energy bandpass and transmission are reduced.

Magnetic sector MSs are frequently double focussing and utilize the fact that ions in a uniform magnetic field follow a circular path. Ions with a given mass to charge ratio pass between slits to the detection system. Magnetic sector instruments have a mass range which is typically 1 to 250 atomic mass units (amu). Advantages of this type of MS include a) excellent mass resolution, adjustable from 200 to

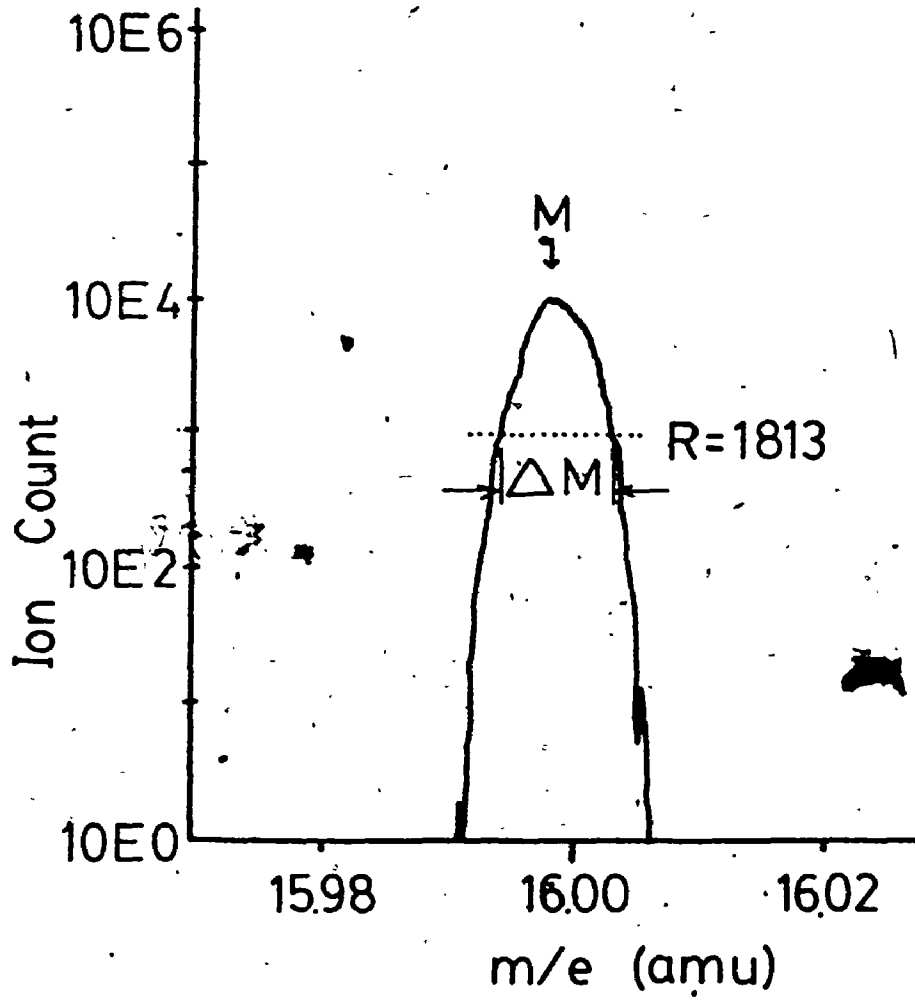


FIGURE 6 Mass resolution

10,000 b) the capability of filtering high energy ions and c) a first-order correspondence between object and image planes (64). Disadvantages include a) slow scanning speed over a given mass range, b) the presence of a magnetic field and c) their large size.

Quadrupole MSs are composed of four conducting rods to which direct current and radio frequency signals are applied. Ions with a narrow range of mass to charge ratios are transmitted while others are forced into unstable trajectories of increasing amplitude and are not detected. Advantages of quadrupole MSs include a) the absence of a magnetic field, b) rapid mass switching, c) a large mass range (1 to 10,000 amu) and d) compactness. Disadvantages are a) poor mass resolution (20 to 500) especially at low masses, and b) the inability to filter high energy ions or electrons.

Aside from the limitations imposed by the MS on the ion microscope or ion microprobe, the primary ion optics of ion microprobes with small diameter ion sources make them superior for analyses requiring high spatial resolution.

1.4 ANALYTICAL CONSIDERATIONS

In planning SIMS analysis and in the interpretation of SIMS information, a number of factors must be carefully considered to evaluate if they will or are influencing the analysis. These factors may be related predominately to the

instrument conditions under which the analysis will be performed or may result from some interaction between the bombarding species and the specimen. Instrument operating conditions can be optimized to reduce or eliminate a) mass interferences, b) the crater wall effect or c) memory effects. Other factors such as d) specimen charging, e) diffusion, f) segregation, g) preferential sputtering, h) recoil implantation and i) cascade mixing; result in the transport of material in the specimen during the sputtering process.

High mass resolution is required to distinguish between monatomic ions and cluster ions. For example, $^{28}\text{Si}^+$ has an atomic weight of 27.97693 amu and $^{27}\text{AlH}^+$ has a molecular weight of 27.98936 amu (65). The true mass differs from the integer mass by the mass defect. A separation of these masses in order to provide a 10% valley between peaks of equal count rate requires a mass resolution of 2251. In some instances, energy discrimination is an alternative to using high mass resolution conditions. Monatomic species of higher kinetic energy may be detected if low energy cluster ions are eliminated. Unfortunately, this tactic is unsuccessful with a cluster ion such as ^{27}AlH which has an energy distribution very similar to ^{28}Si . Furthermore, the cluster ion may be the signal of interest rather than the monatomic species, in which case the use of high mass resolution conditions is mandatory.

Crater edge effects degrade depth resolution during depth profiling and result from sampling the secondary ion signal over a range of depths during a measurement, i.e. when the field of view of the spectrometer includes a portion of the crater wall. Surface roughness may also lead to contributions of secondary ions from a range of depths. The primary ion beam is rastered in SIMS instruments in order to obtain uniform sample erosion. Ion microprobes attempt to eliminate the crater wall effect by electronically gating the detector so that the secondary ion signal is acquired only when the primary ion beam is in the central portion of the crater. An ion microscope accomplishes the same effect by limiting the field of view of the mass spectrometer by means of a mechanical aperture positioned on an image plane. Magee et al. have shown that the dynamic range of implant profiles is dramatically increased by rastering the primary ion beam, electronically gating the secondary ion signal and by reducing the field of view of the spectrometer (66). A high velocity neutral component accompanies all ion beams as a consequence of the ion generation and transportation process. The neutral component is not rastered with the primary ion beam so it strikes the crater wall if no precautions are taken and generates secondary ions from a range of depths when the electronic window is open. The neutral flux is not generally a concern with an ion microscope if the flux is uniform over the field of view of the spectrometer.

Care must be taken however, in positioning the specimen and primary ion beam to ensure that the axis of the field of view of the secondary ion optics lies in the centre of the crater (67). Material from the crater wall may also be transported to the zone in which information is gathered by sputtering or surface diffusion. This is combatted by increasing the rastered area or by decreasing the field of view.

Material which has been sputtered from the specimen will be deposited on sample holders, lens and apertures. This coating may be resputtered during subsequent analyses and reach the detector. This is called the memory effect (66) and is greatly influenced by instrument design; specifically, the nature and location of any lens near the target. The memory effect is controlled by cleaning and replacing lens and components or by coating these components with another species of sputtered material--immediately before a crucial analysis. It has been shown that this coating procedure improves the detection limit for a ^{11}B implant in Si. from 10^{15} to 5×10^{13} atoms/cm³ (40).

Specimen charging may seriously limit the SIMS analysis of low conductivity specimens. Since there is a net electric charge inherent in bombarding a specimen with a primary ion beam, the region under bombardment may build up a local charge which may deflect the primary ion beam and limit the

secondary ion signal: Specimen charging can be reduced by a) coating the specimen with a conductive layer prior to or during analysis so that excess charge is dissipated, b) the use of an electron flood gun to balance the charge of a positive primary ion beam or c) neutralizing the primary ion beam in a high pressure gas chamber before it bombards the specimen. In addition, a novel solution has been reported which allows the specimen to charge to an equilibrium level within an apertured region (68). Although secondary ion signals from such a region are less intense, the signals from most constituents are still large and free from cluster ion interference.

The transport of atoms within the specimen may occur by a number of diffusion assisted mechanisms during ion bombardment including: a) thermal diffusion, b) radiation enhanced diffusion and c) space charge enhanced diffusion. Thermal diffusion can bring about compositional changes over regions much greater in size than the distances covered by the range of primary ions. This is normally a concern for sputtering at elevated temperatures and was observed by Rehn et al. (69) investigating Cu-Ni alloys with Auger electron spectroscopy (AES). About the same degree of Ni enrichment (Cu depletion) of the surface was found during Ar⁺ bombardment for specimen temperatures up to 300°C. At higher temperatures, Cu depletion extended many atomic layers below the surface providing a long-range driving force for Cu

diffusion. Shikata and Shimizu (70) observed Cu diffusion at 300°C for a Cu₅₀-Ni₅₀ alloy and estimated the diffusion coefficient of Cu to be $\sim 10^{-14}$ cm²/sec. This value is much larger than expected ($\sim 10^{-20}$ cm²/sec) for Cu-Ni alloys (71) at this temperature. However, the alloy used in this study was polycrystalline and contained a number of defects which can aid diffusion. Defects are also introduced by ion bombardment.

Radiation enhanced diffusion may occur during sputtering since many of the lattice atoms are displaced during a collision cascade. This creates vacancies, interstitials and other lattice defects which enhance diffusion. The diffusion coefficient at 25°C for Cu in a Cu-Ni alloy was found to vary almost linearly from 1.8 to 8.0×10^{-16} cm²/sec with Ar⁺ ion energy which was increased from 0.5 to 2 keV (20).

Space charge enhanced diffusion causes a dramatic effect, especially when depth profiling insulators. Gossink et al. examined sodium implanted at an energy of 80 keV in silicon dioxide to a dose of 10^{15} atoms/cm² (72). The sodium profile obtained by SIMS analysis using O⁻ bombardment is shown in Figure 7 and indicates a projected range of about 100 nm. This is close to the calculated range of 110 nm. The measured sodium profile with O₂⁺ bombardment on the same sample is shown in Figure 8. The profile is completely distorted and indicates the sodium is driven to the SiO₂/Si.

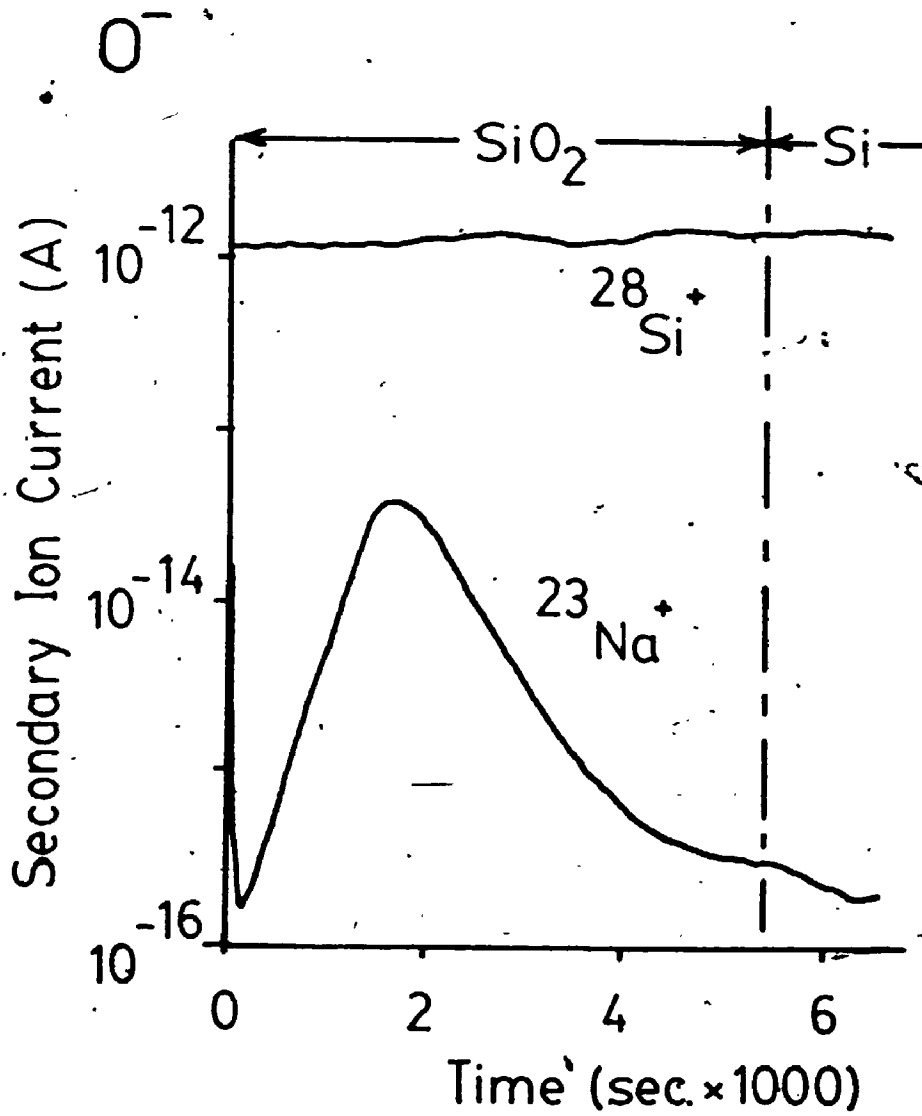


FIGURE 7 Profile of sodium in silica glass using $^{16}\text{O}^-$ bombardment

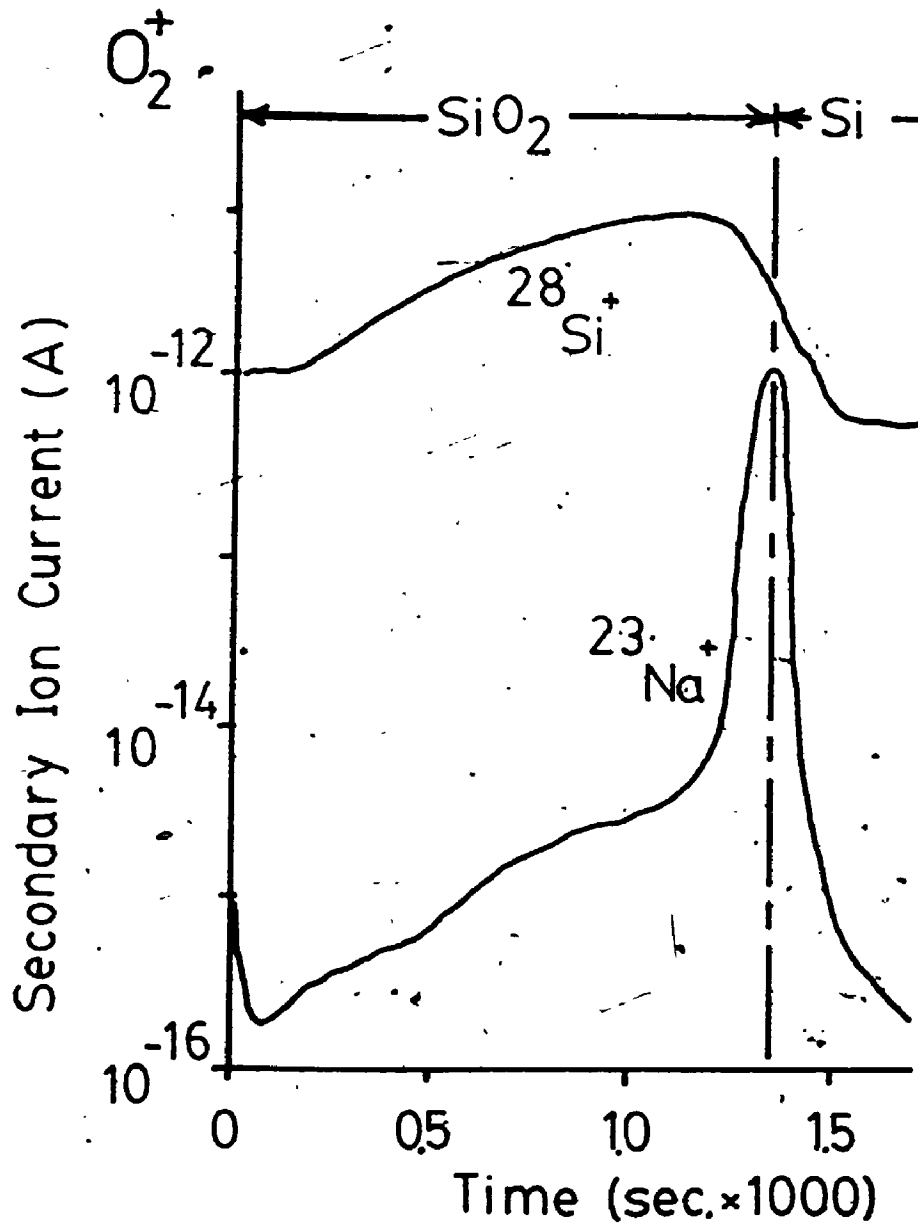


FIGURE 8 Profile of sodium in silica glass using $^{16}\text{O}_2^+$ bombardment

interface by the change in polarity of the primary ion. A silver film sandwiched between layers of ZnO has been studied by Johnston et al. (73). Progressively better results were obtained in using O_2^+ , O^- , Ar^+ and Xe^+ primary ion beams. A 5 keV Xe^+ primary beam gave results which agreed within $\pm 10\%$ of Rutherford backscatter analysis (RBS) results--an independent analysis technique. Space charge enhanced diffusion and mixing were both suspected to play a role in explaining these observations.

Surface segregation has occurred if the surface composition of an alloy is different from the bulk. Segregation may enhance or reduce the sputtering of an alloy component. Comparisons of surface segregation to radiation enhanced segregation show opposite behaviour for many binary metal alloy systems. That is, if alloy M-N shows enrichment of M because of surface segregation, then under ion bombardment a depletion of M is observed. The surface composition of binary alloys is expected to be enriched by the alloy element with the lower heat of vaporization according to a thermodynamic model (74). However, within four atomic layers the composition becomes the same as the bulk alloy. Calculations for Cu-Ni alloys predict enrichment in Cu in the surface region in agreement with Auger Electron Spectroscopy (AES) analysis by Quinto et al. (75). During Ar^+ bombardment, these workers found Ni enrichment in accordance with the above observations. Radiation enhanced segregation may occur

if a driving force exists between the bombarded surface and the surrounding defect-free zone.

Liau (76) has observed that as a rule of thumb the heavier component of an alloy is generally found to be enriched in a surface layer following sputtering. Au enrichment greater than the bulk composition for Cu_3Au was observed within 4 nm of the surface for noble gas sputtering (77). Arsenic enrichment has been found for bombardment of GaAs by He, Ne and Ar (78); however, conflicting reports exist showing a Ga surface enrichment using ions of rare gases with 0.5 to 2 keV energies (79-81). No enrichment was observed in a study of the $\text{Al}_x\text{Ga}_{1-x}\text{As}$ system (82). The surface enrichment of the high vapour pressure component above its equilibrium concentration can lead to spontaneous desorption (83). This mechanism of desorption would limit surface segregation. In a similar vein, Wittmaack (84) has proposed that for bombardment of $\alpha\text{-Si}$ with Ar and Xe, a steady-state condition is reached where each inert gas ion striking the specimen causes the ejection of one previously implanted gas atom.

Preferential sputtering takes place when atomic species of a multicomponent solid are not sputtered in proportion to their surface concentration. This interpretation of preferential sputtering is equivalent to postulating "different ejection probabilities of the different sputtered species" (85).

It may occur due to a) the nature in which energy from collisions is shared between different atoms in the solid, b) the different binding energies and c) chemical interactions between the primary ions and atoms of the solid, leading to the formation of compound surface layers. Preferential sputtering of one component from the surface results in the formation of an altered layer in the near surface region. This altered layer is stoichiometrically different from the bulk composition and is generally thicker than the depth from which material is sputtered. At high fluences of primary ions a dynamic equilibrium may be obtained if mechanisms such as diffusion, segregation, knock-on and cascade mixing result in the transportation of material to and from the altered layer. Extensive reviews of preferential sputtering and near surface composition changes have been carried out by Kelly (86), Carter and Colligon (87) and Betz and Wehner (88).

Recoil implantation and cascade mixing should be minimized during SIMS analysis if at all possible. Failing this, it is important to recognize these phenomena and include them in any interpretation of results. The simplest case of recoil implantation occurs if a primary ion undergoes a close to "head-on" collision with an atom of the specimen and momentum is transferred to the atom, causing it to recoil and be driven into the specimen. The energy transferred, E_2 , in an elastic collision between a primary ion of mass m_1 and

energy E_1 and atom of mass m_2 with zero initial energy according to the laws of conservation of energy and momentum is

$$E_2 = \frac{4m_1m_2}{(m_1+m_2)^2} E_1 \sin^2 \left(\frac{\pi - 2\theta_2}{2} \right) \quad (4)$$

where θ_2 is the angle between the vector describing the velocity of the centre of mass of the two particles and the velocity of the recoil. For a head-on collision, $\theta_2 = 0$ and then

$$E_2 = \frac{4m_1m_2}{(m_1+m_2)^2} E_1 \quad (5)$$

and the maximum energy is transferred. The probability distribution of energy transfer is determined by the cross-section of the atomic collision which varies as a function of initial energy, E_1 . Of course in the conditions employed for SIMS sputtering, a great number of collisions occur, both between primary ions and atoms and between atoms to which energy has been transferred and other atoms in their equilibrium condition. These subsequent collisions are called a cascade.

Cascade or recoil mixing refers to displacements as a result of a collision cascade and has been modeled by computer simulation (89) and utilizing transport theory (19, 90-92). Littmark and Hofer (90) predict that the depth distribution of momentum, $F_p(x)$ for Si bombarded with Si (Figure 9) is negative (particle velocity outward away from

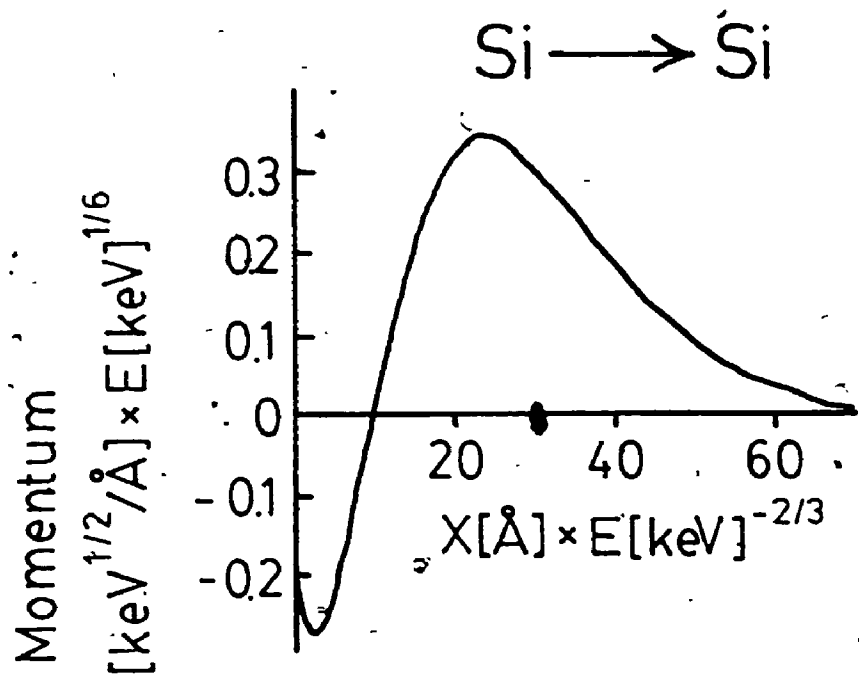


FIGURE 9 Predicted depth distribution of momentum (90)

the specimen) at the surface, peaks at shallow depths then passes through zero to become positive at larger depths. A thin tracer layer (2 nm) in Si sputtered with 5 keV Ar at normal incidence would become mixed according to its position relative to the surface (Figure 10). Their model predicts that the normalized sputter yield of the tracer broadens and the maximum in the distribution shifts towards the surface as the tracer's origin is shifted to greater depths.

Mixing is readily observed during the depth profiling of thin films on a substrate. The Pt-Si (76) system has been examined to study mixing using high energy Xe⁺, while Williams (93) reported exponential tails in the profiles of C, Si₃N₄, NiSi, PdSi, PtSi and Au on Si sputtered by 20 keV Cs⁺. Wack and Wittmaack (94) investigated Li, B, N, O, F, Na, Mg and Al implants in Si sputtered with either O₂⁺ or Ar⁺. They characterized the exponential tails of these low energy (3 to 5 keV) implants with a decay length, λ . The tail of the experimentally determined profiles is described by the equation

$$I_m(z) = \bar{I} \exp(-(z-\bar{z})/\lambda) \quad (6)$$

where the intensity $I_m(z)$ is the observed count rate of mass m at depth z , \bar{I} is the count rate at a reference plane located at \bar{z} from the surface. The observed decay lengths are shown in Figure 11. They interpreted the high λ -values for

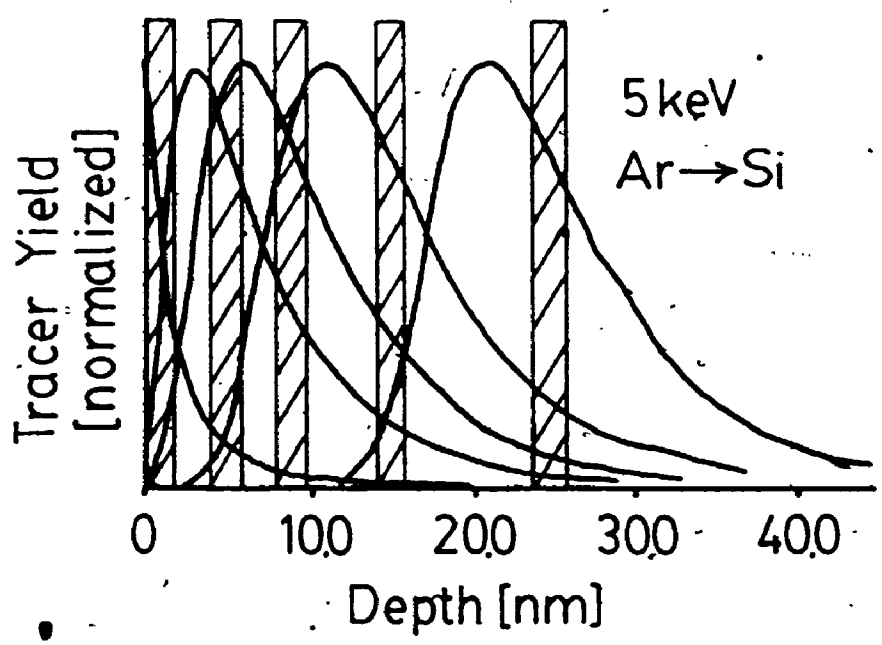


FIGURE 10 Predicted tracer profiles of sputtered atoms for square-shaped tracers positioned originally at different depths (90)

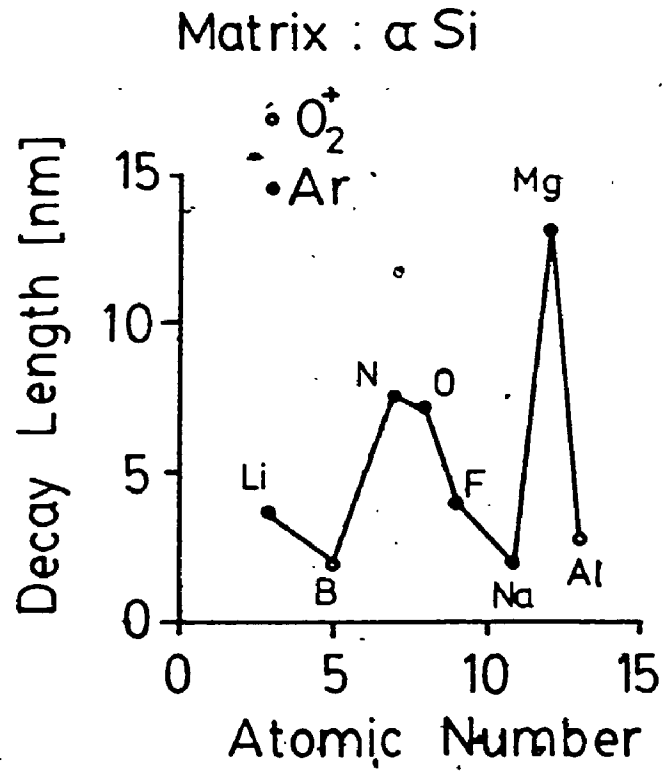


FIGURE 11 Measured decay lengths for implants in silicon (94)

N, O, and Mg as the result of radiation enhanced diffusion. When they compared their results to those of Littmark and Hofer (90) they found satisfactory agreement. The decay length predicted by Littmark and Hofer's model of mixing for Si in Si sputtered by 5 keV Ar⁺ was 5 nm. Lidzbarski and Brown (95) examined a variety of thin films on Si with Cs⁺, O⁻ and O₂⁺ primary ion beams at a number of energies. λ was found to increase linearly with primary ion energy but the rate at which λ changes with energy, $d\lambda/dE$, varies with the primary ion. Au and Pt films exhibited very long decay lengths with practically no energy dependence under Cs⁺ bombardment.

1.5 SPUTTERING

The total sputter yield, Y , resulting from the ion bombardment of the specimen is defined as the average number of atoms of the specimen removed per incident particle,

$$Y = \frac{\text{number of atoms of the specimen removed}}{\text{number of incident particles}} \quad (7)$$

or

$$Y = \frac{\text{(number of neutral atoms + number of monatomic atoms + number of molecules x number of atoms per molecule + number of molecular ions x number of atoms per molecular ion) leaving the specimen}}{\text{total number of incident particles}} \quad (8)$$

The sputter yield may be determined for incident particles other than ions, it can be defined for projectiles such as

atoms, neutrons, electrons or photons. Sputtering by primary molecular ions may be calculated per incident molecule. In determining sputter yields only atoms of the specimen which have been removed are counted; the incident particles which are implanted and subsequently sputtered are not included.

The partial sputtering yield of an element in a multi-component system may be defined as

$$Y_i = \frac{\text{number of atoms of element } i \text{ of the specimen removed}}{\text{number of incident particles}} \quad (9)$$

so that the total sputter yield is

$$Y = \sum_i Y_i \quad (10)$$

The component sputter yield is defined as

$$Y_M^c = \frac{Y_M}{C_M^s} \quad (11)$$

where C_M^s is the atomic concentration of element M on the surface.

Physical sputtering takes place above a threshold of about 20 eV. The sputter yield increases with increasing primary ion energy and, for a given primary ion energy and species, the yield increases as the average mass of the specimen increases (96). The sputter yield reaches a broad maximum in the energy region of 5 to 50 keV. Three regimes

of physical sputtering have been proposed (97): a) the single knock-on, b) the linear cascade and c) the spike regime. In the single knock-on process, energy is transferred from the primary ion to the specimen atoms. These atoms may undergo a small number of further collisions before being sputtered from the specimen. This process is characteristic of interactions in the low energy region. In the linear cascade regime, recoil atoms are energetic enough to generate higher order recoils, while in the spike regime the majority of atoms within a given volume share the energy of the bombarding ion (Figure 12). The linear cascade region is characteristic for most keV and MeV ions except for the heaviest ions which tend to generate spikes. Sputtering in the linear cascade regime has been described by a transport model of Sigmund (98). In addition to physical sputtering, chemical sputtering may occur if compounds with low binding energies are formed on the surface (99). There is often no distinction drawn between physical and chemical sputtering and at an extremely high flux of primary ions where high temperatures are generated in the specimen, even evaporation may occur (Figure 13).

An extensive review of experimentally determined sputter yields of single element solids has been carried out by Andersen and Bay (100). The sputtering of multicomponent solids has been reviewed by Betz and Wehner (88). The sputter yield of aluminum by various primary ions as a function of

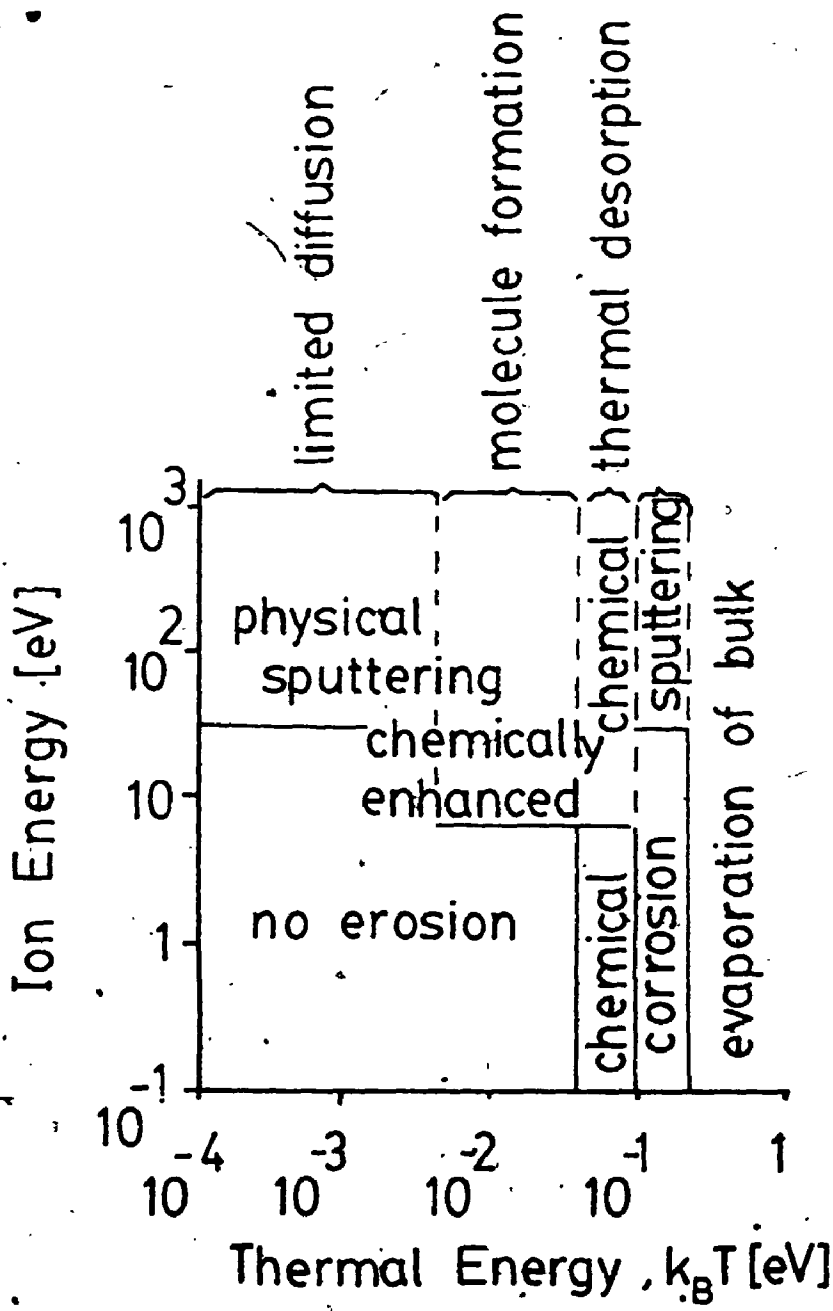


FIGURE 13 Sputtering and evaporation regions defined by ion energy and thermal energy (99)

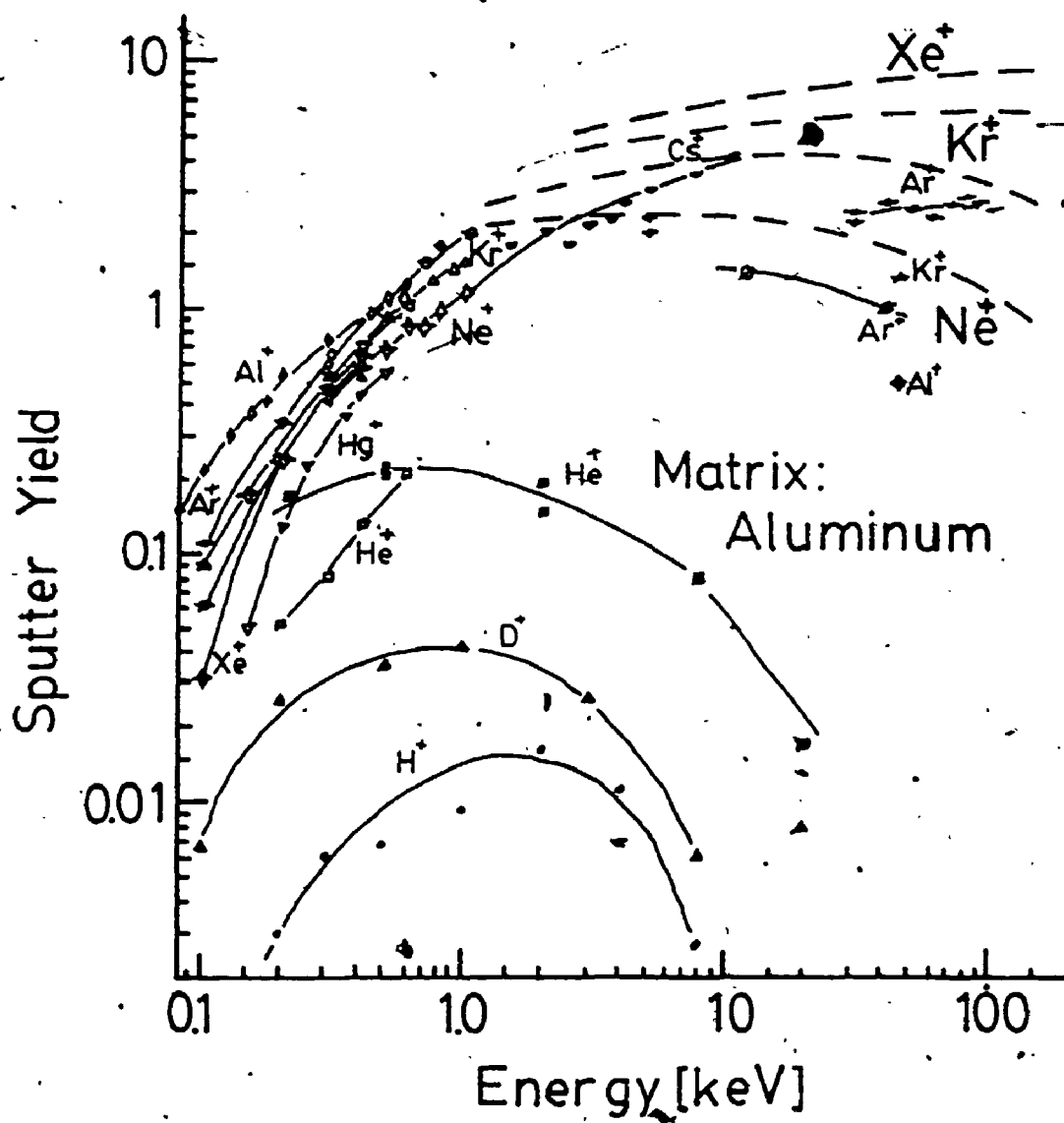


FIGURE 14 Experimental sputter yield data for Al (100)

ion energy is shown in Figure 14. Solid lines join sets of data from particular researchers. Dashed lines are predicted yields for ions of inert gases according to Sigmund's equation (97)

$$Y = \frac{0.042 \alpha (m_2/m_1) S_2(E_1, z_1, z_2)}{N_D E_s} \quad (12)$$

where E is the energy of the primary ion of atomic number z_1 and mass m_1 sputtering a solid of atomic number z_2 , mass m_2 , atomic density N_D and surface binding energy E_s . The nuclear stopping power of the specimen is $S_2(E_1, z_1, z_2)$ and α is an energy independent function of the mass ratio. This equation was derived for normal ion incidence and assumes that inelastic scattering, chemical sputtering and sample crystallinity effects are insignificant. Details of these calculations are outlined in reference 100.

The scatter apparent in the reported sputter yield of Al in Figure 14 has been attributed to insufficient characterization of experimental conditions (100). The trend nevertheless, of increased sputter yield with primary ion mass and energy is clear. The sputter yield of Cu with 45 keV ions (Figure 15) shows the general increase in yield for increasing ion mass with pronounced maxima for inert gases at high fluences (99). The sputter yield decrease to near zero for some ions at high fluences is attributed by the authors to the creation of an alloy layer.

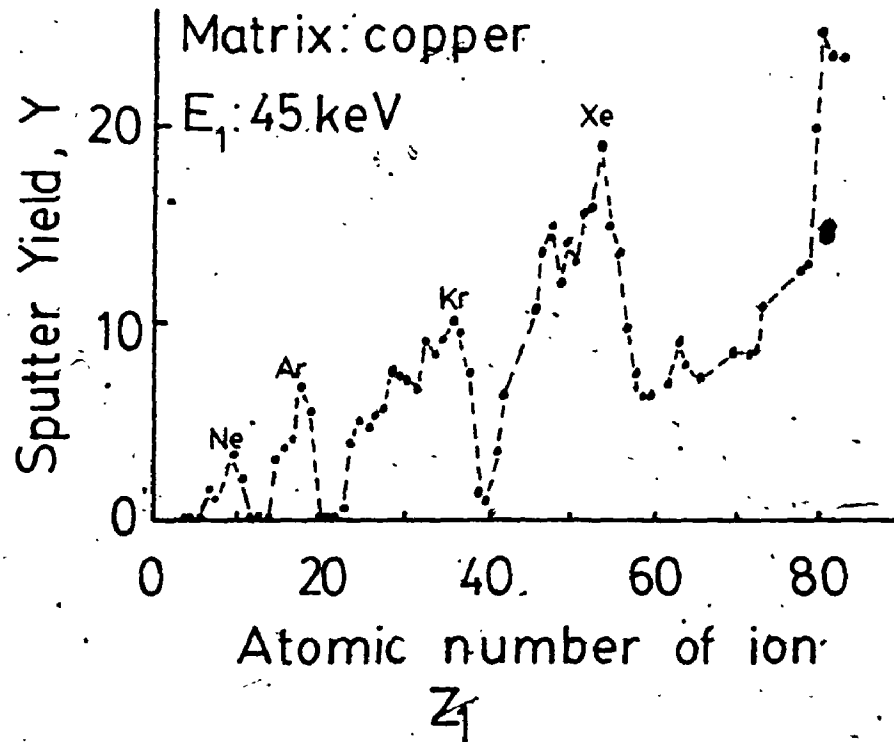


FIGURE 15 Sputter yield of Cu with 45 keV ions of atomic number Z_1 (99).

The sputter yield increases with the angle, θ_s , of the primary ion beam up to a maximum at an angle between 70° and 80° (Figure 16). The sputter yield decreases at larger angles as a consequence of the increased reflection of the primary ion beam (100). The function $(\cos\theta)^{-1}$ is plotted for comparison.

The sputtering of pure metals has been described by elastic collisions and collision cascades in the target, however, the description of the sputtering phenomena in alloys is more complex. Primary ions may react chemically with one or more of the alloy components resulting in the formation of compound layers. These layers have different surface binding energies and accordingly, different sputter yields. Eckstein et al. (101) has estimated surface binding energies, E_s , from the heat of atomization, ΔH_{at} , using the equation

$$\Delta H_{at} = 2 \Delta H_f(MN) + \Delta H_s(M) + \Delta H_s(N) \quad (13)$$

where ΔH_s is the heat of sublimation and ΔH_f is the heat of formation of the molecule MN from the components M and N. For a surface in equilibrium

$$E_s(M) = E_s(N) = \frac{\Delta H_{at}}{n_b} \quad (14)$$

with n_b atoms per molecule. A surface which has an enrichment in component M is estimated as a linear function $\Delta H_s(M)$ and

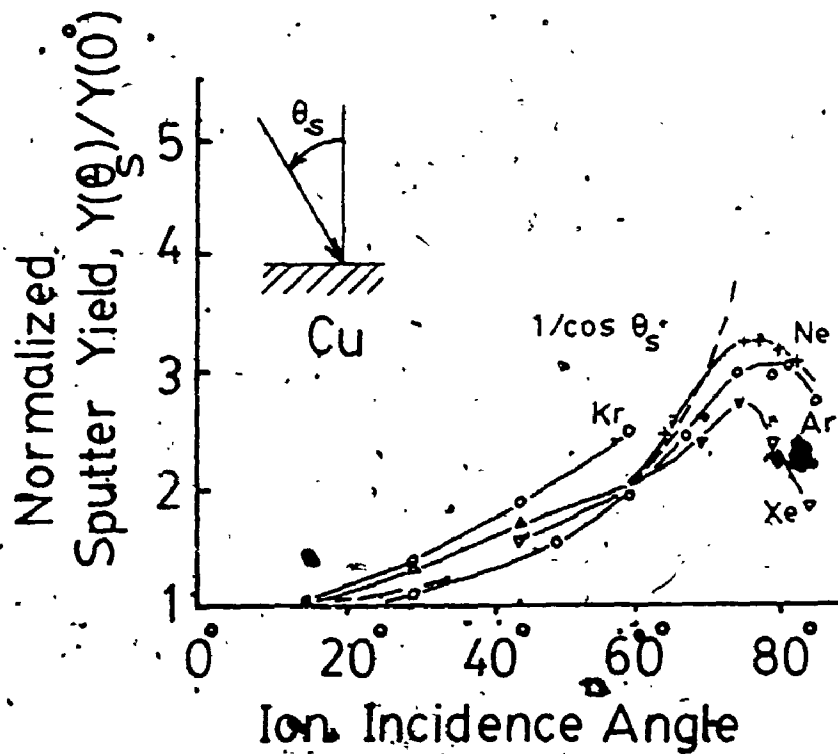


FIGURE 16 Sputter yields of Cu as a function of primary ion beam angle, θ_s (100)

$$E_s(M) = \Delta H_s(M) + \Delta H_f(MN) \quad (15)$$

Tsunoyama (102) has observed a decrease in surface roughness in sputtered surfaces for compounds with increasing binding energy. Compounds formed with a high vapour pressure component such as oxides result in not only compositional changes but also in structural changes. The ion bombardment of oxides and compounds can lead to amorphization (103) or crystallization of a near surface layer (104). This depends on ion energy and fluence as well but is generally observed at energies of less than tens of keV and with fluences greater than 10^{13} ions cm^{-2} . Fluences below this value generally produce individual point defects.

Inelastic collisions in the cascade process lead to electronic ionization and excitation which also contribute to sputtering. Furthermore, the angular and energy distribution of the different constituents may differ, especially at non-normal primary ion incidence (104).

1.6 IONIZATION

For pure elements, the secondary ion yield has been observed to vary by orders of magnitude depending on whether the surface is clean or oxidized, Table 1. In consideration of this, Klaus (106) concluded, as others have in the past that

TABLE 1. • SECONDARY ION YIELD (after Ref. 106)

Element	Surface Condition	
	Clean	Oxidized
Cr	10^{-3}	1.2
Cu	1.4×10^{-4}	4.5×10^{-3}

"the wide variation in secondary ion yield often makes quantitative interpretations difficult, if not impossible. On the other hand, careful comparisons of hundreds of different spectra may lead to conclusions applicable in very pure and thin-sandwiched layer technology."

This wide variation in ion yield also makes the formulation of a comprehensive theory of ionization difficult, if not impossible. Looked at in a positive light, this is a rich and largely unexplored territory of chemistry and physics.

In a fundamental series of experiments, Higatsberger and Klaus observed a linear dependence of positive and negative secondary ion count rate over a limited range of primary ion energy, primary ion mass for inert gases and primary ion current density (107). Others (108) have failed to confirm even these elementary observations. Little wonder then that theories clash or that observations conflict with theory (for example 109-111). One can see how observations of secondary ion count rate can vary from one researcher to another on the basis of sample preparation alone, in some cases, if the ion yield varies by as much as 10^3 for an oxidized surface. Other sources of variation exist and ones which originate in the SIMS instrument are discussed in later sections.

In more complex studies, where researchers bring in a wealth of data and try to explain the basic ion formation mechanism through interpretation of new information (109)

while ignoring inherent assumptions produce more controversy (110), sometimes followed by a retraction (114). Wittmaack (112) observed in an investigation of the production of multiply charged ions of silicon that Si_2^+ and Si_2^- ions have similar kinetic energy distributions in the high energy region. This suggests, according to him, that the stability of these ions is not influenced by the charge state and furthermore the results of the study support the conclusion that Si^{2+} and Si^{3+} (and $\text{SiL}_{2,3}$ MM Auger electrons) are formed by Auger de-excitation of excited atoms in vacuo. He argues that multiply charged ions had they not been produced at some distance from the surface would show a strong angular dependency which he did not observe. In another study (113), secondary ion emission from a Be surface was monitored in the presence of oxygen which should change the work function of the surface by a considerable amount and hydrogen which should produce little change. The authors concluded that the results were inconsistent with emission in which ionization occurred by a mechanism of Auger de-excitation but that it was possible to express the secondary ion yield in terms of a site exclusion model where the oxygen "covered" surface atoms have a higher probability of being sputtered as ions than those that are not "covered".

A number of mechanisms of ionization have been proposed to govern the observed secondary ion yield. The task of any general theory of ionization is to account for these diverse

phenomena. Williams (114) has outlined a number of experimental "facts" which a general theory should be capable of explaining:

- 1) positive secondary ion yields of different elements sputtered from a common matrix show an inverse exponential dependence on the ionization potential of the sputtered ion (115),
- 2) positive secondary ion yields are greatly enhanced by oxygen or other electronegative species at the sputtered surface (116),
- 3) negative secondary ion yields are enhanced by oxygen (117),
- 4) negative secondary ion yields are greatly enhanced by Cs or other electropositive species (118),
- 5) ion energy distributions generally peak at low energies and exhibit tails to high energies,
- 6) excited neutral yields and ion yields may proceed by a common mechanism but excited neutral yields are much lower than ion yields (119) and
- 7) excited neutral yields are enhanced by oxygen (120) but not by cesium (121).

Furthermore, he argues that "bulk crystal band-structure concepts are particularly inappropriate to the discussion of electronic events at the disordered surface sputtering site."

The first five points outlined above are generally

7

accepted as legitimate observations, although the measurement of energy distributions is fraught with pitfalls (60). Bulk crystal band-structure models, as shall be discussed, have shown remarkable success even though they may not be applicable to insulators. Some specimens with good overall electrical conductivity show local electrical charging and deflection of the primary ion beam due to the formation of a local altered surface layer during SIMS analysis. Items 6 and 7 above have been criticized by Reuter (122), who points out the misconception many people have in believing the generalization that the bulk of sputtered particles are ions. More than 95% of all sputtered particles are, in fact, atoms; at least in the case of argon bombardment of metallic targets. Exceptions to this generalization exist, such as for pure Cu and Ag substrates.

During sputtering, ionization may occur as a result of electronic coupling (123). The departing atom and substrate share electrons in the conduction band due to normal bonding (at least in the case of metals) and as the result of electrons excited into the conduction band from the sputtering-collision process. High energy collisions between ion cores can produce a variety of excited electronic states before the atom can be considered to have left the substrate. These collisions affect the local electron configuration of the substrate as well as that of the departing atom or ion. Lattice atoms which are sharing the cascade energy may be

in an excited, metastable state and any that attempt to leave the solid do so as ions (autoionization (29)) if the escape probability is favourable and the surface barrier is high (Figure 17). For inert gas ion bombardment, the majority of ions are neutralized by recombination with electrons from the conduction band. The formation of surface compounds with electronegative species such as oxygen or nitrogen may raise the surface work function and hence the barrier height which electrons must overcome to be available for positive ion neutralization. Electropositive elements reduce the work function and elements with high electron affinities have an optimum environment for a high negative ion yield.

De-excitation processes lower the energy of sputtered particles and in a single stage or multi-stage process lead to ionization. Such processes include

- 1) a resonance-tunneling of an electron from one state to another of equal energy, one belonging to the sputtered atom or ion and the other the substrate; with the electron capable of moving in either direction,
- 2) an Auger transition in which one electron falls to a deep vacant level while a second electron is emitted simultaneously,
- 3) a radiative process in which a core level is filled and an X-ray or lower energy photon is emitted.

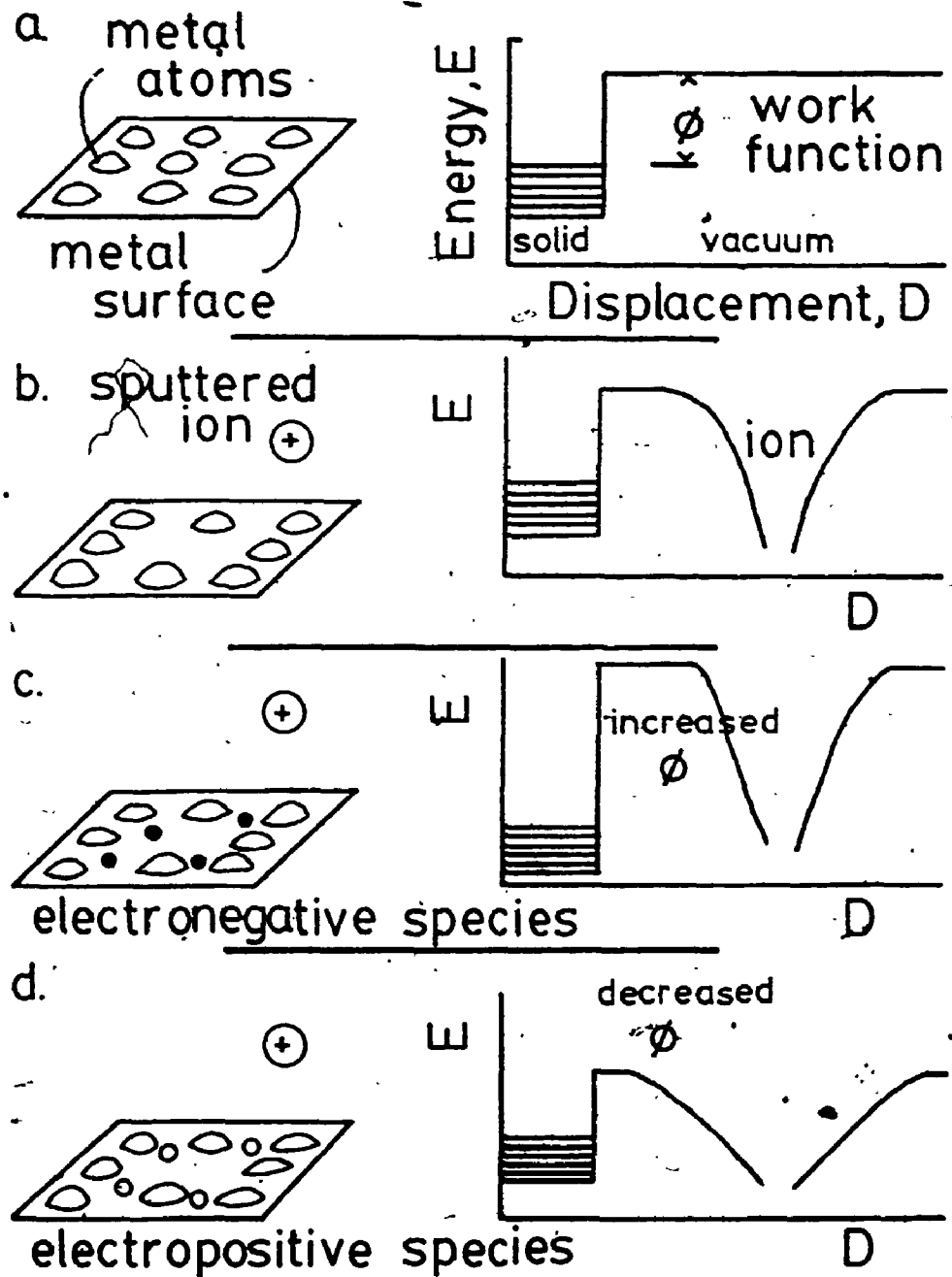
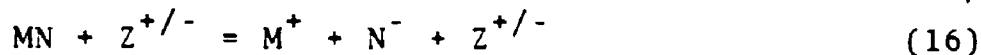


FIGURE 17 Ion emission from a metallic surface.

a) prior to emission, b) barrier becomes finite during emission, c) decreased opportunity of neutralization, d) increased opportunity

For negative ion emission, Kaminsky (125) has outlined the following possible mechanisms:

- 1) charge exchange with the surface layer,
- 2) capture of electrons with radiation emission,
- 3) electron capture by an atom in the presence of another body,
- 4) electron capture by a molecule followed by dissociation,
- 5) dissociation of a molecule by ion-molecule interactions such as



- 6) resonance ionization of excited atoms.

Electronic interactions such as bonding and dissociation between the surface and sputtered material are possible due to the absence of surface bonds which would ordinarily connect exposed atoms with those of the bulk.

Clean metallic surfaces are highly reactive and capable of forming strong bonds or even of breaking molecules into atomic or molecular constituents. Molecular dissociation requires much less energy (on the part of the molecule) than it does in a liquid or gas because of the contribution of energy from the surface if molecular fragments bind to the surface with a net release of energy (126). Fragments readily diffuse across the surface to encounter other adsorbed

molecules. The incorporation of molecules or atoms into the surface through the formation of chemical bonds is called chemisorption. Weak absorption is called physisorption.

Andersen (127) was the first to observe that the secondary ion yield varied by over 10^4 (Figure 18) for pure elements, while the total sputter yield only changed by a factor of 5. He noted a correspondence between ion yields and the filling of electron shells, and proposed that the probability of ion neutralization, P , is governed by the work function

$$P \propto \exp(-\phi_B/k_B T) \quad (17)$$

or

$$P \propto \exp(-(\phi - I_1)/k_B T) \quad (18)$$

where ϕ is the work function, ϕ_B is the surface barrier height, I_1 is the first ionization potential, k_B is Boltzmann's constant and T is the absolute temperature. Under ion bombardment with an electronegative gas, the surface barrier ϕ_B is often large, case 1 of Figure 19. However, some metals such as In have very low surface barriers when bombarded with oxygen, case 2. Gold has a high ionization potential and a low surface barrier, case 3. Andersen felt that the probability of positive ion neutralization by tunneling electrons would be very small but that thermionic electron emission was likely, case 4. Others have argued (11) that the probability of ion neutralization by thermionic

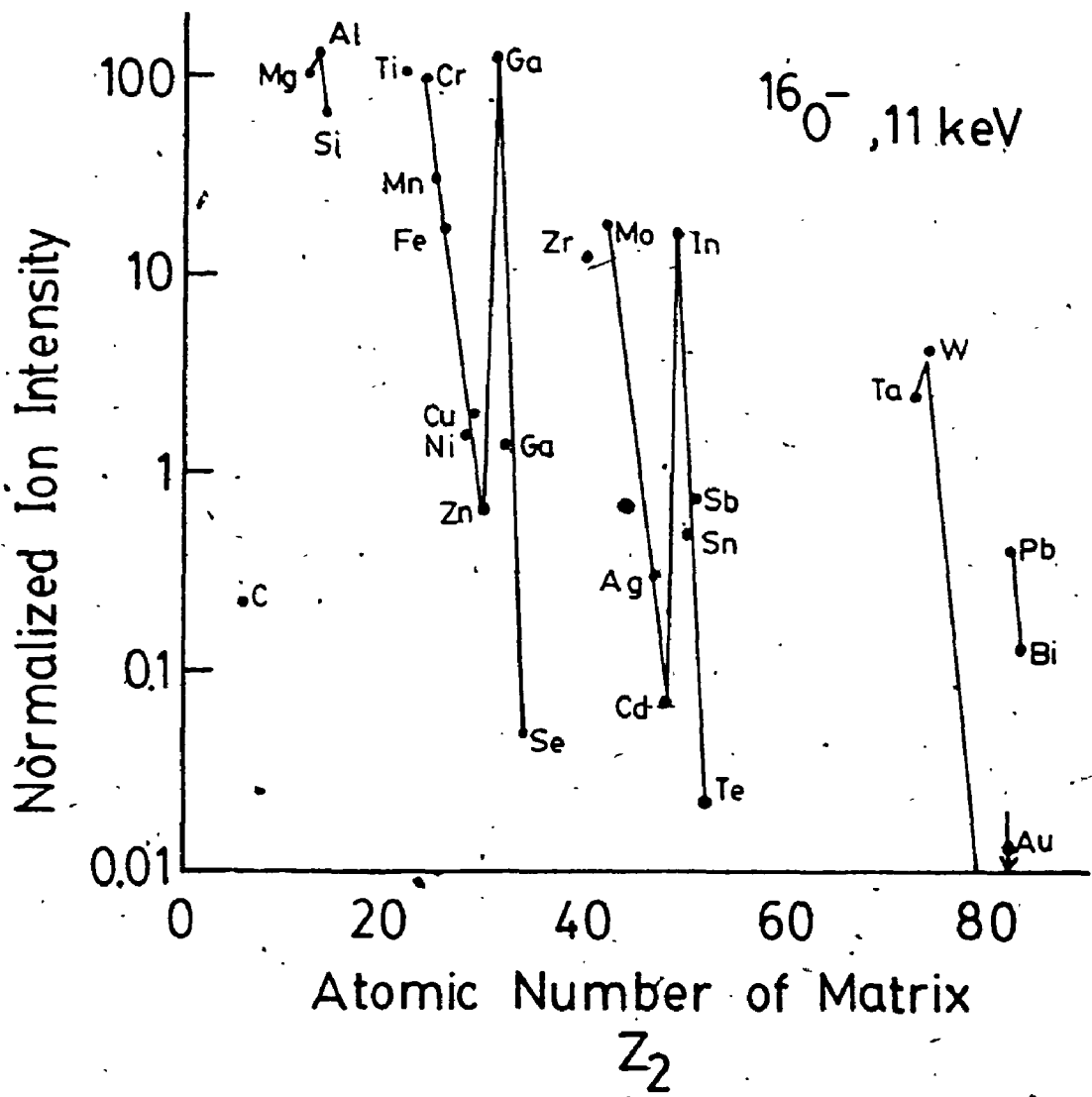


FIGURE 18 Relative ion intensities of pure elements, bombarded with $^{16}\text{O}^-$

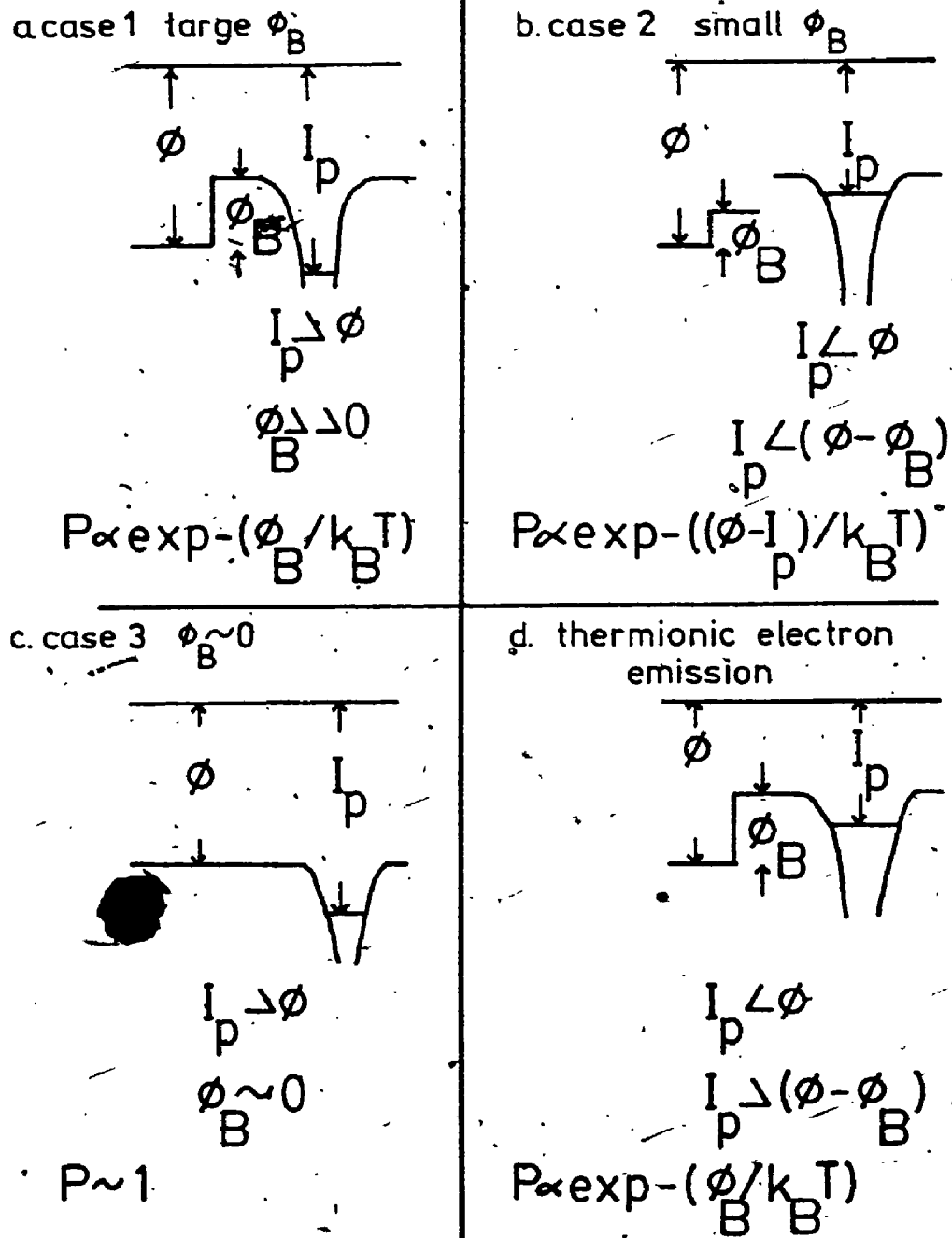


FIGURE 19 Probability of neutralization of a sputtered ion (127):

- a) Al, Si and Ti with O^- bombardment
- b) In, Ta and Sn with O^- bombardment
- c) Au with O^- bombardment
- d) electron emission

emission is only of the order of 10^{-8} .

The positive secondary ion yield, Andersen believes, decreases due to sputtered ion neutralization by electron transfer from the surface especially as the ionization potential increases. The negative ion yield increased with electron affinity and with the adsorption of Cs which decreased the work function and allowed electrons to tunnel to sputtered particles.

Both tunneling and Auger processes have been described by Hagstrum (128) with a rate equation of the form

$$Q = C_1 \exp(-C_2 x) \quad (19)$$

where Q is the transition rate, x is the distance of the atom or ion from the surface or other body and parameter C_1 is about 10^{-16} to $10^{-17} \text{ sec}^{-1}$ while C_2 is 0.2 to 0.3 nm^{-1} which is determined by the rate of fall-off of the electron wave function at the surface.

Slodzian (24) has proposed that for non-metallic bonds, the ionization process can be drastically changed because of the suppression of the screening effect of conduction electrons and the modifications of the electronic environment. An example would be the ionic compound NaCl which has a very high yield of Na^+ and Cl^- ions. Since Na and Cl possess an ionic state in the lattice, a collision cascade would directly expel an ion. The situation would be less

clear for covalent compounds or oxides in which the bonds formed often have only a partial ionic character.

This "bond-breaking" model has received continued support since it was proposed. Local bond-breaking was found (130) to be a more suitable description of the secondary ion yield of Si bombarded with Ar in the presence of either a) oxygen, in which case SiO_2 was detected by XPS coincidental with enhanced Si^+ emission, or b) nitrogen, absorption on the surface which lead to Si_3N_4 formation. In another revealing study, Gnaser (131) has found an exact 1:1 correspondence between M^+ and O^- count rates measured simultaneously in a special quadrupole SIMS for 12 pure elements during oxygen bombardment. This lends credence to a molecular dissociation/bond-breaking process.

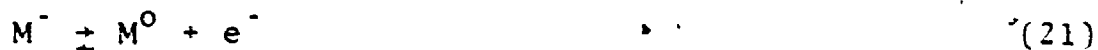
No model has been as hotly debated since its introduction as the local thermal equilibrium (LTE) model (28). The working hypothesis is that the majority of sputtered ions, atoms, molecules and electrons are in thermal equilibrium with each other and that a low density "plasma", at the surface, behaves according to the Saha-Eggert ionization equation

$$K = \left(\frac{2\pi m_e T}{h^2} \right)^{3/2} \frac{e^{-m_{M^+}}}{m_{M^+}} \frac{Z_{M^+} Z_e}{Z_{M^0}}$$

$$\exp(-E/k_B T)$$

(20)

where K is the equilibrium constant, h is Plank's constant, T is the equilibrium temperature, m is the mass of the particles, Z is the internal partition function and E is the dissociation energy for the reaction



Both experimental and theoretical evidence disputing the existence of an equilibrium plasma have been presented.

A nonadiabatic, nonequilibrium thermodynamical theory of positive and negative charge formation has been proposed by Sroubek (132). Low energy collisions such as those typical of cascades produce ions according to the empirical relations

$$R_M^+ = \exp\{[\phi_M - I_M]/k_B T_M^+\} \quad (22)$$

$$R_M^- = \exp\{[A_M - \phi_M]/k_B T_M^-\} \quad (23)$$

where R_M^+ and R_M^- are the positive and negative ionization probabilities of the particle M respectively. ϕ_M is the effective Fermi energy, T_M is the effective temperature, I_M is the ionization potential, and A_M is the electron affinity. These equations have the forms expected for a thermal surface ionization process but ϕ_M and T_M do not necessarily have a thermodynamical significance according to Sroubek. Indeed, in this model for the same substrate, T_M^+

and T_M^- usually have very different values. T^+ is about twice as large as T^- for most sputtered atoms.

The validity of equation (22) is confirmed by observations of Morgan and Werner (135). The relationship between I_M and R_M was determined for various species sputtered from the same matrix. The ionization coefficient of one sputtered species may be modified by a change in the electronic structure of the surface. Work function changes must influence the intensities of all ions sputtered from the surface by the same factor, $\exp(\Delta\phi/kT^+)$ or $\exp(-\Delta\phi/kT^-)$ for positive and negative ions respectively. Sroubek notes that it is often observed that ions with larger I_M or A_M are influenced less by changes in $\Delta\phi$. Additionally, R is dependent on the kinetic energy of ejected particles, E_k such that

$$R(E_k) \propto E_k^n \quad (24)$$

where $1.5 \geq n \geq 0$. Sroubek's model, which accounts for these observations, is described mathematically by the time dependent Anderson Hamiltonian

$$H = \epsilon_a(t) C_a^+ C_a + \sum_k \epsilon_k(t) C_k^+ C_k + \sum_k [V_{ak}(t) C_a^+ C_k] \quad (25)$$

where subscript a refers to the sputtered atom which is assumed to have one valence orbital, $|a\rangle$, with energy ϵ_a . The subscript k refers to substrate, $|k\rangle$, orbitals with energies ϵ_k . The transfer integral V_{ak} is between orbitals $|a\rangle$ and

$|k\rangle$. C and C^\dagger denote the corresponding creation and annihilation operators. The surface ionization process is schematically represented in Figure 20. When there is no atomic motion in the substrate (a "frozen" substrate), ϵ_k becomes time independent and the only possible mechanism for ionization of sputtered atoms is a nonadiabatic (taking place without heat transfer) transition from $|a\rangle$ to $|k\rangle$ levels above μ_F . The Hamiltonian can be modified for substrate interaction and solved for a substrate of five atoms. By introducing thermodynamical nonequilibrium, i.e. $T \neq T_S$ the temperature of the substrate and by omitting the non-adiabatic transfer of electrons from $|a\rangle$ orbitals to empty $|k\rangle$ orbitals, Sroubek obtained

$$R^+ \propto (E_k)^n \exp\left(-\frac{I - \phi}{k_B T_S}\right) \quad (26)$$

$$\text{where } n = \frac{\gamma_a \delta}{4\gamma k_B T_S} \quad (27)$$

γ and δ are assumed to be constants, γ_a is a parameter characterizing the spatial dependence of $\epsilon_a(x)$.

In general, equation (26) shows the expected dependence of R^+ on E_k and I . As well, the parameters γ and γ_a characterize the ionization coefficient in terms of microscopical parameters of the substrate and sputtered particle, respectively. It also predicts that the ion is formed at the distance x_0 from the surface. Sroubek concluded, however, that other models and the model proposed above "cannot predict

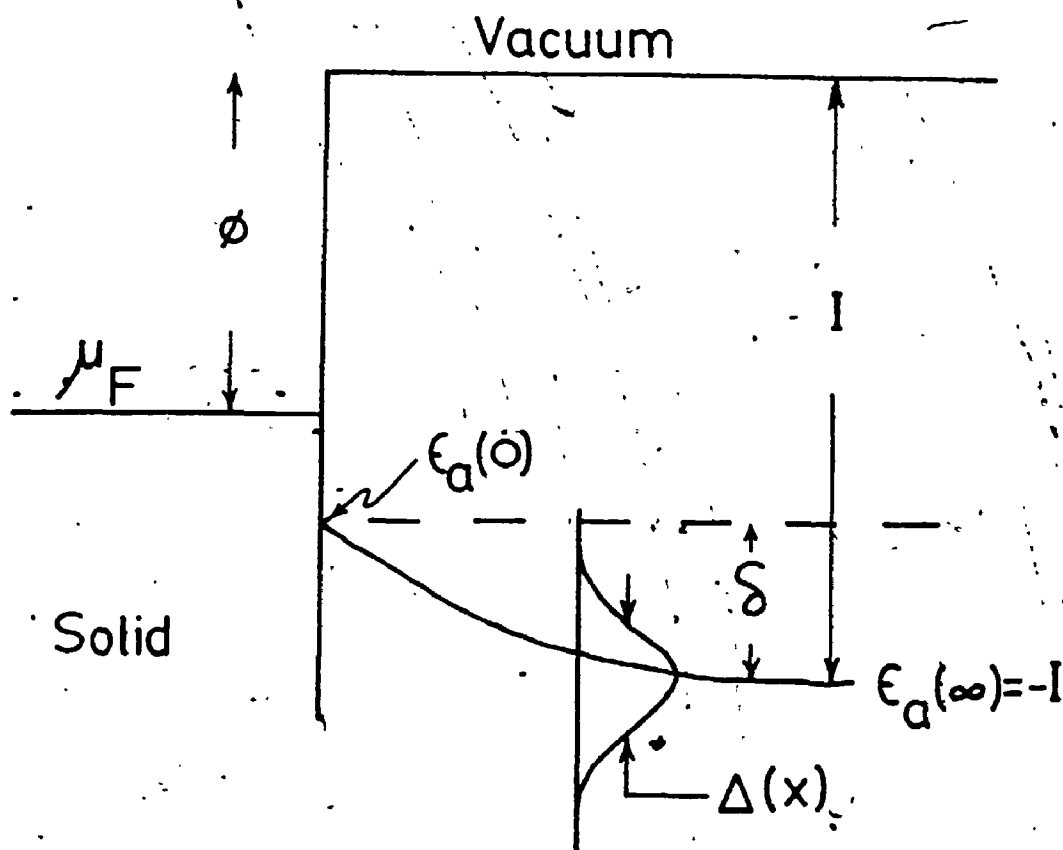


FIGURE 20 .Energy relationships for surface ionization (132)

quantitatively the ionisation probability because they are ...conceptually too simple."

Krohn (133) has pointed out that surface ionization by thermal desorption is accurately described as an equilibrium process whereas secondary ion emission is not. The secondary ion yield is proportional to the Boltzmann temperature factor in equation (18) and the same factor tends to dominate the behaviour of the Saha-Langmuir equation. Krohn suggests that this temperature factor might be time dependent, i.e. it may decrease with time following the impact of the primary ion. The time between primary ion impacts is, on average, about 10^{-10} seconds for a primary ion current of 1 nA. Harrison et al. (136) have estimated that the duration of a collision cascade is about 10^{-10} seconds (a one eV electron traverses one atomic diameter in about 10^{-16} seconds). Thus collision cascades and ionization events would seem to occur in the time interval between primary ion impacts.

The ionization process has been represented by Lang (134) as a semi-infinite lattice of positive ions smeared out into a homogeneous background--the so-called *jellium*. A metal is treated as a non-interacting Fermi gas of work function ϕ . Solution of the modified Hamiltonian leads to an equation predicting the probability of ionization,

$$P^+ = \exp\left(\frac{-2\Delta(Z_c)}{\gamma V_1 c}\right) \quad (28)$$

with Z_c the critical distance for energy level crossings of level-width function Δ , the velocity V_1 of the sputtered ion perpendicular to the surface and γ is a substrate constant. Comparisons between theoretical predictions and experimental data indicate that this model, with its simplifying assumptions about the substrate, provides some insight into the ionization process.

Recent conceptual advances in the field of electron desorption of gases has led Knotek (137) to propose that mechanisms which explain ion desorption may also be responsible for the ionization of sputtered particles. The mechanism is a more sophisticated re-stating of Andersen's (127) 1970 proposal that electrons are stripped from the sputtered atoms by an excitation-Auger decay process. Knotek proposes the generation of core-holes in the complex consisting of the surface and the atoms bonded to it. A core-hole is created by a collision cascade (Figure 21) and decays through the emission of an Auger electron leaving final states containing multiple-valency-holes. These states would be intrinsically localized, contain a large amount of trapped energy and have lifetimes much longer ($>10^{-14}$ sec) than other surface states. Simple Auger events remove a minimum of two electrons while more complex Auger processes can remove up to five electrons. In TiO_2 , the O^{2-} ion loses one electron by decay into the titanium core-hole, and in about 10% of the events two Auger electrons

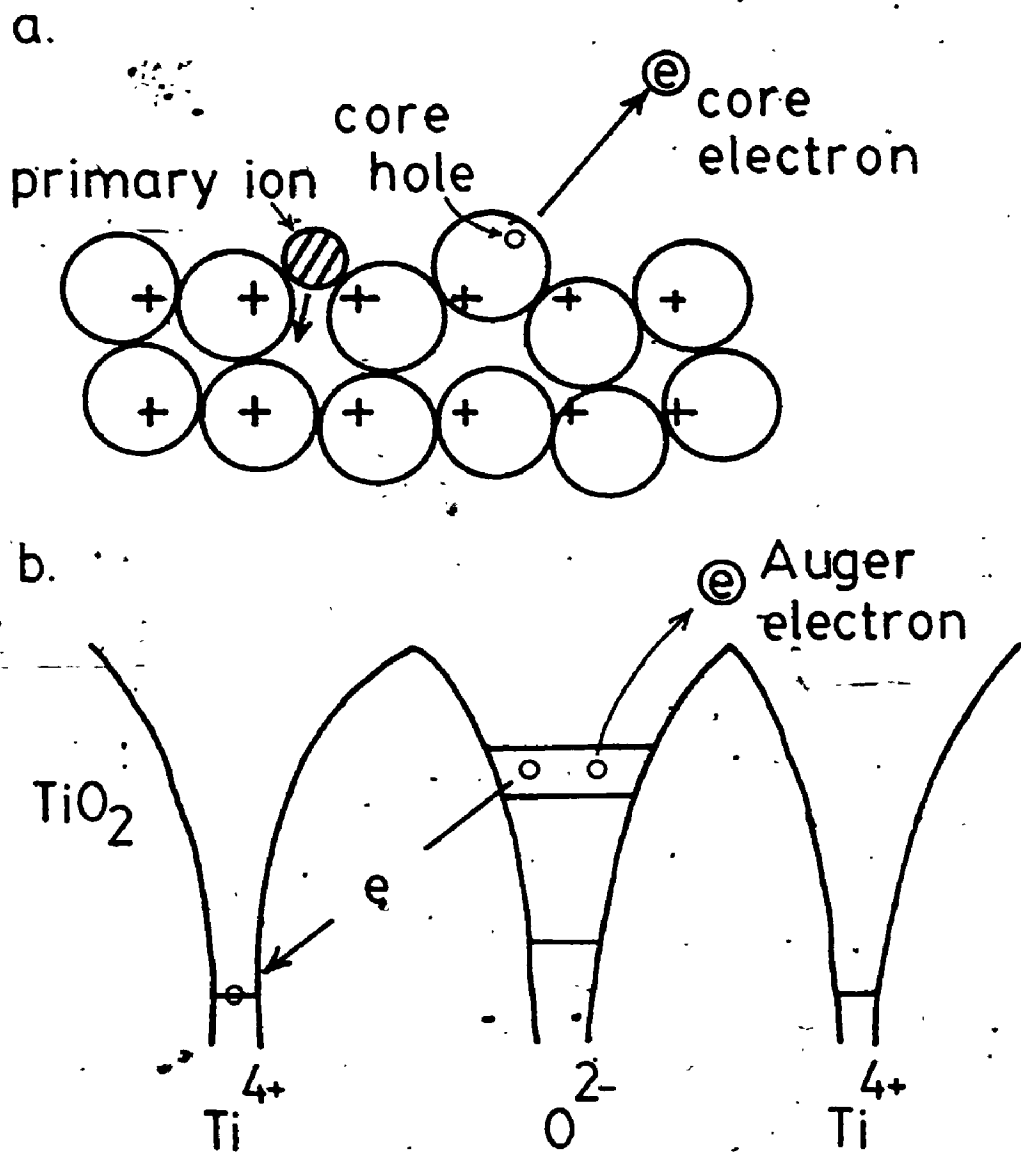


FIGURE 21 Electron transitions (137)

a) Core electron emission

b) Auger electron emission

are emitted transforming the O^{2-} to an O^+ . The unscreened positive titanium cores surrounding this O^+ repel it and result in desorption from the surface.

1.7 MATRIX EFFECTS

Matrix effects are common to a number of analytical techniques, especially those in which a specimen is bombarded with electrons. Convergent beam electron diffraction, high resolution electron microscopy, energy dispersive (and wavelength dispersive) X-ray analysis and electron energy loss spectroscopy, to name only a few techniques, exhibit enhanced sensitivity to heavy elements when low atomic number atoms are also present (138). In SIMS analysis the secondary ion yield does not show a simple correlation with atomic number, ionization potential or electron affinity as one might immediately expect. As well, the variations resulting from matrix effects may be as dramatic as variations caused by oxygen or cesium (114). Matrix effects occur not only in the analysis of metals, glasses and semiconductors but also in the analysis of soft biological materials (139); for which the existence of a matrix effect is attributed to local cellular variations in both physical density and electron density. An extreme example of a matrix effect is shown in Figure 22a. The intensity distribution of Ge^+ is inversely related to the actual concentration, shown in Figure 22b for 210 nm of $PtGe_2$ on pure Ge (140).

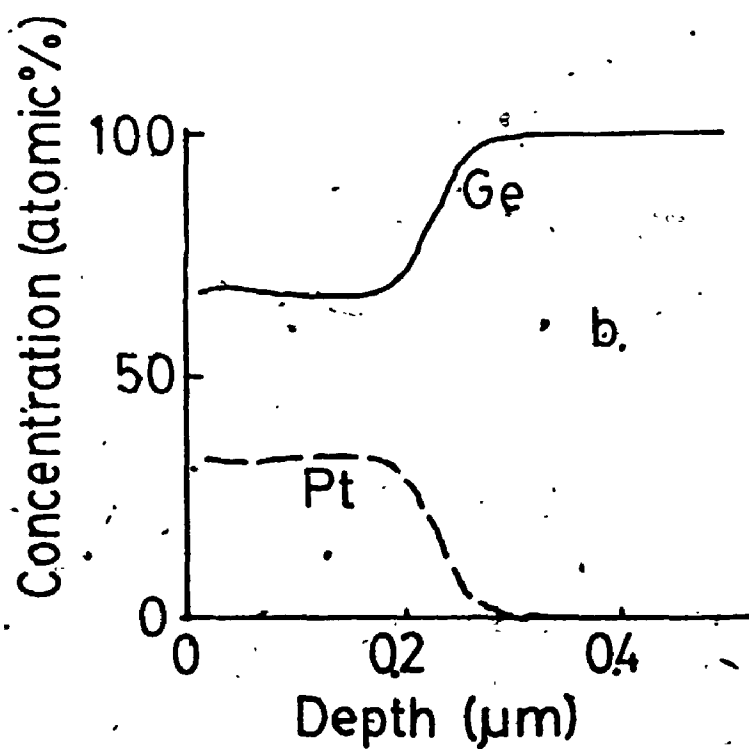
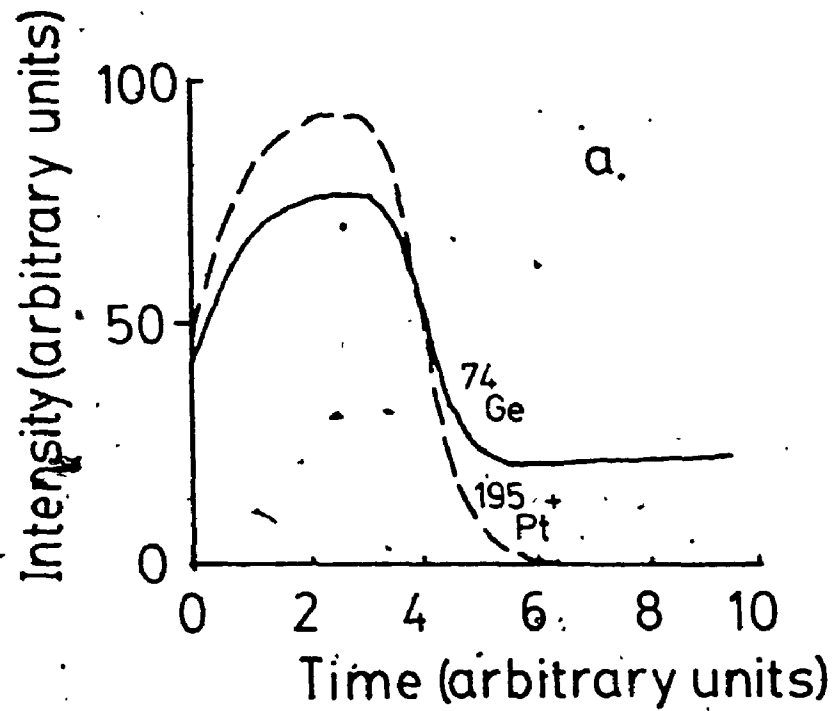


FIGURE 22a) Uncorrected depth distribution profile of PtGe₂ on Ge
 22b) Corrected depth distribution profile of PtGe₂ on Ge

The only model of ionization discussed in the previous section which has been specifically applied to the matrix effect is a modified version of the LTE model. The analysis of impurities in low alloy steels (135), in glasses (141) and GaAs (142) has been reported. Equation 20 may be re-written and ratioed to a reference element, r, such that

$$\frac{C_i}{C_r} = \frac{I_{i+} [Z_{i0}(T)/Z_{i+}(T)] \exp(I_{1,i}/k_B T)}{I_{r+} [Z_{r0}(T)/Z_{r+}(T)] \exp(I_{1,r}/k_B T)} \quad (29)$$

To a first approximation, T is the only matrix dependent parameter. Once T had been established, it was possible to run an essentially standardless analysis and determine the concentration of all elements in a homogeneous sample, with an accuracy of a factor of 2. Figure 23 shows a plot of $\log(I_{i+} M_i^{1/2} Z_{i0}/C_i Z_{i+})$ versus the first ionization potential. The differences in the slope of the lines for glass Q33 (21% Si, 20% Li and 55% oxygen) and K1012 (18% Si, 8% Al, 4% Ca and 61% oxygen) reflect the matrix effect. Figure 24 shows a plot of the same variables for GaAs. This technique has not yet been applied to more complex semiconductors such as those of the $Al_x Ga_{1-x} As$ system.

Deline et al. (109) have proposed that the variations in the observed ion yield can be classified as originating from a) matrices of pure elements, b) different elements contained in a single matrix and c) a given element sputtered from different matrices. They argued that the variations observed

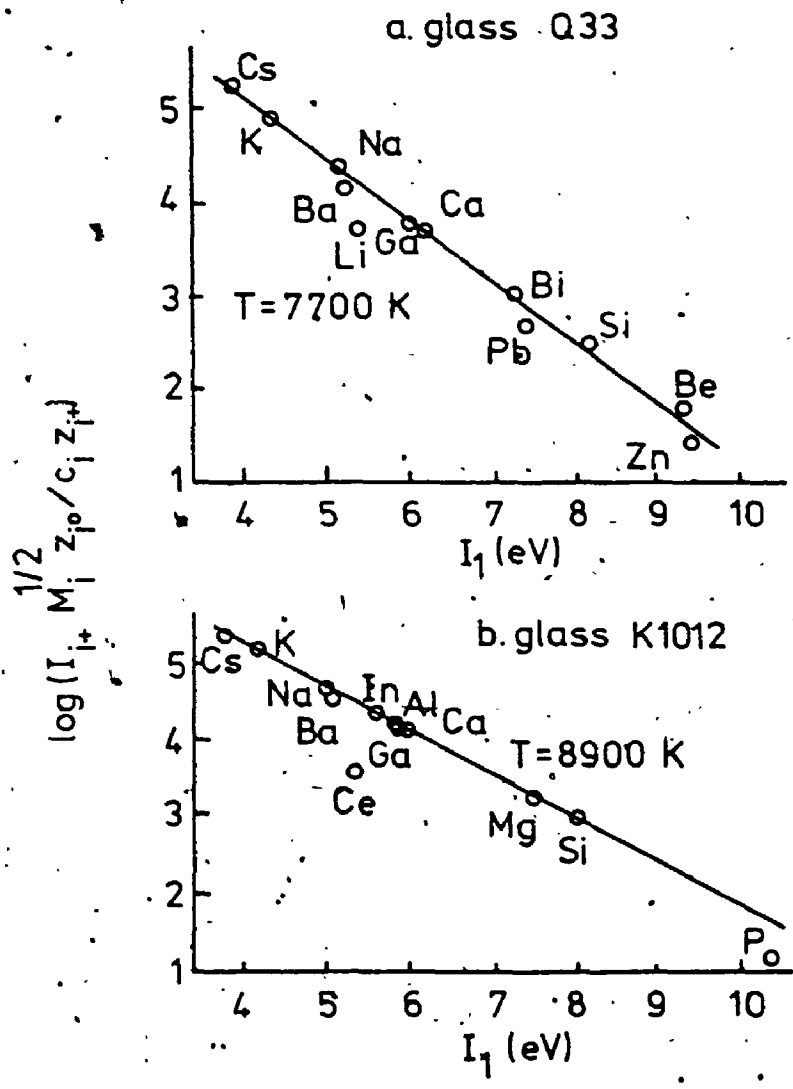


FIGURE 23 Plot of $\log(I_i^+ M_i^{1/2} z_i^0 / C_i z_i^+)$ versus first ionization potential for glasses (141)
 a) Q33. (21% Si, 20% Li and 55% oxygen)
 b) K1012 (18% Si, 8% Al, 4% Ca and 61% oxygen)

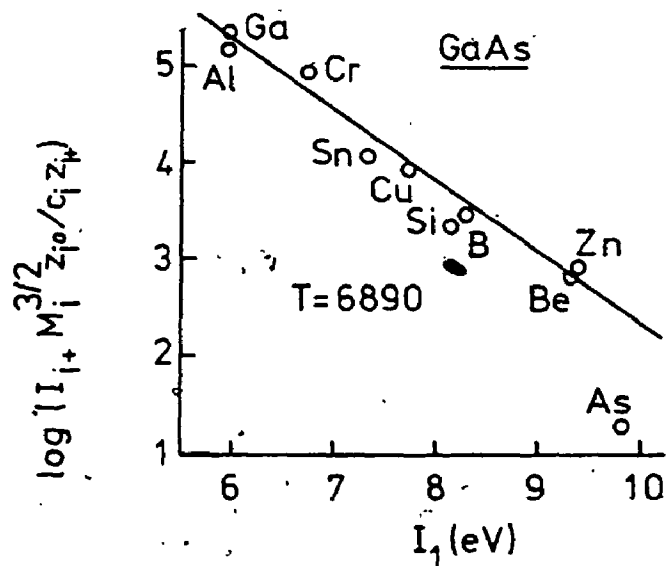


FIGURE 24 Plot of $\log(I_1^+ M_i^{3/2} Z_i^0 / C_i Z_i^+)$ versus first ionization potential for GaAs (142)

for a given element from different matrices could be explained, entirely on the basis of sputter yield. They propose that under ion bombardment the surface concentration of the primary ion species, C_p^S is inversely proportional to the sputter yield.

$$C_p^S \propto (1 + Y)^{-1} \tag{30}$$

or for a fixed sputter area, A, and primary ion current density, J, in the near surface region

$$C_p \propto (Y_\ell)^{-1} \propto \frac{N_D A}{YJ} \tag{31}$$

where Y_ℓ is the so called linear sputtering rate in Å/sec. The integrated ion count can be plotted versus the reciprocal of the matrix sputtering rate for oxygen, Figure 25. They concluded that "the substrate matrix effect is merely an artifact which arises because the sputtering yield determines the near-surface concentration of the enhancing species".

Wittmaack (110) has criticized the above work on the grounds that the distinction between the above classifications b) and c) is arbitrary and points out that equation (30) is a zero-order approximation of ion retention during sputtering. The steady-state surface number density of primary ions n_p^S and concentration C_p^S of implanted projectiles at the surface are

2



1.0



1.1



1.25



1.4



1.6

15
30
32
36
40
45



2.8



3.2



3.6



4.0



2.5



2.2



2.0



1.8



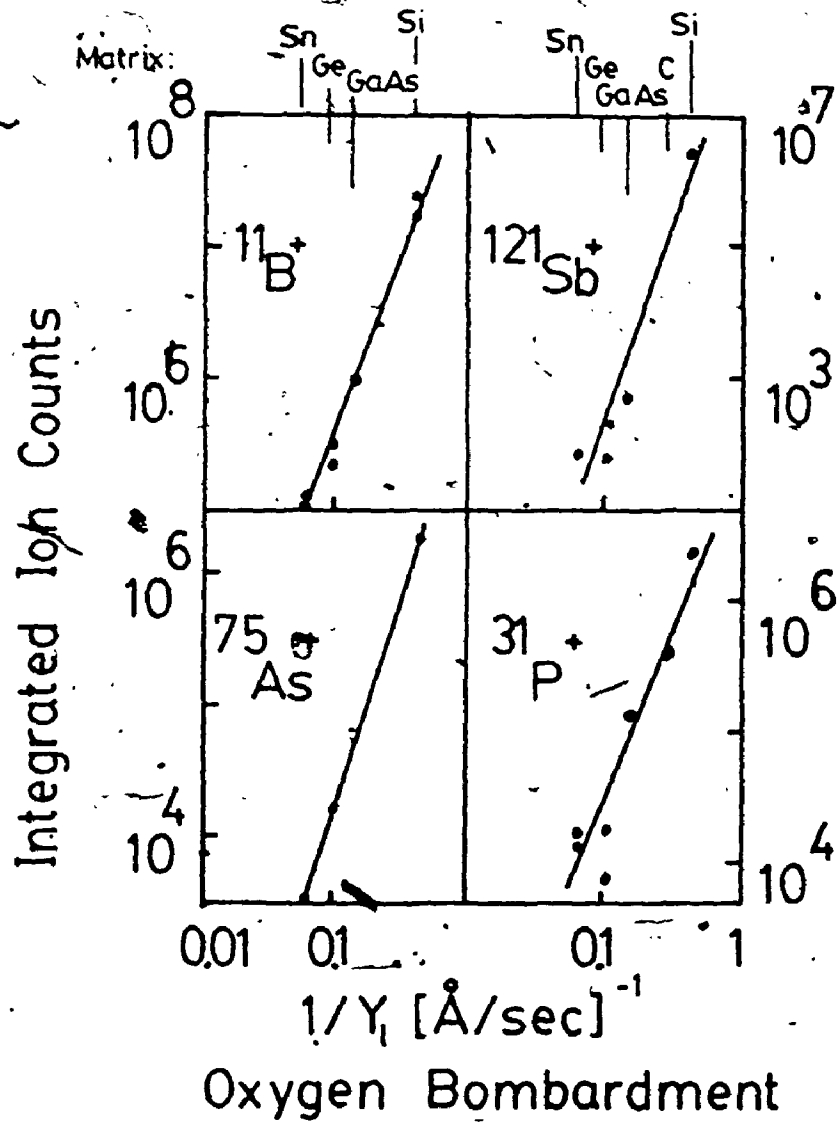


FIGURE 25 Integrated positive ion counts versus the reciprocal of the matrix sputter rate (109)

$$n_p^s = \frac{\xi N_D}{Y} \quad (32)$$

where ξ is the primary ion accommodation coefficient ($\xi = 1$ - the backscatter coefficient of primary ions) and

$$C_p^s = \frac{n_p^s}{n_p^s + N_D} = \frac{\xi}{(\xi + Y)} \quad (33)$$

In the Deline et al. treatment, ξ is assumed to be unity, whereas in practice ξ ranges from 0.5 to 0.9 for SIMS analysis conditions. Furthermore, assuming $\xi = 1$ for ion bombardment, of Si where $Y = 0.3$ would predict $n_p^s/N_D = 3$, i.e. that SiO_3 would form and not SiO_2 which has been observed experimentally (143). Wittmaack replotted the Deline et al. data as in Figure 26c and observed a better straight line fit when the substrate density is included. In addition, he noted that Y_2 is not actually a sputter yield but an erosion rate. Wittmaack concluded that under the experimental conditions employed in the above measurements, the steady-state oxygen concentration in the outermost layers was low and that the data (Figure 26) "masks variations in the physical and/or chemical processes involved, and thus prevents an understanding of the ionization mechanism". Similar arguments applied in the case of the Cs analysis. Later studies (144, 145, 154, 155) have failed to support Deline et al. and Williams (114) concluded that the correlations were "...somewhat mystifying..." and resulted "...from a fortuitous cancellation of terms..." or were due

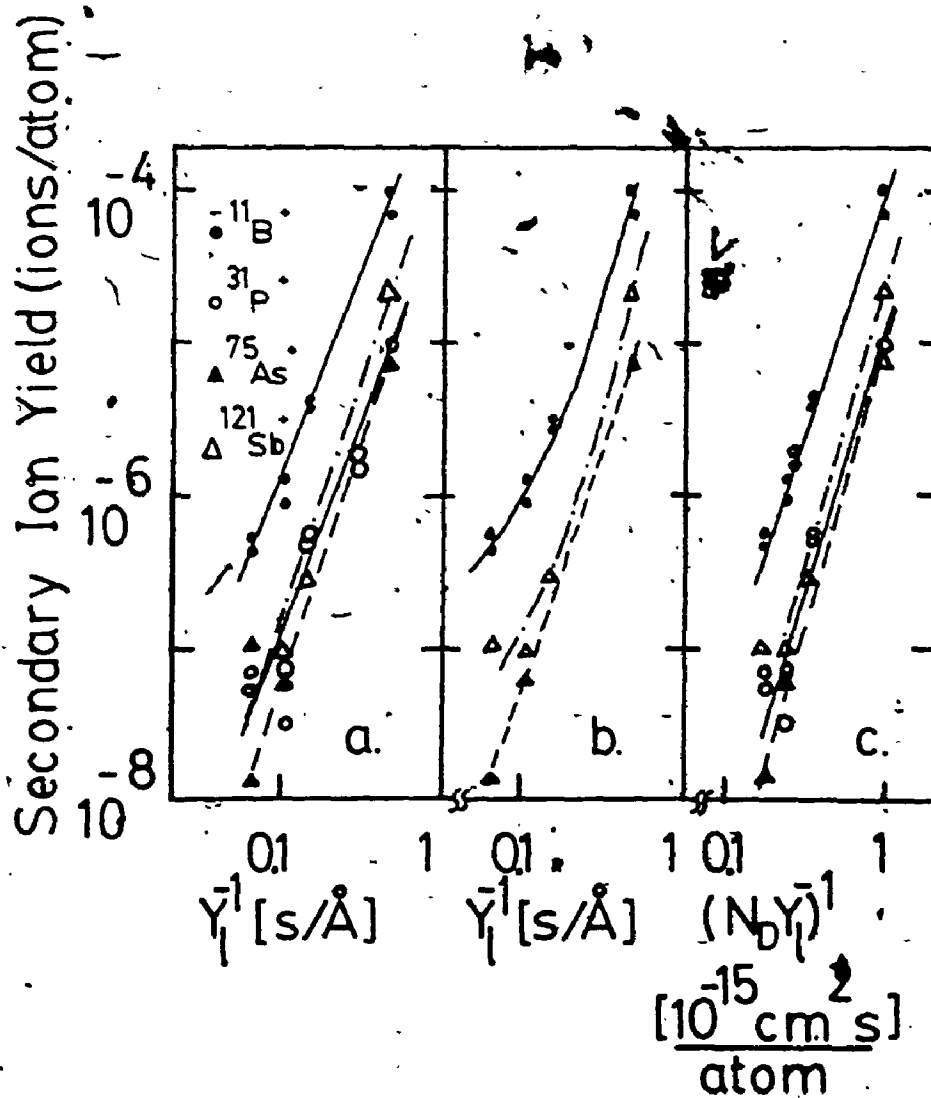


FIGURE 26 Secondary ion yield as a function of the reciprocal of the erosion rate a) and replotted b). The reciprocal substrate emission rate per unit area $(n_0 \bar{x})^{-1}$ is shown in c) (110)

to preferential sputtering.

Researchers at Université de Paris Sud in Orsay, France have proposed that emission of monatomic ions, such as Fe^+ , Ni^+ and Cr^+ , from binary and ternary alloys and their oxides is a linear function of the atomic concentration (146, 147). The Orsay group, as they choose to call themselves (148), have demonstrated that for a binary alloy MN, the secondary ion yield of M^+ in the alloy MN is a function of the concentration C_M and the ion yield of M^+ in the pure element M, plus the ion yield of N^+ in pure N times its concentration. That is

$$B_{MN}^M = B_M^M C_M + B_N^N C_N \quad (34)$$

A matrix effect is said to exist if the relative ionization coefficient ρ_{MN}^M differs from unity (123)

$$\rho_{MN}^M = \frac{B_{MN}^M}{B_M^M} \quad (35)$$

or the non-linear ionization coefficient, k_N^M is different for different alloys

$$k_N^M = \frac{B_{MN}^M}{B_{MN}^N} \quad (36)$$

so that

$$\frac{I_{MN}^M}{I_{MN}^N} = \frac{C_{MN}^M}{C_{MN}^N} k_N^M \quad (37)$$

Matrix effects observed for metal alloys of transition elements diluted (<1%) in Fe, Co, Ni and Cu are shown in Table 2. No matrix effect is observed for the major element. The matrix effect increases when the solute element is on the left-hand side of the transition series and the matrix on the right. Small effects are observed with neighbouring elements. The matrix effect for concentrated (>1%) alloys may be significant for some, as is the case of Fe in FeNi alloys but not for others, for example Ni in FeNi (Figure 27). A number of facts tend to support the concept that the matrix effect is due to the local environment of the emitted ion and not the overall composition of the solid. The ionization yield becomes,

$$\beta_{MN}^M = \sum_{\text{all environments}} P(e) \beta_e^M \quad (38)$$

where P is the probability of finding a given environment e where the secondary ion yield is β_e^M . For example, a strong enhancement of the ion yield of transition elements with partially filled d-shells is observed when these are diluted in a transition metal host with a complete or almost complete d-shell.

Sibdzian has attempted to incorporate the above findings into the "bond-breaking" model by considering an M atom surrounded by oxygen atoms and in collision with an N atom. The probability of ionization by a "bond-breaking" process

TABLE 2. RELATIVE IONIZATION COEFFICIENTS, ρ_i (Reference 123)
Ar⁺ bombardment:

Solute ($<1\%$)	Matrix			
	Fe	Co	Ni	Cu
Ti	-	-	10	27
V	-	-	13	5.7
Cr	2.7	-	46	10
Mn	2.8	3.7	3.1	2.7
Fe	-	0.8	0.7	1.3
Co	0.7	-	0.4	0.2
Ni	1.3	1:1	-	2.8
Cu	1.1	1.7	1.2	-

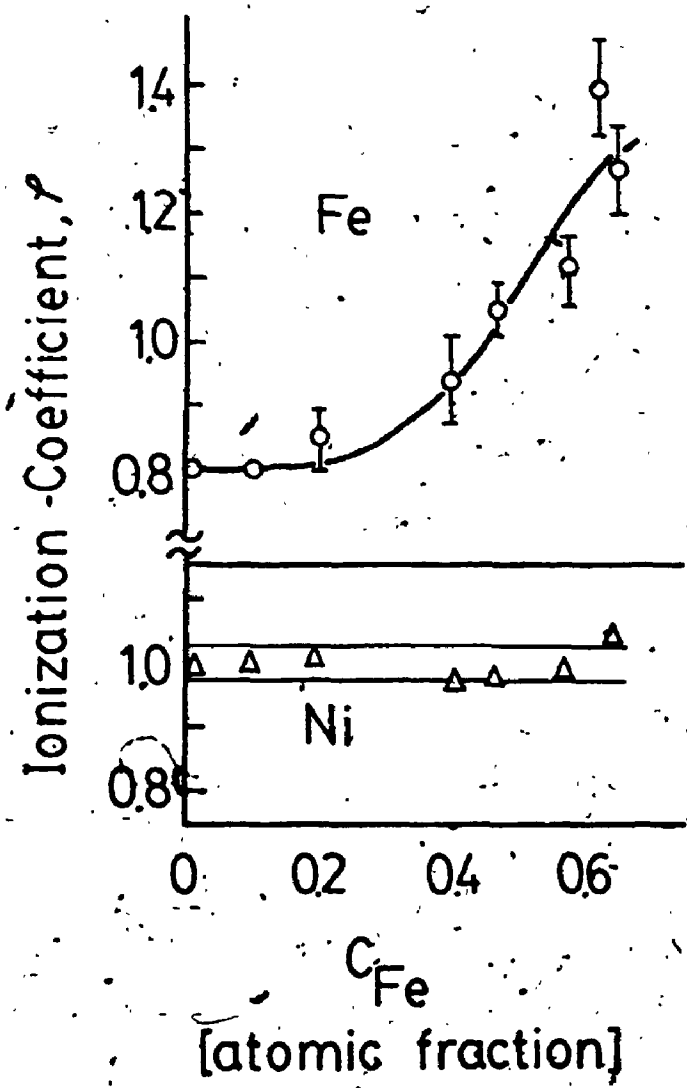


FIGURE 27 Relative ionization coefficient for Fe and Ni (123) with Ar^+ bombardment.

between atoms N and N would go "through some averaging procedure to account for different ionization processes, energy and angular distributions" leading to the linear approximation of equations (34)-(38). This account has been described by Pivin and Roques-Carmes (149) as Slodzian's "fully developed" model accounting for the matrix effect.

In fact, it is possible to start with equation (2), apply it to alloy MN and ratio the intensity of the components which gives.

$$\frac{I_{MN}^M}{I_{MN}^N} = \frac{J C_M Y_{MN} A \beta_{MN}^M \eta_M}{J C_N Y_{MN} A \beta_{MN}^N \eta_N} \quad (39)$$

Assuming that the primary ion current, sputter yield and area terms cancel and that $\eta_N = \eta_M$, equation (39) becomes

$$\frac{I_{MN}^M}{I_{MN}^N} = \frac{C_M \beta_{MN}^M}{C_N \beta_{MN}^N} \quad (40)$$

Comparing equation (37) with equation (40) we see that

$$k_N^M = \frac{\beta_{MN}^M}{\beta_{MN}^N} \quad (41)$$

It may also be recognized as the empirical quantitative analysis discussed earlier, the relative sensitivity factor approach.

Independent evaluation of the Orsay model of secondary

ion emission^o by Yu and Reuter (150) has shown that the model is not universal. Agreement was shown for the Cr-Ni, Cr-Fe and Fe-Ni systems but not for Cu-Ni, Pd-Ni and Ag-Pd alloys.

Yu and Reuter have proposed two general rules for matrix effects (144) on the basis of their investigations. These rules are applicable to binary alloys with oxygen bombardment,

Rule I: "When M forms a stronger oxide than N, the presence of M enhances the emission of N^+ , while the presence of N suppresses the emission of M^+ ."

Rule II: "When M forms a stronger oxide than N, the presence of M sharpens the energy distribution of N^+ , while the presence of N broadens the energy distribution of M^+ ."

By stronger oxide, Yu and Reuter presumably mean a larger heat of formation, $\Delta H_f^{\circ},_{298}$ since they begin by discussing these values. XPS analysis was performed simultaneously with SIMS analysis and large changes in ion yield were accompanied by significant changes in XPS spectra but an exact quantitative correlation between the two could not be made due to photoelectrons originating from much larger escape depths. The formation of mixed oxides was observed and a shift to higher binding energies of the Ni 2p electrons with increasing Cr content (Figure 28) indicated an increasing positive charge on the Ni atom, leading to the ion yield enhancement (Figure 29). This is direct evidence of the interaction between the primary ion species and the alloy

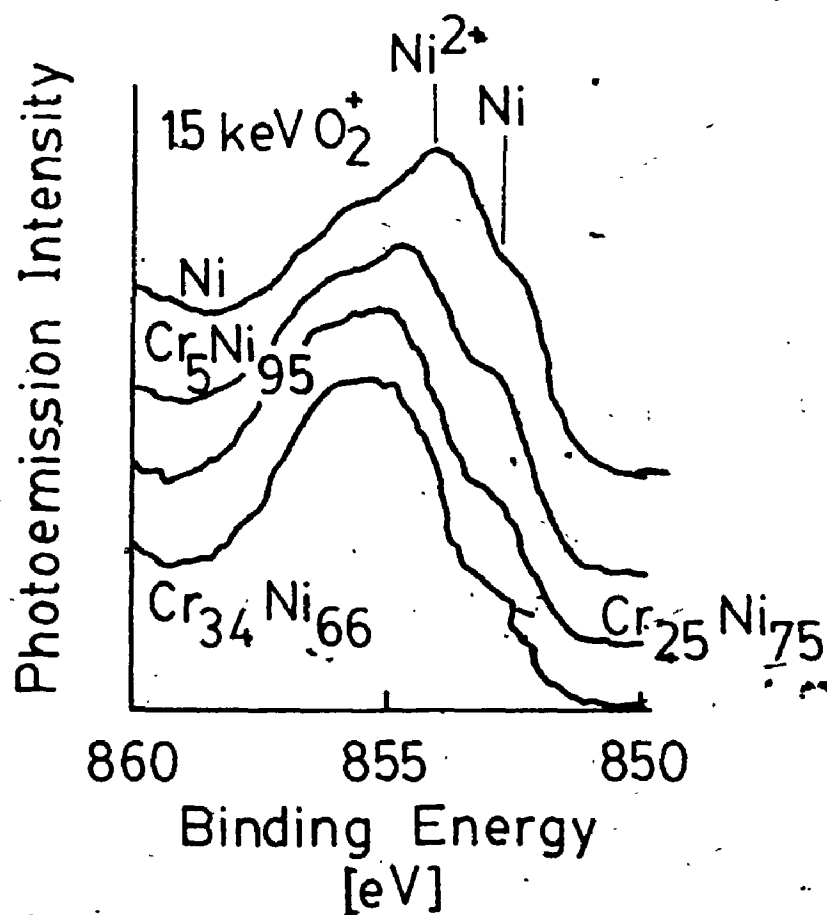


FIGURE 28 Ni 2p_{3/2} photoemission spectra of Cr-Ni alloys after steady-state bombardment with 15 keV O₂⁺ (144).

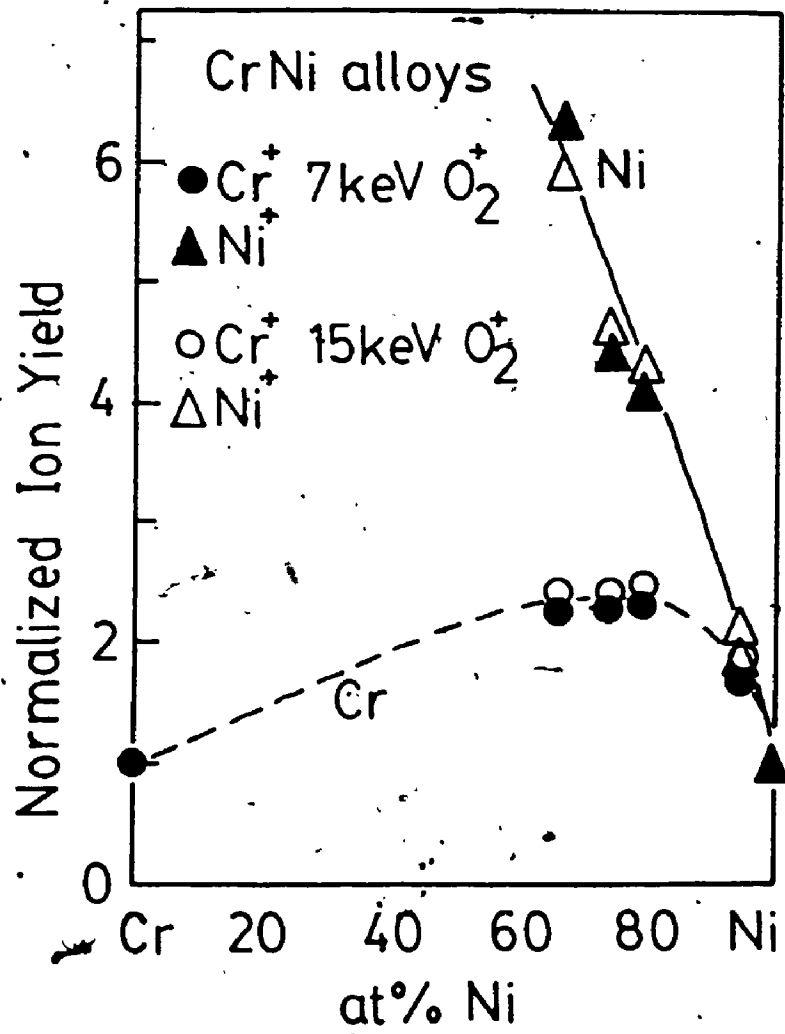


FIGURE 29 Normalized ionization probabilities of Cr⁺ and Ni⁺ for O₂⁺ bombardment (144)

components. A change in electronic structure is taking place during oxygen ion bombardment and coincides with enhanced ion emission. Yet close examination of Figure 29 indicates that it violates Rule I! In fact, only two of the five systems obey the proposed rule (Fe-Ni and Ag-Pd) while the others do not (Cr-Ni, Cu-Ni and Pd-Ni). Inspection of the values discussed by Yu and Reuter in their paper of ΔH_f^0 show that they differ from published values (Table 3) and are not the values given in Yu and Reuter's reference (151). The values cited by Yu and Reuter for Fe_2O_3 and Cu_2O are a factor of two smaller, for no accountable reason. Another measure of the strength of the oxide bond is the bond energy between a metal atom and an oxygen atom. These values, as may be seen from Table 3, do not prove to be an acceptable alternative for the explanation of the matrix effect. There is no advantage in using the bond energy over the heat of formation in explaining the matrix effect observed by Yu and Reuter.

The universal validity of Rule II has been placed in question as well since Taga (152) has observed no changes in the energy distribution of secondary ions for the TiAl and CuAl systems. Furthermore, the ion yield for these systems was contrary to what would be expected under Rule I.

TABLE 3
HEAT OF FORMATION AND BOND ENERGY (151, 156)

Oxide	ΔH_f° kcal mol ⁻¹	Oxide Pair	Bond Energy kJ mol ⁻¹
CrO ₂	-140	Cr-O	427
Fe ₂ O ₃	195	Fe-O	408
NiO	58	Ni-O	392
PdO	21	Pd-O	234
Cu ₂ O	40	Cu-O	342
Ag ₂ O	7	Ag-O	213

1.8 MATRIX EFFECTS IN THE $\text{Al}_x\text{Ga}_{1-x}\text{As}$ SYSTEM

SIMS was used by Koval et. al. (153) to determine Al and Ga concentration profiles in $\text{Al}_x\text{Ga}_{1-x}\text{As}$ hetero-structures. The secondary ion current of AlGa^+ was correlated to the Al concentration (Figure 30), and the secondary ion current of Al^+ was found to be linearly related to the Al concentration (Figure 31). The secondary ion currents of Al and Ga were the only ion species reported. An erosion rate of $0.05 \mu\text{m hr}^{-1}$ was obtained for a primary ion beam of 7.0 keV Ar^+ with a current density of $5.0 \mu\text{A cm}^{-2}$. No variation in sputter yield with Al concentration was measured.

A study of the ionization probability of Be, Ge and Sn dopants and the matrix elements Ga and As in the $\text{Al}_x\text{Ga}_{1-x}\text{As}$ system was published by Meyer, Maier and Bimberg (154). Dopants were ion implanted in $\text{Al}_x\text{Ga}_{1-x}\text{As}$ layers grown by liquid phase epitaxy (LPE) on (100) oriented semi-insulating GaAs substrates. Analyses were performed with an Atomika SIMS which had a Physical Electronics scanning Auger electron spectrometer attachment. A 10 keV O_2^+ primary ion beam was used. The angle between the incident ion beam and the surface normal was 10° , and the angle between the incident electron beam and surface normal was 60° . The detected Auger electrons had an average emission angle of 10° with respect to the surface normal. The pressure in the sample chamber was 10^{-6} Pa, dominated by gas leakage from the ion

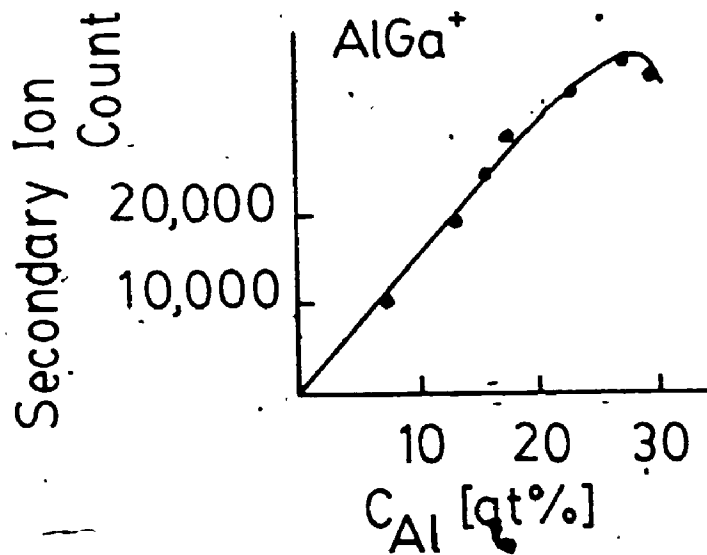


FIGURE 30 Secondary ion count of $AlGa^+$ as a function of Al concentration in $Al_xGa_{1-x}As$ with Ar^+ bombardment (153)

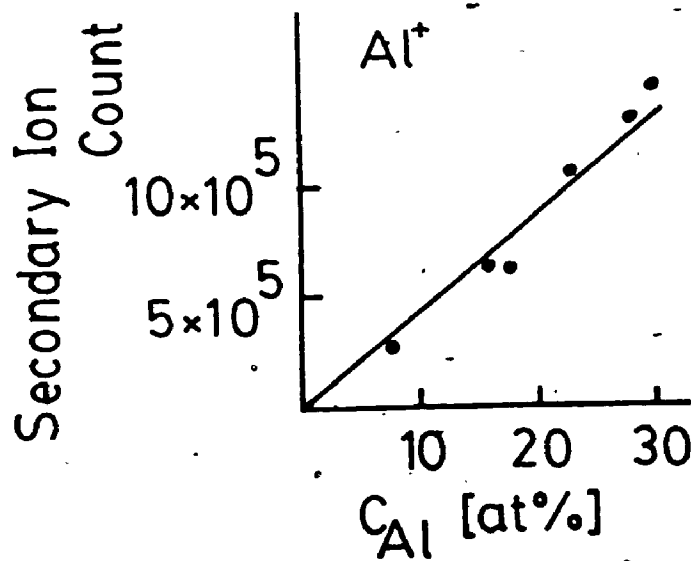


FIGURE 31 Secondary ion count of Al^+ as a function of Al concentration in $Al_xGa_{1-x}As$ with Ar^+ bombardment (153)

source. The number of counted secondary ions was corrected for 100% transmission of the quadrupole MS. Low mass resolution (<200) conditions were used and no dead time count rate correction of the detection and counting systems appears to have been carried out. These factors may help explain why aluminum ions were not monitored and why many ion yield values are missing in the tabulated results. Meyer et al. omitted "unrealistically high-yield values", and claimed that these values arose from "changes of the composition of the epitaxial layer due to oxidation of Al." No supporting data was provided as evidence of this conclusion, and their statement tends to be in conflict with their other claim of either incomplete (GaAs) or complete (AlAs) oxidation of the surface (again in the case of AlAs no data is presented). A 15% mean deviation between repeated analyses was reported. No individual analysis, i.e. depth profile, was presented.

The secondary ion yield was defined by Meyer et al. as the number of detected positive secondary ions of element M per sputtered atom of element M (this is actually the practical ion yield, see equation (1)). In the case of dopants:

$$(\beta\eta)_M^+ = \frac{(\text{integrated count})}{(\text{implanted dose} \times \text{area of analysis})} \quad (42)$$

with β and η being the ionization probability and instrument transmission, respectively. The secondary ion yield of the matrix constituents was determined from

$$(Bn)_M^+ = \frac{I_M^+}{2Jf_M C_M Y} \quad (43)$$

where I_M^+ is the count rate (ions per second) of an isotope (isotopic abundance f_M) of element M with atomic concentration C_M . J is the primary ion flux density (number of ions $\text{cm}^{-2} \text{sec}^{-1}$). The factor 2 accounts for molecular O_2^+ used as a primary ion.

The secondary ion yield for the elements monitored in this study is shown in Figure 32. The ion yield varies as a function of Al concentration and is normalized to GaAs. Meyer et al. claim that the matrix dependence of the ionization yield is strongly influenced by the element in disagreement with Deline et al. (109). Furthermore, the results were in agreement with Yu and Reuter (144) inasmuch as the variation of the ionization probability was "connected with the variation of the degree of oxidation". However, no specific correlation with bond energy was shown in support of this statement.

In order to clarify the point, the data of Meyer et al. has been plotted in Figure 33. This shows the sputter yield as a function of the surface concentration of oxygen and indeed there appears to be a good correlation. If the relative ion yield is plotted as a function of the inverse of the sputter yield (Figure 34), in the manner of Deline et al. (109), non-linear behaviour is evident.

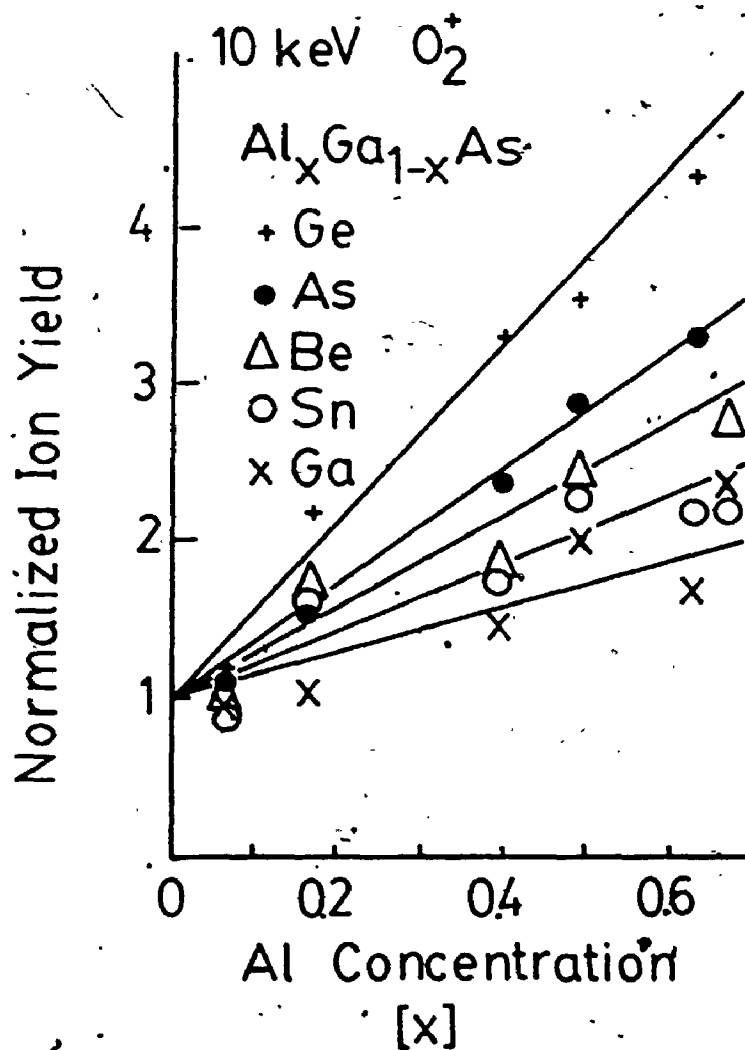


FIGURE 32 Relative ion yield of dopants and matrix species in $Al_xGa_{1-x}As$ (154)

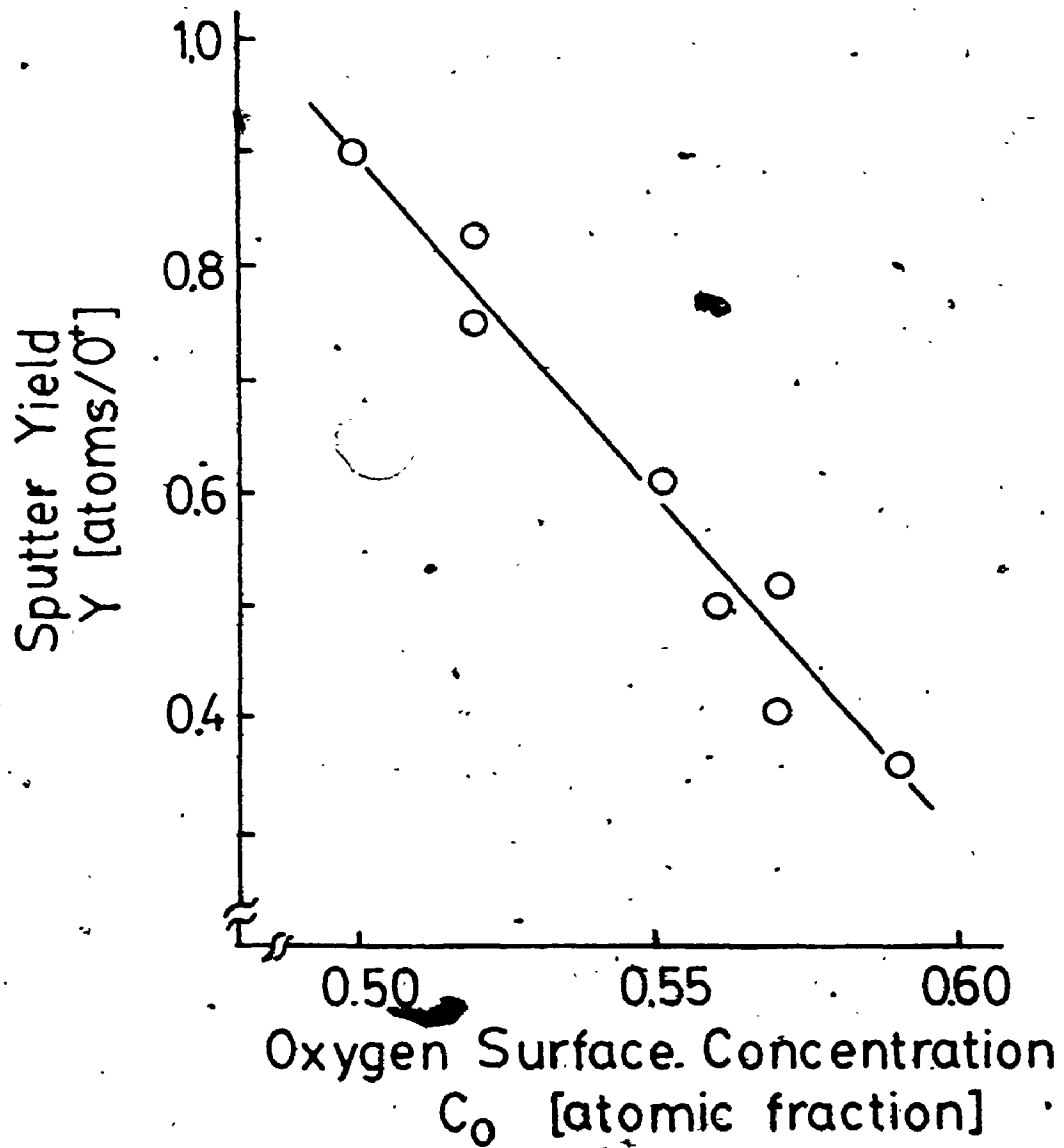


FIGURE 33 Sputter yield versus oxygen surface concentration

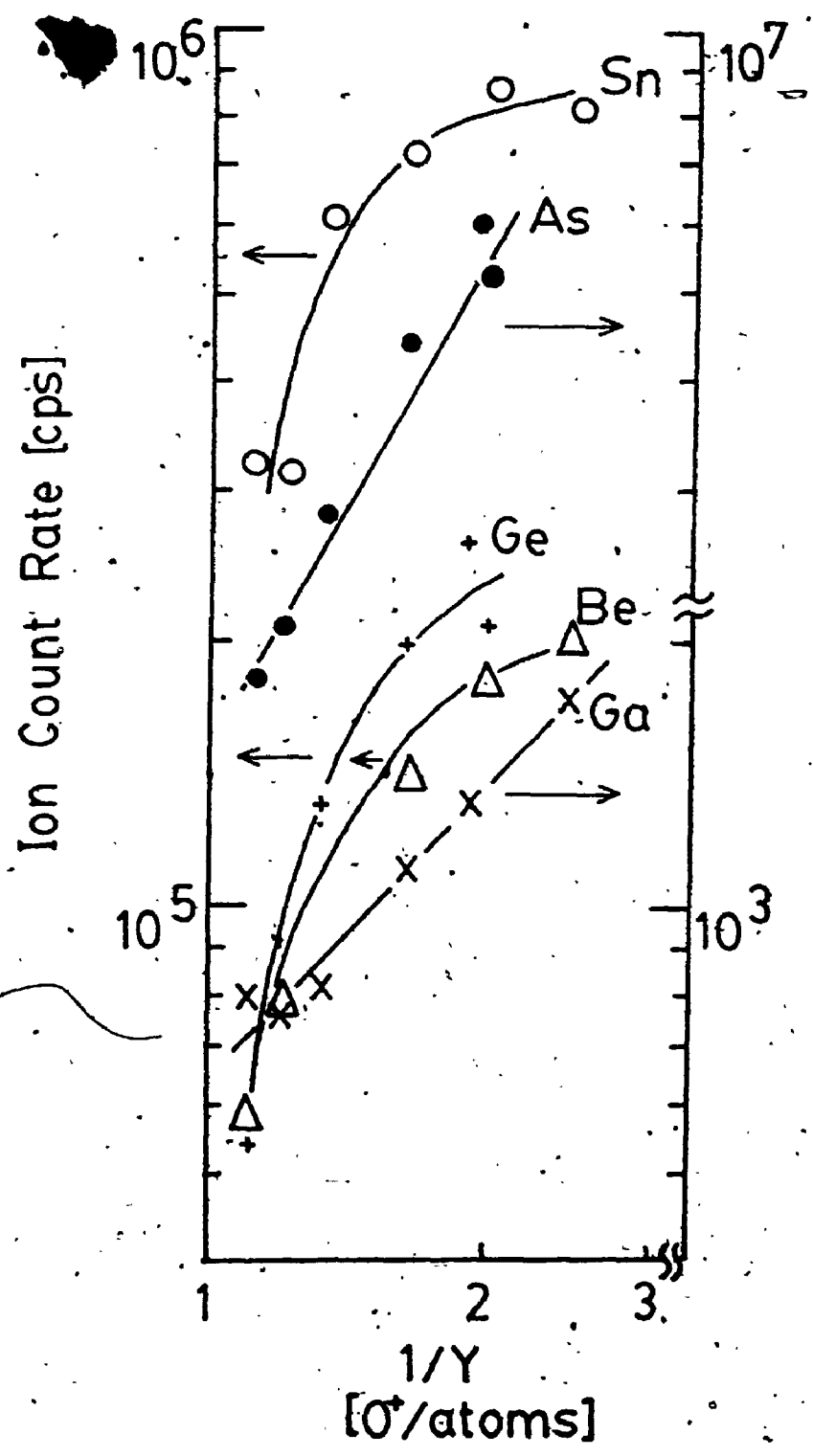


FIGURE 34 Ion count rate versus reciprocal sputter yield

Secondary ion kinetic energy distributions showed no dependence on the composition of the sample, in conflict with Rule II of Yu and Reuter (144). The AES results (Figure 39) showed "incomplete oxidation of the surface". Surface segregation during ion bombardment resulting in As depletion is clearly shown in Figure 35.

Secondary ion yields and sputter yields were also found to be linear functions of matrix composition in the $\text{Al}_x\text{Ga}_{1-x}\text{As}$ system in a study by Galuska and Morrison (155). The dopants ^9Be , ^{11}B , ^{28}Si and ^{31}P were ion implanted in $\text{Al}_x\text{Ga}_{1-x}\text{As}$ layers grown by molecular beam epitaxy on semi-insulating GaAs substrates. A Cameca IMS-3f ion microscope using an O_2^+ 5.5 keV primary ion beam was used for SIMS analysis. Positive secondary ions were monitored under low mass resolution (~ 250) conditions. The residual gas pressure was 3×10^{-6} Pa. No dead time correction for the detection and counting system was carried out. (A depth profile of $^{11}\text{B}^+$, which is shown to vary by two orders of magnitude, was the only depth profile presented in the report (Figure 36); $^{11}\text{B}^+$ suffers from very little mass interference.) Secondary ion count rates of Al and Ga ions were not monitored. The secondary ion signals were integrated and the background signals subtracted.

Samples were depth profiled in groups of four by using a multiple sample holder. The group of samples always

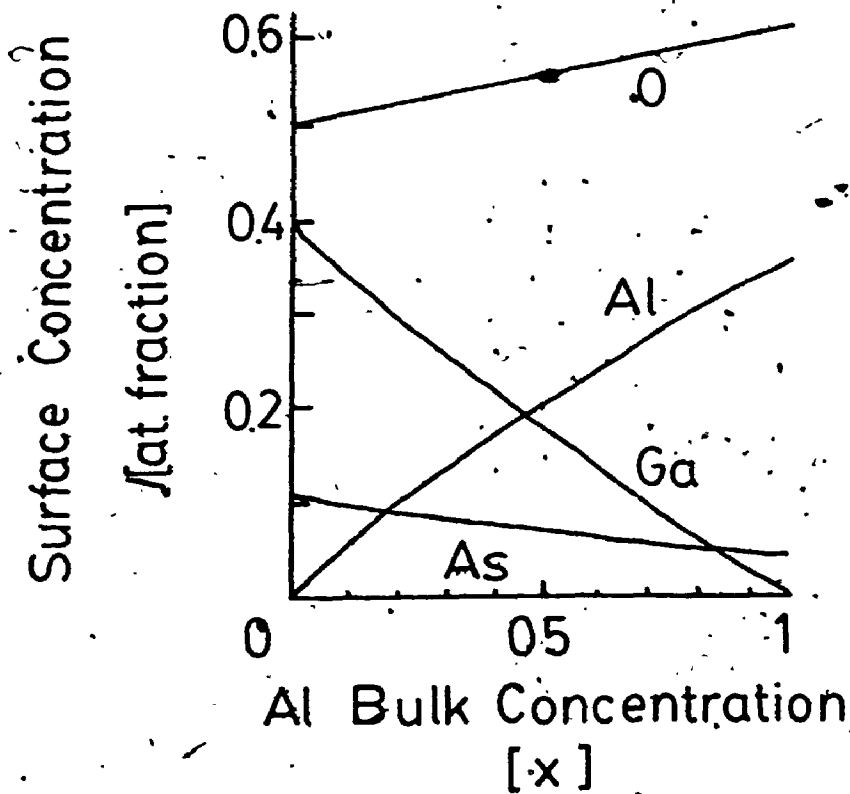


FIGURE 35 Surface concentration of $\text{Al}_x\text{Ga}_{1-x}\text{As}$ determined by Auger electron spectroscopy versus bulk Al fraction (154)

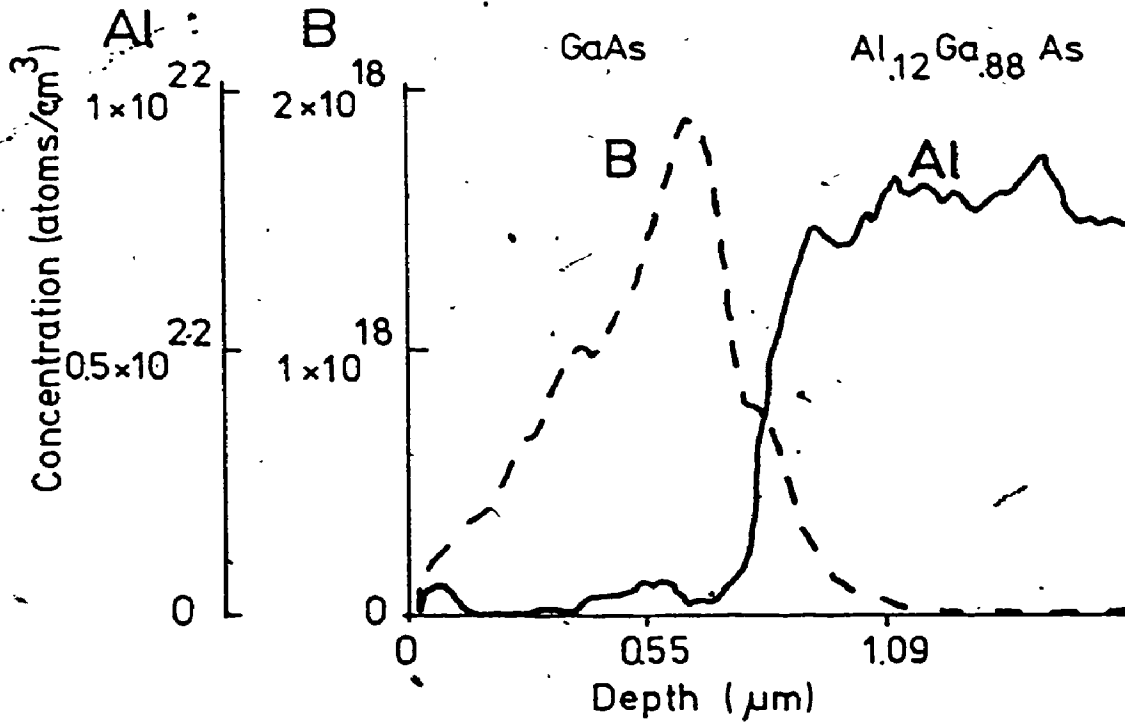


FIGURE 36 Depth distribution of $^{11}\text{B}^+$ in GaAs. The Al concentration is inferred from the $^{75}\text{As}^+$ signal (155).

included a GaAs standard. The primary ion beam was focused and instrument parameters were set for this group of samples. Instrument parameters were not manipulated until the sample group was analyzed. The sample stage was manipulated to allow for analysis of each specimen in turn.

Analysis of the data indicated to Galuska and Morrison that operator adjustment and indeterminate instrumental fluctuations influenced the secondary ion collection and instrument transmission causing the ion yield to change drastically between analyses. The practical ion yield of the dopant in $\text{Al}_x\text{Ga}_{1-x}\text{As}$ was ratioed to the practical ion yield in GaAs and the result was termed the relative ion yield. This was found to provide the best precision. (The relative ion yield is equivalent to the Meyer et al. (154) treatment of their data, so called secondary ion yields are normalized to the same species in GaAs.) Galuska and Morrison found that the poorest precision of analysis resulted from comparing ratios of relative sensitivity factors using ^{75}As as the reference species from different groups of analyses.

Galuska and Morrison concluded that the poorer precision of the ion yield information can be attributed to the poor reproducibility of individual ion yield measurements. The precision of ion yields was estimated to be 60%, relative sensitivity factors to be 24% and ion yields (normalized to

GaAs of sample group) to be 9%. The sputter yield was not determined since the primary beam current could not be accurately measured. A sputter yield relative to GaAs was measured.

Individual data points for the calibration of relative ion yields are omitted from Galuska and Morrison's work, but correlation coefficients were provided. Figure 37 shows a comparison of Galuska and Morrison's equations with those determined by Meyer et al. (154). Overall, the secondary ion yields and relative sputtering yield was found to be a linear function of matrix composition. However, little agreement can be seen between the two groups of researchers. The slope of the lines for As^+ are the only ones which are somewhat similar. The normalized ion yield of Be^+ was found by Meyer et al. to be slightly less than As^+ while Galuska and Morrison found that the ion yield for Be increased very drastically with Al content.

On the basis of the information gathered in this study, Galuska and Morrison (145) have proposed that Slodzian's (148) assertion that ion yields could be expressed as linear functions of matrix composition, i.e. equation (38)

$$\beta_{MN}^M = \sum_{\text{all } e} P(e) \beta_e^M$$

could apply to the bond energy $\bar{\Omega}$. That is

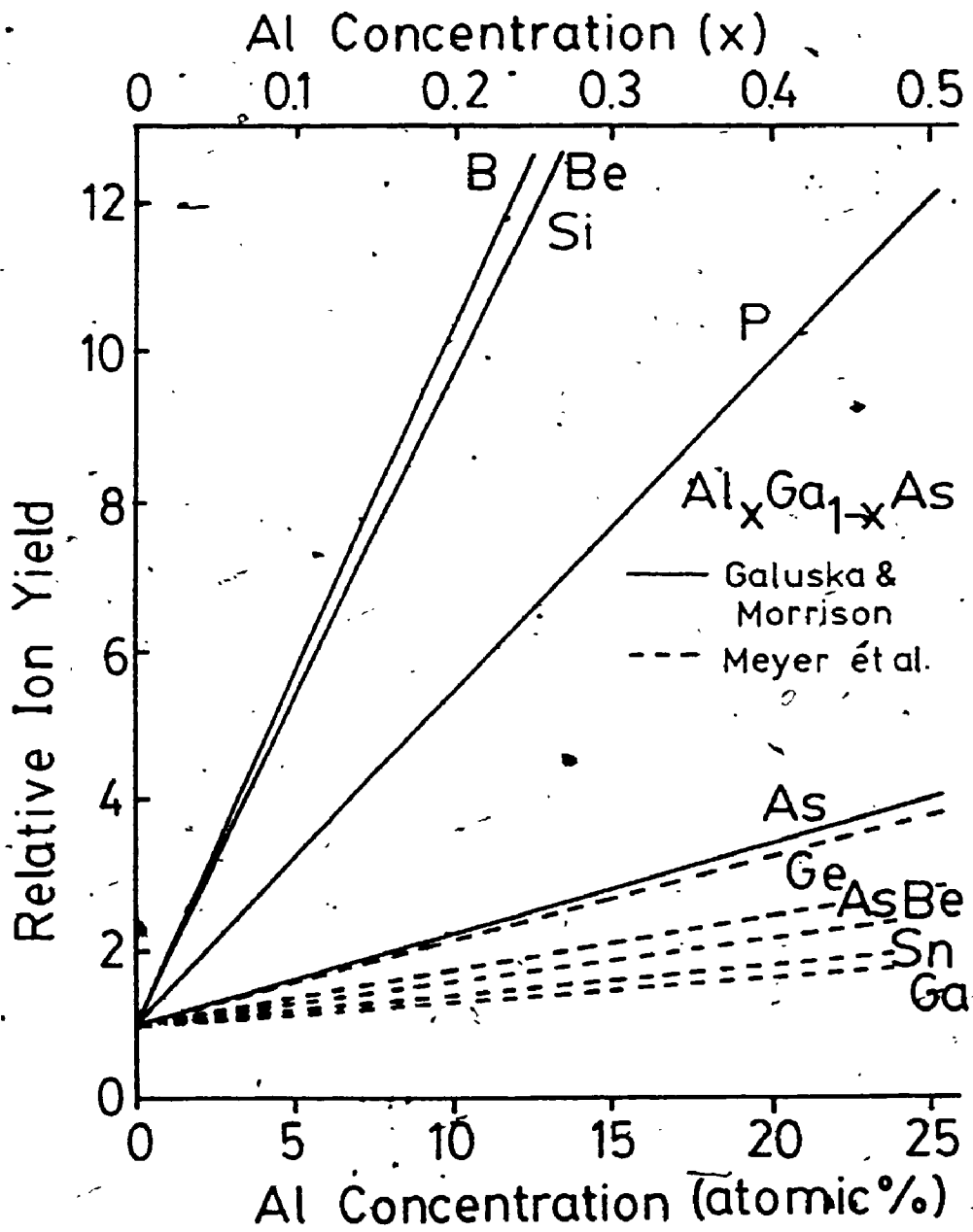


FIGURE 37 Relative ion yields versus bulk Al fraction

$$\bar{\Omega}_{\text{matrix}} = \sum_i \text{all matrix elements } C_i \Omega_i^{\text{O}} \quad (44)$$

where C_i = atomic fraction

Ω_i^{O} = bond energy - diatomic between i and oxygen

Galuska and Morrison (145) found a linear relationship between the average matrix bond energy to oxygen and the relative ion yield of dopants in $\text{Al}_x\text{Ga}_{1-x}\text{As}$, InP, InSb, GaP and GaSb. They found as well "that this linearity could be improved by using slightly modified bond energy values". Table 4 shows the values obtained in the literature (156) by Galuska and Morrison and the modified values. The uncertainty in the literature bond values can be as large as $\pm 20 \text{ kcal mol}^{-1}$.

The normalized ion yield for Be versus the modified values of the matrix bond energy for Galuska and Morrison's data (linear correlation coefficient of 0.998) is shown in Figure 38. The correlation is much poorer (correlation coefficient of 0.604) if the literature values of bond energy are used as plotted in Figure 39. Surprisingly, the $\text{Al}_x\text{Ga}_{1-x}\text{As}$ data of Meyer et al. in combination with the InP, InSb, GaP and GaSb data of Galuska and Morrison provides a better correlation (correlation coefficient of 0.826, Figure 40), if the literature values of bond energy are used. Another interesting point raised by this analysis is that only the *matrix to oxygen* values of bond energy are included in the calculation. The sputtered dopant ion has been ignored.

TABLE 4. ELEMENT-OXYGEN DIATOMIC BOND ENERGIES

Element	Bond Energy (156)	Modified Bond Energy (kcal mol ⁻¹)	Difference
Al	116	116	0
Ga	68	68	0
As	115	115	0
P	120	115	5
In	77	67	10
Sb	89	114.6	-25

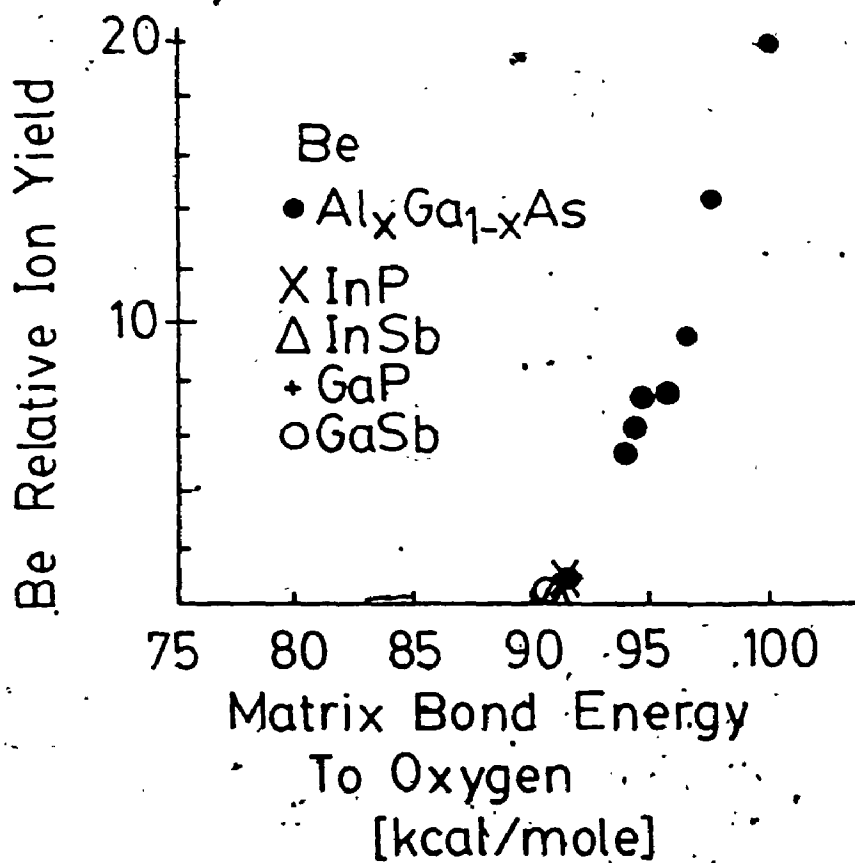


FIGURE 38 Relative ion yields versus modified bond energies (145)

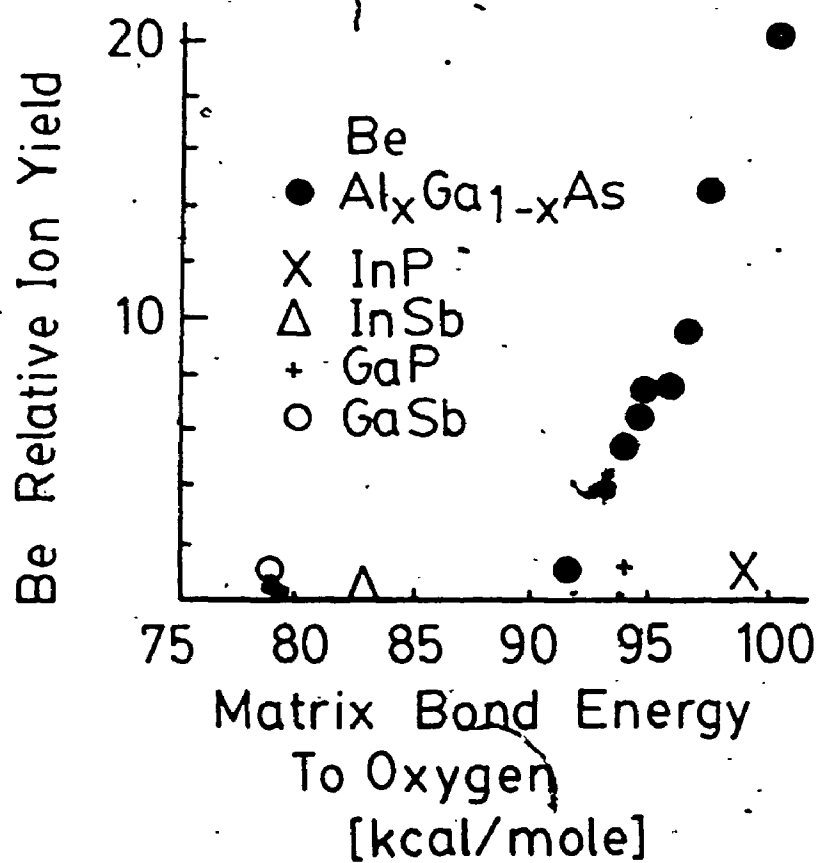


FIGURE 39 Relative ion yields versus literature values of bond energies

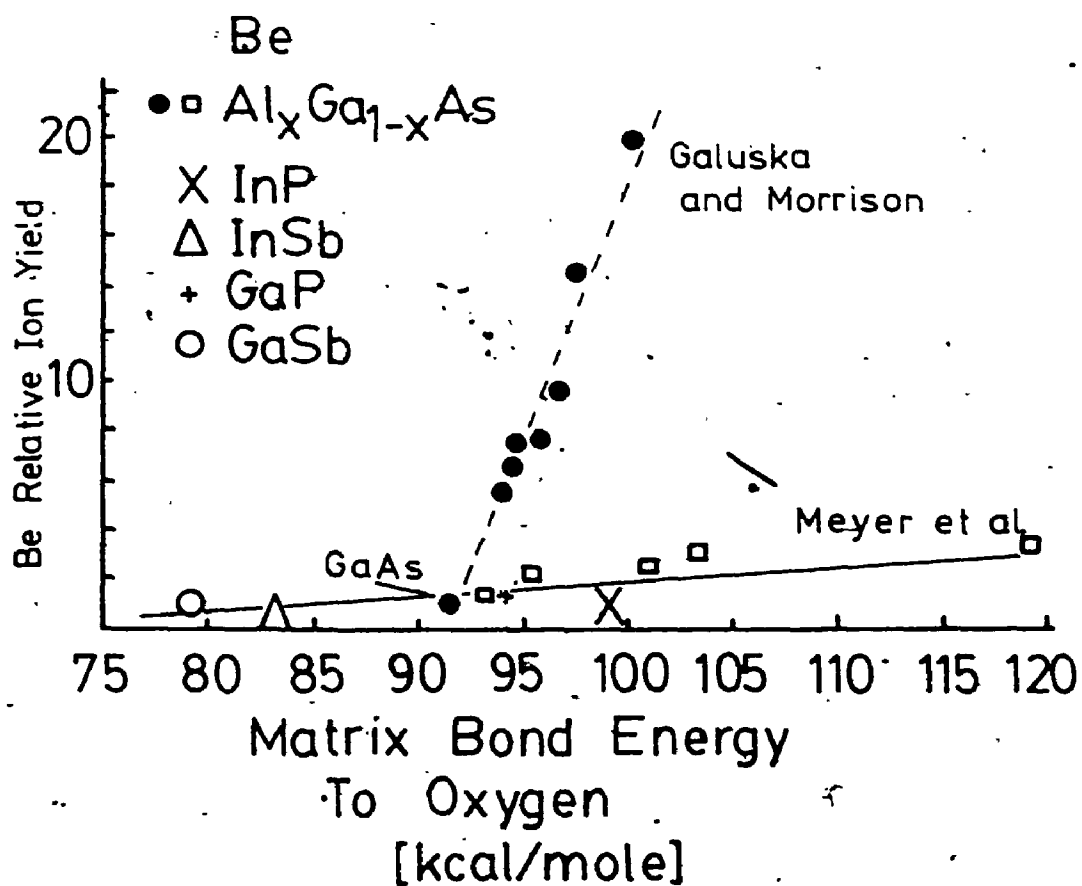


FIGURE 40 Relative ion yield of Meyer et al. (154),
 — Galuska and Morrison (145) versus literature
 values of bond energies

As well, if the surface of the sputtering site is not fully oxidized then some sputtered ions may originate from sites where oxygen is not incorporated. In these cases, the bond energy between all matrix components may be important and not just the bond energy between the major components and oxygen.

CHAPTER 2

THE ION MICROSCOPE

2.1 INTRODUCTION

Castaing and Slodzian (54) were the major contributors to the basic design of the Cameca IMS-3fTM ion microscope. This complex instrument has many components and controls to focus and deflect the ion beams by either magnetic or electric fields. The many controls are necessary to enhance the instrument's flexibility, allowing it to be applied to a broad range of samples, but the interactions which exist between the controls make the operation of the ion microscope complicated. The wide latitude of control also permits compensation for long term instrument drift. Instrument parameters may show a systematic variation over a period of time due to sputtering and coating of the internal instrument components by the primary and secondary ion beams. The careful selection and control of instrument parameters is necessary in order to obtain an accurate and repeatable measure of secondary ion intensities. The optimum parameters produce highly sensitive measurements which are reproducible and free from any instrument artifacts. The correct alignment of the ion beams and choice of instrument conditions are based on an understanding of each component of the instrument, a knowledge of how these components interact and even, in some cases, a perception of how the specimen interacts

with the instrument! Specimen outgassing, charging and the memory effect are a few of the ways in which the specimen itself may influence the measurement conditions.

A schematic of the Cameca IMS-3f ion microscope is shown in Figure 41.

Two different ion sources were used in this investigation. A cold cathode duoplasmatron generates a positive O_2^+ or negative O^- ion beam from a high purity (99.999%) oxygen feed gas which is the most commonly used gas for the IMS-3f. Experience has shown that the use of argon results in the rapid erosion of the cathode and a fouling of insulators leading to power supply failure. The polarity of the primary ion beam extracted from the duoplasmatron is determined by the polarity of the accelerating voltage (up to ± 20 KV). The optimum position of extraction of ions from the plasma depends on the polarity of the extracted ions; generally the centre of the plasma yields highest positive ion intensities while best negative intensities are extracted from the shoulders of the plasma.

The second source generates a Cs^+ primary ion beam. Caesium is vapourized in a heated reservoir and passes through a heated tungsten frit. The caesium atoms are almost 100% ionized as they leave the surface and are accelerated to as much as 15 keV energy in a positive electric potential.

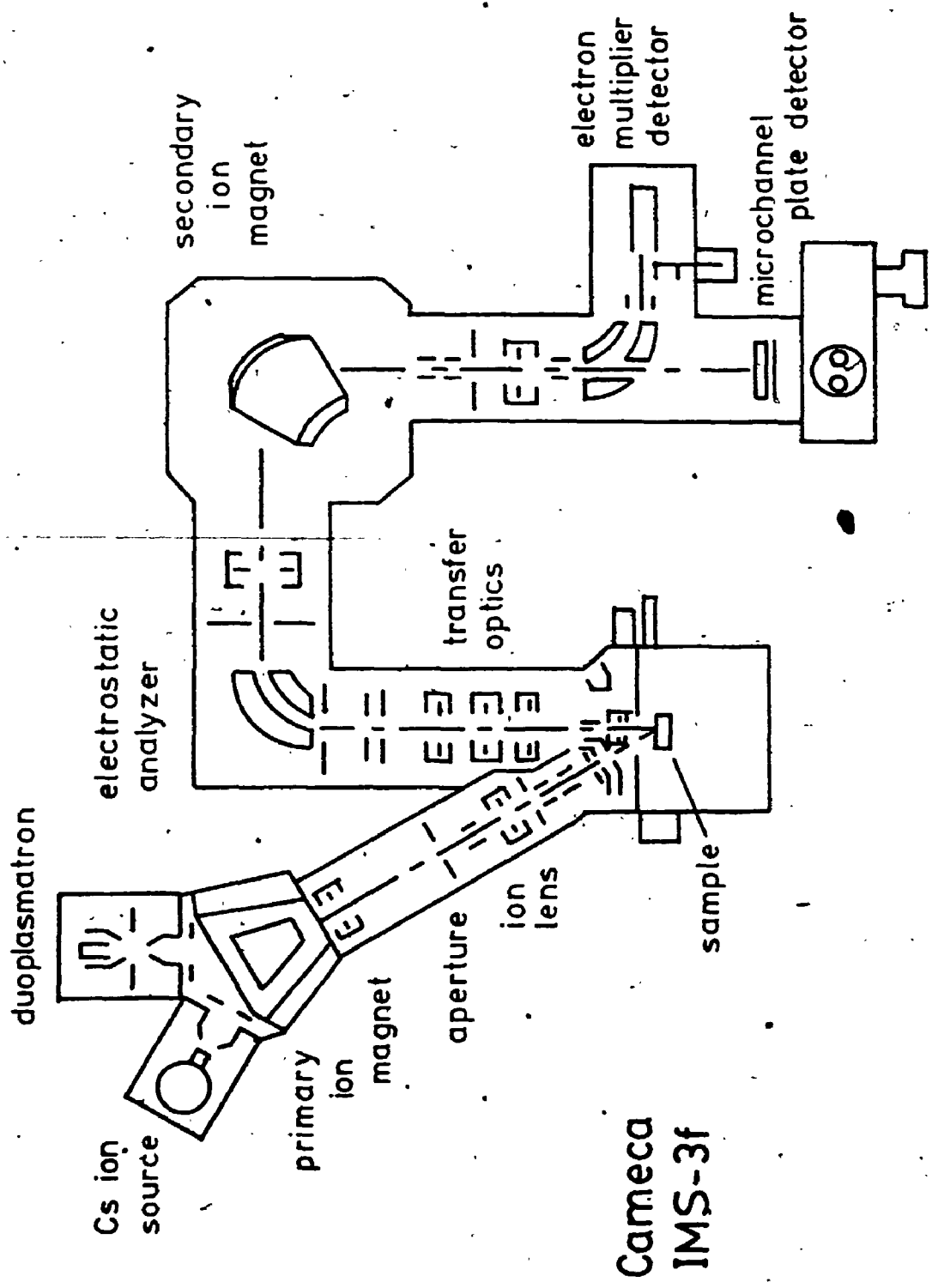


FIGURE 41 Schematic representation of the Cameca IMS 3f™ (trade mark)

The specimen itself is maintained at a potential of ± 4.5 kV so that the bombarding ion energy is the result of the sum of the potential of both the ion source and the specimen. The term "net energy" will be used here to designate the energy of the primary ion incident on the specimen.

The primary ion magnet selects the primary ion species and aligns the ion beam from the ion source with the axis of the first downstream lens in the primary ion column. Only one ion source is functional, at any given time, since the sources share the same primary magnet. The neutral and undesired components of the ion beam are eliminated by collisions with apertures, lenses and structural components. Ions with the selected mass to charge ratio are then focussed on a molybdenum aperture by a unipotential lens. The aperture is initially 400 μm in diameter (but is rapidly eroded by the ion beam) and results in a 10% peak height mass resolution of about 200. Next, the primary ions are aligned by a deflector before entering another unipotential lens. The function of this lens is to regulate the intensity of the ion beam by controlling the fraction of the ion beam which passes through a second aperture. The beam then passes through a set of stigmators followed by a pair of deflectors. These deflectors control

- a) the position of the beam on the specimen
- b) rastering of the beam and

- c) deflection of the beam from the specimen to the so-called "Faraday cup".

(The "Faraday cup" is a container into which the primary ion beam can be deflected so that no particles escape except the electrons which flow to or from the container by way of a sensitive current meter.) A final lens element focuses the primary ion beam to a minimum diameter of about 1 μm . The axis of the primary ion column is 30° from the normal to the plane of the specimen surface. The primary ion column upstream of the second primary aperture is maintained at a pressure of 10^{-3} to 10^{-5} Pa by a 110 l s^{-1} turbomolecular pump. The pressure in the sample chamber is normally 6×10^{-6} Pa.

The specimen is inserted into the analysis chamber by way of an introduction chamber pumped by a second 110 l s^{-1} turbomolecular pump. In the analysis chamber the specimen sits above a 1000 l s^{-1} liquid helium cryopump. The specimen may be translated in the plane which is perpendicular to the secondary ion column (denoted the X-Y plane) to select the analysis area on the specimen. A crude microscope allows visual positioning of the specimen. The secondary ion column has two 500 l s^{-1} ion pumps maintaining a pressure of 10^{-7} to 10^{-6} Pa.

Secondary ions emitted from the sample are accelerated to 4.5 keV energy by the potential applied to the specimen

holder and the ground potential at the immersion lens located 5 mm in front of the sample. Secondary ion polarity is determined by the polarity of the sample voltage. Ions pass through a hole in the immersion lens into the transfer optics which serves to maximize the collection efficiency for secondary ions and focuses the image crossover on the entrance slit and contrast aperture of the mass spectrometer. The mass resolution of the mass spectrometer can be varied by external adjustment of the widths of the entrance slit, the exit slit and the energy slit. This mass resolution is variable from 250 to over 10,000. The contrast aperture limits the energy and angular dispersion of the secondary ions. The field aperture is located between the contrast aperture and the electrostatic analyzer (ESA). The field aperture limits the analysis area. The ESA disperses the secondary ions according to their energy and allows the correct geometry to be maintained for entrance to the magnetic sector of the mass spectrometer. The secondary ions pass through an adjustable energy slit and spectrometer lens before the secondary magnet. Secondary ions must be focussed onto the correct plane of the magnet for minimum distortion of the ion image. The combined use of electric and magnetic sectors gives a double focussing mass spectrometer since the ion beam is focussed first for kinetic energy by the ESA and then for mass-to-charge ratio by the magnet. This layout is known as a Nier-Johnson geometry. The secondary ions may be

detected by a sensitive multistage electron multiplier, a second Faraday cup devoted to secondary ions or a micro-channelplate electron multiplier. The multistage electron multiplier is used in the pulse counting mode while high-count rate signals are deflected and measured ~~in the~~ Faraday cup. To create an ion image, the secondary ions are focussed on an image plane at the front surface of the micro-channelplate. Ions striking the microchannels generate electrons which are accelerated down the microchannels creating additional electrons as a consequence of collisions with the walls. These electron cascades which emerge from the microchannels strike a fluorescent screen thus giving the visible ion image. The screen can be viewed by a light microscope or the image may be recorded with a 35 mm camera system.

The IMS-3f is controlled by a Hewlett Packard 9845B computer which is also used to acquire, display, store and analyze the secondary ion signals. Fourteen separate programs, stored on a magnetic tape cassette, control the analysis sequence. Each program performs a different function such as depth profiling, measuring isotope ratios or acquiring a mass spectrum. The software was issued by Gerard Favier of Cameca on December 13, 1979 and was supplied to Surface Science Western for use with their instrument which was received in March 1981.

The computer is interfaced to the SIMS instrument to automatically perform the following functions:

- 1) deflect the primary beam from the specimen to the Faraday cup,
- 2) read the primary beam current,
- 3) read strategic voltages,
- 4) control primary beam scanning,
- 5) control the mode of secondary ion detection,
- 6) control the specimen X and Y position,
- 7) control the imaged field,
- 8) read the secondary ion signal either in a Faraday cup or an electron multiplier,
- 9) control the secondary ion magnet,
- 10) read the secondary ion intensities,
- 11) control the specimen offset voltage.

Shortly after the Surface Science Western IMS-3f was commissioned, areas of deficiency were identified. As a consequence, the instrument was modified to improve its operation as solutions came to light and funding permitted. Inefficient and erroneous computer programs were revised, as discussed in section 2.2. Equipment modifications were carried out by the staff of Surface Science Western and this author. Major or significant modifications include the replacement of the electron multiplier pre-amplifier to reduce the dead time and improve the sensitivity of the

counting system. A residual gas analyzer was installed which facilitated the detection and repair of numerous minor vacuum leaks. As a result, the analysis chamber pressure was reduced by about a factor of ten to 5×10^{-7} Pa. A precision gas control valve was installed to flood the analysis chamber with high purity gases. A scanning ion imaging display of the detected secondary ion signal was installed. Using this system, the field of analysis can be quickly centred in the rastered area and crater wall effects are eliminated. Sample translation in the X and Y plane frequently shifts the analysis region close to the crater wall (67) and without this innovation there is no provision for detecting and correcting this situation prior to each analysis.

2.2 COMPUTER SOFTWARE

The Cameca IMS-3f is controlled by a Hewlett-Packard 9845B minicomputer with 187,146 bytes of memory. Data generated during a SIMS analysis may be stored on tape on one of the two 217 K byte magnetic tape cassettes. Computer programmes which control the IMS-3f are read from the second cassette, however the instrument is not fully automated. An operator of the SIMS instrument must

- a) in Stage 1, establish the correct conditions prior to each analysis,

- b) in Stage II, monitor the instrument status during an analysis and,
- c) decide whether the data obtained from the analysis is acceptable, before continuing with the next analysis. The computer software is key to any SIMS analysis, since it determines the methodology of the analysis.

Each of the fourteen, originally supplied, computer programs interacts with the SIMS user in the manner described above. The programs a) request conditions, b) display data during the analysis and c) enquire if the data should be printed and stored. This seems to be a reasonable procedure, yet several problems were encountered in the manner in which this strategy was implemented. A major flaw in the supplied software was the inconsistency between the way in which the SIMS was controlled to establish the operating conditions (Stage I above) and the way in which the SIMS was controlled during actual analysis (Stage II). Inconsistencies were also apparent in the computer control of the instrument by different programs. As a result, the SIMS instrument could not perform acceptable analyses with the supplied programming, especially in the high mass resolution mode. The software was revised to overcome these deficiencies and enhanced to improve data handling and analysis.

The original computer programs were stored on magnetic tape cassettes and read off the cassette by pushing an

appropriate function key on the HP 9845.

Each program used in routine SIMS analysis is a variation of a simple series of steps in which the secondary ion magnet is set to align the m/e of interest with the detector, followed by the measurement of the ion count over an interval of time. In the computer programs named "Bar Graph" and "Mass Spectrum" the magnet is incremented through the m/e range specified by the SIMS operator. The "High Resolution" program increments the magnetic field from slightly below the m/e of interest to slightly above while recording and displaying the secondary ion count. "Isotope" changes the magnetic field in a cycle of selected m/e 's, while recording the ion count and determining the ratios of ion counts. The "Depth Profile" program shifts the magnetic field in a cycle of selected m/e 's; at each value it records the ion count. This information was then plotted as count versus cycle number. Later measurement of the crater depth allows the conversion from a cycle number to a depth scale. "Step-Scan" shifts the sample in the X-Y plane after a cycle of m/e count rate measurements. The "Energy" program is an exception to the above strategy; the magnetic field is held constant and the potential of the specimen is changed while recording the secondary ion count. The remaining seven programs were either simple variations of the above, monitored the stability of the instrument or provided instrument calibration routines for the use of the above programs.

The revised computer software, designated MAGO (for magnet operations), was restructured into one large computer program which was resident in the 9845 memory. This had the benefit of improved efficiency of operation of the SIMS while making the fullest use of the available computer capacity. No longer were several minutes of time wasted in waiting for programs to be read from the cassette tape (this delay could occur as frequently as every ten or fifteen minutes). Each analysis function (function referring to the above original program functions) now responds virtually instantaneously. The functions are interfaced in a manner that allows rapid switching by depressing the appropriate function key from, for example, the high resolution function which helps align the instrument in the high mass resolution mode to the depth profile function, and back, as is routinely required. This repeated iteration between program functions could not have been performed under the previous software system with the existing constraints on SIMS analysis time. This tactic saved more than time, it enhanced performance. Under the original software structure, SIMS users often struggled in vain, in pursuit of a single acceptable high resolution depth profile.

The incorporation of analysis functions into one computer program also allowed the functions to share subroutines, resulting in an overall 37% reduction in program steps but more importantly making the operation of the SIMS consistent

for each function. For example, the high mass resolution function now cycles the secondary magnetic field in the same series of steps as the depth profile function. In fact, in a preliminary stage of the high resolution function the magnet is cycled through the m/e series to overcome any magnetic "memory" and to reach a steady-state hysteresis loop prior to high resolution alignment.

The original computer program had provisions for determining the precise magnetic field for the m/e of interest by two methods. First by a computer algorithm which changes the magnetic field and stores the ion count. The sum of the product of the digital output V_D controlling the magnet and the ion count I_D can be divided by the total sum of the ion count measured over the range to determine V_C , peak centroid,

$$V_C = \frac{\sum V_D I_D}{\sum I_D} \quad (45)$$

A situation can be anticipated under high mass resolution conditions where several nearby m/e signals have similar ion counts. That situation would lead to the incorrect magnetic field being chosen. A situation such as this has occurred in practice, Figure 42.

The second alternative provided in the original program was to allow the operator to adjust the magnetic field by a manual control to maximize the count at the peak position. Digital circuitry then would determine and store the final

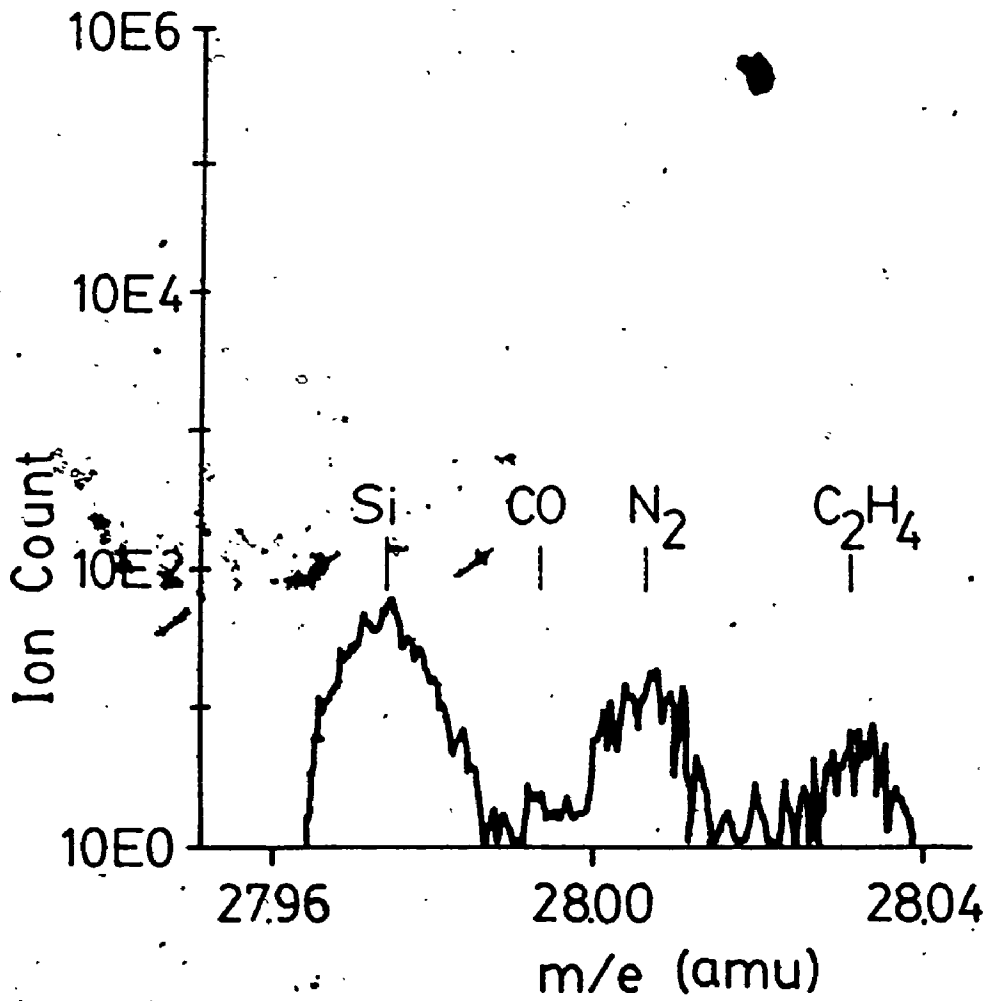


FIGURE 42 Mass spectrum showing molecular interferences

digital voltage value to reposition the magnet. Several problems arise in this situation. The final magnet position is dependent on magnet history--because of hysteresis. Thus the operator would carefully adjust the magnet control while watching a bouncing linear and logarithmic secondary ion count rate indicator for maximum intensity. Inevitably, the magnet would be shifted beyond the peak and the control would have to be reversed and the process repeated. This reversal of course proceeded in an arbitrary manner, and hence the magnet history (and the control of the hysteresis) became uncertain. As a consequence, when the computer re-set the magnet in its controlled but different path to final setting, the actual magnetic field differed slightly from the manually set value and the optimum secondary ion signals were not measured.

An alternate method was devised for the computer program MAGO. The high resolution program provides a graph of ion count versus m/e on the computer screen. - The operator can control a cursor which may be positioned on the screen to request from the computer the exact digital value which was output to obtain the magnetic field at that position in the mass spectrum (Figure 43). Numbers written to the screen correspond to the 19 bit digital value sent to the digital to analog voltage converter which controls the magnet. Sixteen bits correspond to the first number, three bits to

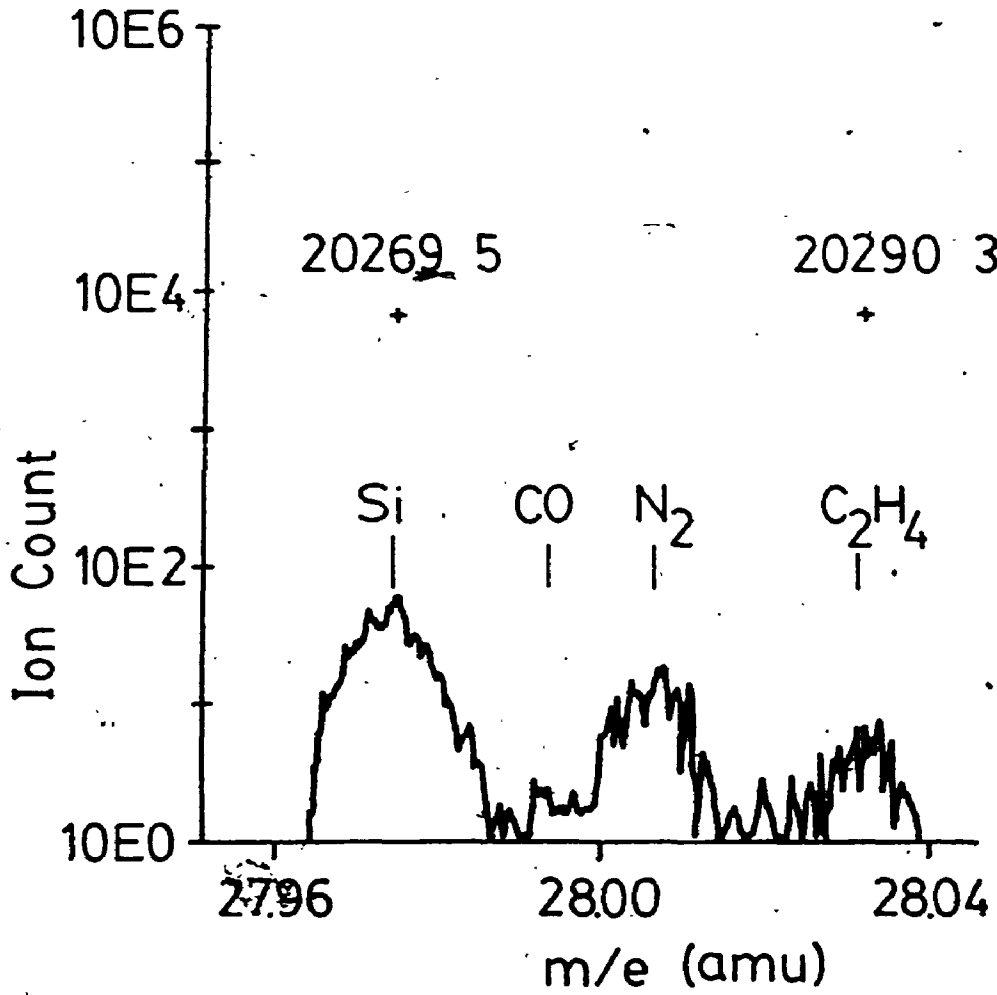


FIGURE 43 Mass spectrum with magnetic field parameter displayed

the second number. These values, designated "magnetic field parameters" could be stored and input as an option into other program functions. This option is an alternative to manual magnet positioning or the centroid calculation and duplicates the cycling of the magnetic field during an analysis.

Another important feature incorporated into MAGO is the correction of the measured ion intensities for counting system dead time (discussed in section 2.5) which was not taken into account in the original software. MAGO also has a number of new graphics features which enhance the presentation of SIMS data. Each m/e is designated by its number as the data is collected during a depth profile; as a result the SIMS operator can easily distinguish which plotted point corresponds to a given m/e . The depth profile function plots the ion count versus time as opposed to the original cycle number. A labeling routine allows for descriptive annotations to be added to the plotted data. Secondary ion counts, times and other relevant information may be printed at the operator's option to provide analysis documentation. The program revisions described above have been provided to a number of large corporations in the United States of America and MAGO is now used there and at Surface Science Western on a routine basis. The wide acceptance of these revisions has proven that they were necessary and

utilitarian. The program and a users guide to the operation of this software is available from Surface Science Western (158).

2.3 SAMPLE PREPARATION

Wafers of (100) GaAs from Cominco Limited were doped to a level of 3.0×10^{18} silicon atoms cm^{-3} and layers of $\text{Al}_x\text{Ga}_{1-x}\text{As}$ were grown by liquid phase epitaxy (LPE) by workers at Bell-Northern Research in Ottawa. The subscript x was determined to be 0.066 ± 0.001 , 0.210 ± 0.005 and 0.400 ± 0.005 by photoluminescence (PL) spectroscopy and Auger electron spectroscopy (AES). Each of the above layers were grown on a different GaAs substrate.

The isotope ^{28}Si was ion implanted into GaAs, $\text{Al}_{0.21}\text{Ga}_{0.79}\text{As}$ and $\text{Al}_{0.40}\text{Ga}_{0.60}\text{As}$ to a dosage of 1×10^{15} atoms cm^{-2} at energies of either 25 keV or 50 keV. The isotope ^{52}Cr was ion implanted into another set of GaAs, $\text{Al}_{0.21}\text{Ga}_{0.79}\text{As}$ and $\text{Al}_{0.40}\text{Ga}_{0.60}\text{As}$ samples to a dosage of 1×10^{15} atoms cm^{-2} at an energy of 50 keV or 25 keV and at a dosage of 3×10^{13} atoms cm^{-2} at 50 keV. Ion implantation was carried out at the Research Chemistry Branch of Atomic Energy of Canada Limited in Chalk River, Ontario. Additional ion implantations were carried out on semi-insulating samples of GaAs at Hughes Research Laboratories, Malibu, California, where ^{28}Si was implanted to a dose of 10^{14} atoms cm^{-2} and

100 keV and ^{52}Cr was implanted to a dose of 10^{14} atoms cm^{-2} at 125 keV. All of the above ion implantations were performed at room temperature with the ion beam at 7° from the surface normal (to limit ion channeling).

2.4 ANALYSIS CONDITIONS AND PROCEDURES

An oxygen primary ion beam ($^{16}\text{O}_2^+$) with a net energy of 8.0 keV or a caesium ion beam ($^{133}\text{Cs}^+$) with a net energy of 14.5 keV was rastered over a $250 \times 250 \mu\text{m}$ area during analysis. A field aperture restricted the analysis area to a $60 \mu\text{m}$ diameter region within the rastered area. Positive or negative secondary ions were monitored for O_2^+ and Cs^+ primary ions, respectively. Analysis was performed under low and high mass resolution conditions as well as with voltage offset for energy discrimination.

Samples were depth profiled in groups of two to four specimens using a specially constructed stainless steel sample holder. For a high mass resolution analysis, the following procedure was adhered to. At the beginning of an analysis period, the primary ion beam was aligned within the primary ion column, the secondary ion beam was also aligned within its column and the conditions for high mass resolution were obtained. Alignment was achieved using a $\text{Al}_x\text{Ga}_{1-x}\text{As}$ specimen and the correct magnetic field parameters could then be determined by holding the primary beam

stationary in the centre of the area viewed by the secondary ion optics. As the primary ion beam eroded the specimen, the secondary ion signal would arise from a range of depths and a constant implant signal could be attained. In this manner, one can make use of the crater wall effect to help in initial instrument alignment. Once the correct magnetic field parameters were chosen, the depth profile function was selected in the computer program. The m/e, count time and magnetic field parameters were input. Next came the steps which were repeated every time a new depth profile was initiated. The sample stage was shifted to a fresh area on a specimen and the primary beam was switched on to the specimen. The primary ion beam was aligned with the secondary ion optics using the oscilloscope method mentioned in section 2.1. The primary ion beam was switched off the specimen, into the Faraday cup. The sample was shifted again to a fresh location but only a short distance, of the order of 500 μm , and the depth profile was begun. During the first seconds of the profile, the primary beam position could be adjusted again if required. By following this procedure, the need to adjust other instrument controls was eliminated. Other samples could be loaded into the SIMS and analyses could be performed without altering the original instrument settings. To perform the next depth profile, it was necessary to repeat only the steps of shifting the sample stage, aligning the beam, a small shift of stage and analysis.

Using this method, the huge variations in ion yield observed by others performing repeated analyses were eliminated. The source of such variation is indeed operator adjustment and instrument fluctuation as predicted by Galuska and Morrison (155).

2.5 STATISTICAL ERRORS

The standard deviation σ , for the measurement of random secondary ions is

$$\sigma = \sqrt{N} \quad (46)$$

where N is the total number of counts. The measured secondary ion count is the sum of actual secondary ions N_T , plus the background N_B . Therefore,

$$\sigma = \sqrt{N_T + N_B} \quad (47)$$

The absolute error in the measured concentration decreases as N_T becomes smaller; nevertheless, the percentage error becomes larger. Considering a typical case, for a count rate above background of 150 counts per second for a 5 second counting period, the standard deviation is

$$\sigma = \sqrt{(150 + 10/60)5} = \sqrt{750.83} = 27 \text{ counts}$$

since the background count is typically 10 counts in 60 seconds. This corresponds to 3.6% of the value of the measured count. In general, the value of the standard deviation

will vary from about 0.3% near the peak concentration for a silicon implant such as studied here to about 10% for silicon concentrations of 10^{15} atoms cm^{-3} .

Ion counts are corrected for dead time of the detection and counting system according to the equation (159)

$$I_{\text{corrected}} = \frac{I_{\text{measured}}}{(1 - \tau_d I_{\text{measured}})} \quad (48)$$

where τ_d is the system dead time. No background subtraction of ion count was performed. Noise in the detection and counting system is less than 10 counts per minute.

Crater depths were measured with a DektakTM surface profilometer. Crater measurements were duplicated and measured in two mutually perpendicular directions. The accuracy of measurement was determined to be $\pm 8\%$.

CHAPTER 3

EXPERIMENTAL RESULTS

3.1 IMPLANT PROFILES

The measured values of secondary ion count versus time, for samples of $\text{Al}_x\text{Ga}_{1-x}\text{As}$ implanted with ^{52}Cr , obtained by depth profiling using a $^{16}\text{O}_2^+$ primary ion beam are shown in Figures 44 to 52. The same samples analyzed with a $^{133}\text{Cs}^+$ primary ion beam are shown in Figures 53 to 61. Implanted samples of ^{28}Si which were depth profiled with $^{16}\text{O}_2^+$ gave results which are shown in Figures 62 to 67 while those depth profiled with $^{133}\text{Cs}^+$ gave Figures 68 to 73. The higher energy implants of ^{52}Cr and ^{28}Si into GaAs are shown in Figures 74 to 77. Each figure has a legend showing the implant species, the energy (keV), dose (atoms cm^{-2}), the substrate, primary ion species and the mass resolution or voltage offset. The depth profiles shown in these figures were performed under a variety of primary ion beam current densities as it reflects common practice to change the primary ion current to obtain different erosion rates. Since the rate of data collection by the SIMS instrument is more or less constant (or at least fixed by convention for a group of analyses), changing the erosion rate will change the eroded depth for a given time period. In this study, each sample was depth profiled at least three times with

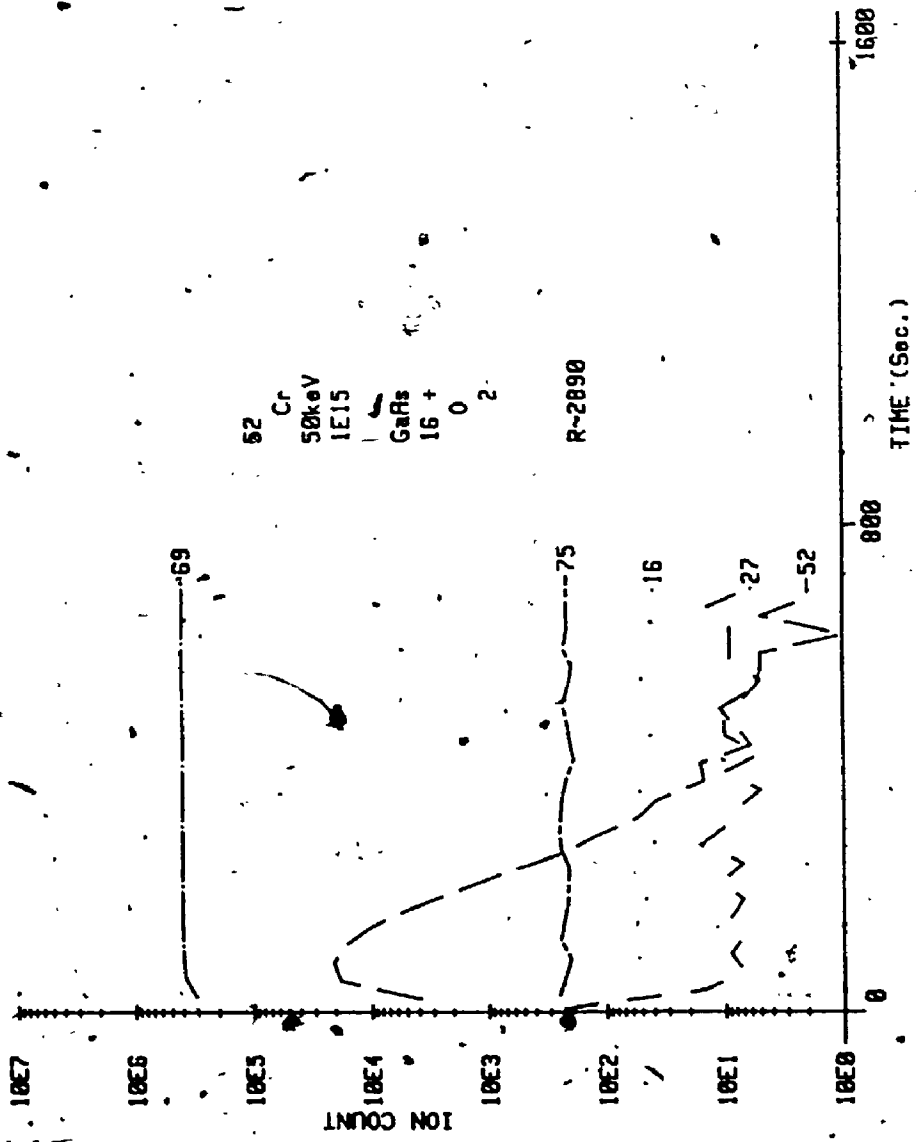


FIGURE 44. Secondary Ion Count Distributions of Cr in GaAs

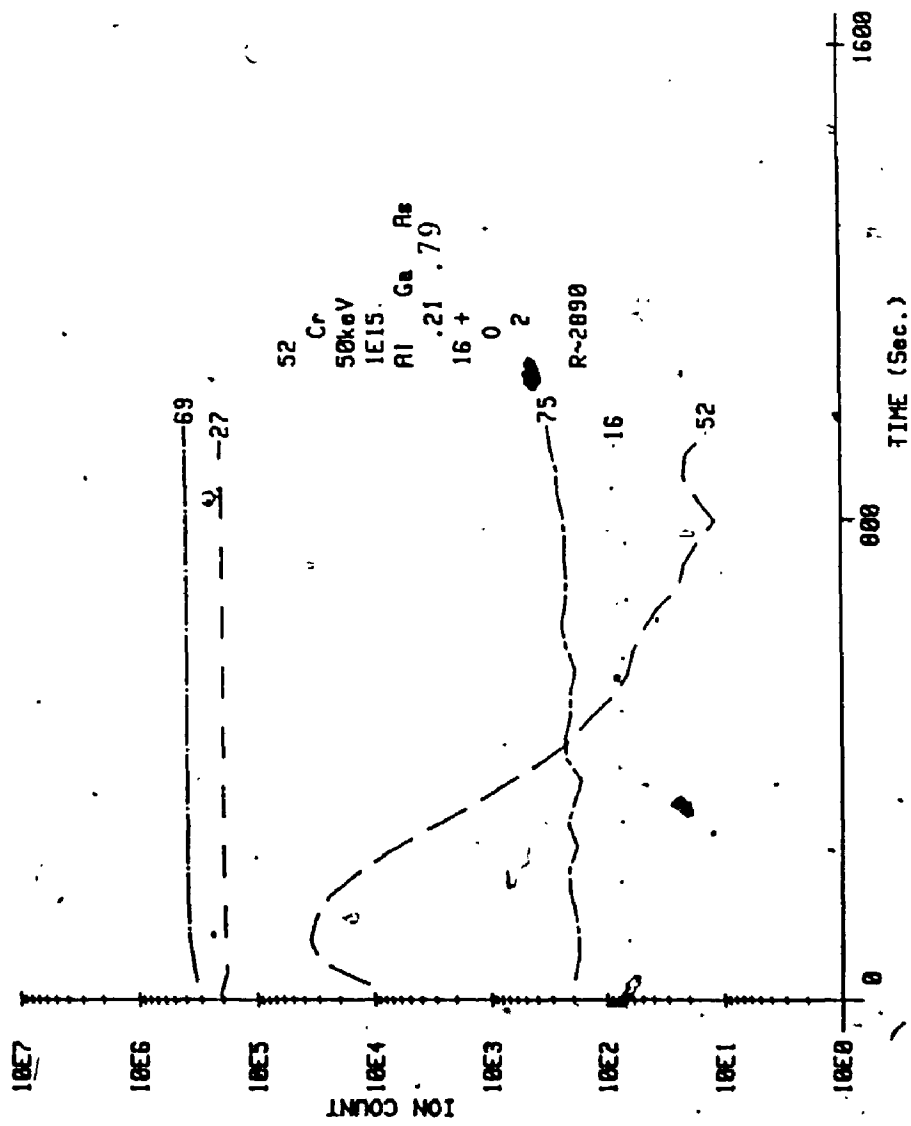


FIGURE 45 Secondary Ion Count Distribution of Cr in Al.21Ga.79As

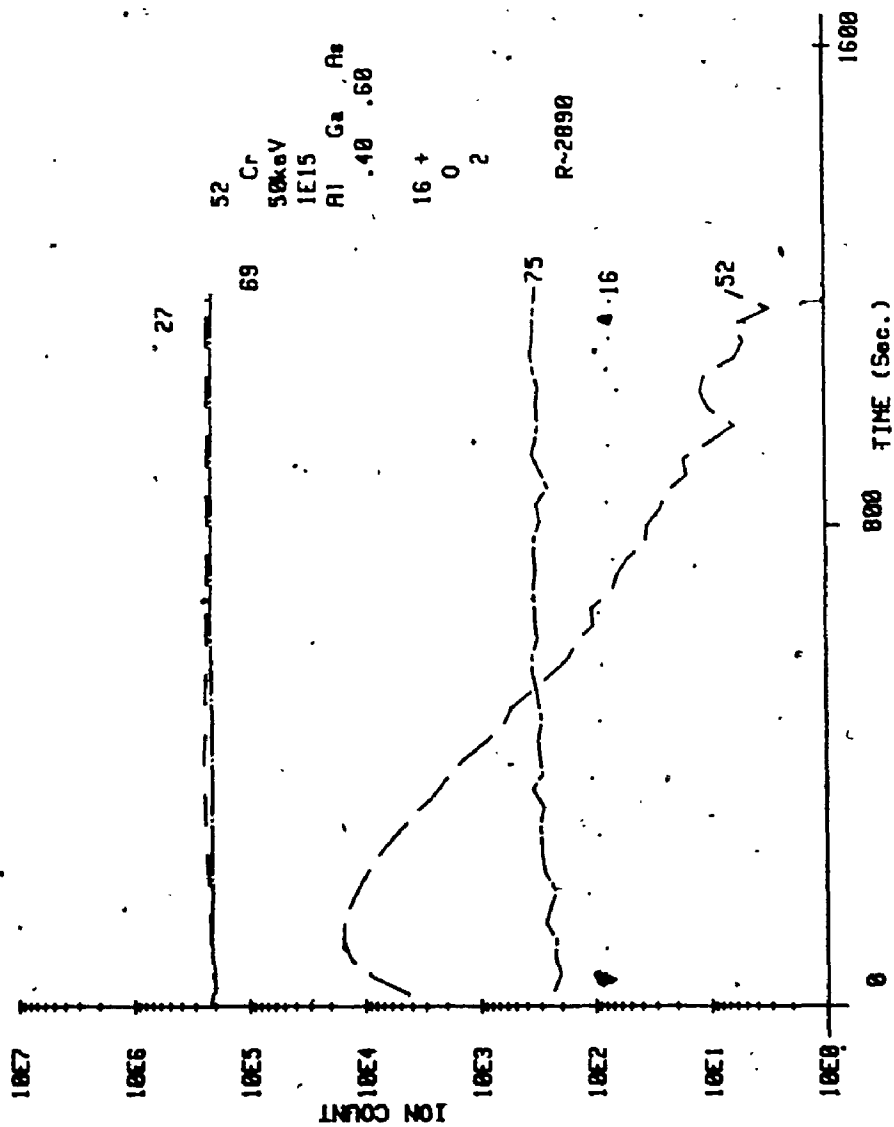


FIGURE 46 Secondary Ion Count Distributions of Cr in Al₄₀Ga₆₀As

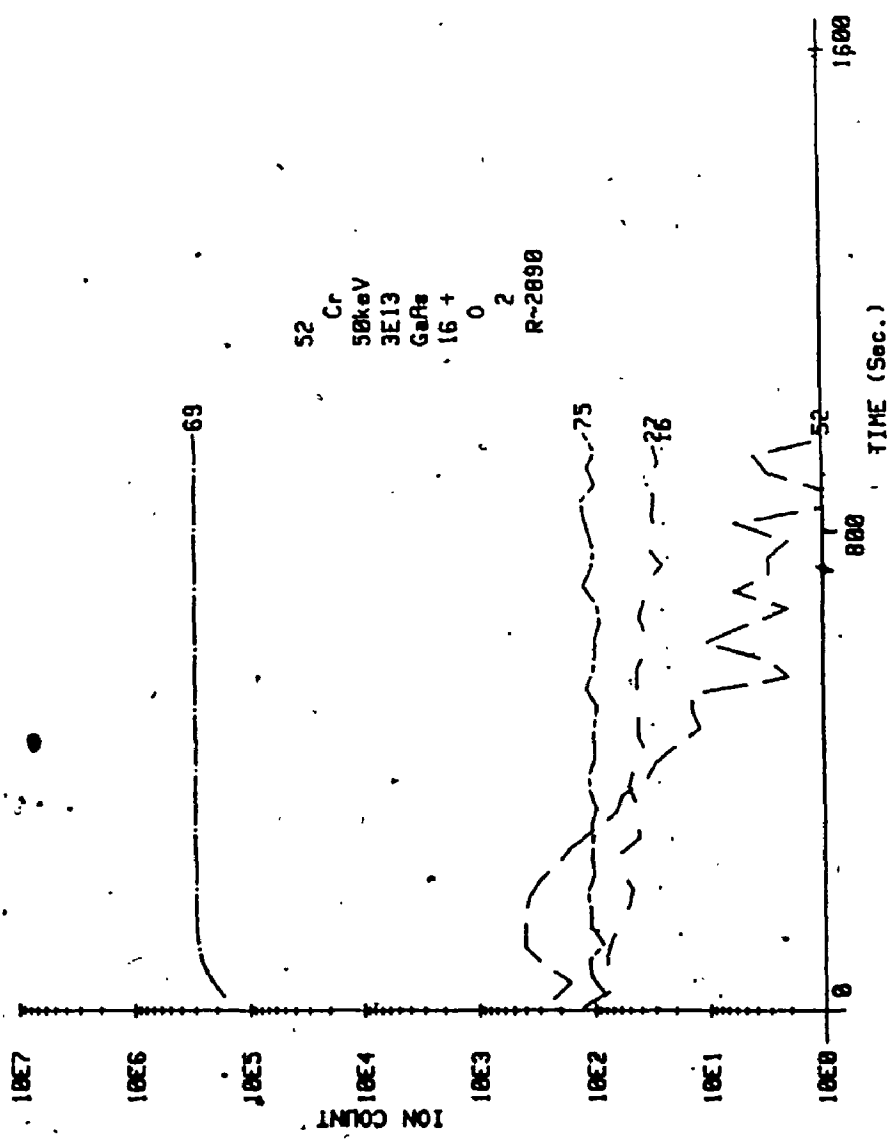


FIGURE 47 Secondary Ion Count Distributions of Cr in GaAs

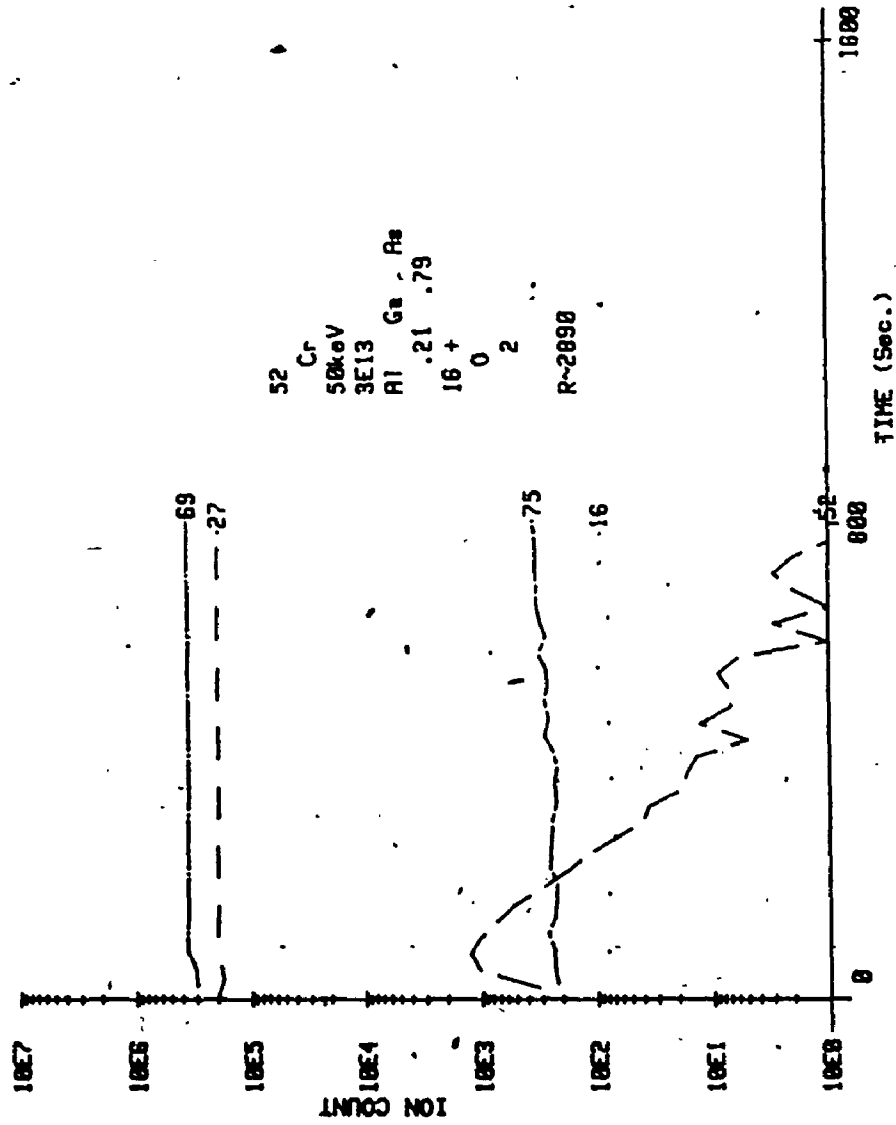


FIGURE 48 Secondary Ion Count Distributions of Cr in Al_{0.21}Ga_{0.79}As

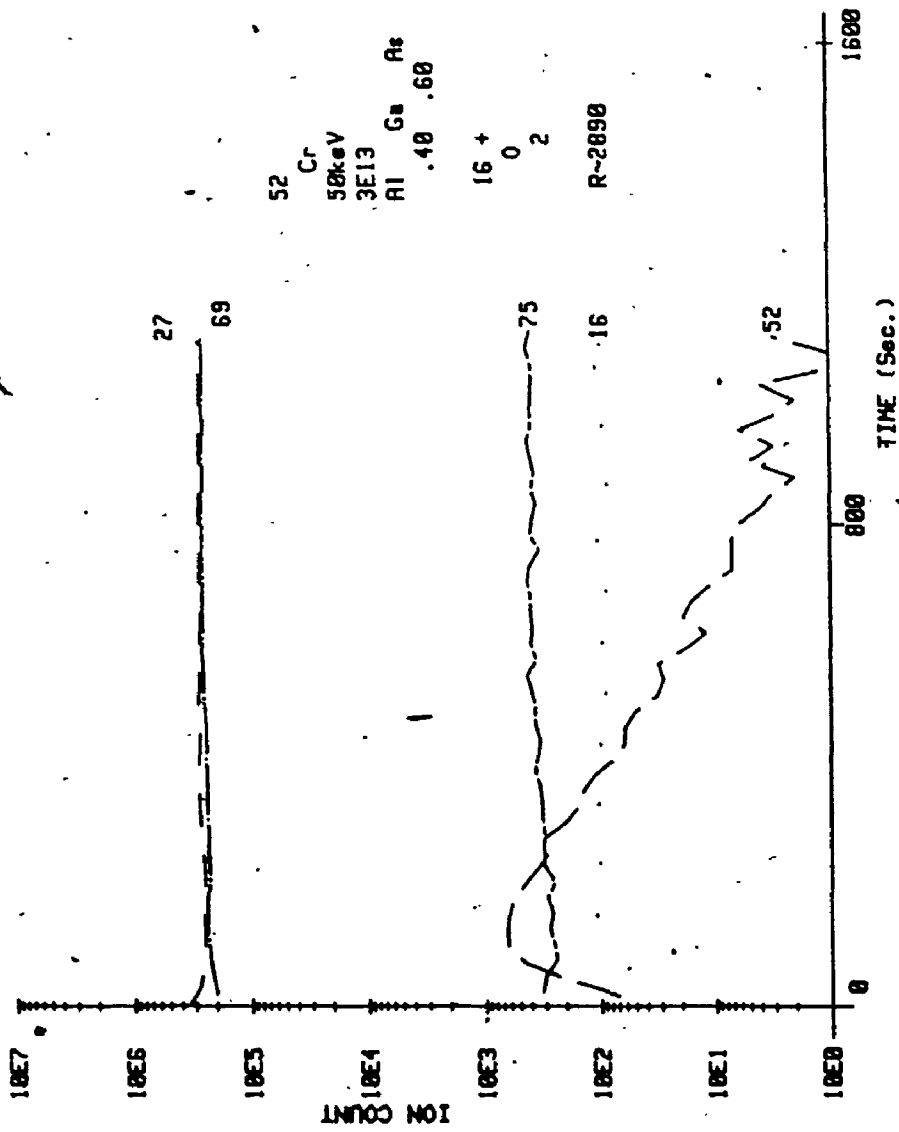


FIGURE 49 Secondary Ion Count Distributions of Cr in Al₄₀Ga₆₀As

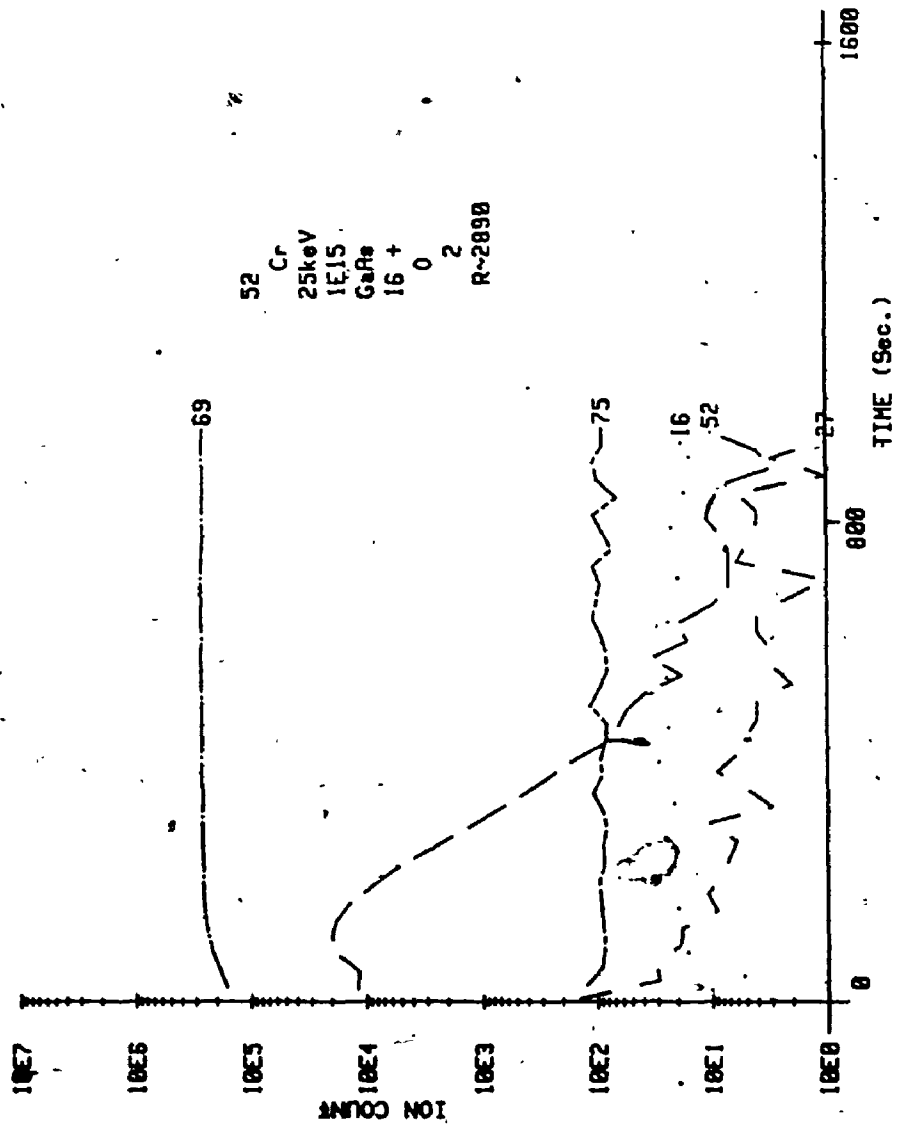


FIGURE 50 Secondary Ion Count Distributions of Cr in GaAs

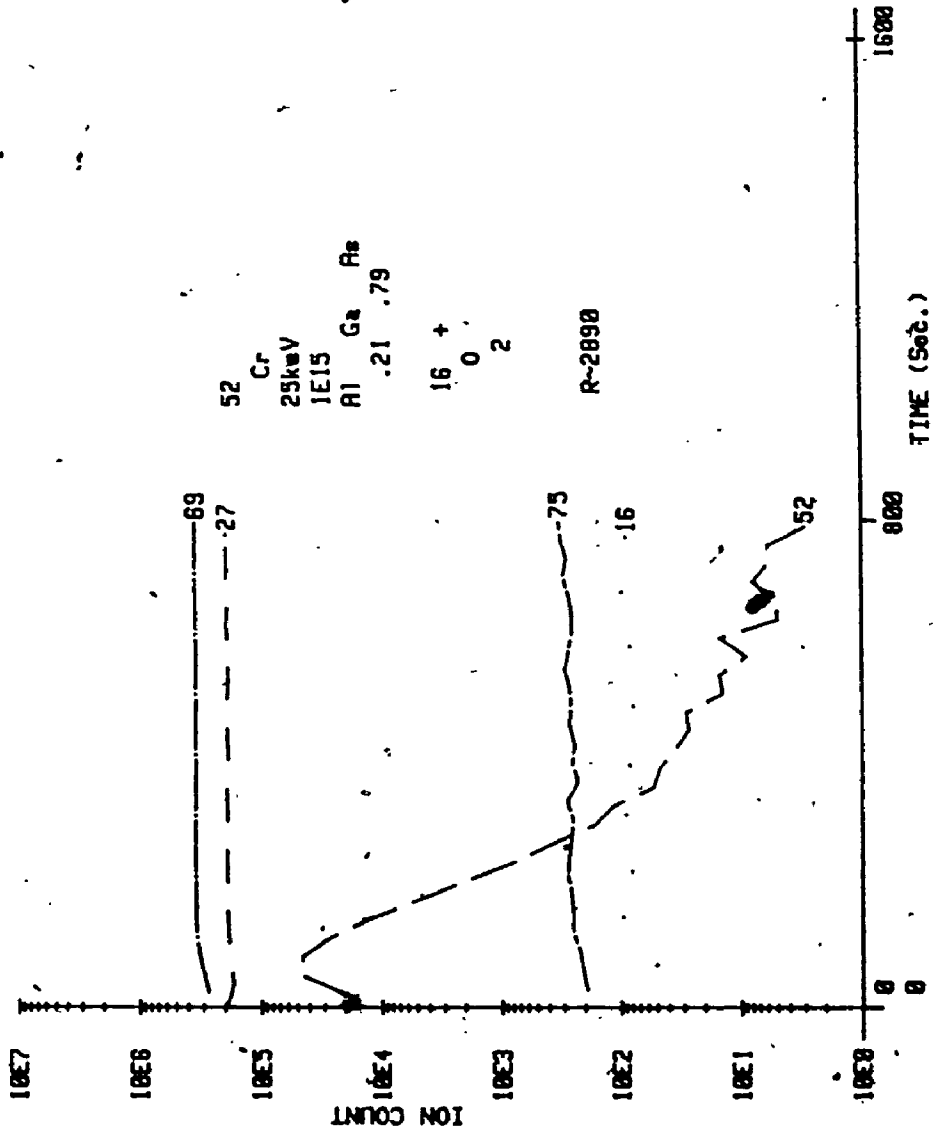


FIGURE 51 Secondary Ion Count Distributions of Cr in Al.21Ga.79As

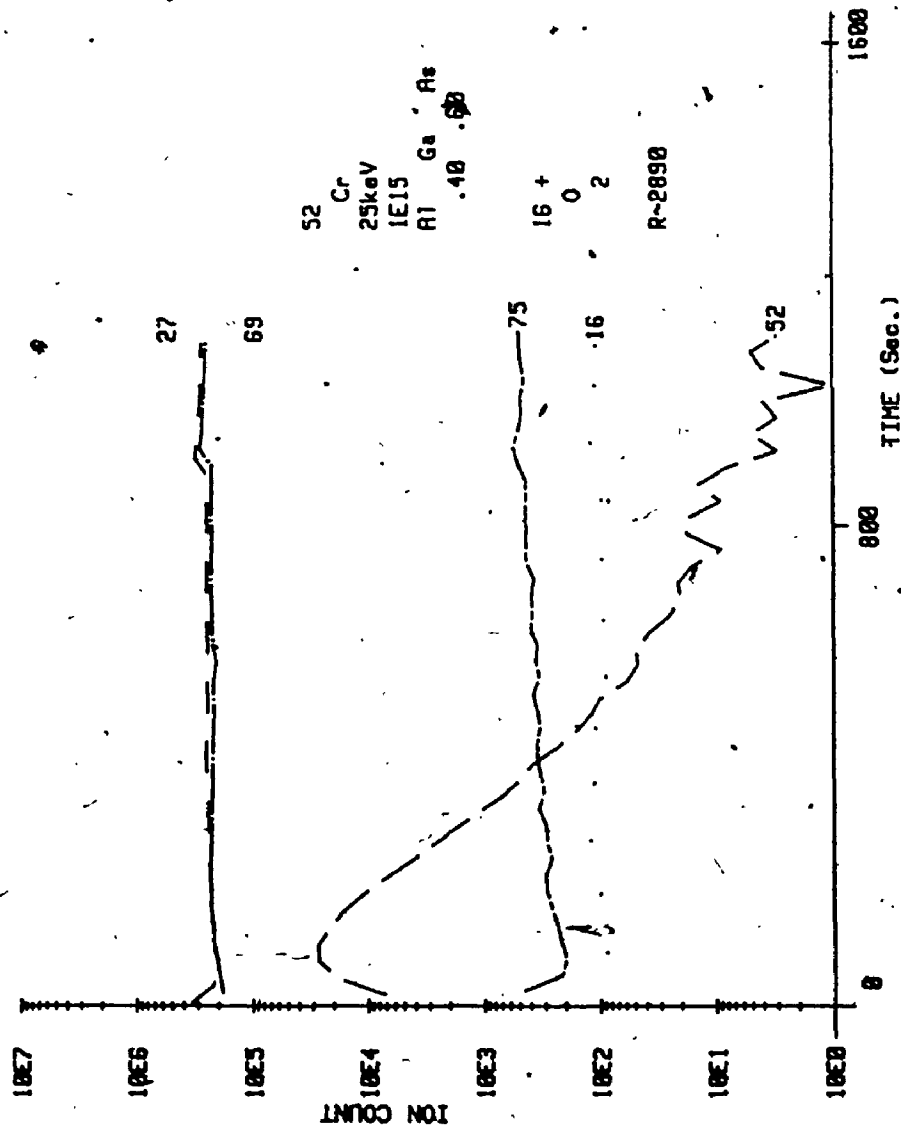


FIGURE 52 Secondary Ion Count Distributions of Cr in Al.04Ga.60As

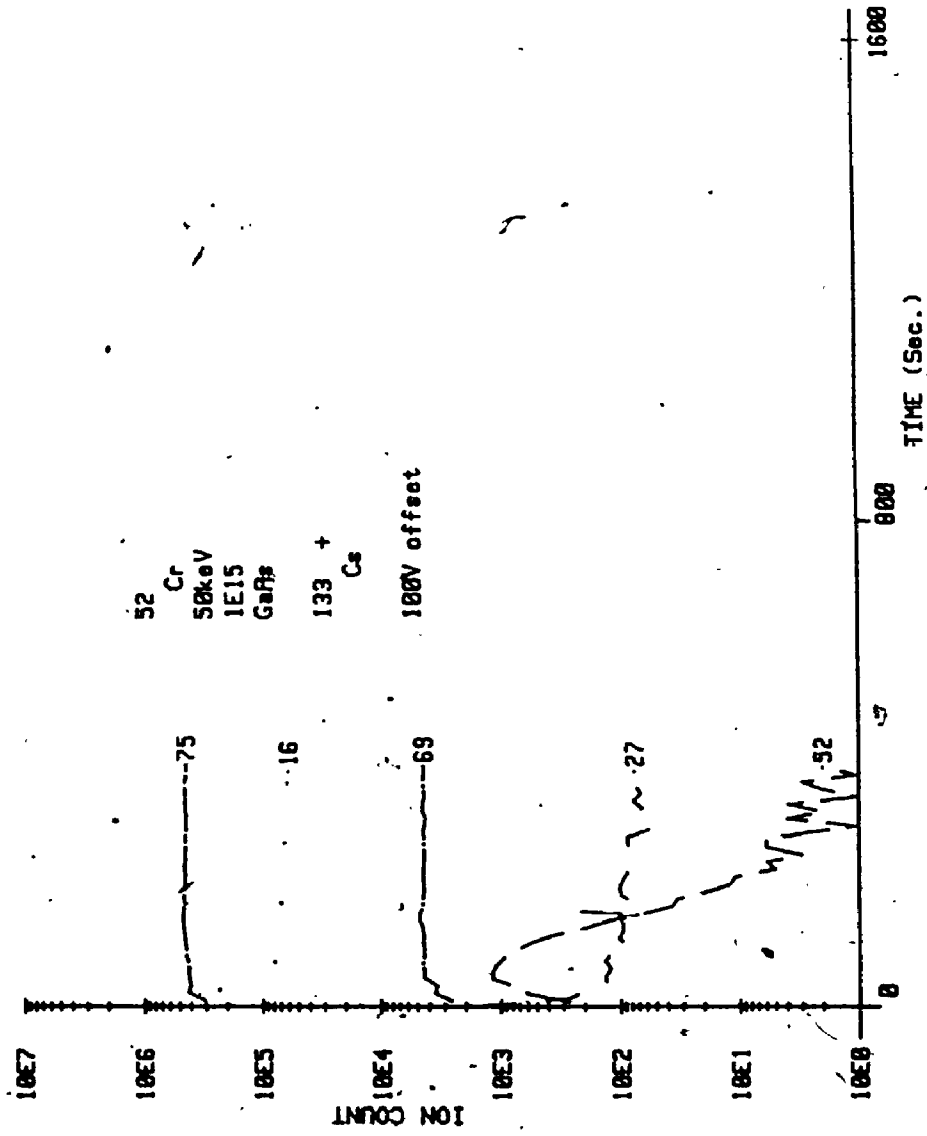


FIGURE 53 Secondary Ion Count Distributions of Cr in GaAs

6

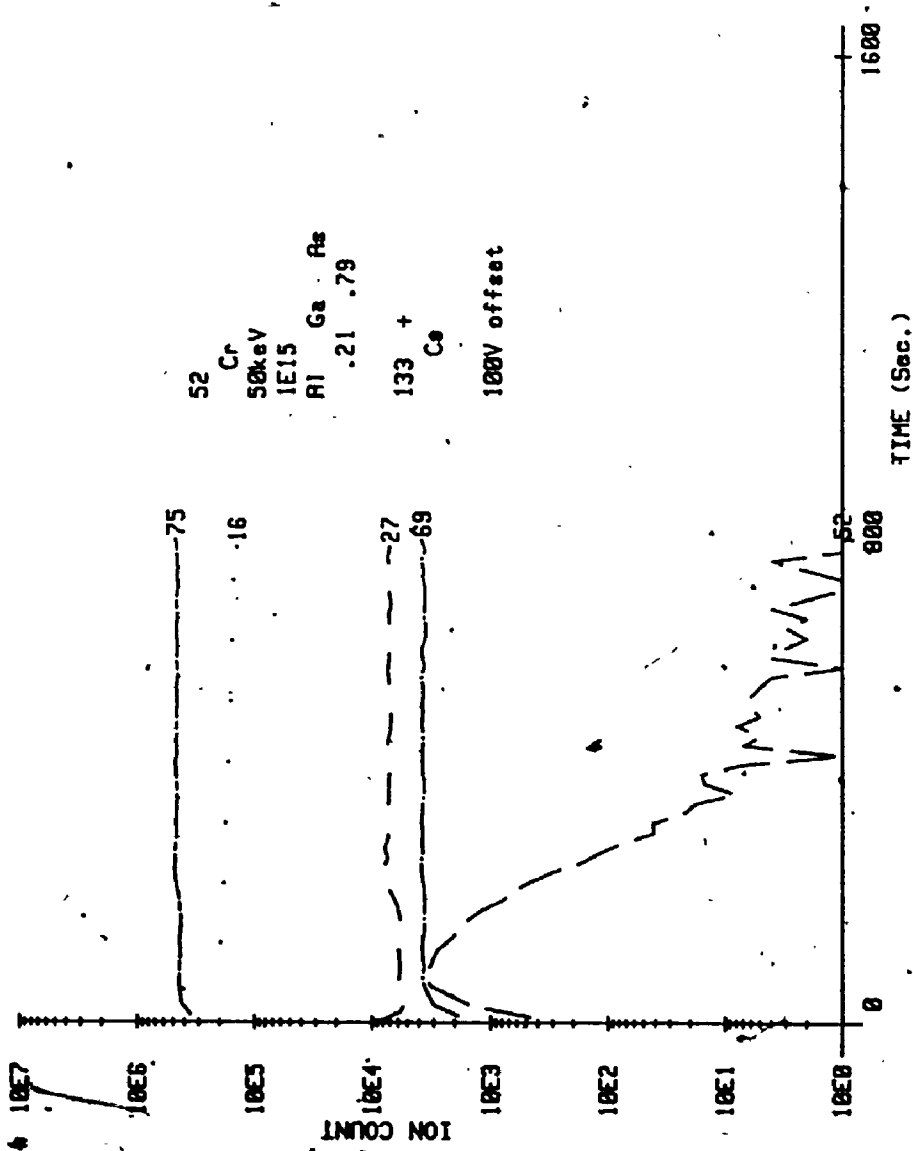


FIGURE 54 Secondary Ion Count Distributions of Cr in Al_{0.21}Ga_{0.79}As

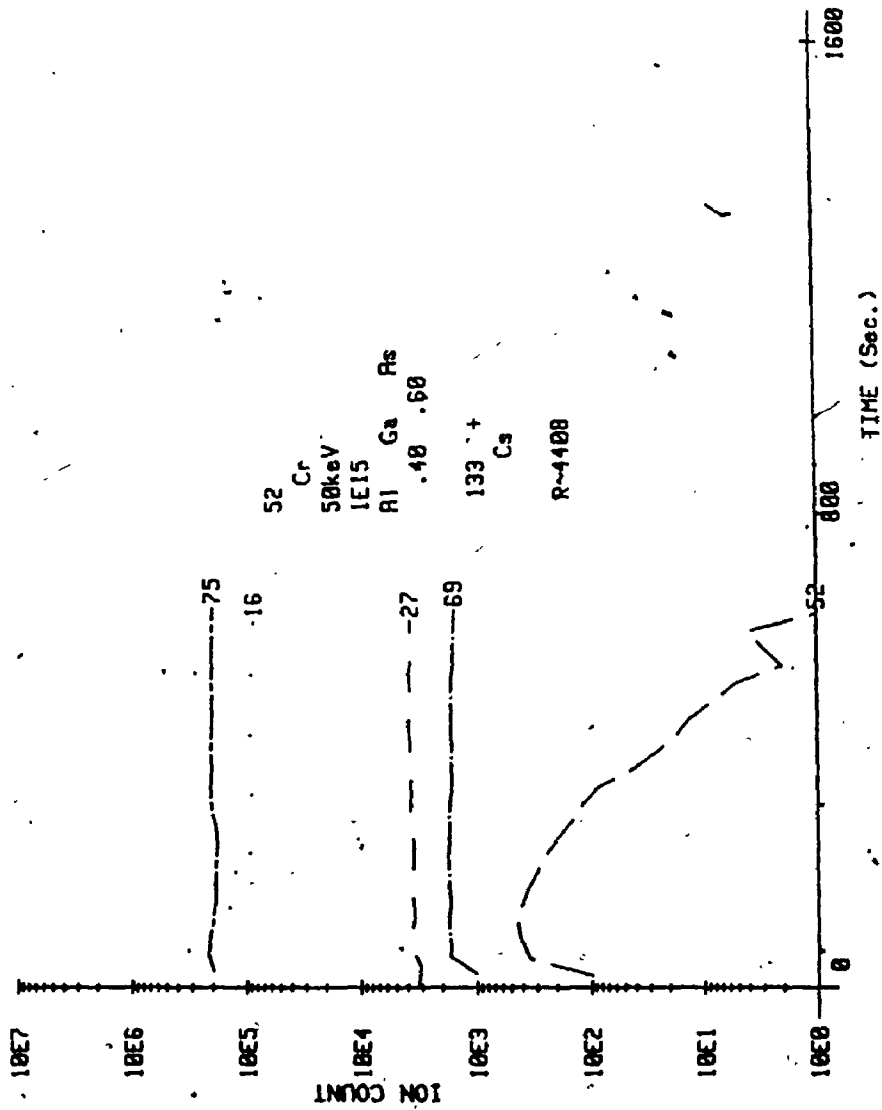


FIGURE 55. Secondary Ion Count Distributions of Cr in Al₄₀Ga₆₀As

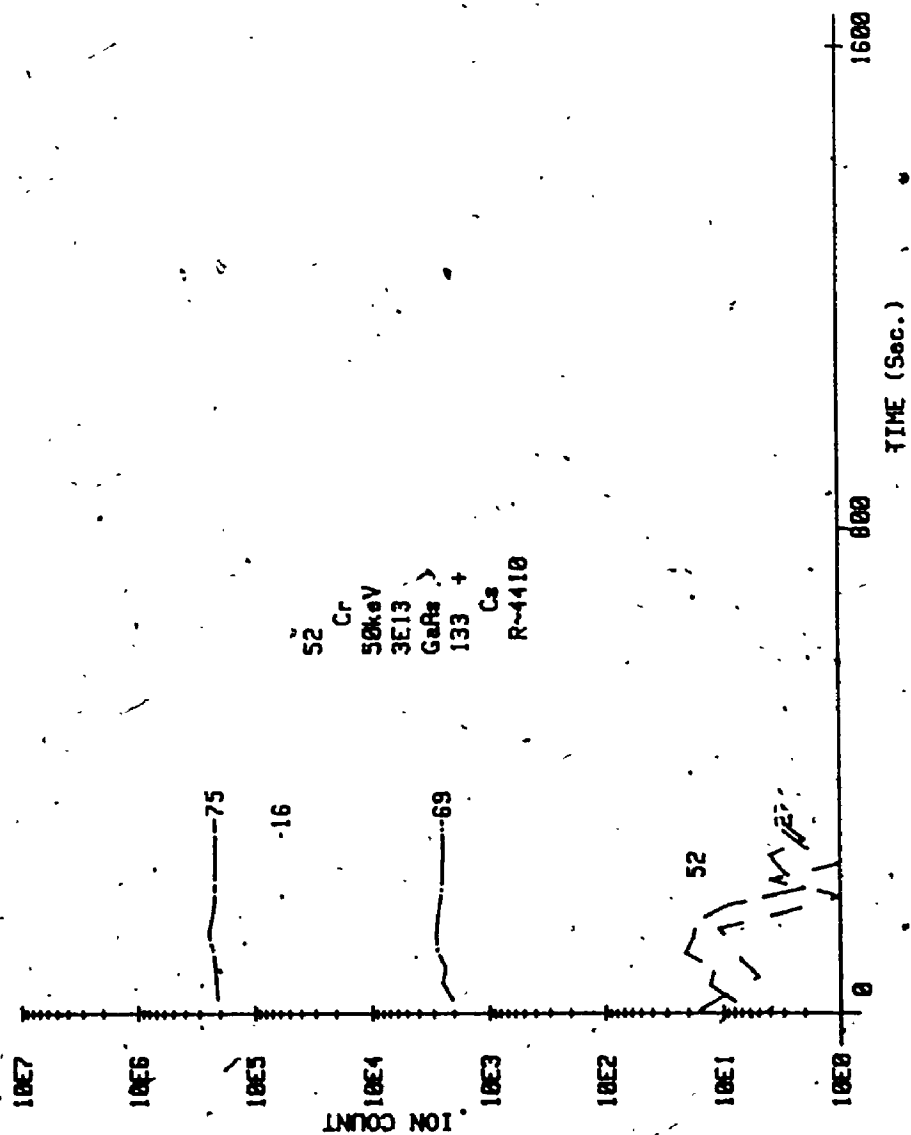


FIGURE 56 Secondary Ion Count Distributions of Cr in GaAs

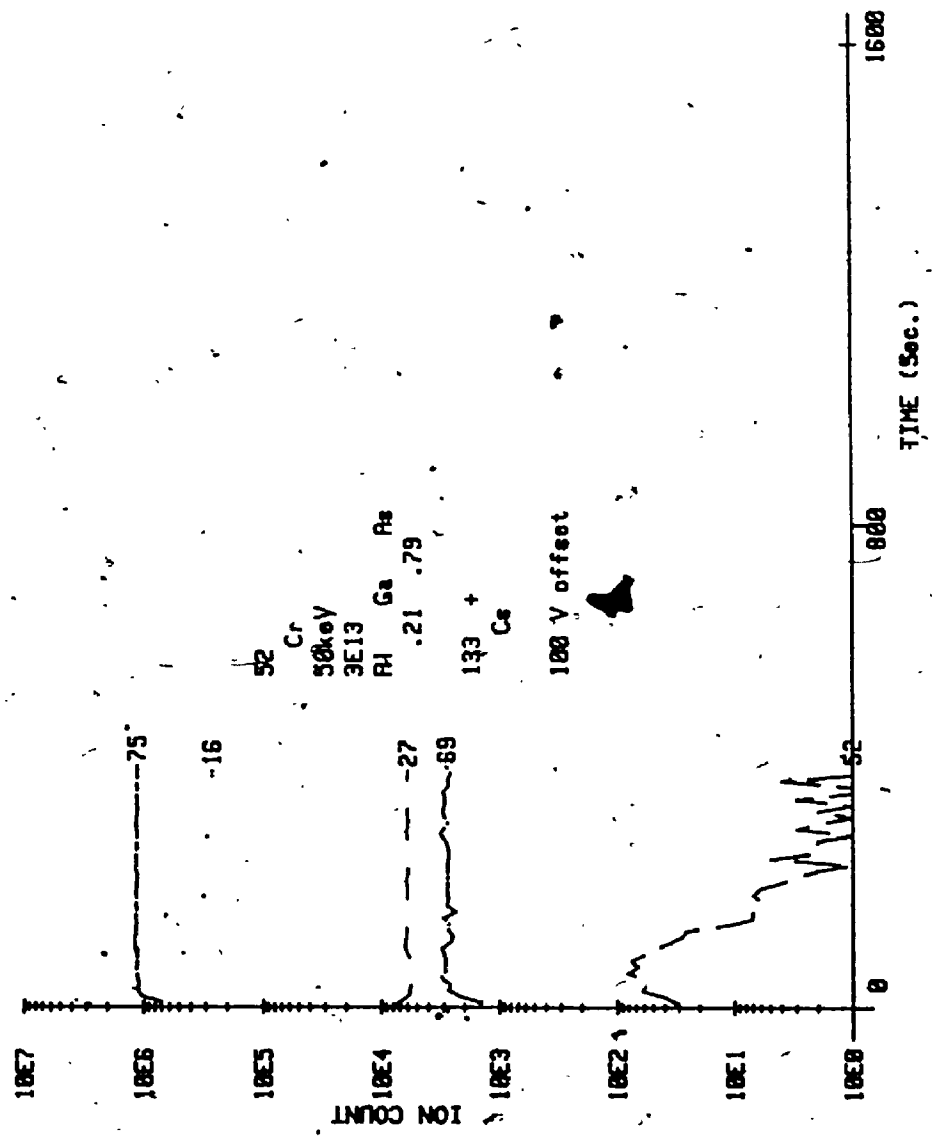


FIGURE 57 Secondary Ion Count Distributions of Cr in Al_{0.21}Ga_{0.79}As

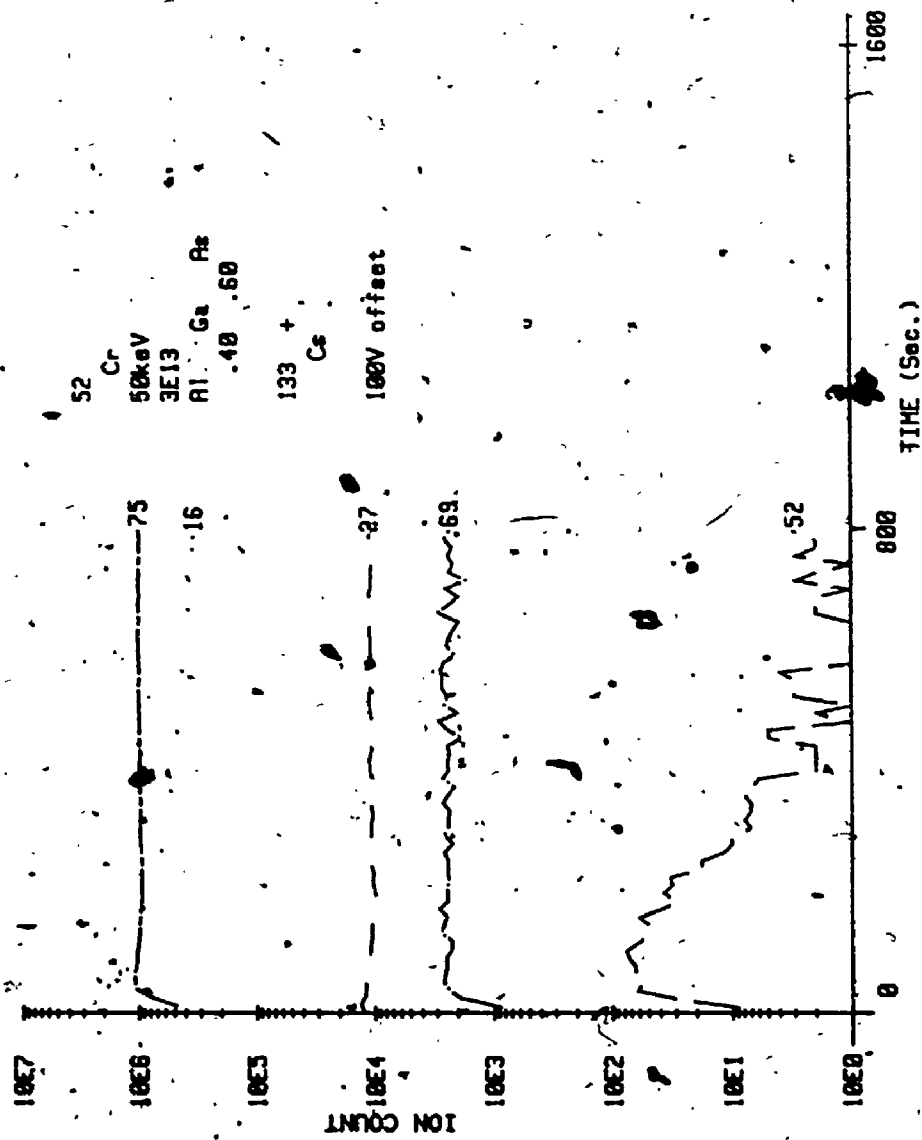


FIGURE 58 Secondary Ion Count Distributions of Cr in Al $_{40}Ga_{60}As$.

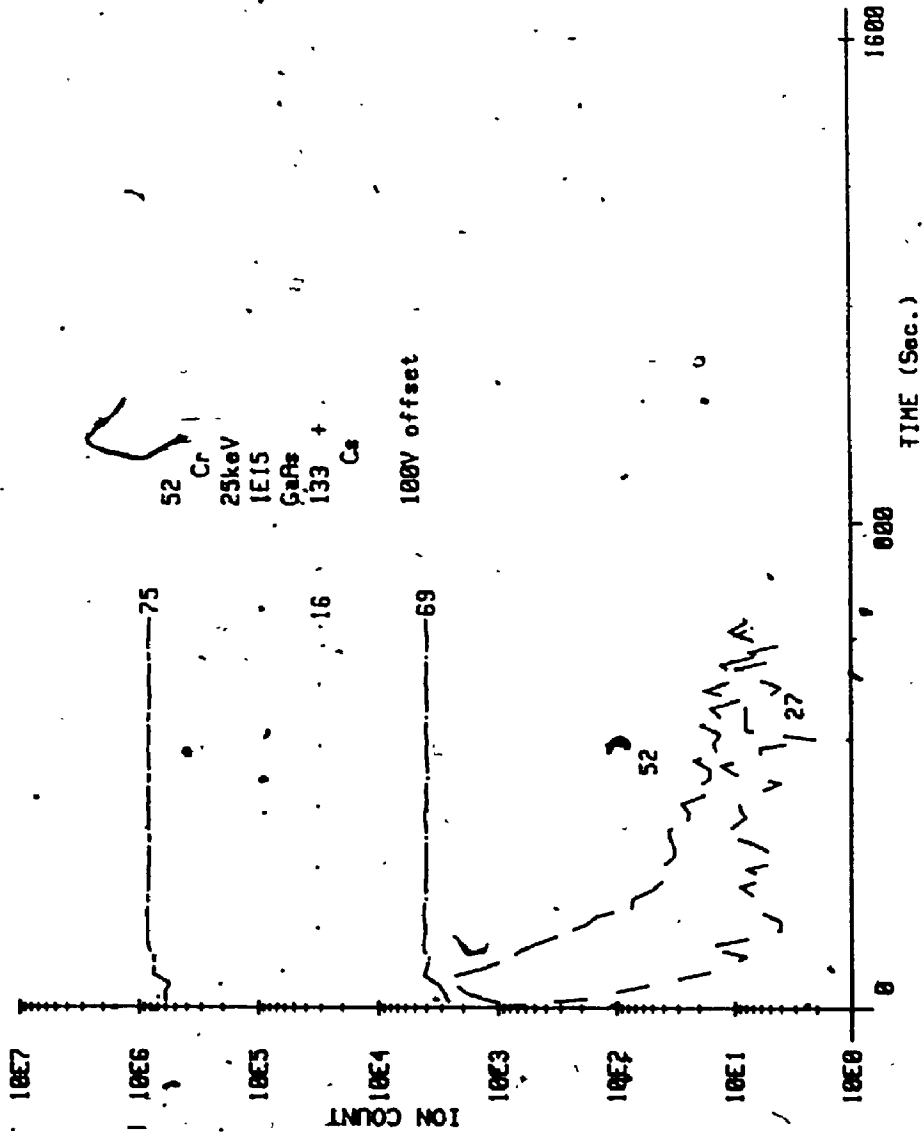


FIGURE 59 Secondary Ion Count Distribution of Cr in GaAs

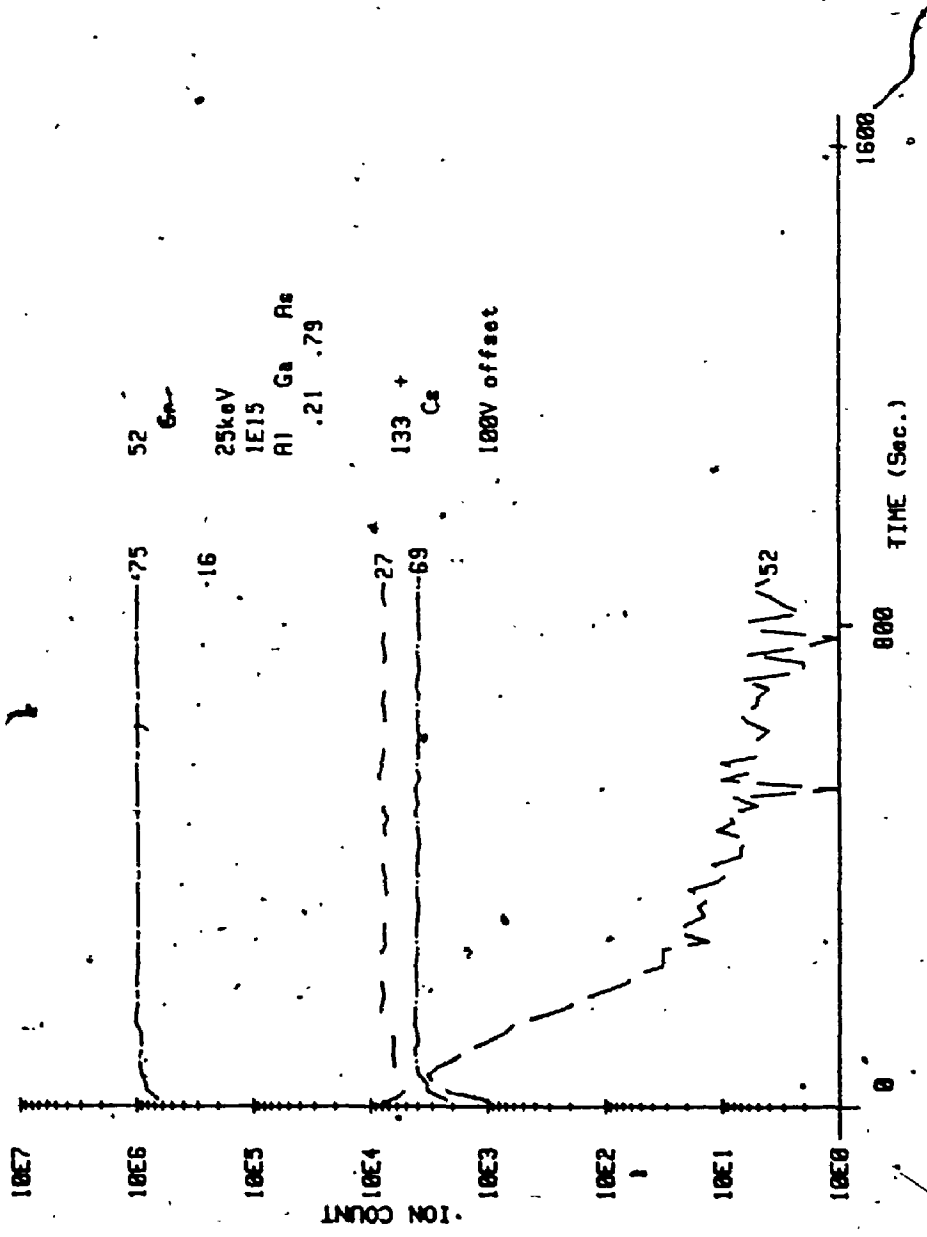


FIGURE 60 Secondary Ion Count Distributions of Cr in Al_{0.21}Ga_{0.79}As

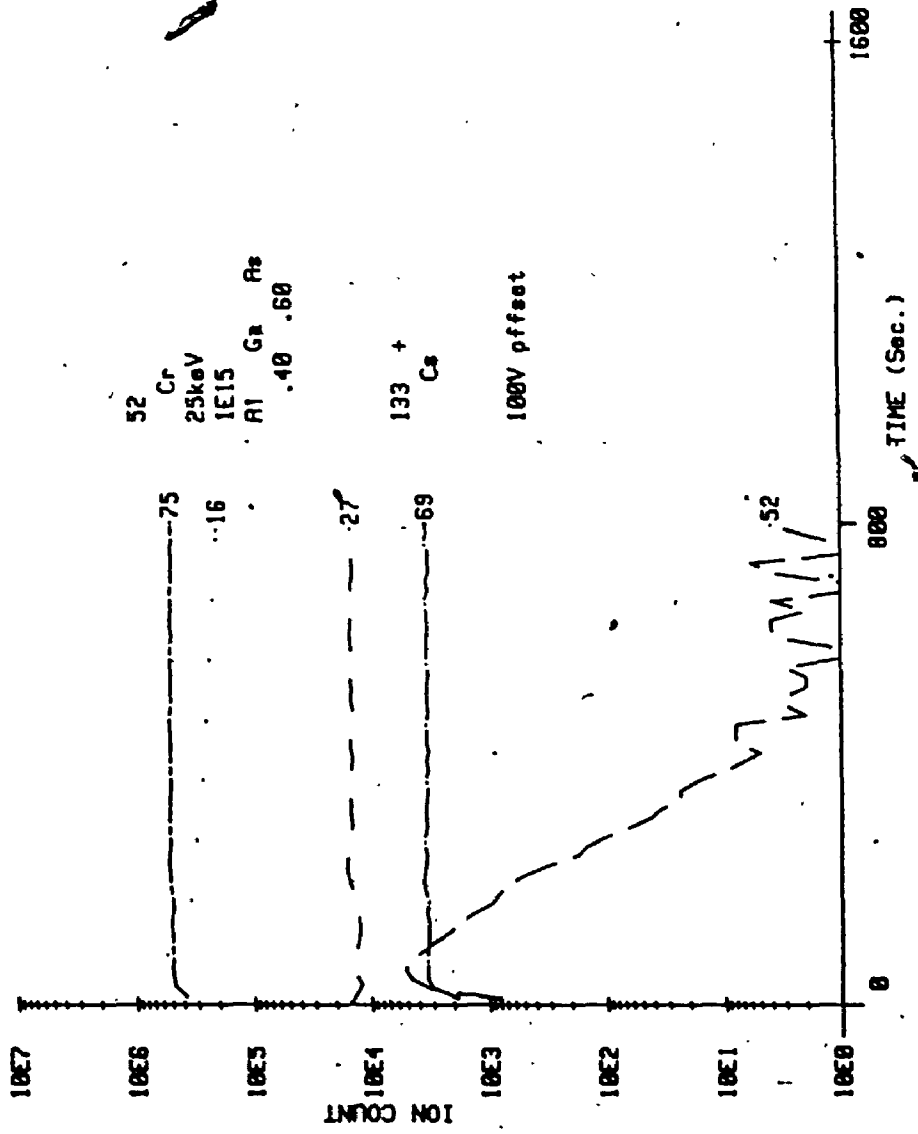


FIGURE .61 Secondary Ion Count Distributions of Cr in Al_{.40}Ga_{.60}As

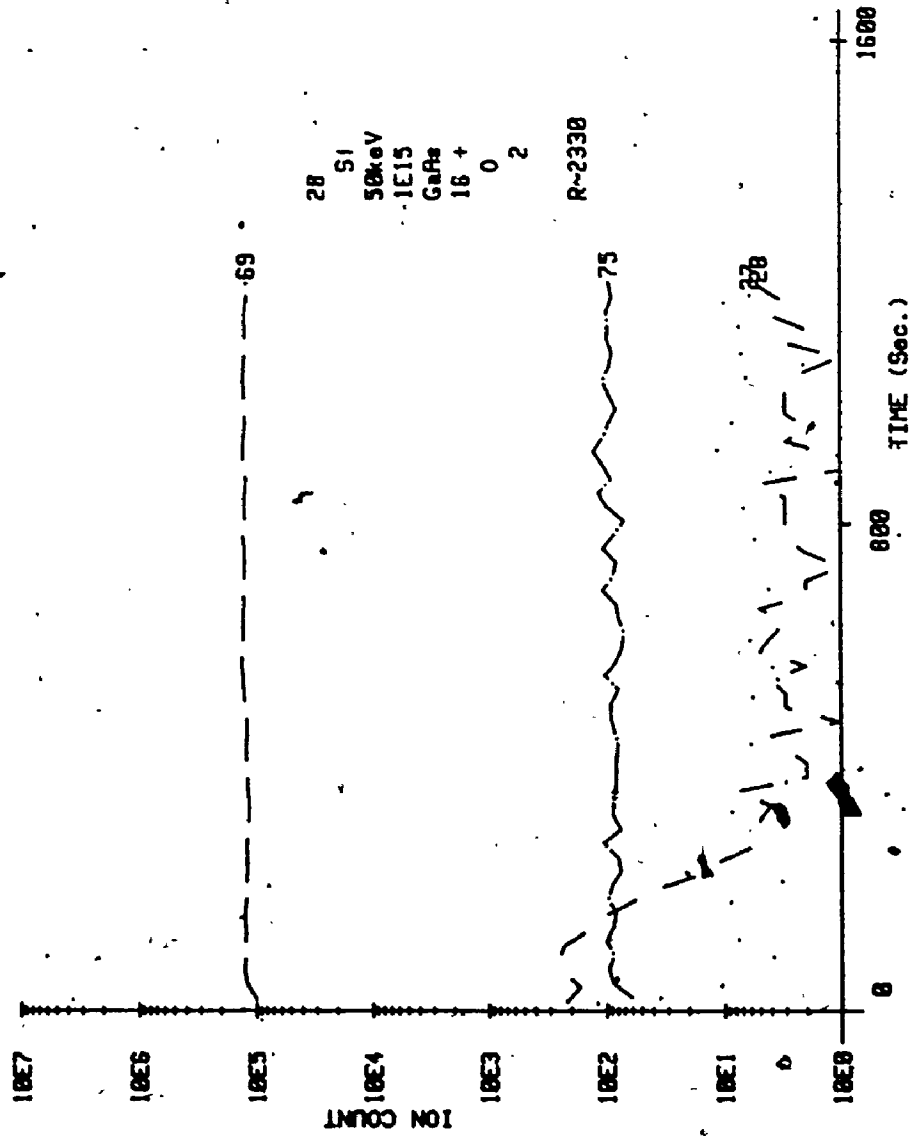


FIGURE 62 Secondary Ion Count Distributions of Si in GaAs

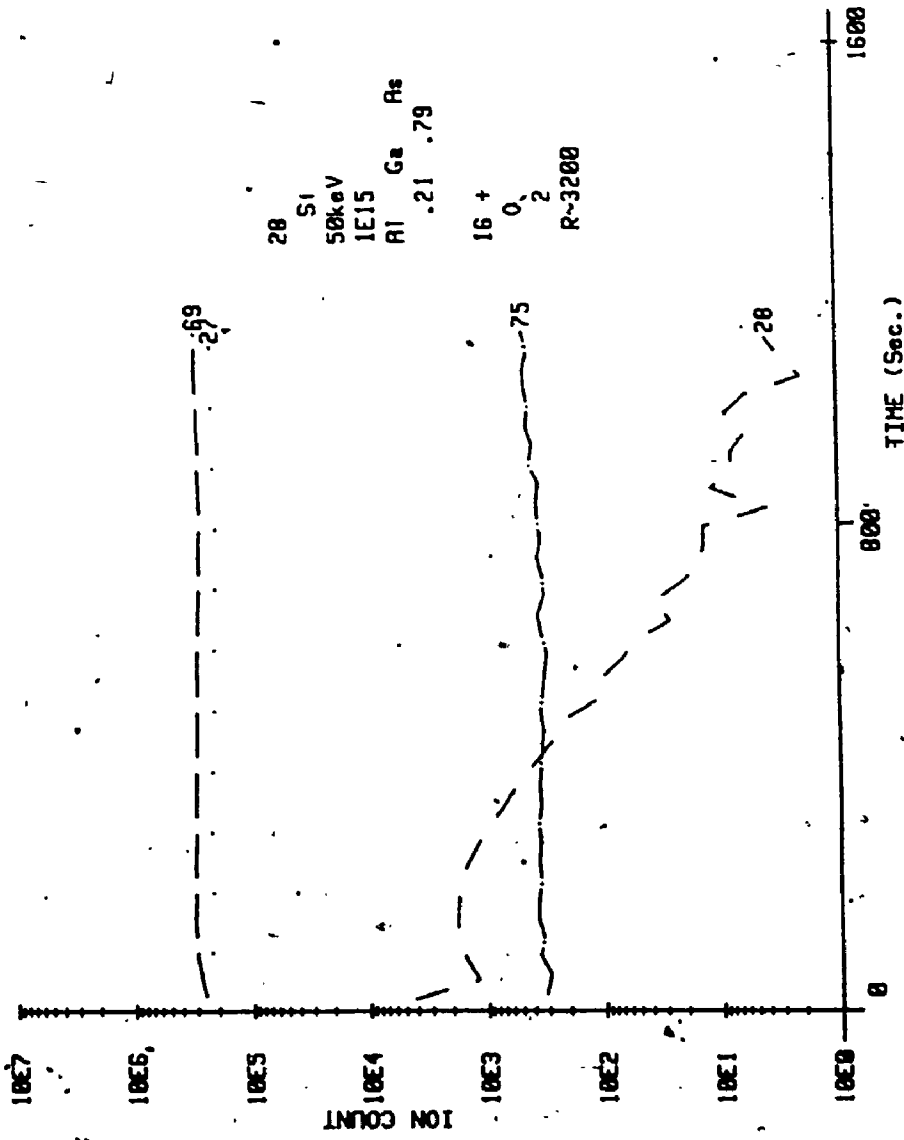


FIGURE 63 Secondary Ion Count Distributions of Si in Al_{0.21}Ga_{0.79}As

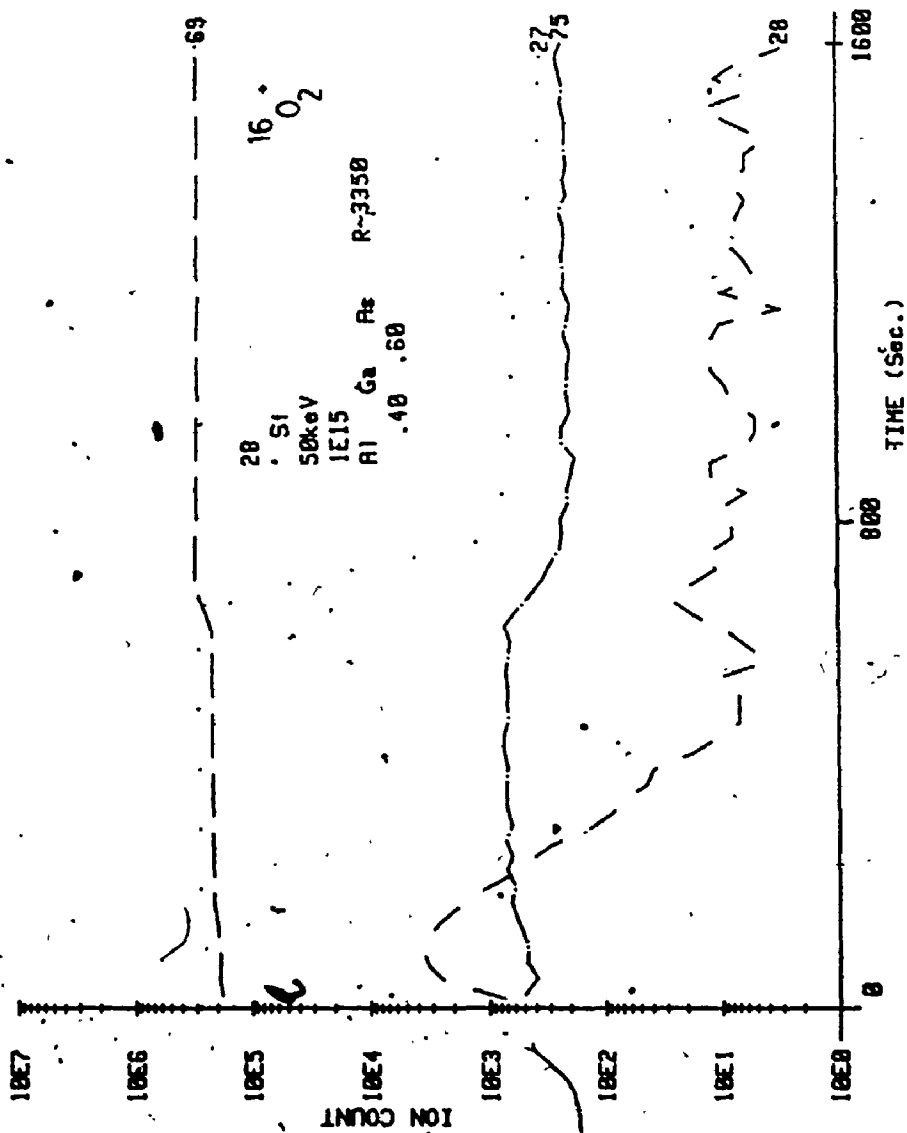


FIGURE 64 Secondary Ion Count Distributions of Si in Al_{0.40}Ga_{0.60}As

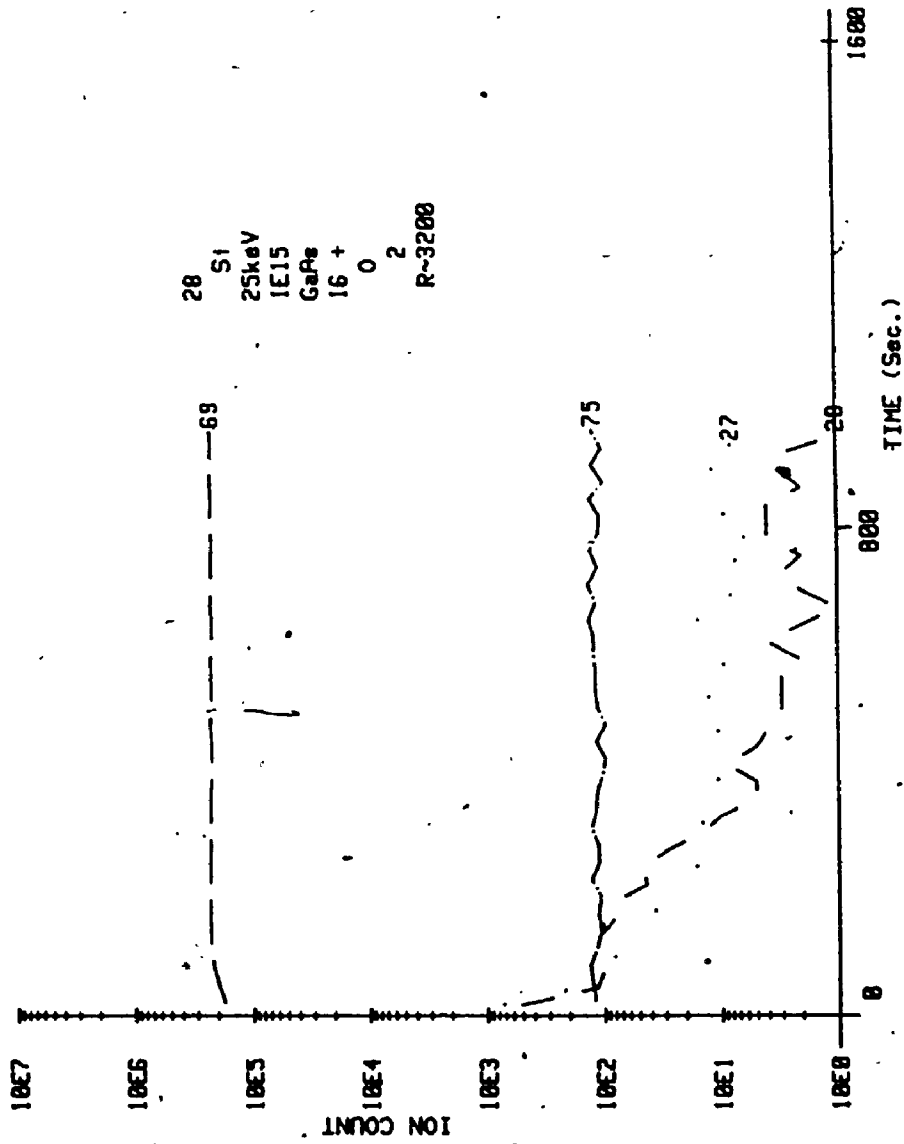


FIGURE 65 Secondary Ion Count Distributions of Si in GaAs

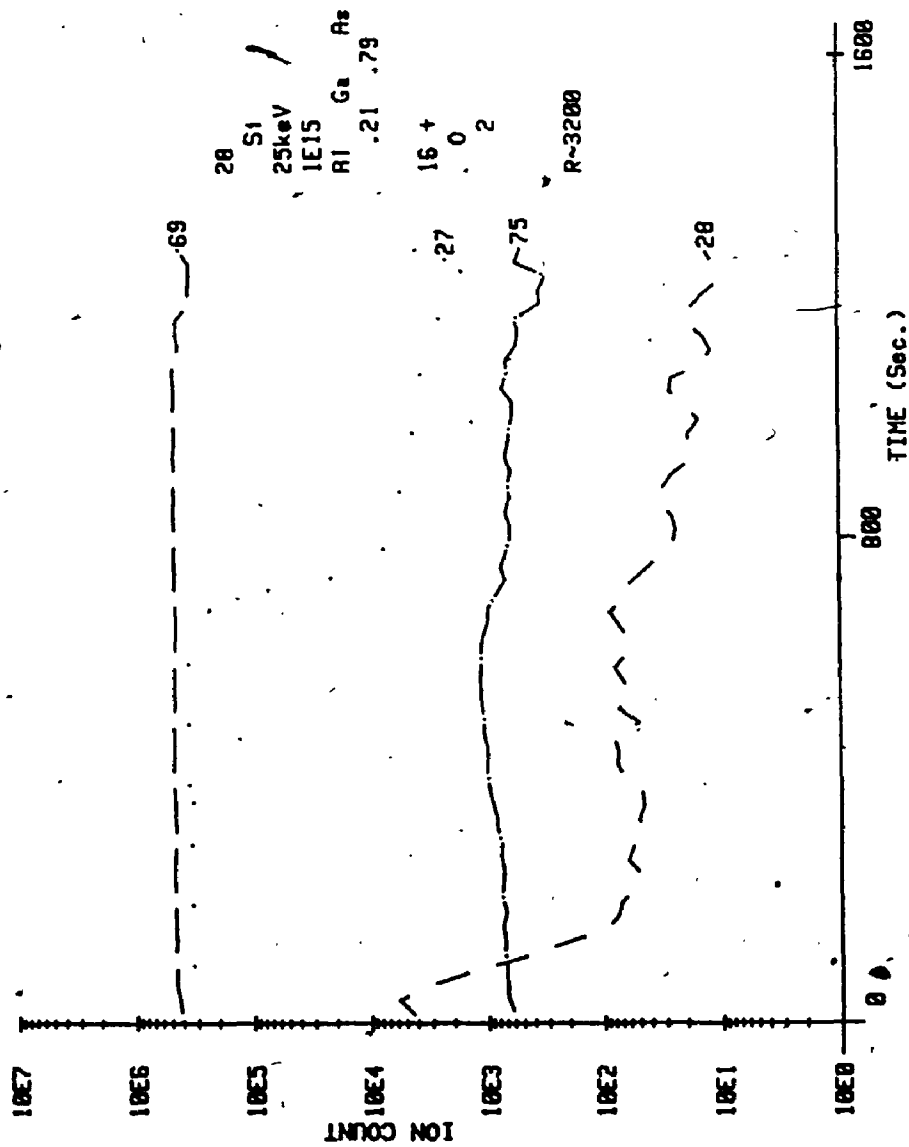


FIGURE 66 Secondary Ion Count Distributions of Si in Al_{.21}Ga_{.79}As

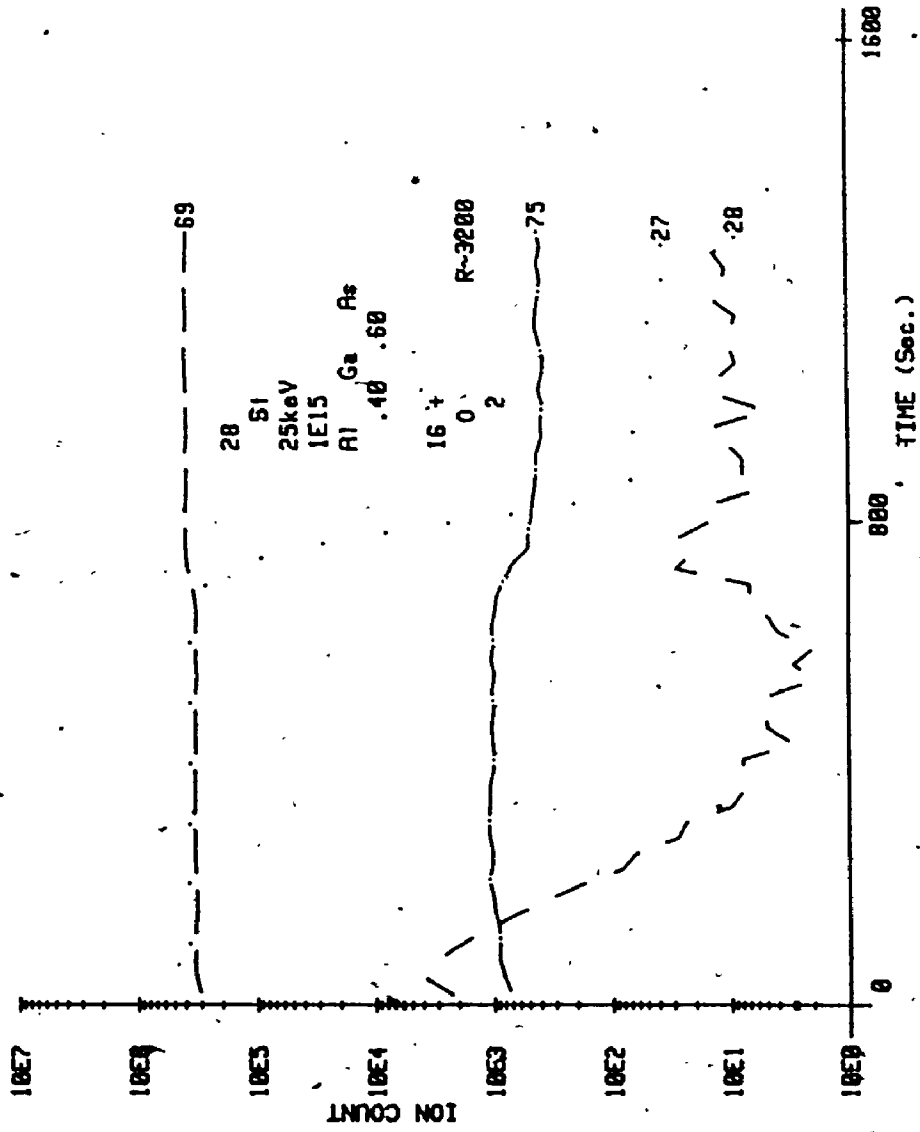


FIGURE 67 Secondary Ion Count Distributions of Si in Al₄₀Ga₆₀As

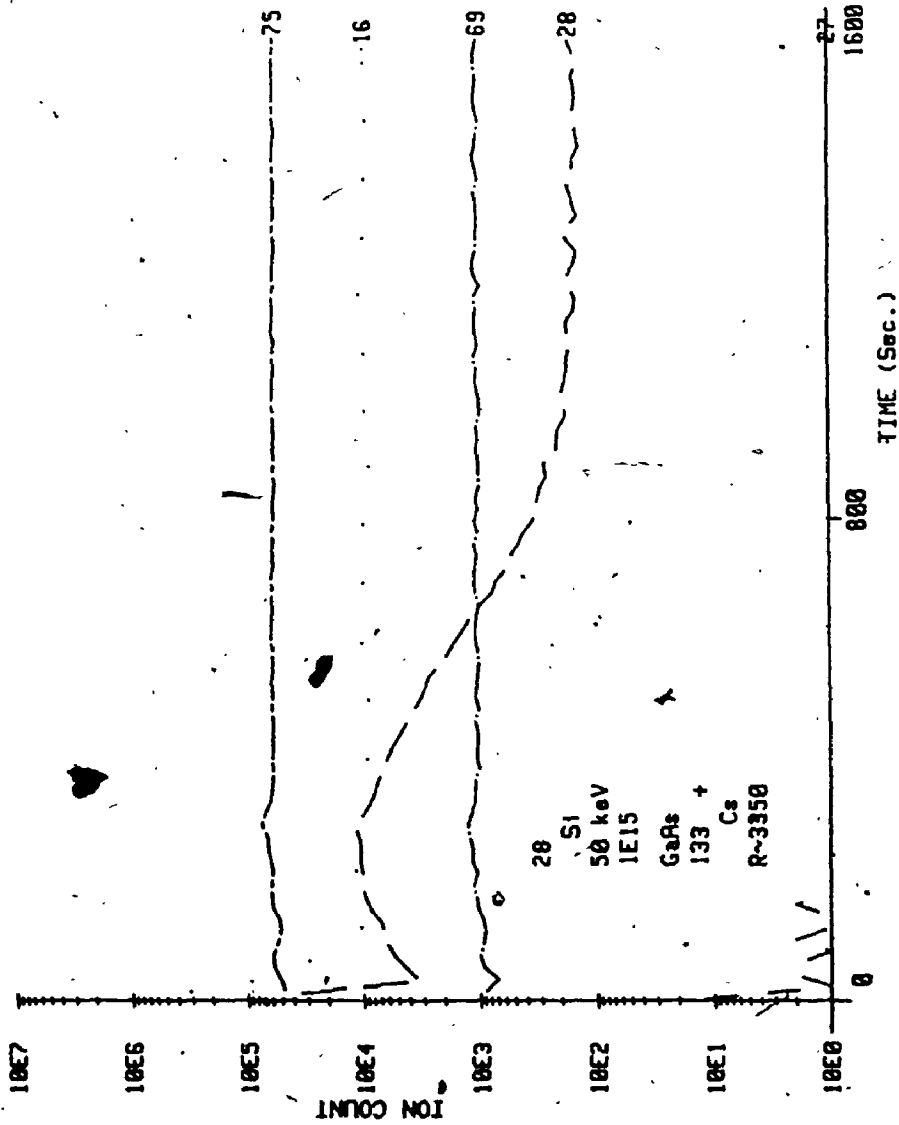


FIGURE 68 Secondary Ion Count Distributions of Si in GaAs

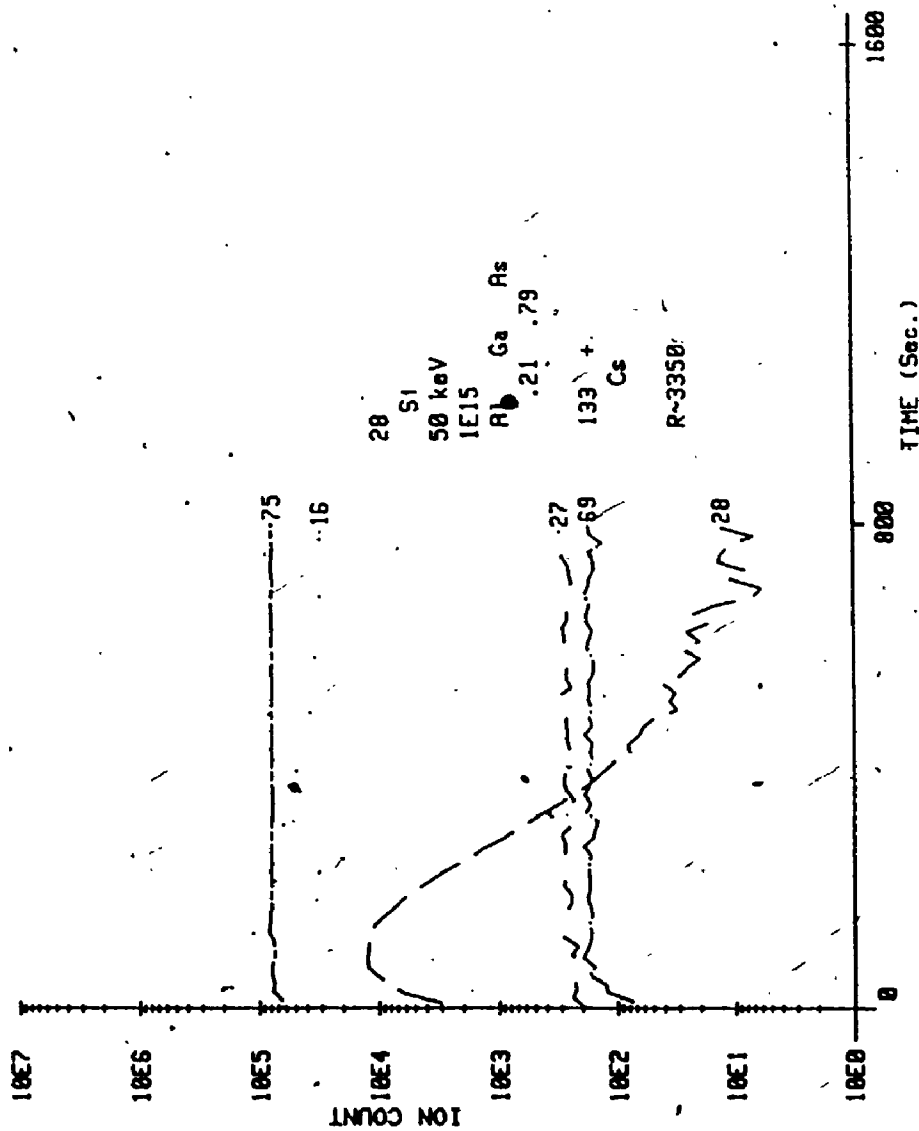


FIGURE 69 Secondary Ion Count Distributions of Si in Al_{.21}Ga_{.79}As

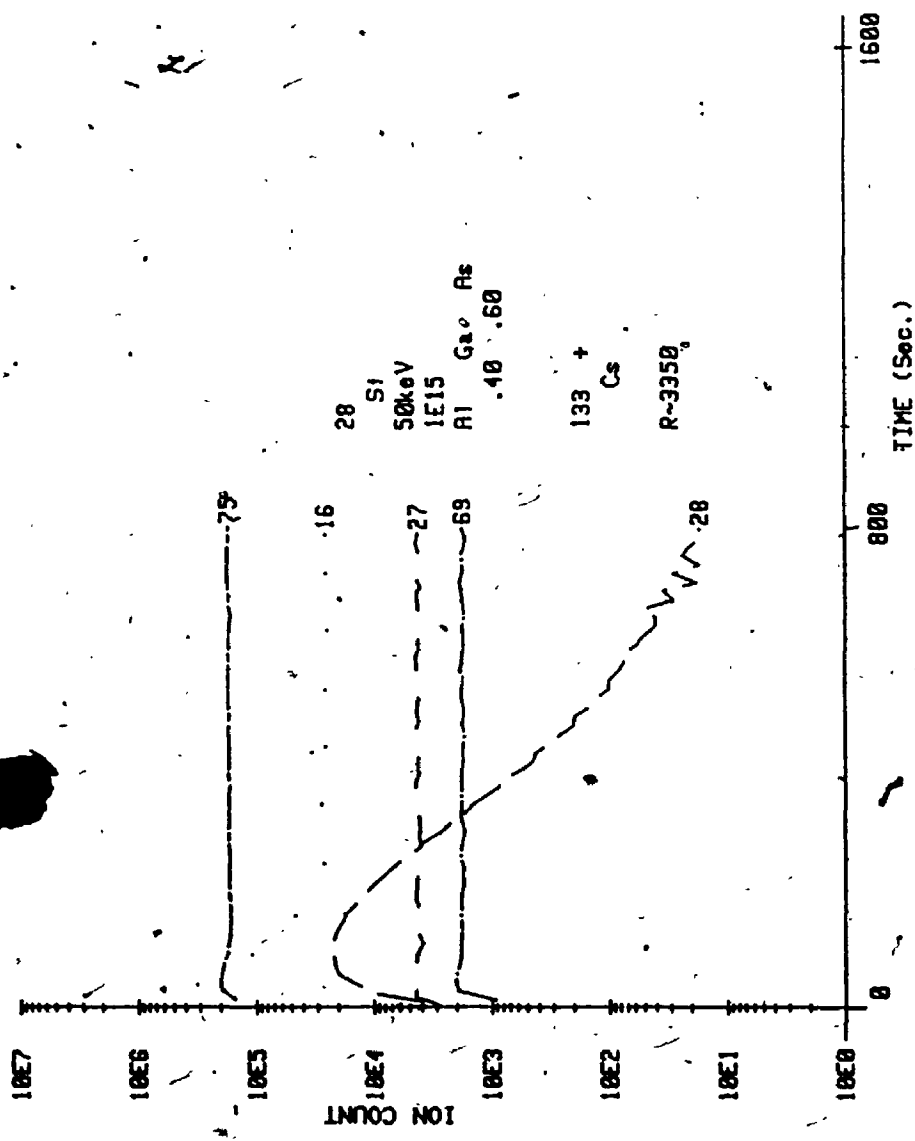


FIGURE 70 Secondary Ion Count Distributions of Si in Al₄₀Ga₆₀As

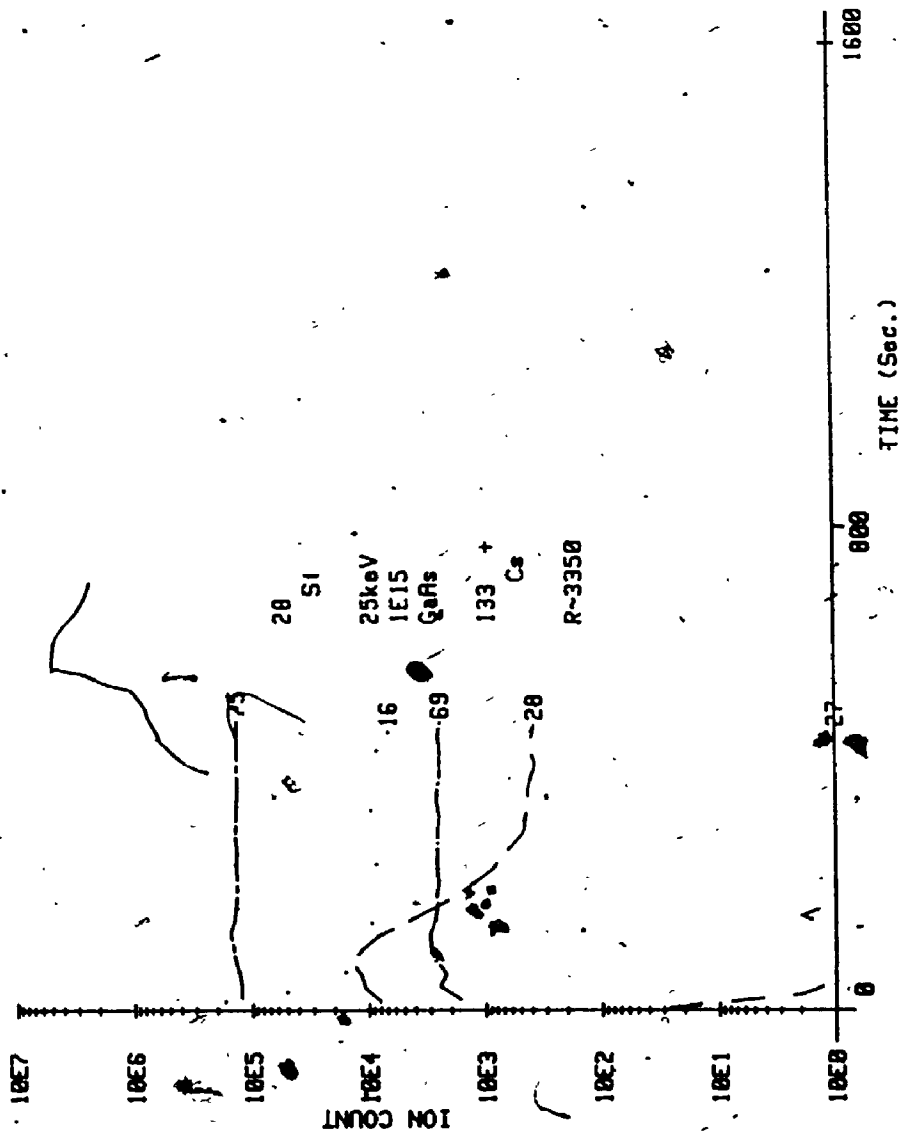


FIGURE 71 Secondary Ion Count Distributions of Si in GaAs

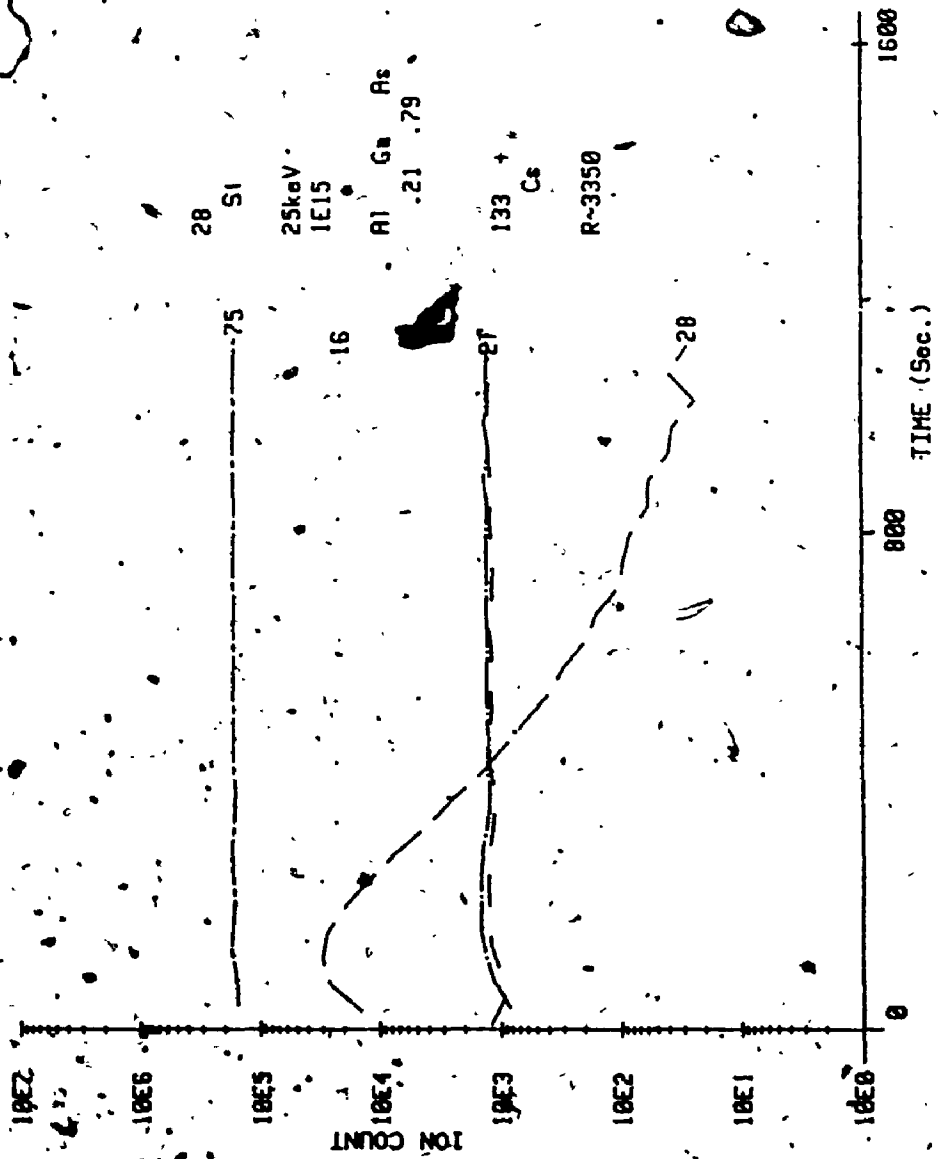


FIGURE 72 Secondary Ion Count Distributions of Si in Al₂₁Ga₇₉As

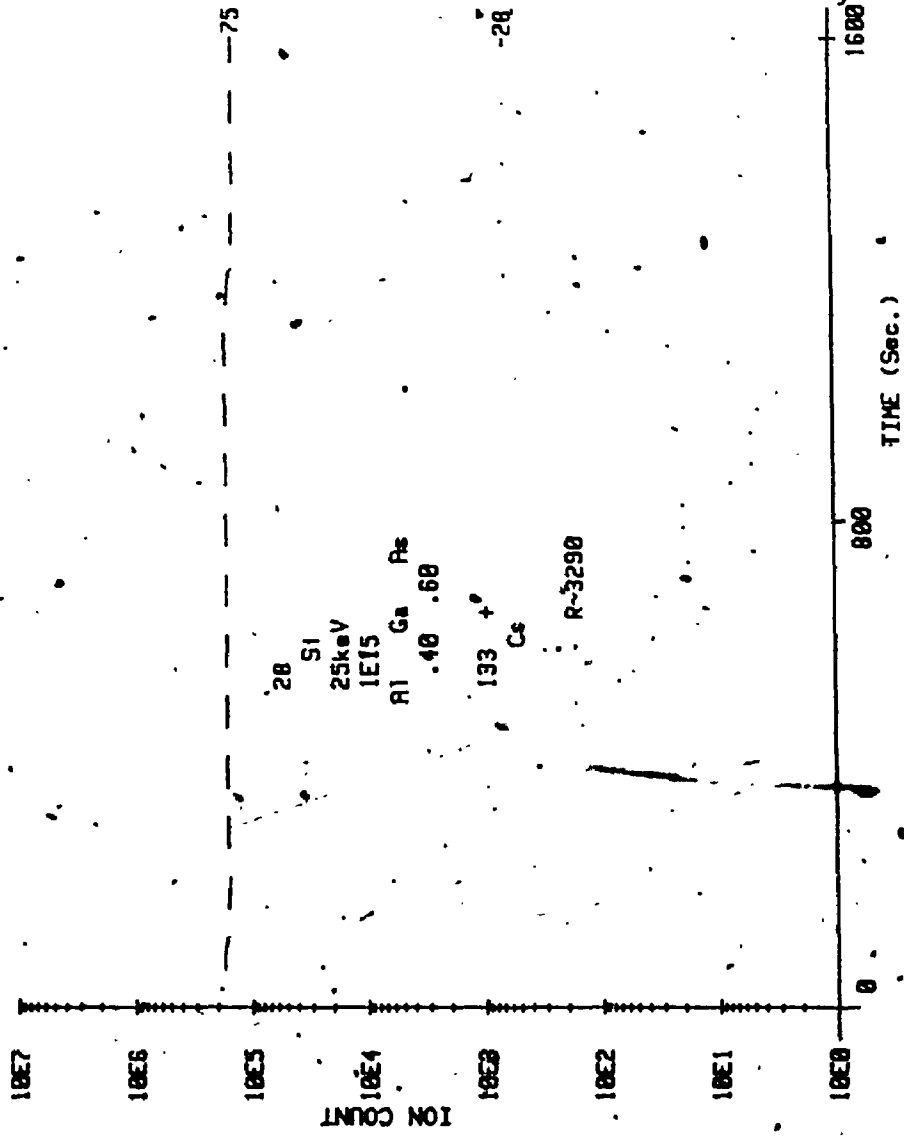


FIGURE 73. Secondary Ion Count Distributions of Si in Al_{.40}Ga_{.60}As

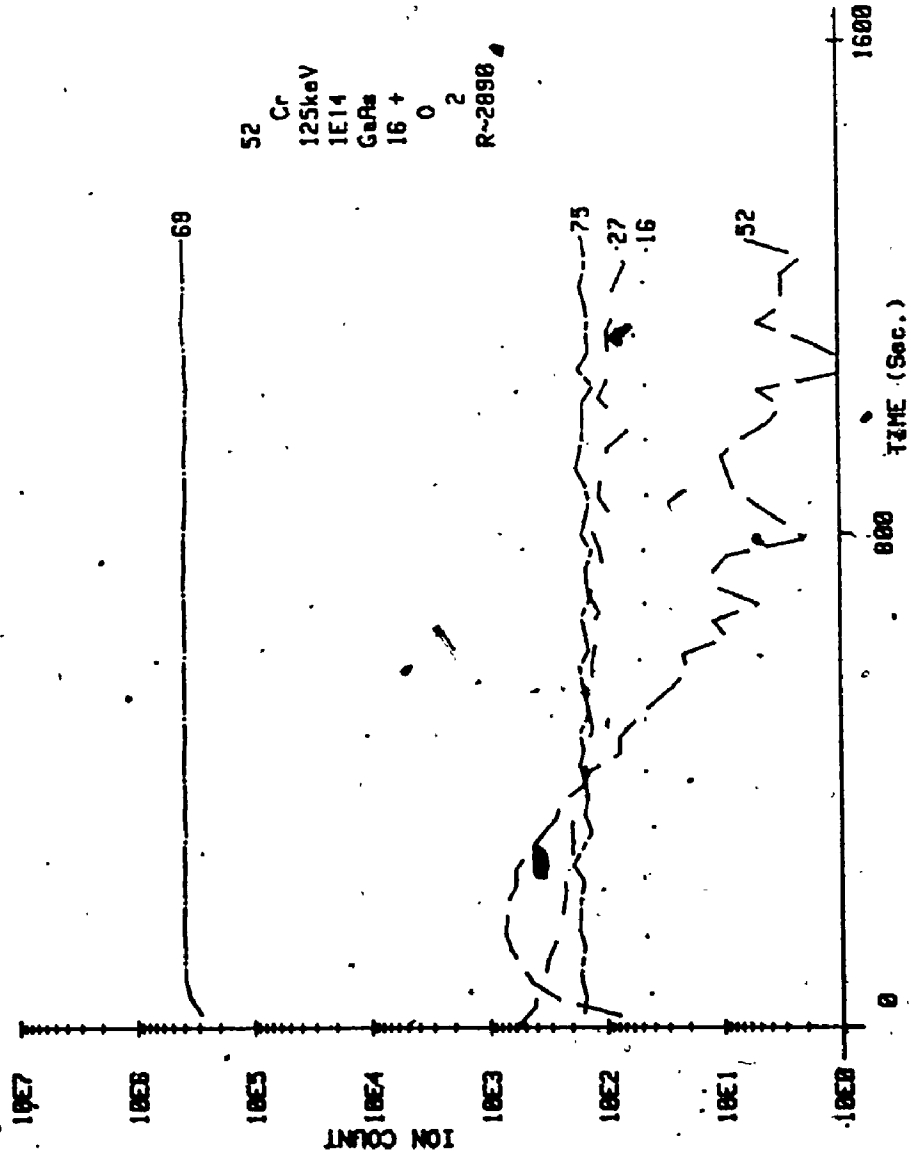


FIGURE 74 Secondary Ion Count Distributions of Cr in GaAs

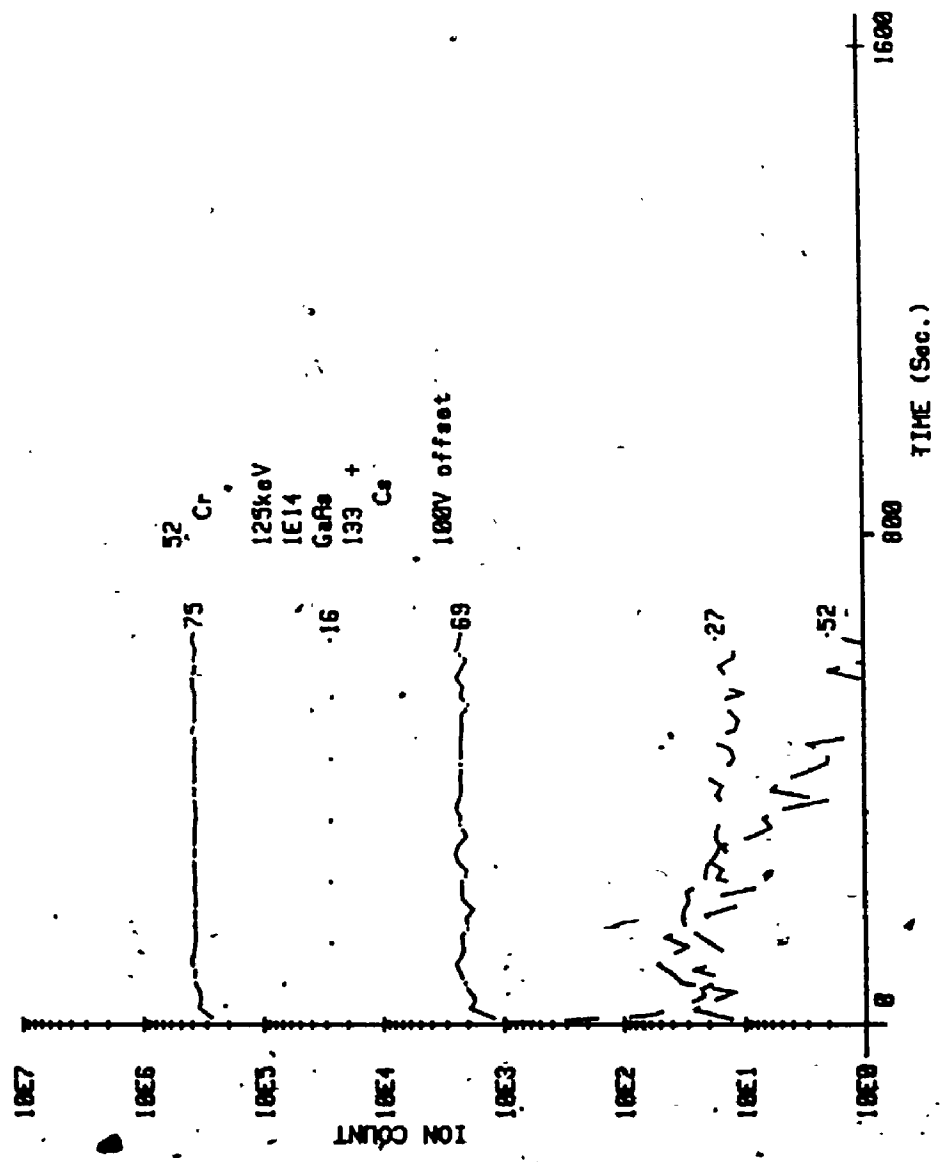


FIGURE 75 Secondary Ion Count Distributions of Cr in GaAs

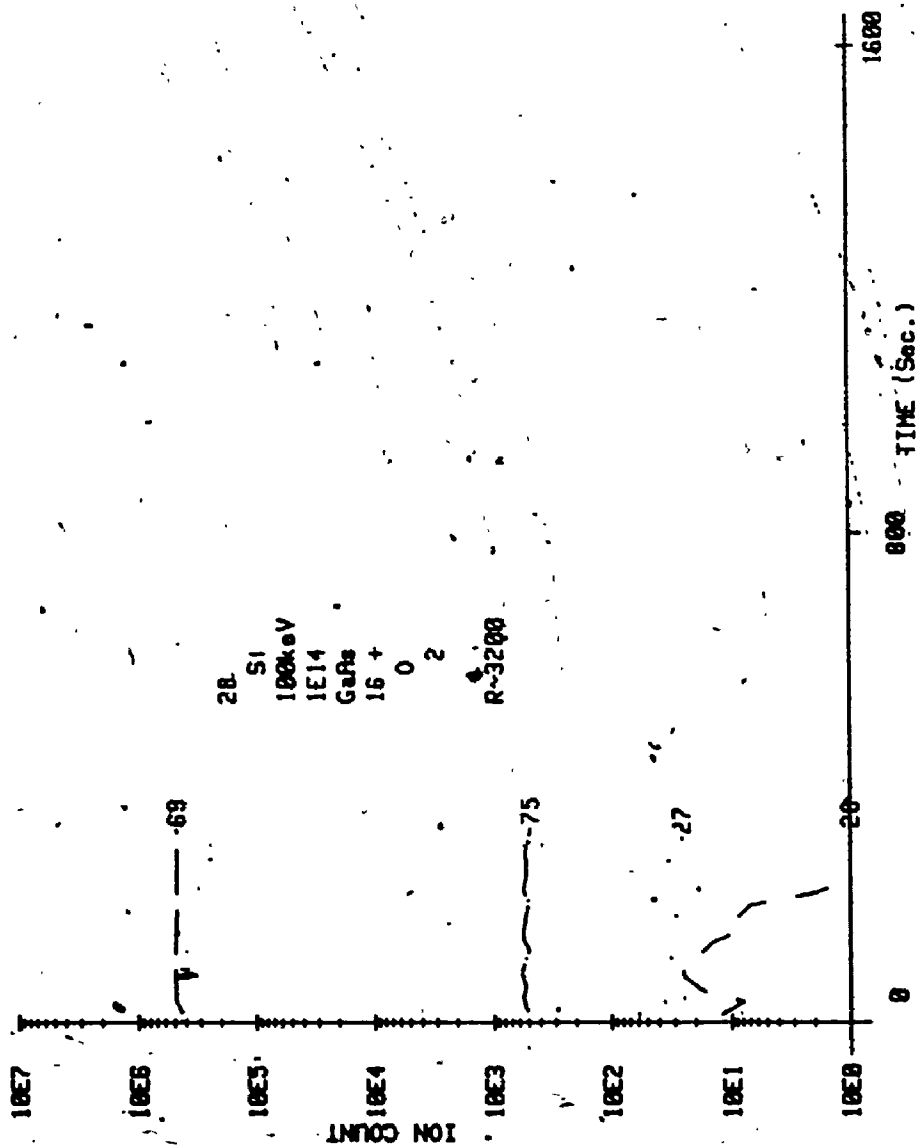


FIGURE. 76 Secondary Ion Count Distributions of Si in GaAs

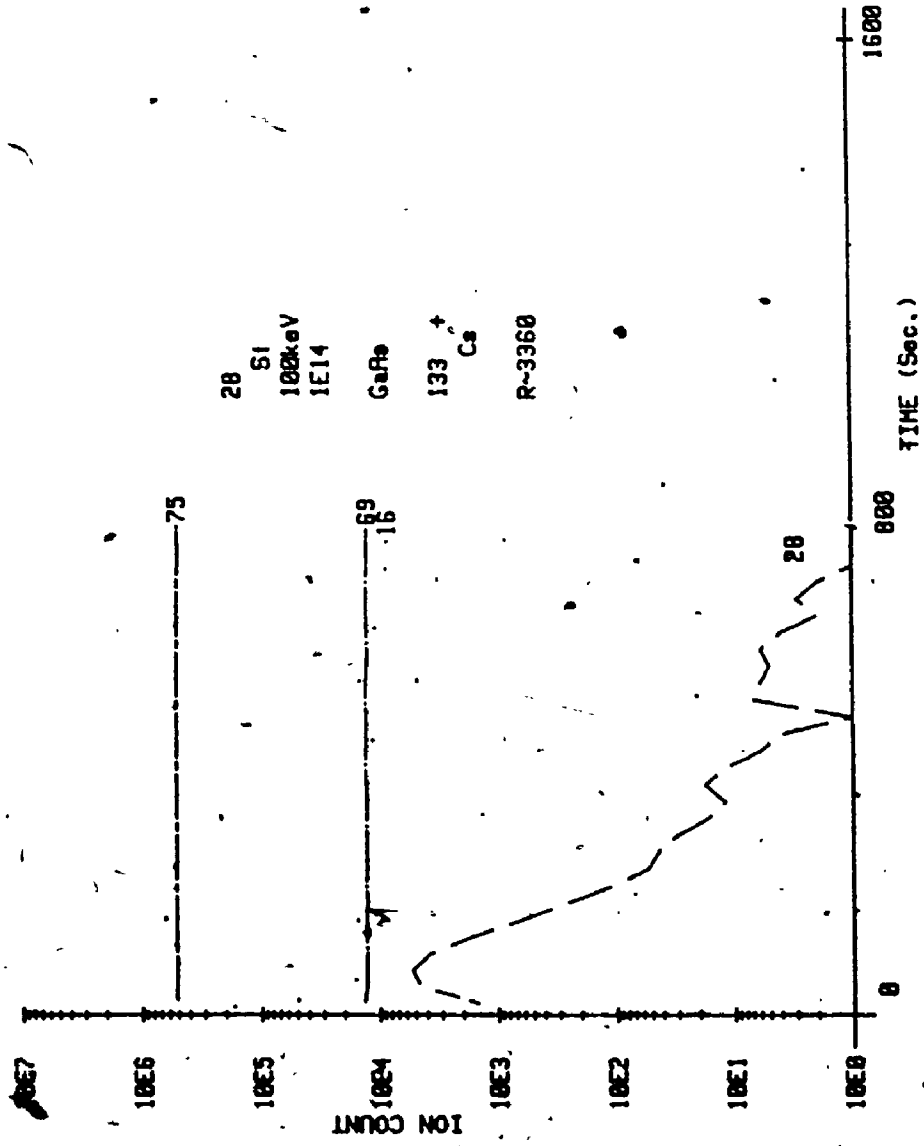


FIGURE 77 Secondary Ion Count Distributions of Si in GaAs

a low primary ion current density in order to obtain a large number of data points to establish the shape of the implant profile. Other depth profiles were carried out only to the projected range of the implant, in order to accurately determine this depth. Some depth profiles were performed deep into the $\text{Al}_x\text{Ga}_{1-x}\text{As}$ layer to measure the shape of the profile and determine the sputter yield. Still other depth profiles continued through the interface into the base GaAs substrate. Analysis occurred over a one year time frame and some samples were profiled repeatedly.

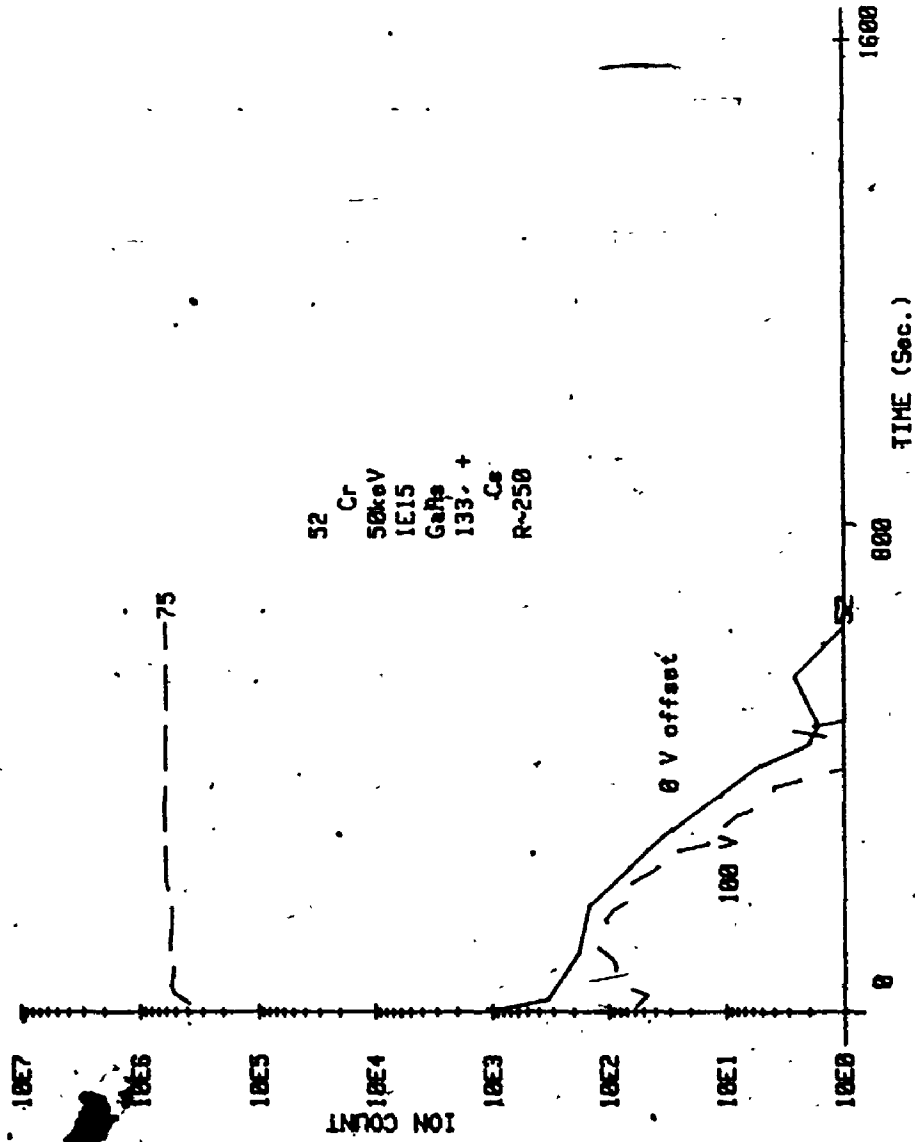
Before discussing the depth profiles in detail, an examination of molecular interferences is necessary. Figure 78 shows a depth profile with three ion species. The matrix species ^{75}As increases slightly from the surface until it reaches a steady-state value. There are two ion species shown which are labelled m/e 52. That shown with the solid line was obtained without voltage offset. This distribution falls continuously from the surface. The m/e 52 ion species shown with the dotted line was obtained with a 100 volt sample offset to discriminate against low energy molecular ions which are interfering with the ^{52}Cr signal. The distribution shown by the dotted line increases from the surface, reaches a maximum and then decreases. This is the expected shape of the implant distribution. By making use of high mass resolution conditions (Figure 79) both the ^{52}Cr implant and the molecular interference, in this case,

identified as $^{12}\text{C}_4^1\text{H}_4$, can be monitored.

A comparison of low (~250) and high (≥2500) mass resolution depth profiles provides some perspective as to the need for the latter. Figure 80 shows that the ^{28}Si implant in $\text{Al}_{.40}\text{Ga}_{.60}\text{As}$ can be completely obscured by an interfering signal under low mass resolution conditions. The depth profile in Figure 81 indicates that if the concentration of the ^{28}Si implant is great enough it can be seen despite the molecular interference ^{27}AlH . In this figure, the peak of the implant is just above the background. Increasing the primary ion current density and improving the vacuum conditions tend to lower the $^{27}\text{AlH}^+$ signal, but these measures never significantly improved the analysis. In Figure 81 the m/e signal is recorded twice, in a low mass resolution state; once under normal conditions and second with a -100 volt bias applied to the sample.

An analysis under high mass resolution conditions is shown in Figure 82. The results are free from molecular interferences such as due to $^{27}\text{AlH}^+$ which is identified in Figure 83. Inspection of the depth profile in Figure 80 shows that the low mass resolution m/e 28 signal begins at a high level at the surface, presumably due to

- 1) the presence of molecules containing hydrogen (e.g. H_2O and hydrocarbon compounds) which are absorbed on



52 Cr
50keV
1E15
GaAs
133. +
Cs
R-250

FIGURE 78 Secondary Ion Count Distributions of Cr in GaAs

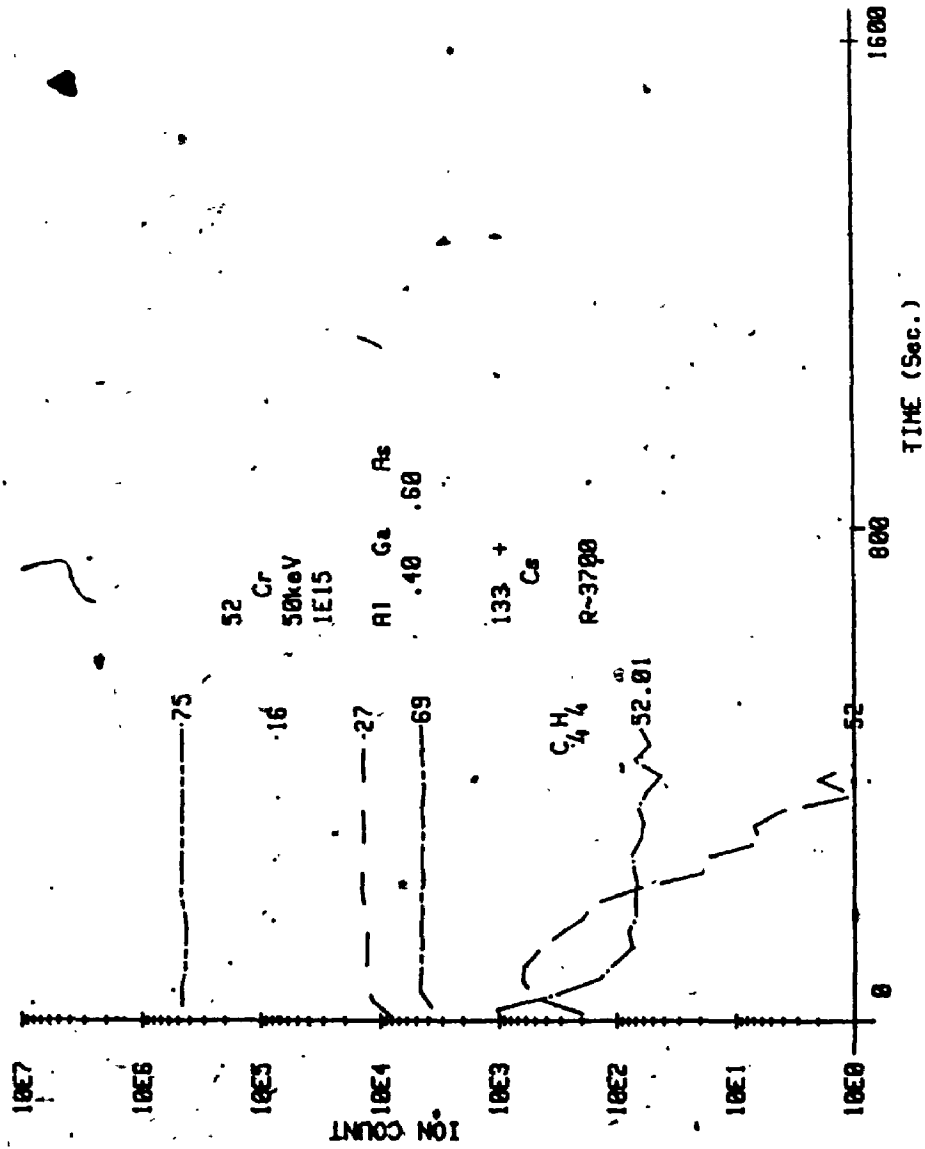


FIGURE 79 Secondary Ion Count Distributions of Cr in Al₄₀Ga₆₀As

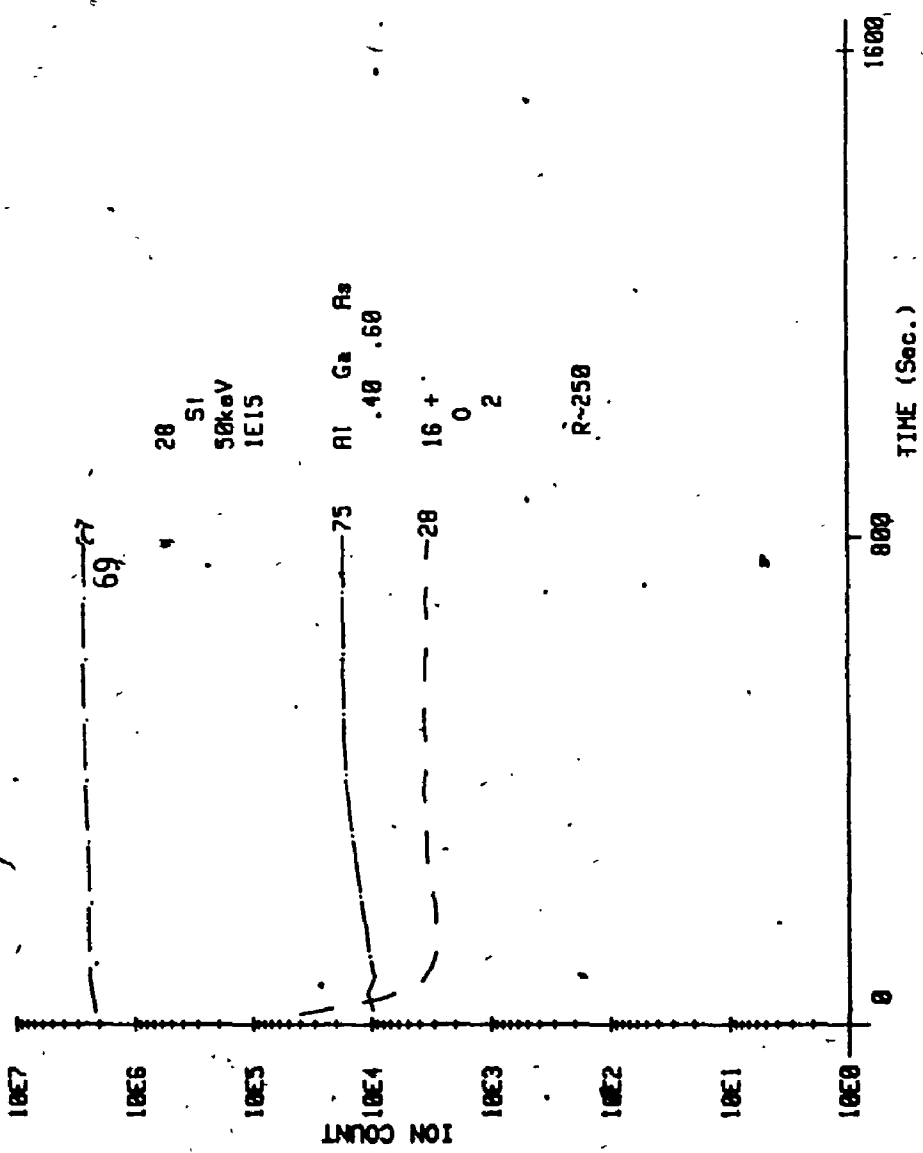


FIGURE 80 Secondary Ion Count Distributions of Si in Al.40Ga.60As

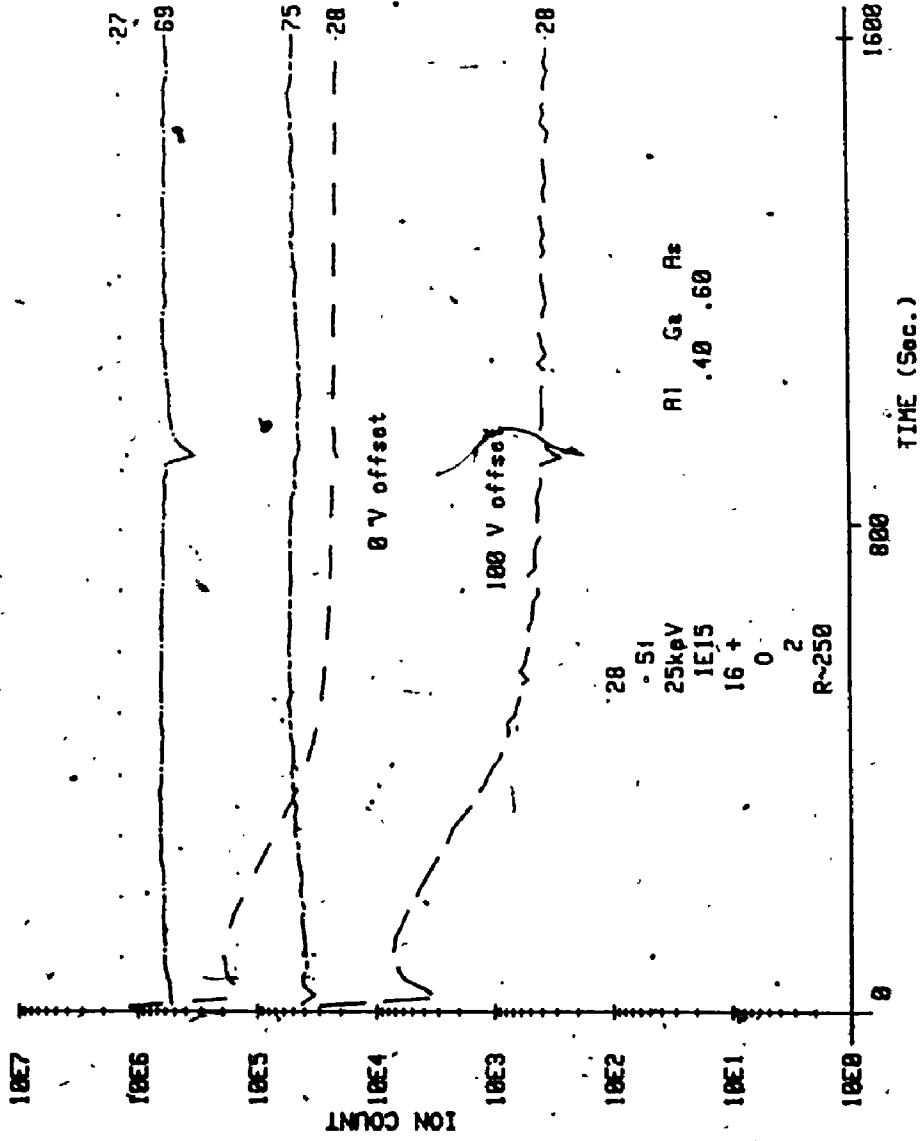


FIGURE. 81 Secondary Ion Count Distributions of Si in Al_{0.40}Ga_{0.60}As

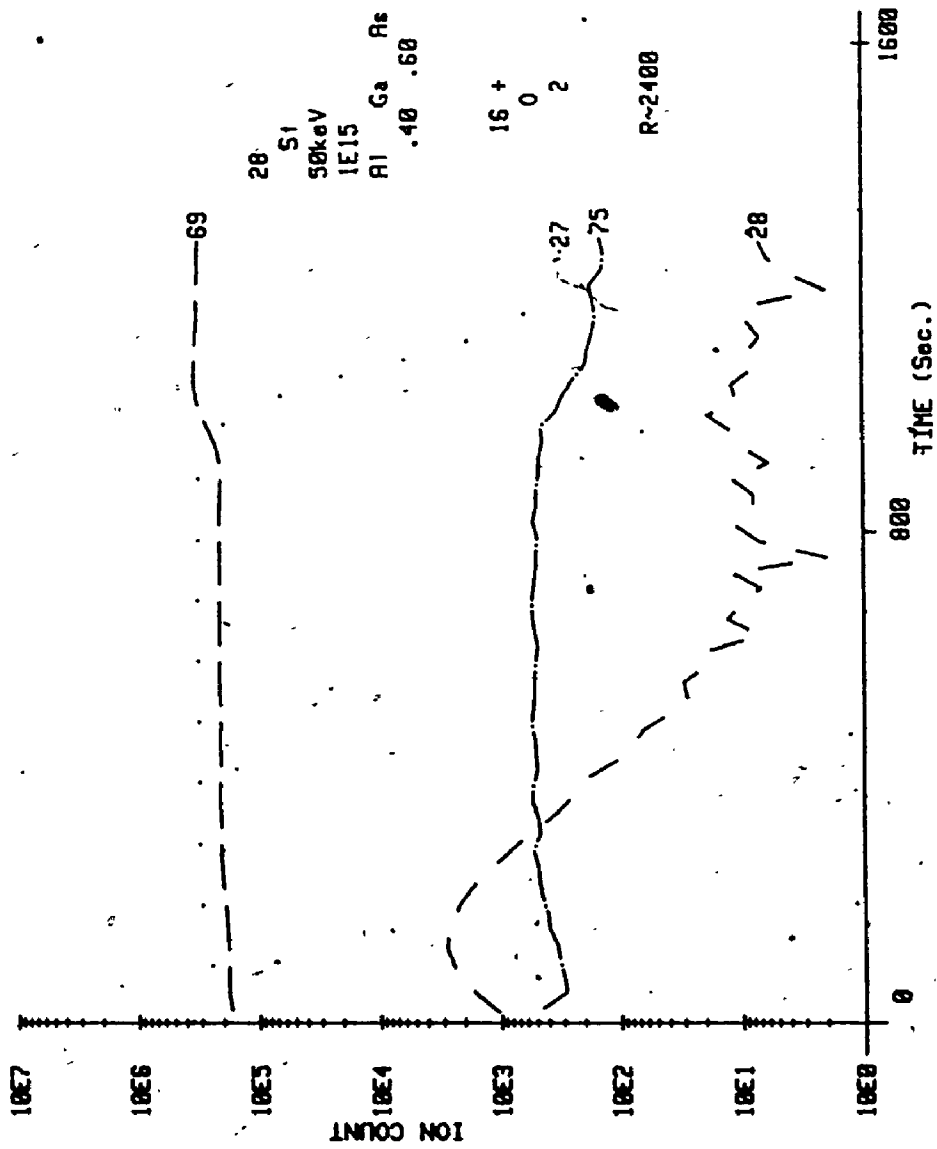


FIGURE 82. Secondary Ion Count Distributions of Si in Al_{0.40}Ga_{0.60}As

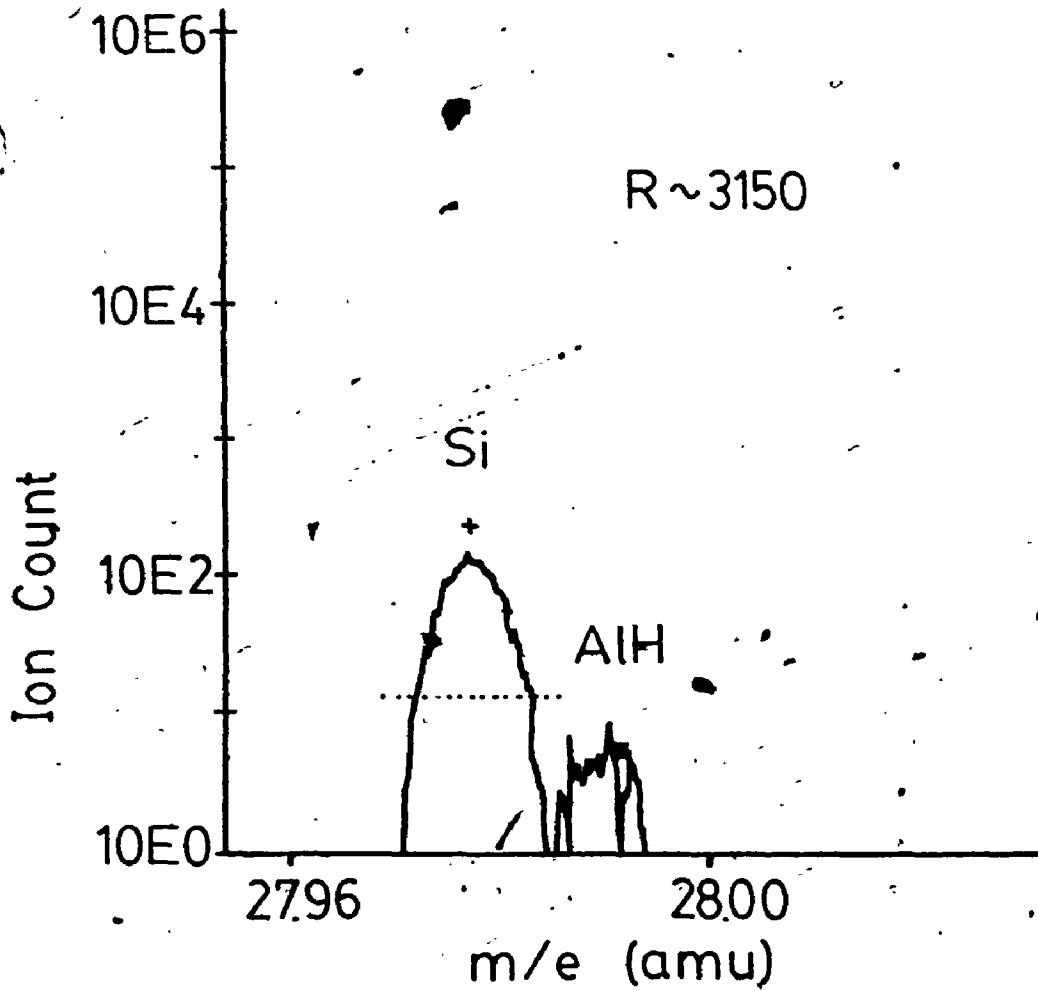
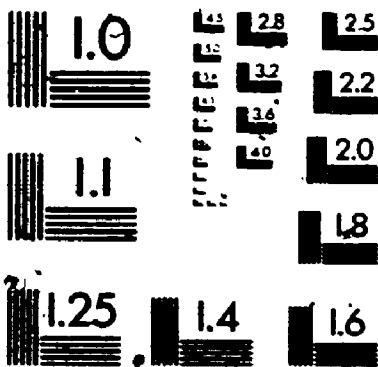


FIGURE 83 Mass spectrum of Si and AlH

3

of/de

3



- the surface; these decompose under ion bombardment and then combine with Al to form AlH and
- 2) the surface transient period in which the primary ion species builds in concentration until it reaches a level sustained by dynamic equilibrium.

The 28 signal in Figure 80 then drops to a steady-state value in the bulk. The high mass resolution signal (Figure 82), on the other hand, increases from the value measured at the surface until it reaches a peak value at the projected range of the implant. The signal then decreases by about a factor of a thousand. The shape of the signal is typical of many implants in semiconductor materials. The signals of m/e 27 and 69 are almost identical in low mass resolution mode but m/e 69 is lower than m/e 27 in high mass resolution. The signal, m/e 75 maintains its shape under high mass resolution conditions but is attenuated even more than m/e 27 or 69.

The group of figures 44 to 61 contains information obtained in depth profiling implants of ^{52}Cr . Figure 44 shows this implant in GaAs, examined with an O_2^+ ion beam. The $^{52}\text{Cr}^+$ signal changes by over four decades in this profile. Depth profiles shown in Figures 44 to 52, 55 and 56 were performed under high mass resolution conditions while Figures 53, 54 and 57 to 61 show depth profiles performed in low mass resolution with only the $^{52}\text{Cr}^-$ signal offset

by +100 volts. Greater dynamic range, the difference between signal maximum and minimum obtained during a continuous depth profile of the implant species, is generally obtained for the ^{52}Cr implant with O_2^+ bombardment.

Five m/e signals, 16, 27, 52, 69 and 75, are monitored in Figure 44. The m/e 27 signal arises from the trace amount of ^{27}Al in the sample and from the SIMS memory effect. The $^{27}\text{Al}^+$ signal falls from a high surface level to a low background level after about 30 seconds, and, in this case, a fluence of about $2.25 \times 10^{16} \text{ O}_2^+$ ions cm^{-2} . The m/e 16 and 75 signals quickly achieve steady-state value and show a small variation with time. The m/e 69 signal rises from the surface level and reaches a steady-state value.

Figure 45 follows the same general trends as Figure 44. As a consequence of the higher aluminum concentration the $^{52}\text{Cr}^+$ signal is more prominent. The ion count of $^{27}\text{Al}^+$ is now close to the level of the $^{69}\text{Ga}^+$ ion count. The $^{75}\text{As}^+$ signal shows a slight upward trend in this profile. The same trends are repeated in Figure 46 which is the sample with the greatest concentration of aluminum. The ion count of the $^{27}\text{Al}^+$ species is greater than that of $^{69}\text{Ga}^+$.

The trends shown in Figures 47 to 49 follow the pattern established above as is the case in Figures 50 to 52. The sharp increase shown for m/e 27 and 69 signals in Figure 52 at about 900 seconds is thought to be caused by an increase

in the primary ion current. Figure 54 shows an increase in m/e 27 and 75 signals at about 200 seconds.

The depth profile shown in Figure 62 is of a sample of GaAs implanted with ^{28}Si . Four m/e signals are monitored, 27, 28, 69 and 75. The $^{28}\text{Si}^+$ signal falls from a high surface level then increases to the peak of the profile, following which it decreases to a low value.

The features shown in Figure 63 follow the same general trend as in Figure 62; however, as a consequence of the higher Al concentration the $^{28}\text{Si}^+$ signal is enhanced. The ion counts of all signals are increased. The $^{27}\text{Al}^+$ signal is now close to the level of the $^{69}\text{Ga}^+$ signal. The same trends are repeated in Figure 64 which is the sample with the greatest concentration of Al. The depth profile in this analysis has continued through the $\text{Al}_x\text{Ga}_{1-x}\text{As}$ layer, past the interface and well into the GaAs substrate, at about 650 seconds. Thus, it is possible to compare ion intensities as the substrate changes during a depth profile. When a GaAs implanted sample was depth profiled following an $\text{Al}_x\text{Ga}_{1-x}\text{As}$ sample which had been profiled into the GaAs substrate, the same ion count rates (within measurement error) were observed for the $^{69}\text{Ga}^+$ and $^{75}\text{As}^+$ matrix signals. The $^{28}\text{Si}^+$ signal in the GaAs substrate corresponded to the doped substrate concentration i.e. the background levels showed the same ion count.

In Figure 64, the $^{27}\text{Al}^+$ signal is greater than the $^{69}\text{Ga}^+$ signal until the $\text{Al}_x\text{Ga}_{1-x}\text{As}/\text{GaAs}$ interface where the $^{27}\text{Al}^+$ signal falls rapidly to a background level. The $^{27}\text{Al}^+$ signal falls from 90% of its highest value to 10% of that value in about 35 nm, according to later depth measurements. The $^{69}\text{Ga}^+$ signal remains constant until the $^{27}\text{Al}^+$ signal starts to decrease at the interface. Here, the $^{69}\text{Ga}^+$ signal starts to increase until it reaches a high value in the GaAs substrate. The $^{75}\text{As}^+$ signal decreases at a slower rate than either $^{27}\text{Al}^+$ or $^{69}\text{Ga}^+$ to reach a constant level in GaAs. The $^{28}\text{Si}^+$ signal increases from the surface until its peak value at the projected range, it then decreases until it reaches the interface region and the GaAs substrate.

The secondary ion signals shown in Figure 65 are similar to those in Figure 62. Figure 66 is similar to Figure 63 inasmuch as the trends are similar. The trends in Figure 67 are also similar to Figure 64. The secondary ion signal of $^{16}\text{O}^+$ is included to see if its variation will yield additional insight into the analysis. The $^{16}\text{O}^+$ signal follows the $^{75}\text{As}^+$ signal very closely.

Figures 68 to 73 are analyses of the same samples as discussed above (Figures 62 to 67) except the analysis was performed with a Cs^+ primary ion beam and negative secondary ions were monitored. Examination of Figure 68 shows that the most intense matrix signal is now $^{75}\text{As}^-$. The peak of

124

the $^{28}\text{Si}^-$ signal is only an order of magnitude below $^{75}\text{As}^-$. Another order of magnitude below that level is the $^{69}\text{Ga}^-$ signal. The $^{27}\text{Al}^-$ signal is lost after the first few seconds. The $^{75}\text{As}^-$ and $^{69}\text{Ga}^-$ signals rapidly reach constant values. The $^{16}\text{O}^-$ signal falls quickly to a constant level. The profile in Figure 69 was begun within a minute of sample introduction; this explains the downward variation in $^{16}\text{O}^-$, which decreases by a factor of about 20 until it reaches a steady-state value. All other secondary ions which were monitored show an increase from the surface to a steady-state value by the time at which the projected range of the implant is reached.

In Figure 70, $^{16}\text{O}^-$ declines rapidly from the value at the surface until it reaches a steady-state value. The downward trend of $^{16}\text{O}^-$ in the previous figure is not repeated in this depth profile, which was begun 35 minutes after the sample was introduced into the SIMS instrument. The $^{75}\text{As}^-$, $^{27}\text{Al}^-$ and $^{69}\text{Ga}^-$ signals all reach their steady-state values a short time into the analysis. The profiles in Figures 71, 72 and 73 show trends similar to Figures 68, 69 and 70 respectively. Figure 73 monitors only two m/e signals. Secondary ion count distributions of Cr and Si implanted into GaAs at high energies are shown in Figures 74 to 77.

Monitoring the matrix signals resulted in identifying some $\text{Al}_x\text{Ga}_{1-x}\text{As}$ samples with a layer which had less Al than.

expected, such as in Figure 54. In Figure 84, the Al concentration in the outer layer was estimated as 0.18 atomic percent on the basis of the SIMS analysis and this was confirmed by Auger analysis. The change in Al concentration was most evident when analyzed with $^{133}\text{Cs}^+$.

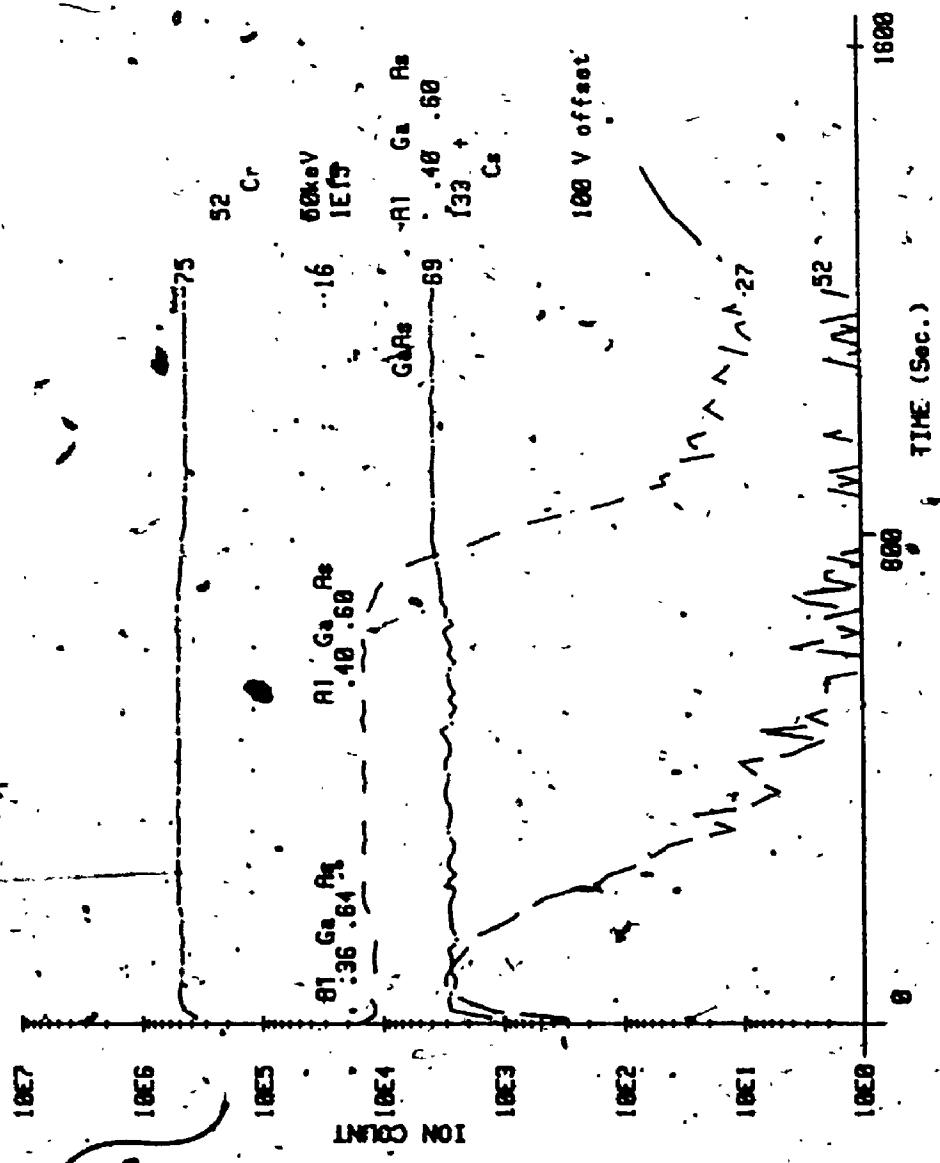


FIGURE 84 Secondary Ion Count Distributions of Cr in Al_{0.40}Ga_{0.60}A

CHAPTER 4
DISCUSSION OF RESULTS

4.1 DEPTH DISTRIBUTIONS

Ion count versus time information for the implant species can be converted to concentration versus depth since the implant dose (concentration per unit area) F is known and the crater depth z_n can be obtained from measurements. Once a linear sputter rate is determined for a given substrate, the depth becomes a straightforward function of time. The concentration of the implant species as a function of depth, $C(z)$, with n data points and ion count $I(z)$; is

$$C(z) = \frac{I(z) \cdot F \cdot n}{z_n \cdot \sum I(z)} \quad (49)$$

The ^{52}Cr concentration versus depth distributions that were determined by using the above equation are shown in Figures 85 to 90. The ^{28}Si concentration versus depth for implants into GaAs and $\text{Al}_x\text{Ga}_{1-x}\text{As}$ are shown in Figures 91 to 96. As expected, the peak of the distribution for the low energy implants is close to the surface. The high energy (100 keV and 125 keV) implants have distributions which extend much deeper into the substrate. Since the higher energy implants are more distributed over a range of depths, the peak concentration is consequently lower, for a given dose of implant species.

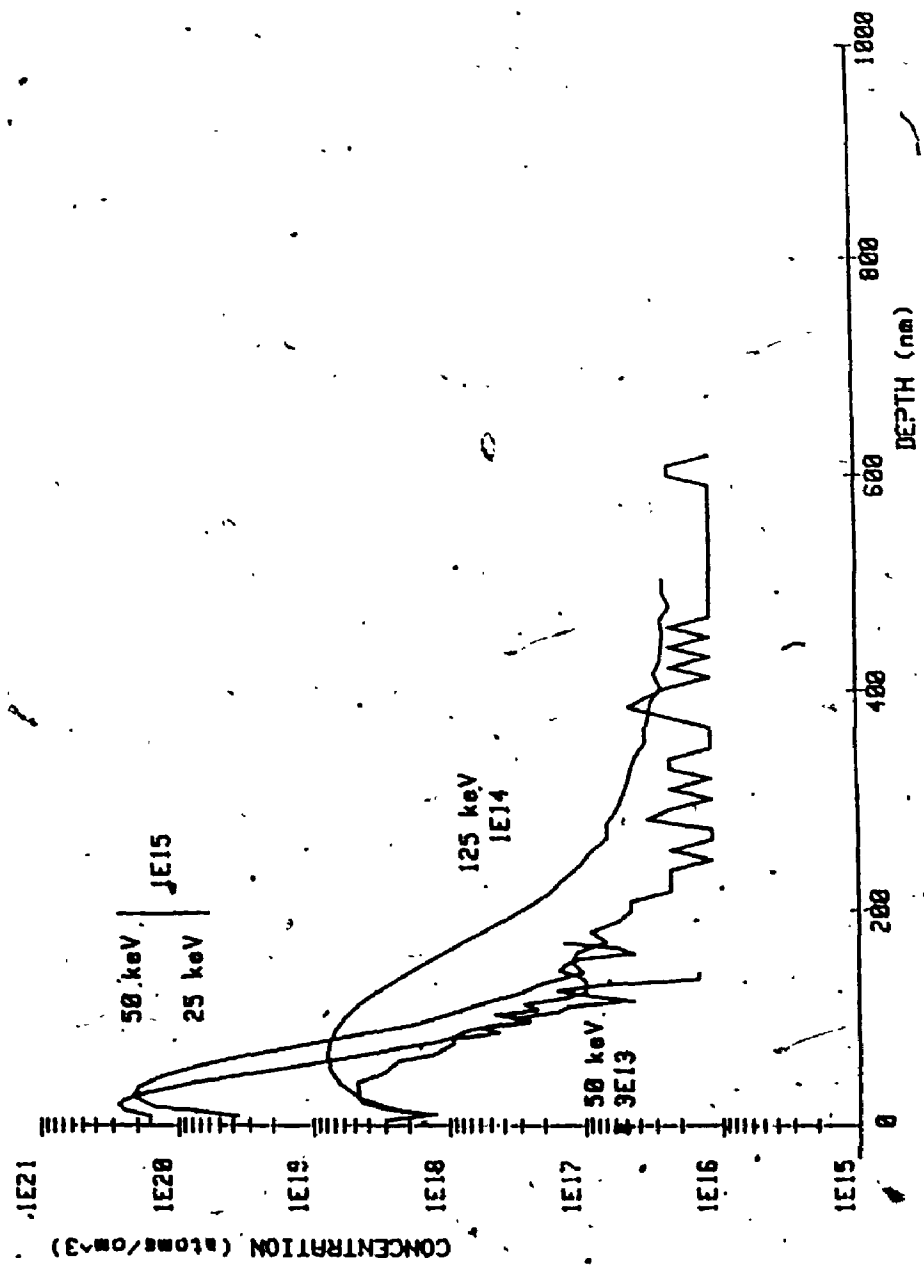


FIGURE 85 Concentration profile of Cr in GaAs profiled with O₂

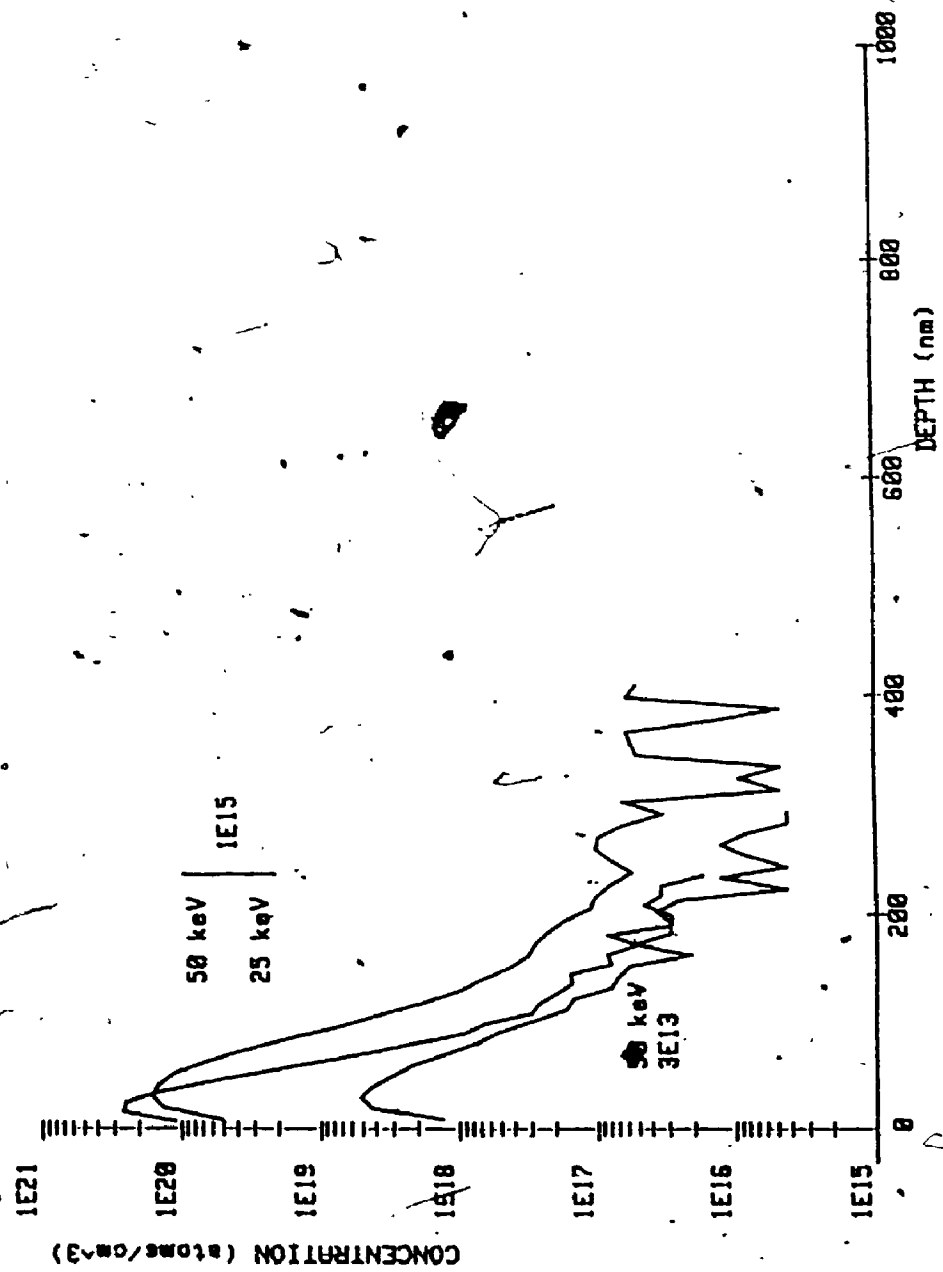


FIGURE 86 Concentration profile of Cr in Al_{0.21}Ga_{0.79}As profiled with O₂

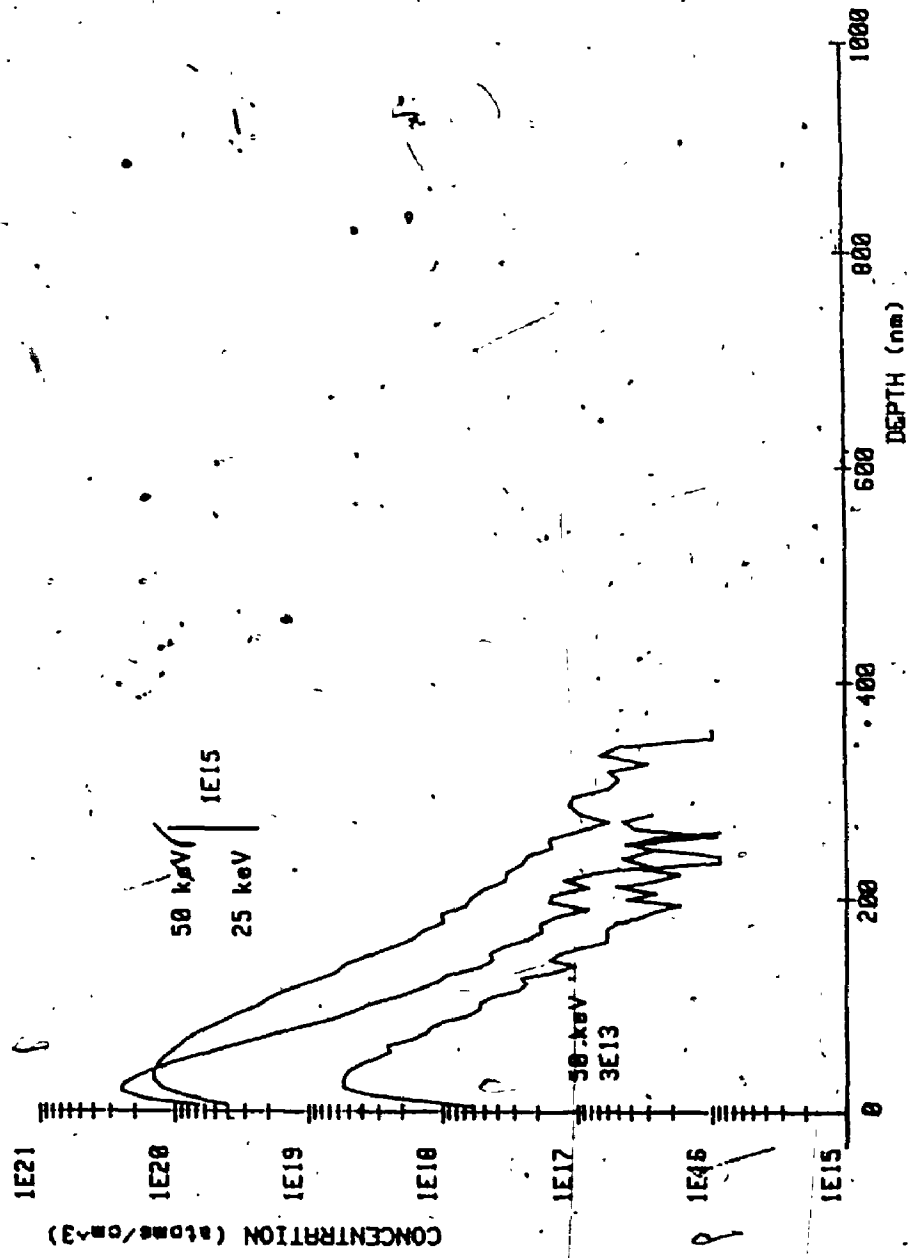


FIGURE 87 Concentration profile of Cr in Al₄₀Ga₆₀As profiled with O₂

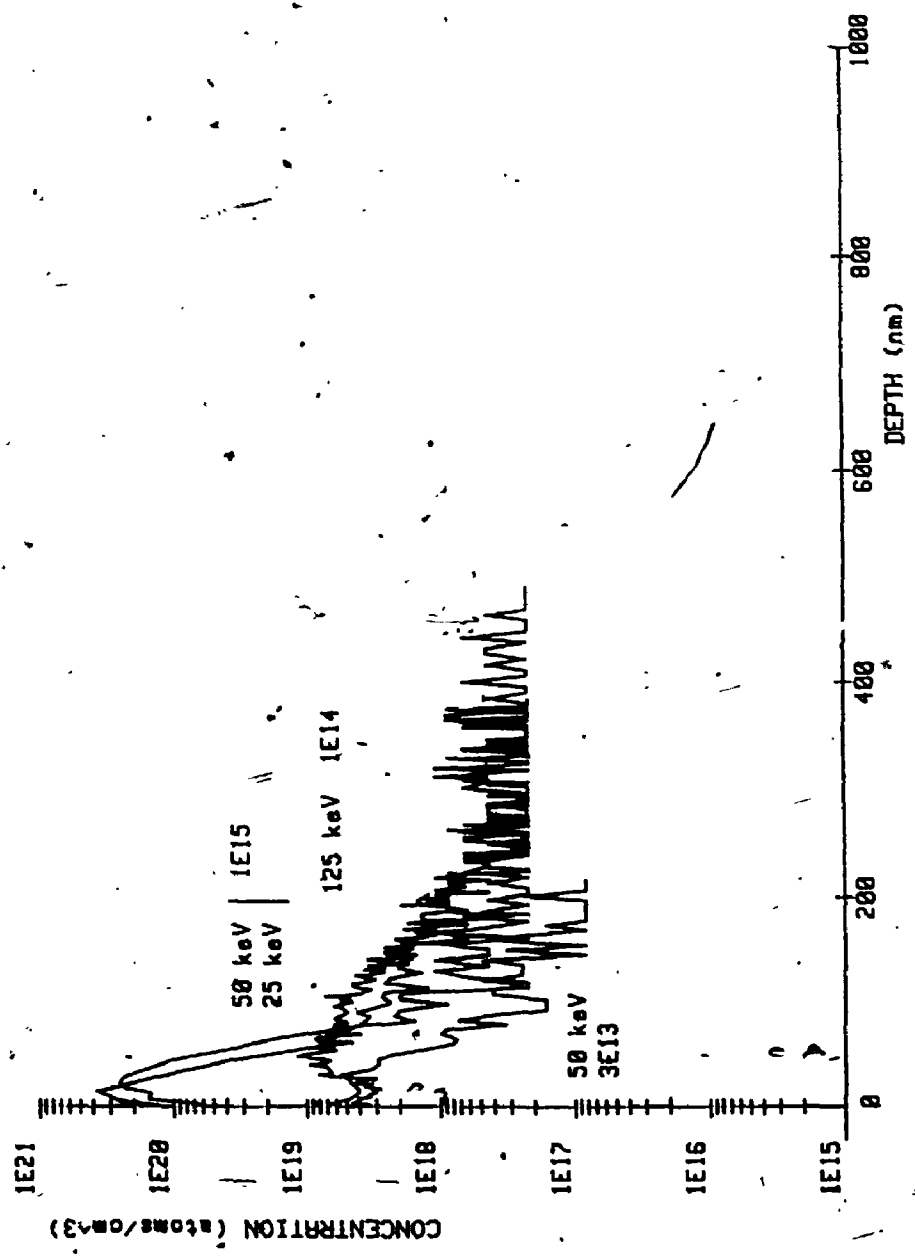


FIGURE 88 Concentration profile of Cr in Al_{0.40}Ga_{0.60}As profiled with O₂

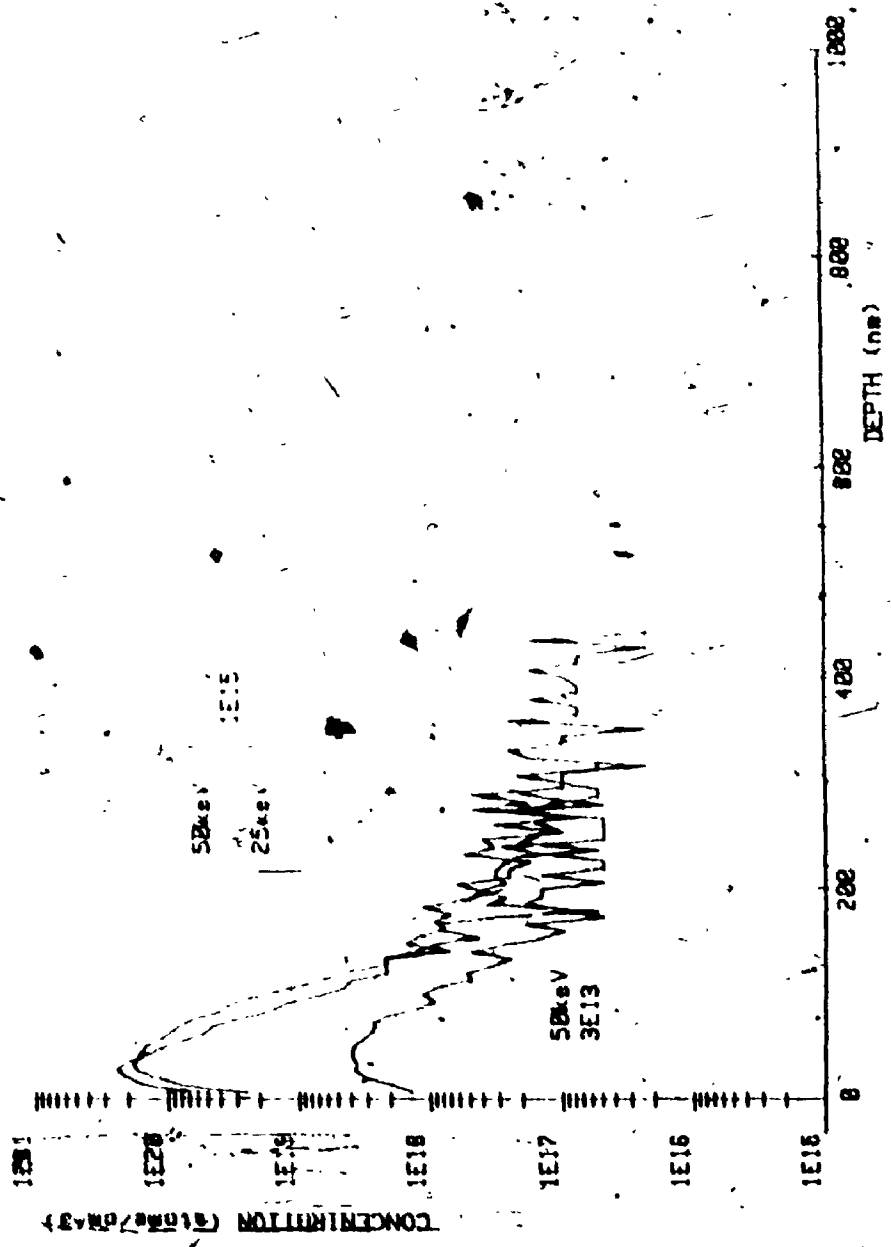


FIGURE 89 Concentration profile Cr in Al_{0.21}Ga_{0.79}As profiled with Cs

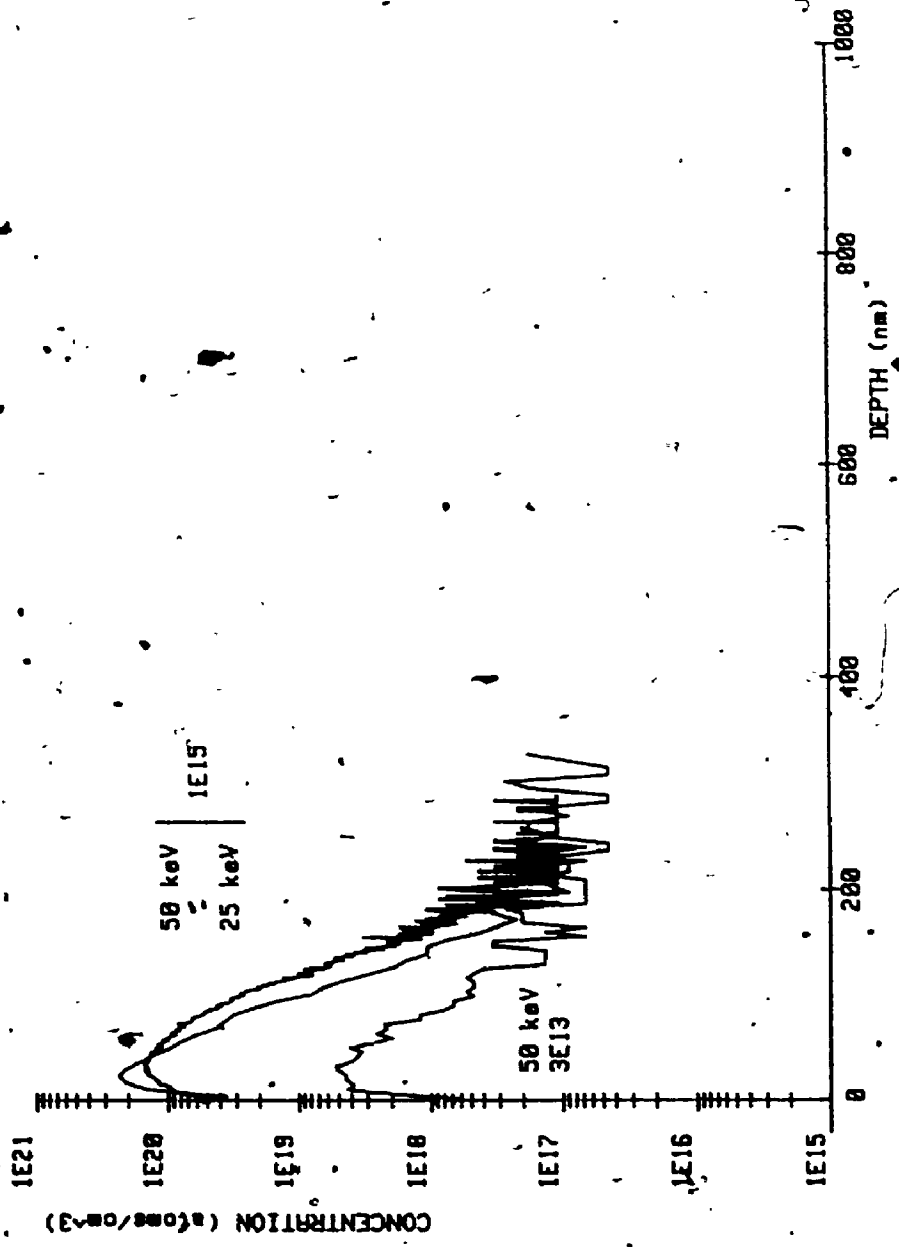


FIGURE 90 Concentration profile Cr in Al₄₀Ga₆₀As profiled with Cs

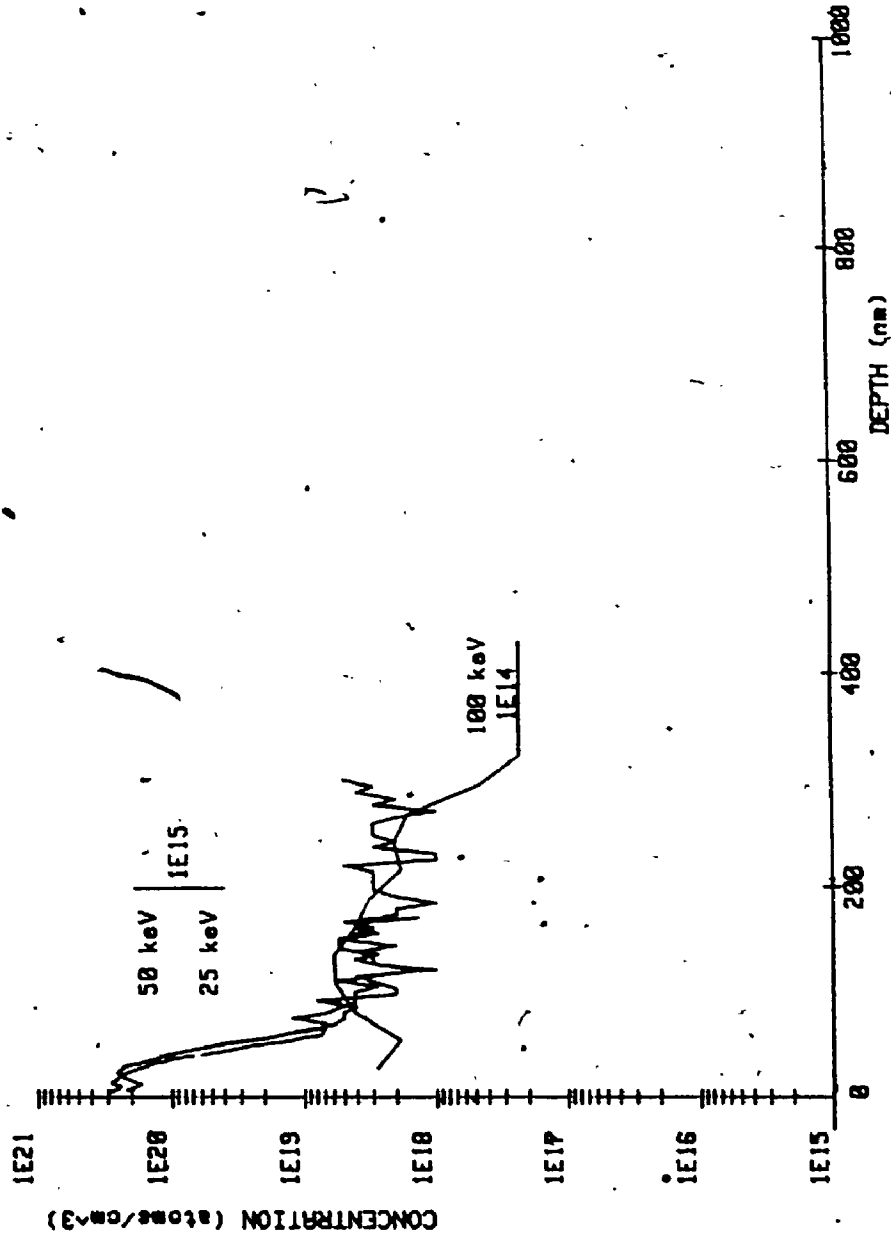


FIGURE 91 Concentration profile Si in GaAs profiled with O₂

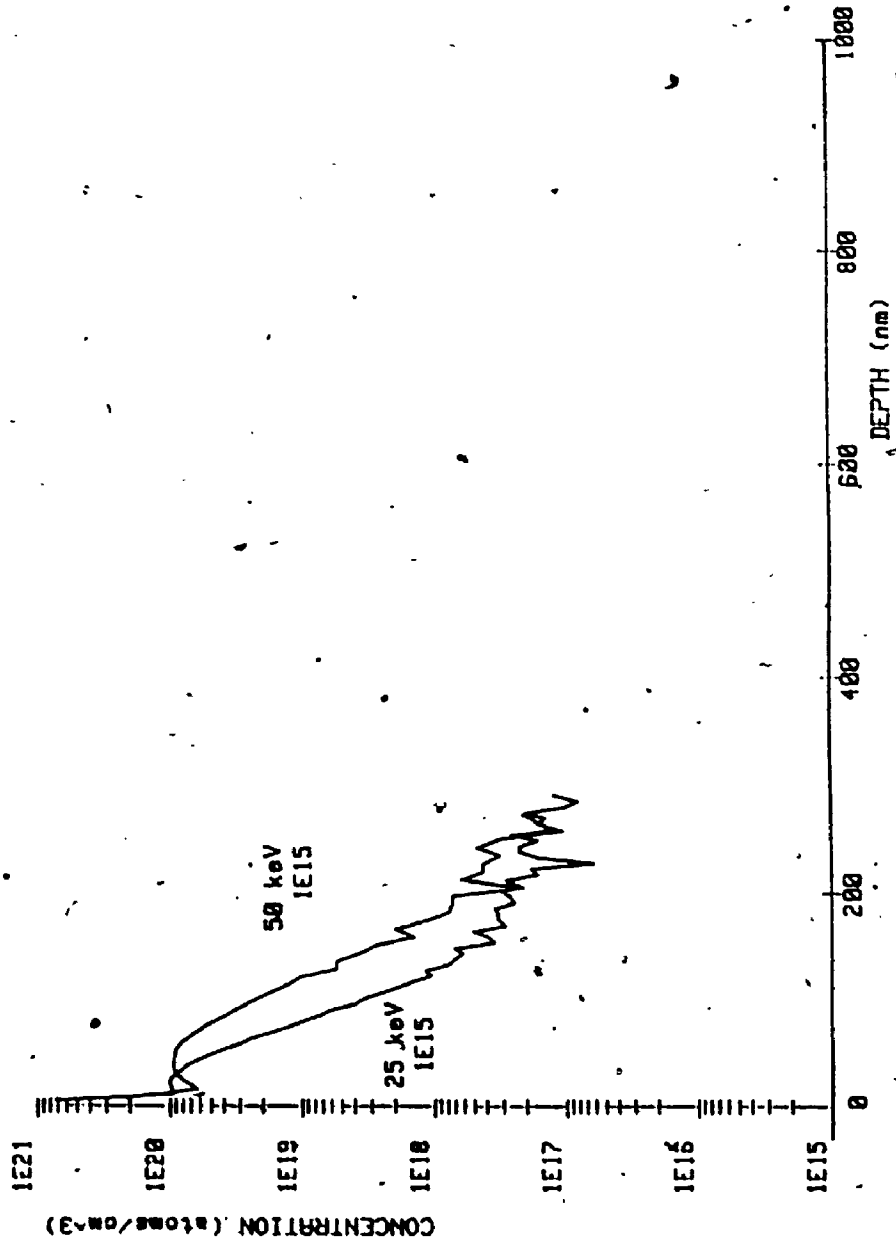


FIGURE 92 Concentration profile Si in Al₂₁Ga₇₉As₁ profiled with O₂

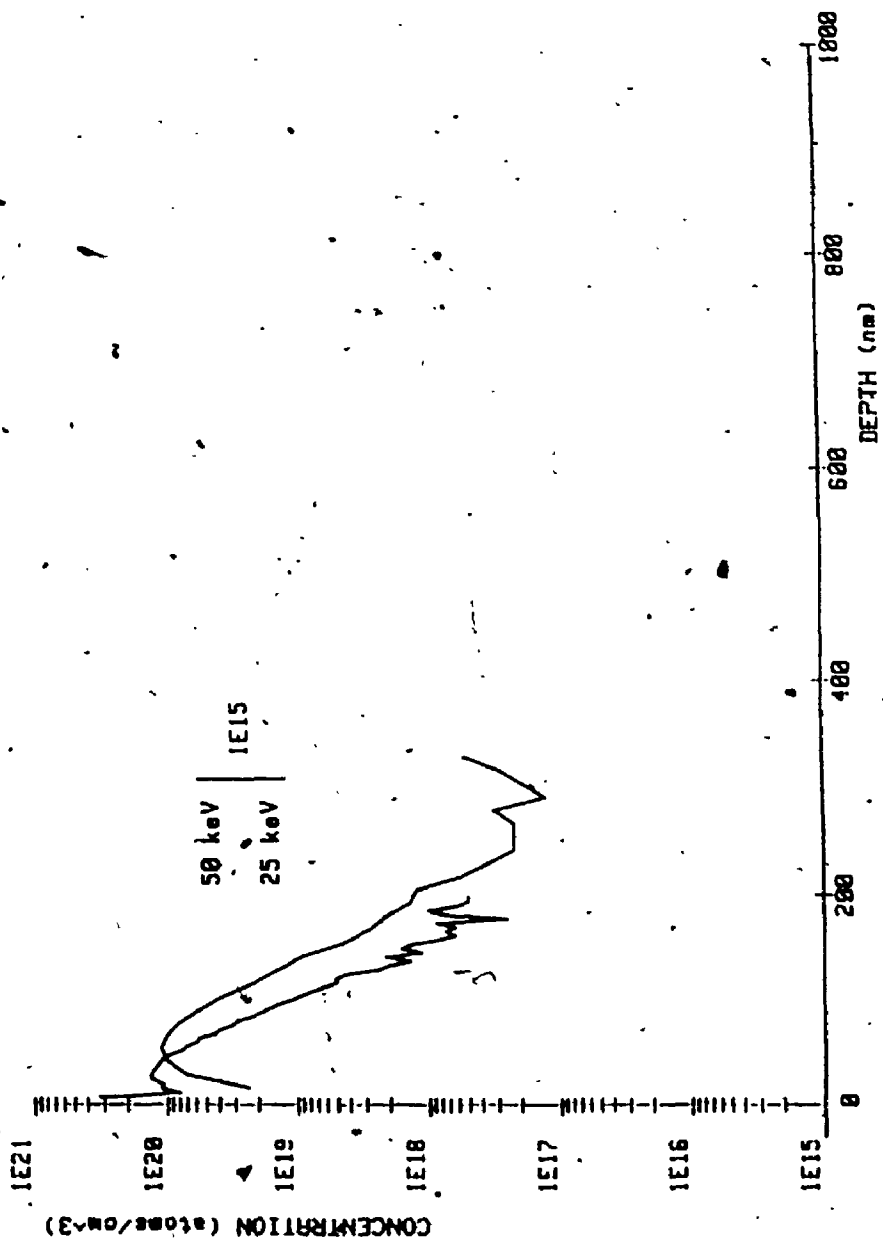


FIGURE 93 Concentration profile Si in Al_{0.4}Ga_{0.6}As profiled with O₂

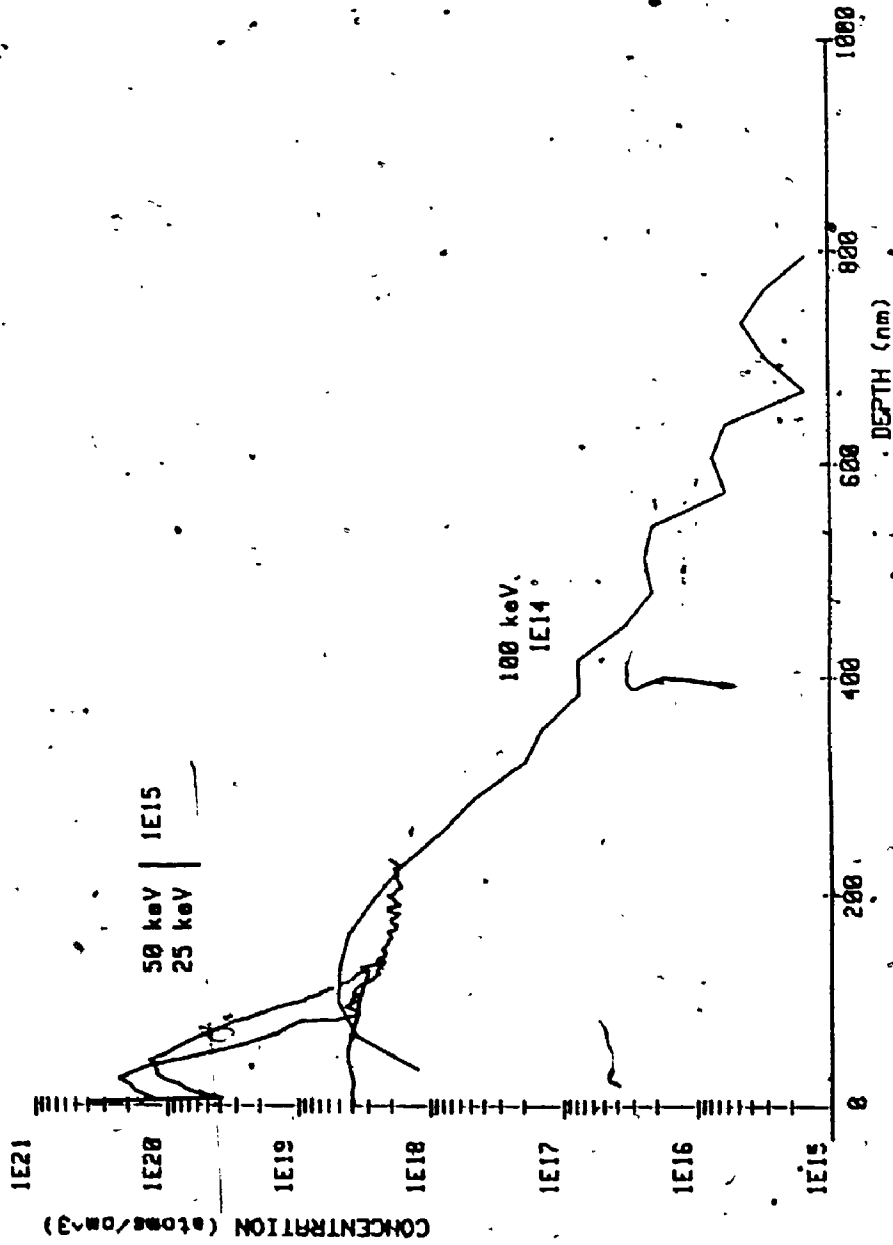


FIGURE.94 Concentration profile Si in GaAs profiled with Cs

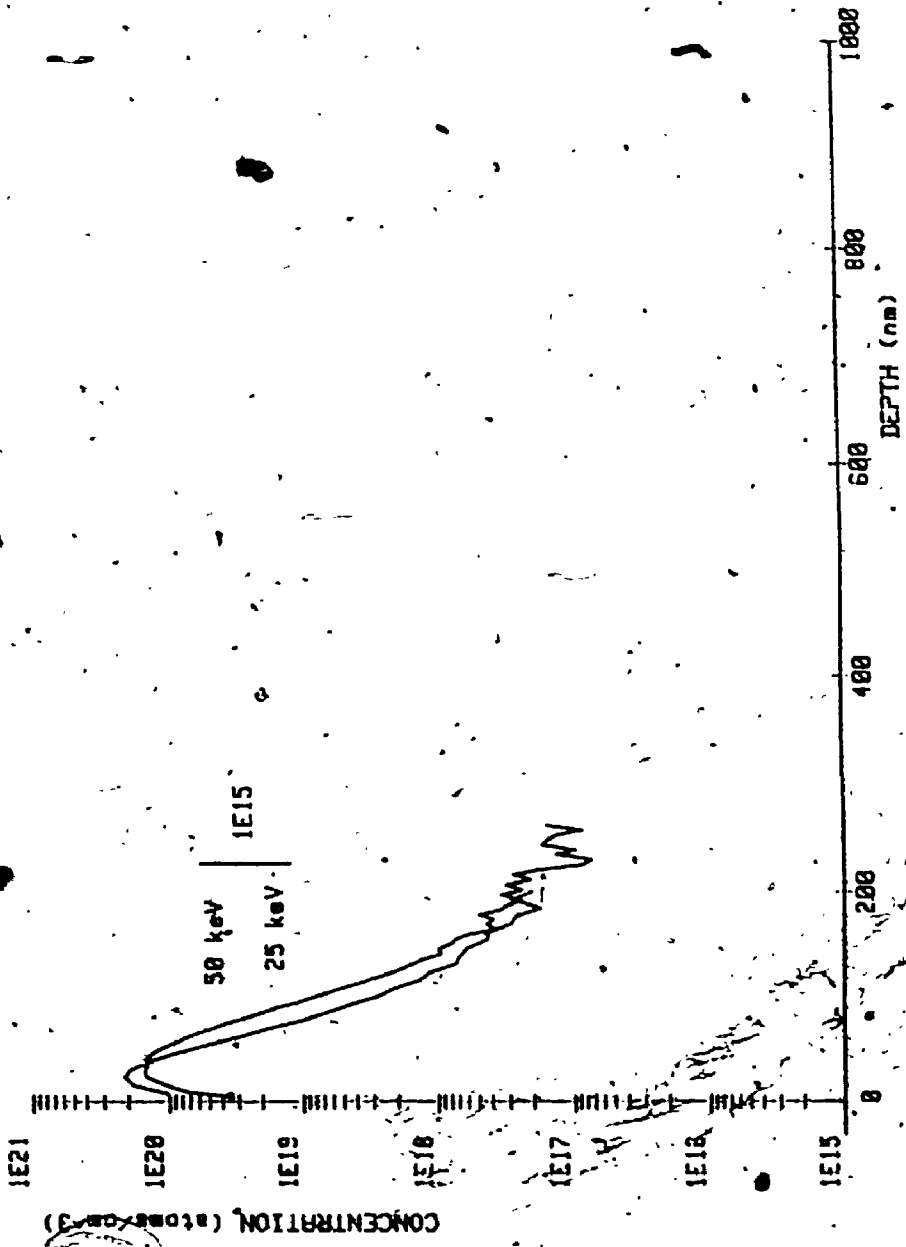


FIGURE 95 Concentration profile 61 in Al₂₁Ga₇₉As profiled with Cs.

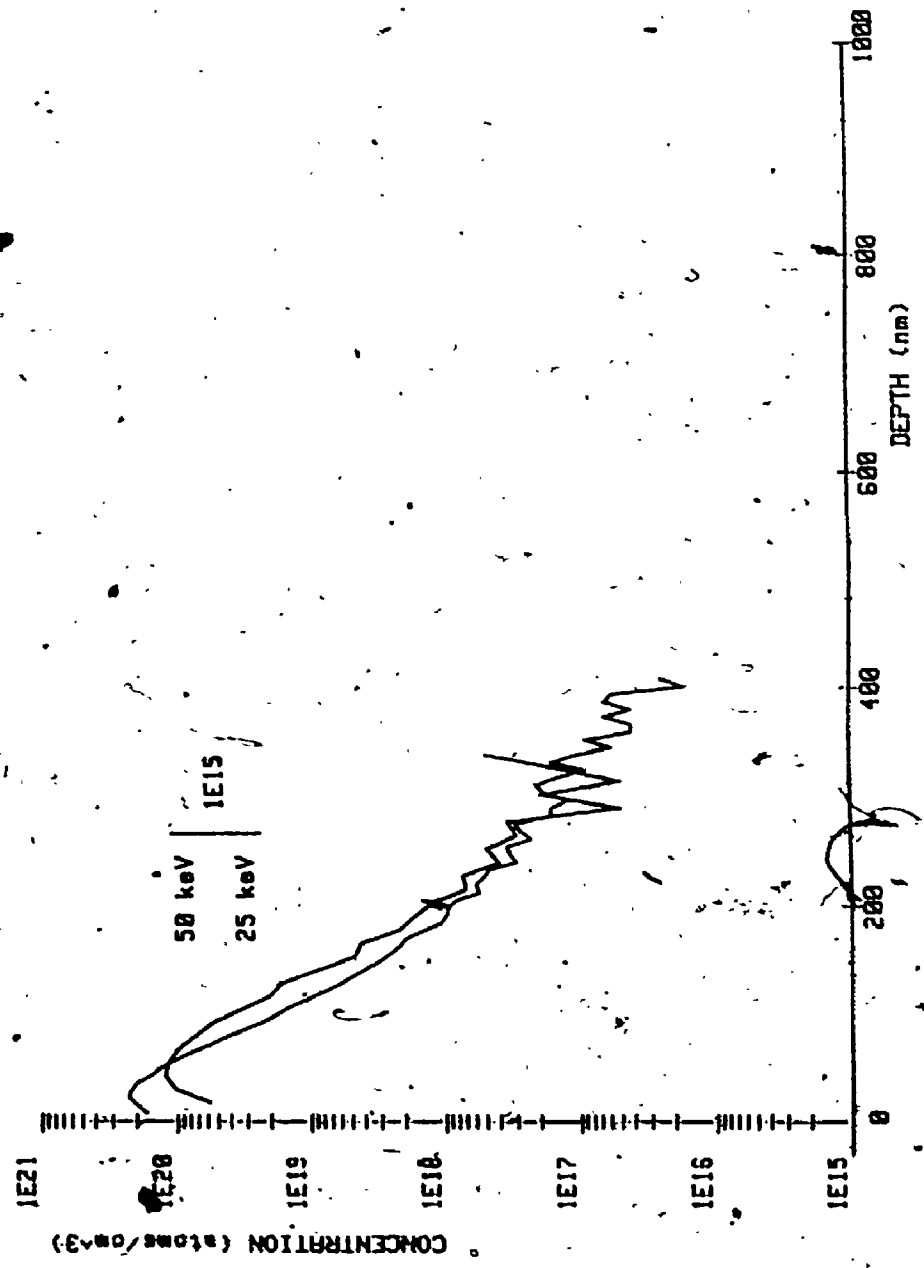


FIGURE 96 Concentration profile Si in Al. 40 Ga. 60 As profiled with Cs

By comparing Figures 91 and 94, it can be seen that silicon implants in GaAs are best profiled with $^{133}\text{Cs}^+$ in order to obtain the greatest dynamic concentration range. Figure 94 shows that the high energy (100 keV) implant in semi-insulating GaAs has a distribution which extends down to a concentration approaching 1×10^{15} atoms cm^{-3} . The minimum detection limit for ^{28}Si in GaAs is about 1×10^{15} atoms cm^{-3} when SIMS depth profiling is performed with an IMS-3f according to Huber et al. (160). The low energy implants shown in Figures 91 and 94 were performed into a GaAs sample which was doped to a level of 3×10^{18} silicon atoms cm^{-3} (2.2×10^{18} ^{28}Si atoms cm^{-3}); accordingly, the implant profile can not be distinguished below this "base" level. The ^{52}Cr implants in GaAs were observed to approach a minimum detectable level of 1×10^{16} atoms cm^{-3} , Figure 85. The minimum detection limit for Cr in GaAs is 3×10^{14} atoms cm^{-3} according to Huber et al. (160) but the IMS-3f in that study had been modified specifically in order to improve the Cr detection limit (161). Nevertheless, the use of O_2^+ gives the greatest dynamic range when depth profiling Cr in GaAs and $\text{Al}_x\text{Ga}_{1-x}\text{As}$.

The projected ranges found in this study are shown in Table 5. These values represent the averages of three profiles completed to the peak concentration. Close agreement is found for analyses with O_2^+ and Cs^+ , indicating that any recoil mixing, segregation or ion induced diffusion process

TABLE 5. PROJECTED RANGE OF IMPLANTS

Implant Species	Energy keV	Dose cm ⁻²	Range, nm			
			GaAs	Al _{0.21} Ga _{0.79} As	Al _{0.40} Ga _{0.60}	As _{0.133} Cs _{0.867}
28Si	25	1x10 ¹⁵	160 ⁺	160 ⁺	27.9	24.5
			133Cs ⁺	133Cs ⁺	48.2	-40.0
			20.0	20.0	22.5	23.0
50	1x10 ¹⁵	1x10 ¹⁴	160 ⁺	160 ⁺	24.2	32.0
			133Cs ⁺	133Cs ⁺	34.3	37.6
			20.0	20.0	32.5	35.0
100	1x10 ¹⁵	1x10 ¹³	160 ⁺	160 ⁺	35.0	39.0
			133Cs ⁺	133Cs ⁺	35.0	35.0
			20.0	20.0	32.2	35.0
52Cr	25	1x10 ¹⁵	160 ⁺	160 ⁺	24.2	32.0
			133Cs ⁺	133Cs ⁺	34.3	37.6
			20.0	20.0	32.5	35.0
50	1x10 ¹⁵	1x10 ¹³	160 ⁺	160 ⁺	35.0	39.0
			133Cs ⁺	133Cs ⁺	35.0	35.0
			20.0	20.0	32.2	35.0
125	50	1x10 ¹⁴	160 ⁺	160 ⁺	24.2	32.0
			133Cs ⁺	133Cs ⁺	34.3	37.6
			20.0	20.0	32.5	35.0
125	125	1x10 ¹⁴	160 ⁺	160 ⁺	35.0	39.0
			133Cs ⁺	133Cs ⁺	35.0	35.0
			20.0	20.0	32.2	35.0

is similar for both species. There is a tendency for the range to increase with Al concentration for a given ion implant. This would be expected theoretically on the basis that the average atomic number and mass of the substrate is decreasing as the Al concentration increases. The stopping power of Al is less than either Ga or As. No other systematic study of range as a function of semiconductor matrix composition exists. The projected ranges determined in this study are compared to theoretical predictions for ^{28}Si in GaAs calculated by Gibbons et al. (162) in Figure 97. The values for ^{52}Cr in GaAs (163) based on Winterbon are also shown in Figure 97. The projected range for low energy Cr implants are expected to parallel those of Si but no previous studies have been performed in this energy region for either implant. Gibbons et al. (162) does not provide any predictions for Cr and the value obtained from other calculations depends a great deal on the scattering cross-sections and stopping power chosen (163). The 25 and 50 keV silicon implants in GaAs agree well with Gibbons et al.'s (162) predictions. The 100 keV silicon implant has an experimentally measured range which is about 40% greater than predicted. The ^{52}Cr range at 125 keV is about 60% greater than predicted. There are no previously published implant profiles in $\text{Al}_x\text{Ga}_{1-x}\text{As}$ to serve as a comparison with this study.

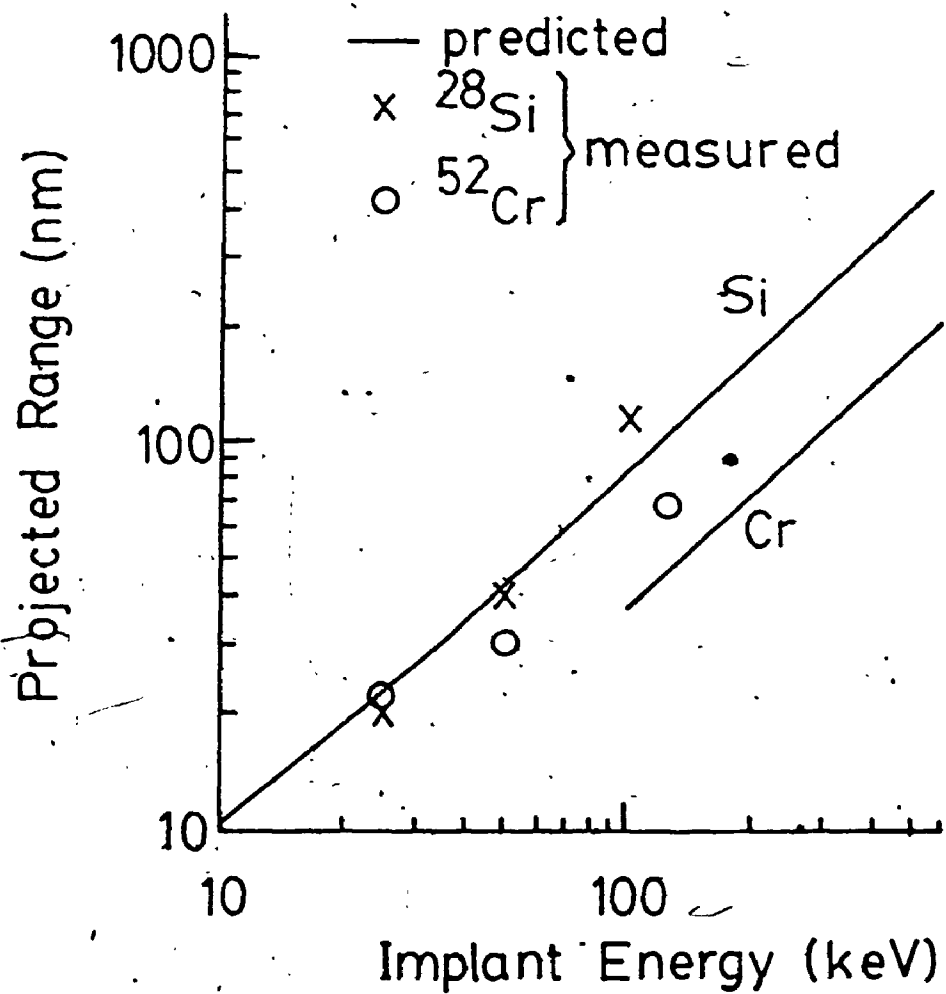


FIGURE 97 Projected range as a function of energy

4.2 SPUTTER YIELDS

In order to determine the sputter yield, the primary ion current must be accurately known. Unfortunately, the IMS-3f falls well short of the mark in routinely measuring the ion current. This is due to the design of the IMS-3f's Faraday cup which does not effectively trap the ion beam. To overcome this, a specially constructed Faraday cup (based on the design of Andersen and Bay (100)) was substituted in place of the sample in the IMS-3f. Figure 98 shows the ion current measured with the substitute Faraday cup versus the ion current indicated by the IMS-3f. The IMS-3f indication of the ion current is not stable over an extended period of time. The internal clock used by the IMS-3f's computer was also in error. It indicated 111% of the actual elapsed time.

The sputter yield was determined as a function of aluminum concentration, for both Cs^+ and O_2^+ and is shown in Figure 99. Also plotted in this figure are predictions of equation (12). The equation was derived for normal ion incidence with rare gas ion species bombarding a pure element substrate. In applying this equation, all substrate parameters were averaged according to the atomic concentration of the major matrix elements; Winterbon's (164; 165) nuclear stopping power was used in the calculation. In spite of these limitations, the measured sputter yields are close to

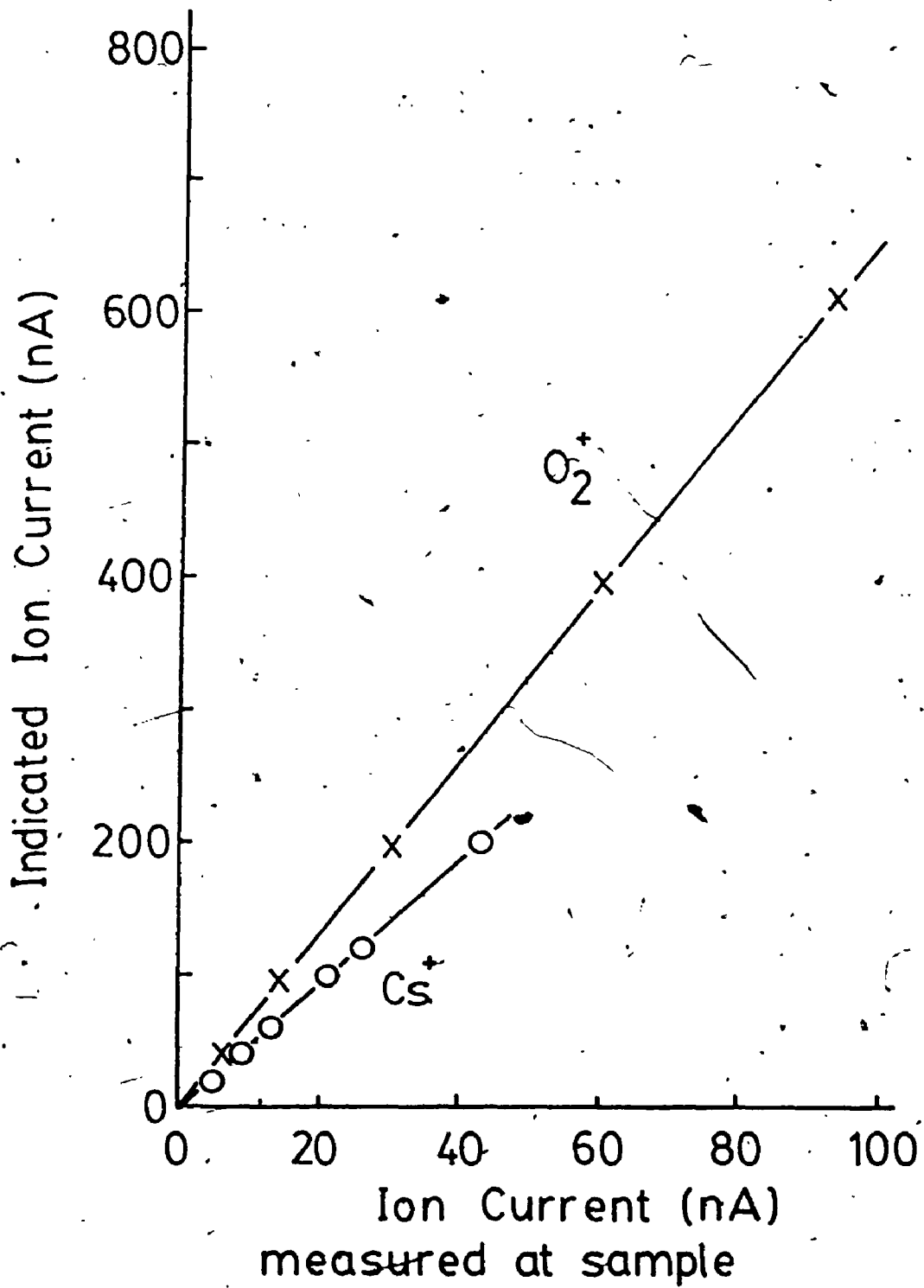


FIGURE 98 Measured versus displayed primary ion current

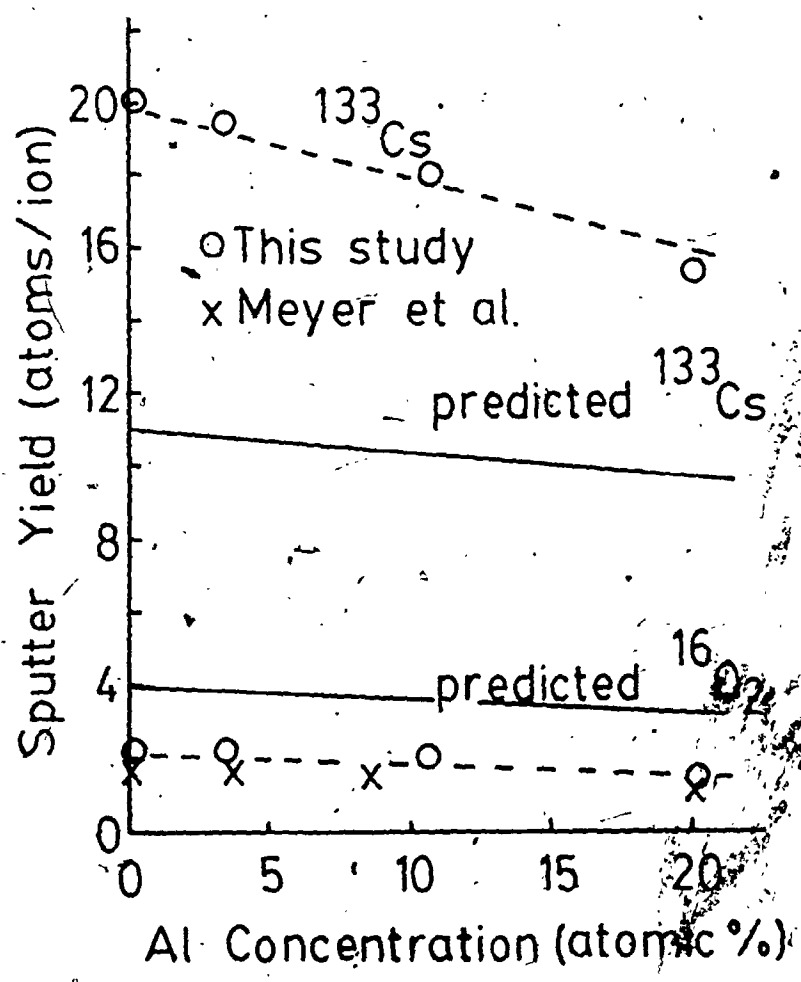


FIGURE 99 Sputter yield variation with aluminum concentration

the calculated values.

4.3. PRACTICAL ION YIELDS

The positive and negative practical ion yields for Si, Cr, Ga and As were determined for each substrate. Figures 100 and 101 show the ratios of the practical ion yields in $\text{Al}_x\text{Ga}_{1-x}\text{As}$ to those in GaAs. The slope of the line, in these figures, indicates the degree of matrix effect. The greater the slope, the greater the ion yield for increasing Al content. In the case of both $^{133}\text{Cs}^+$ and $^{16}\text{O}_2^+$ bombardment, the matrix effect appears to be a linear function of Al concentration. The ratios determined in this study with $^{16}\text{O}_2^+$ bombardment are compared to the ratios determined in previous studies in Figure 102. A minor enhancement of $^{69}\text{Ga}^+$ with increasing Al content agrees with Meyer et al. (154). The degree of $^{75}\text{As}^+$ enhancement observed is about twice as large as seen by Meyer et al. and 50 percent higher than Galuska and Morrison's observations. The measured value of the practical ion yield ratio for $^{28}\text{Si}^+$ was almost a factor of two lower than in Galuska and Morrison's study. It should be kept in mind that the Meyer et al. study was carried out on an Atomica quadrupole SIMS at 10 keV $^{16}\text{O}_2^+$, Galuska and Morrison's study used an IMS-3f magnetic sector SIMS with a net energy of 5.5 keV O_2^+ , and this study used an IMS-3f with a net 8.0 keV O_2^+ ion beam.

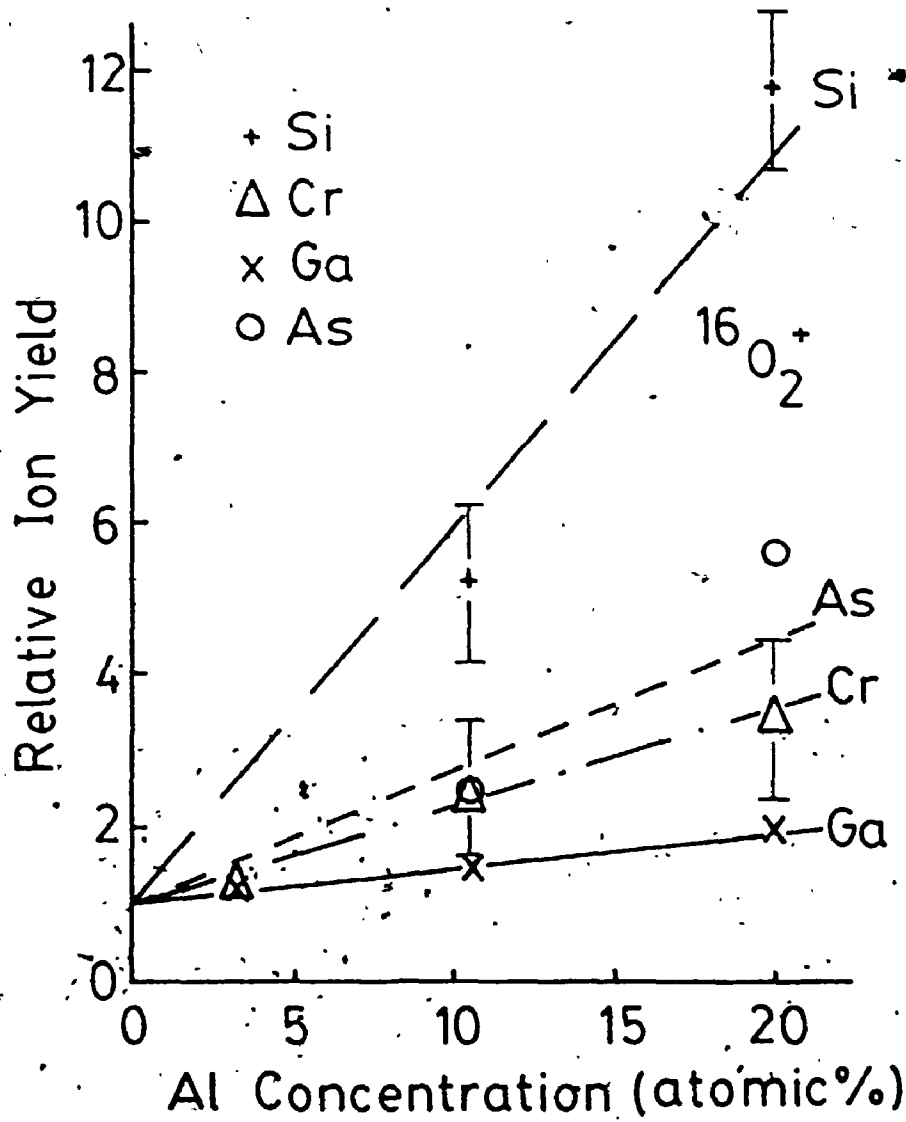


FIGURE 100 Positive practical ion yield relative to GaAs as a function of Al concentration with O_2 primary ion species

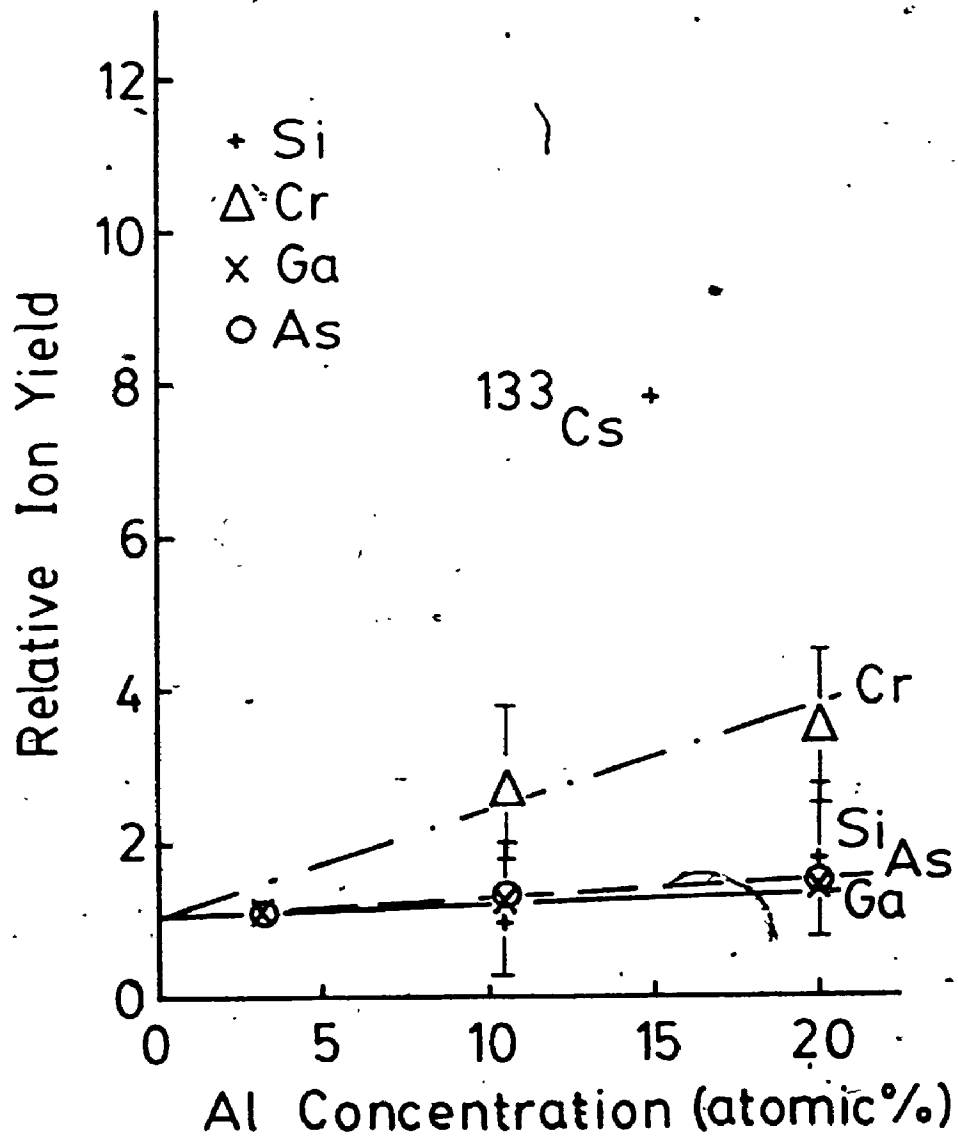


FIGURE 101 Negative practical ion yield relative to GaAs as a function of Al concentration with Cs primary ion species

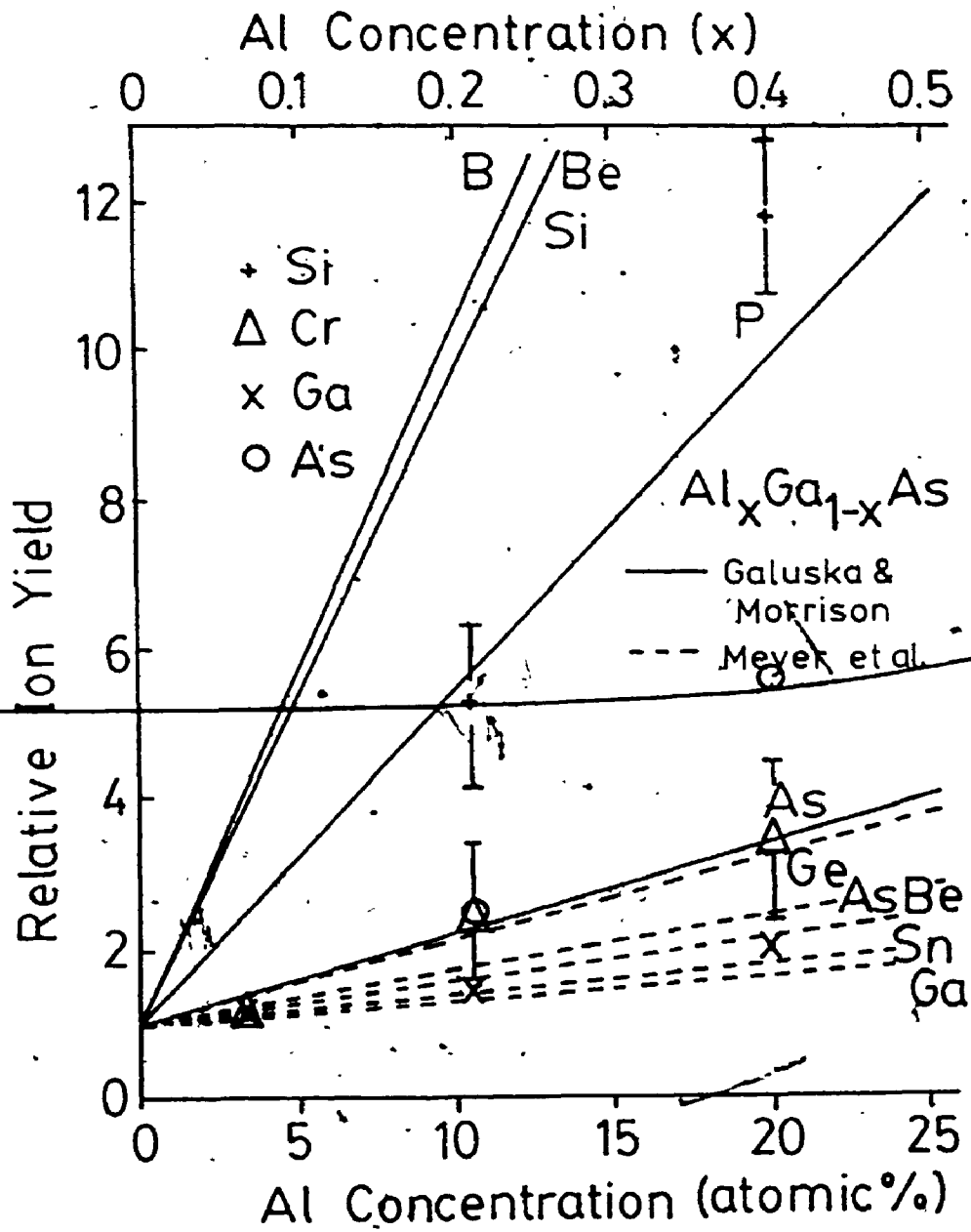


FIGURE 102 Positive relative ion yields of Meyer et al. (154), Galuska and Morrison (155) and this work

No previous studies of the SIMS matrix effect undertaken with $^{133}\text{Cs}^+$ bombardment exist. It is surprising that the matrix effect is minimal for $^{28}\text{Si}^-$, $^{76}\text{As}^-$ and $^{69}\text{Ga}^-$ under $^{133}\text{Cs}^+$ bombardment, while ^{52}Cr has approximately the same slope regardless of whether $^{133}\text{Cs}^+$ or $^{16}\text{O}_2^+$ primary ions are employed.

As discussed in Chapter 1, the modified LTB model of secondary ion emission can be applied to complex matrices. In Figure 103, $\log(I_i M^{3/2} z_i e / c_i z_i^+)$ is plotted as a function of the first ionization potential, as Morgan and Clegg (142) have described for the case of GaAs. Table 6 shows the first ionization potential and electron affinity for these species. While there seems to be a relationship between ionization potential and slope in Figure 103, the correlation is not perfect since As and Si should be switched in order. The semilog plot shows that the slope of the line fitting a given matrix decreases as the Al concentration increases. These slopes correspond to a temperature of 4400 K for GaAs, 3900 K for $\text{Al}_{.21}\text{Ga}_{.79}\text{As}$ and 3600 K for $\text{Al}_{.40}\text{Ga}_{.60}\text{As}$. Computer iteration was necessary until the temperature derived from the slope corresponded to the value selected for the partition function ratio. Arsenic was ignored in deriving the temperature in keeping with previous analysis (142). The accuracy of the one fitting parameter method for quantitative analysis has been found to be

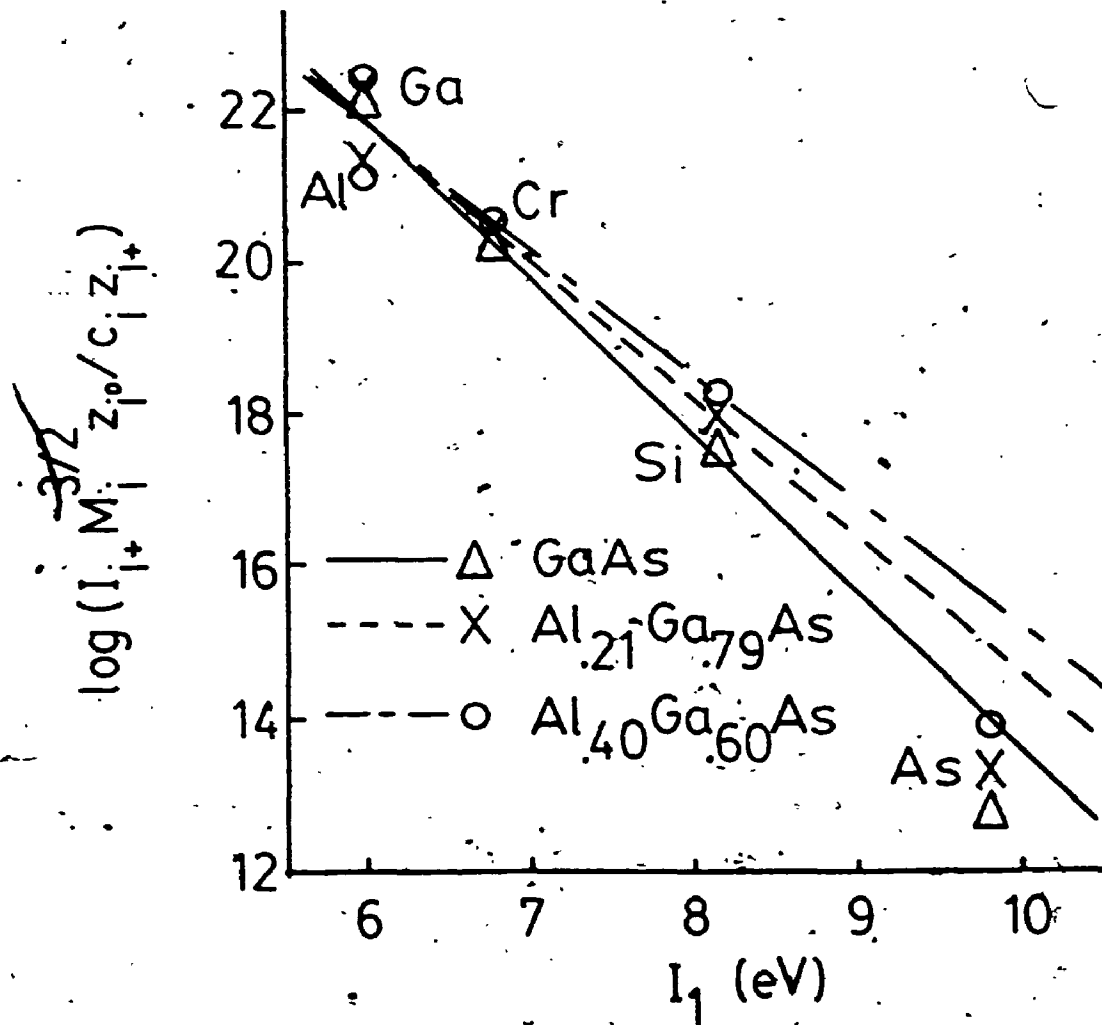


FIGURE 103 Local thermal equilibrium analysis showing $\log(I_{i+} M_i^{3/2} z_{i0} / c_i z_{i+})$ versus first ionization potential

TABLE 6. IONIZATION POTENTIAL AND ELECTRON AFFINITY

Element	First Ionization Potential (166) (eV)	Electron Affinity (166) (eV)
Si	8.2	-2.10
Cr	6.8	-0.66
Ga	6.0	-0.50
As	9.8	-0.80

comparable to that obtainable when relative sensitivity factors are used (141) but this is the first application to the $\text{Al}_x\text{Ga}_{1-x}\text{As}$ system. The LTE method is more versatile since it is not restricted to certain elements but appears to be applicable to all elements.

The fitting of negative ion data with electron affinity is more complex and is shown in Figure 104. The statistical distributions of negative ions and atoms are not known so no partitioning weights have been included. Accurate quantitative analysis would not be possible with the relationship shown in Figure 104.

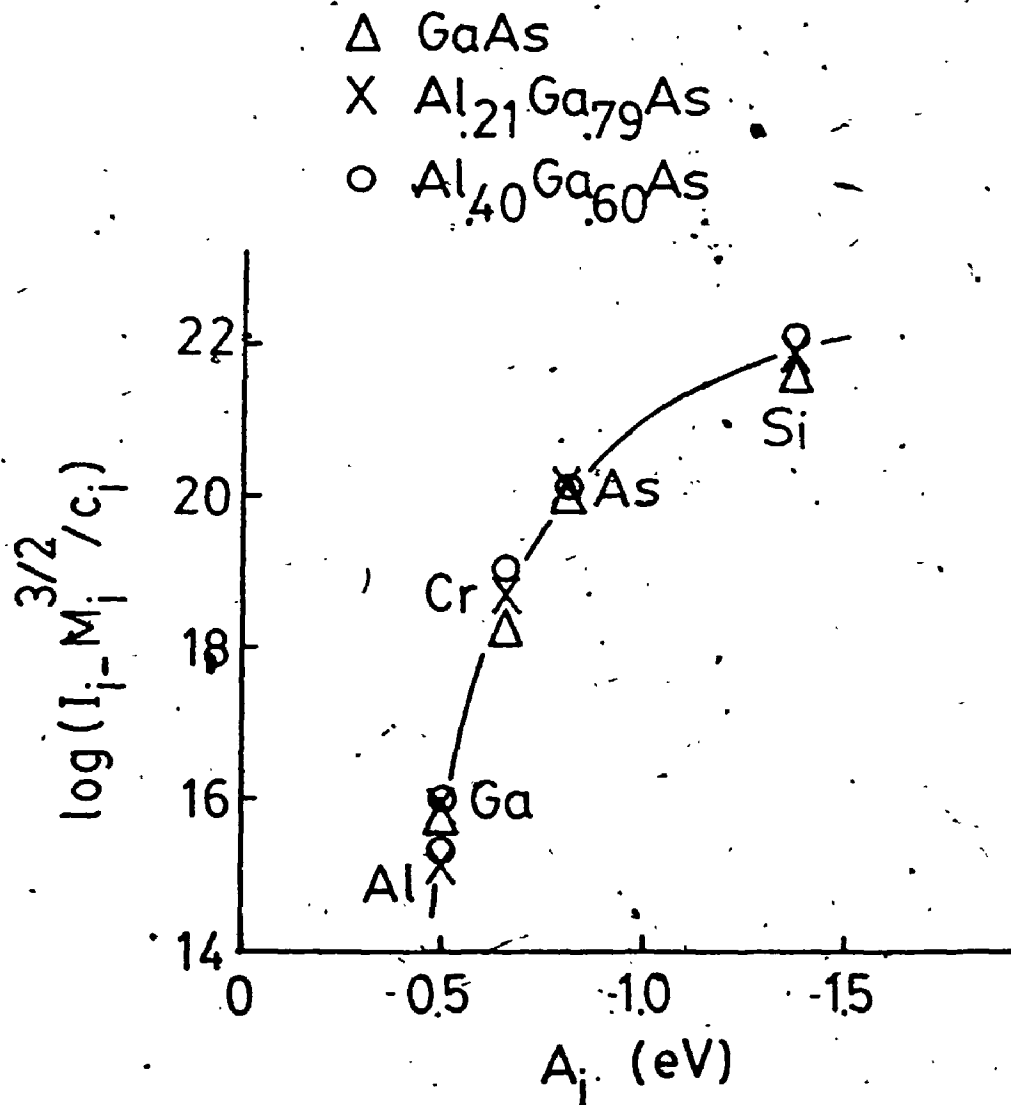


FIGURE 104 Local thermal equilibrium analysis showing $\log(I_i \cdot M_i^{3/2} / c_i)$ versus electron affinity

CHAPTER 5

CONCLUSIONS

The depth distribution of ion implanted samples of GaAs and $\text{Al}_x\text{Ga}_{1-x}\text{As}$ have been measured. Depth profiles of ^{28}Si and ^{52}Cr were measured with $^{16}\text{O}_2^+$ and $^{133}\text{Cs}^+$ while monitoring positive and negative secondary ions, respectively. The results of this study have extended the understanding of the matrix effect in SIMS quantitative analysis of semiconductor samples. This study can claim a number of important features. It is the only study to date to show the depth distributions of ion implants of ^{28}Si and ^{52}Cr in $\text{Al}_x\text{Ga}_{1-x}\text{As}$. The study was unique in its investigation by using techniques which reduced or eliminated molecular ion interferences. This study has shown the variation of both the negative practical ion yield and the sputter yield as a function of Al concentration in the $\text{Al}_x\text{Ga}_{1-x}\text{As}$ semiconductor system under $^{133}\text{Cs}^+$ bombardment. The study has also confirmed that the positive practical ion yield varies linearly with Al concentration but the measured values differ from past studies.

It has been observed here, for the first time, that bombarding with $^{133}\text{Cs}^+$ primary ions and the measurement of negative secondary ions results in less matrix effect than observed with $^{16}\text{O}_2^+$ and positive secondary ions for the species studied. The modified LTE model of Morgan and Clegg can be used to accurately describe the positive secondary

ion yield for quantitative analysis. The negative secondary ion yield does not show a simple linear relationship with electron affinity when analyzed in an LTE manner. The sputter yield decreased as the Al concentration increased for the $\text{Al}_x\text{Ga}_{1-x}\text{As}$ system. The sputter yields and the rate of decrease with Al concentration for $^{16}\text{O}_2^+$ bombardment agreed with Sigmund's model. This was not the case for $^{133}\text{Cs}^+$ bombardment. The simplified model underestimated the sputter yield and the rate of decrease in sputter yield with Al concentration. The projected ranges measured for ^{28}Si implants in GaAs agreed with theoretical calculations. The measured projected ranges for ^{52}Cr implanted into GaAs will provide the basis for comparison of theoretical model predictions as will the measured implant distributions in $\text{Al}_x\text{Ga}_{1-x}\text{As}$.

This study points to the continued need to determine the factors governing both the SIMS matrix effect and ionization mechanisms. To extend the work described in this thesis, further measurements could be made for other dopant ion species in $\text{Al}_x\text{Ga}_{1-x}\text{As}$. The dopant Be would be interesting to evaluate since such wide discrepancy exists between literature values of practical ion yield. From the semiconductor industry's point of view, Fe, Cu, Se, S and Te are important dopant species and both the matrix effect and the detection limit for these species should be determined. Studies of the matrix effect should also be extended to other

matrix and ion implant species. Implantation profiles are known for only a few ion species, matrix and implant energy combinations. These distributions should be evaluated over a broad range and confirmed with other analysis techniques.

REFERENCES

1. Higatsberger, M.J. "Advances in Electronics and Electron Physics", Academic Press, New York, 56: 291 (1981).
2. Czanderna, A.W. ed. "Methods of Surface Analysis", Elsevier Sc., Amsterdam, 1 (1975).
3. Larrabee, G.B. in "VLSI Electronics: Microstructure Science", (Einspruch, N.G. ed.), Academic Press, 2: 37 (1981).
4. Yin Shaiw-Yih in "Microbeam Analysis-1980", (Wittry, D.B. ed.), San Francisco Press, San Francisco, p. 289 (1980).
5. Yin Shaiw-Yih and Wittry, D.B. in "Microbeam Analysis-1981", (Geiss, R.H. ed.), San Francisco Press, San Francisco, p. 342 (1981).
6. Werner, H.W. in "New Developments in Secondary Ion Mass Spectrometry", (Barr, T.L. and Davis, L.E., eds.), ASTM STP 699: 81 (1980).
7. Storms, H.A., Brown, K.F. and Stein, J.D. Anal. Chem. 49: 2023 (1977).
8. Levi-Setti, R., Crow, R. and Wang, Y.L. in "Secondary Ion Mass Spectrometry SIMS V", (Benninghoven, A., Colton, R.J., Simons, D.S. and Werner, H.W. eds.), Springer, Berlin, p. 132 (1986).
9. Bernius, M.T., Ling Yong-Chien and Morrison, G.H. in "Secondary Ion Mass Spectrometry SIMS V" (Benninghoven, A., Colton, R.J., Simons, D.S. and Werner, H.W. eds.), Springer, Berlin, p. 245 (1986).
10. Shepherd, F.R., Vandervorst, W., Lau, W.M., Robinson, W.H. and SpringThorpe, A.J., *ibid.*, p. 350.
11. Williams, P. Surf. Sc. 90: 588 (1979).
12. Blaise, G. in "Material Characterization Using Ion Beams" (Thomas, J.P. and Cachard, A.), p. 143 (1978).
13. Morgan, A.E., de Grefte, H.A.M., Warmoltz, N., Werner, H.W. and Tolle, H.J. Appl. Surf. Sc. 7: 372 (1981).
14. Wittmaack, K. Surf. Sc. 90: 557 (1979).

15. Krauss, A.R. and Gruen, D.M. Surf. Sc. 90: 56 (1979).
16. Blaise, G. and Nourtier, A. Surf. Sc. 90: 45 (1979).
17. Robinson, W.H., Brown, J.D., Johnston, D., and Lau, W.M. in "Microbeam Analysis-1984" (Romero, A.P. and Goldstein, J.I., eds.), San Francisco Press, San Francisco, p. 331 (1984).
18. Littmark, U. and Hofer, W.O. Nucl. Instrum. Meth. 168: 329 (1980).
19. Sigmund, P. and Gras-Marti, A. Nucl. Instrum. Meth. 182: 25 (1981).
20. Ho, P.S. Surf. Sc. 72: 253 (1978).
21. Yu, M.L. and Lang, N.D. Phys. Rev. Lett. 50: 127 (1983).
22. Benninghoven, A. Surf. Sc. 53: 596 (1975).
23. Ganschow, O. in "Secondary Ion Mass Spectrometry SIMS V", (Benninghoven, A., Colton, R.J., Simons, D.S. and Werner, H.W., eds.), Springer, Berlin, p. 79 (1986).
24. Slodzian, G. Surf. Sc. 48: 161 (1975).
25. Boudewijn, P.R. and Werner, H.W. in "Secondary Ion Mass Spectrometry SIMS V", (Benninghoven, A., Colton, R.J., Simons, D.S. and Werner, H.W., eds.), Springer, Berlin, p. 270 (1986).
26. Werner, H.W. Surf. Interface Anal. 2: 56 (1980).
27. McHugh, J.A. Rad. Eff. 21: 209 (1974).
28. Andersen, C.A. in "Secondary Ion Mass Spectrometry", (Heinrich, K.F.J. and Newbury, D.E., eds.), National Bureau of Standards, Washington, SP427 (1975).
29. Blaise, G. Rad. Eff. 18: 253 (1973).
30. Lang, N.D. in "Secondary Ion Mass Spectrometry SIMS V", (Benninghoven, A., Colton, R.J., Simons, D.S. and Werner, H.W., eds.), Springer, Berlin, p. 18 (1986).
31. Jurela, Z. Int. J. Mass Spectr. and Ion Phys. 12: 33 (1973).
32. Schröer, J. Vacuum 22: 603 (1972).

33. Hofker, W.K. Philips Res. Repts. Suppl. 8: 1 (1975).
34. Hong, J.D., Davis, R.F. and Newbury, D.E. in "Proceedings of the Thirteenth Annual Conference of the Microbeam Analysis Society", (Kyser, D.F., ed.) Ann. Arbor, 30-A (1978).
35. Morabito, J.M. in "Secondary Ion Mass Spectrometry", (Heinrich, K.F.J. and Newbury, D.E., eds.) National Bureau of Standards, Washington, SP 427: 191 (1975).
36. Colby, B.N. and Evans Jr., C.A. Appl. Spectr. 27: 274 (1973).
37. Brown, F. and Mackintosh, W.D. J. Electrochem. Soc. 120: 1096 (1973).
38. Hughs, H.L., Baxter, R.D. and Philips, B. IEEE Trans. Nucl. Sci. NS-19: 256 (1972).
39. Boudewijn, P.R. and Werner, H.W. in "Secondary Ion Mass Spectrometry SIMS V", (Benninghoven, A., Colton, R.J., Simons, D.S. and Werner, H.W., eds.), Springer, Berlin, p. 270 (1986).
40. Le Goux, J.J. and Migeon, H.N. in "Secondary Ion Mass Spectrometry SIMS III" (Benninghoven, A., Giber, J., Lécro, J., Riedel, M. and Werner, H.W., eds.), Springer, Berlin, p. 52 (1982).
41. Thomson, J.J. Phil. Mag. 20: 252 (1910).
42. Sawyer, R.B. Phys. Rev. 35: 1090 (1930).
43. Woodcock, K.S. Phys. Rev. 38: 1696 (1931).
44. Thompson, J.S. Phys. Rev. 38: 1389L (1931).
45. Arnot, F.L. and Milligan, J.C. Proc. Roy. Soc. A 156: 538 (1936).
46. Arnot, F.L. Proc. Roy. Soc. A 158: 137 (1937).
47. Arnot, F.L. Proc. Roy. Soc. A 158: 157 (1937).
48. Arnot, F.L. and Beckett, C. Nature 141: 1011 (1938).
49. Sloane, R.H. and Press, R. Proc. Roy. Soc. A 168: 284 (1938).
50. Honig, R.E. J. Appl. Phys. 29: 549 (1958).

51. Herzog, R.F.K. and Viehböck, F.P. Phys. Rev. 76: 855L (1949).
52. Bradley, R.C. J. Appl. Phys. 30: 1 (1959).
53. Andersen, C.A. and Hinthorne, J.R. Anal. Chem. 45: 1421 (1973).
54. Castaing, R. and Slodzian, G. J. Microscopie 1: 395 (1962).
55. Liebl, H. Int. J. Mass Spectrom. Ion Phys. 6: 401 (1971).
56. Liebl, H.J. and Herzog, R.F.K. J. Appl. Phys. 34: 2893 (1963).
57. Sidenius, G. Rad. Eff. 44: 145 (1979).
58. Gomer, R. Appl. Phys. 19: 365 (1979).
59. Magee, C.W. J. Electrochem. Soc. 126: 660 (1979).
60. Wittmaack, K. Nucl. Instrum. Meth. 168: 343 (1980).
61. Hennequin, J.F. J. Physique 29: 957 (1968).
62. Brown, A. and Vickerman, J.C. Surf. Interface Anal. 6: 1 (1984).
63. Odom, R.W., Furman, B.K., Evans Jr., C.A., Bryson, C.E., Peterson, W.A., Kelly, M.A. and Wayne, D.H. Anal. Chem. 55: 578 (1983).
64. Slodzian, G. in "Secondary Ion Mass Spectrometry" (Heinrich, K.F.J. and Newbury, D.E., eds.) National Bureau of Standards 427: 33 (1975).
65. Burdo, R.A. and Morrison, G.H. "Table of Molecular Lines" Cornell University, Ithaca, N.Y. (1973).
66. Magee, C.W., Harrington, W.L. and Honig, R.E. Rev. Sci. Instrum. 49, 4 (1978) 477-86.
67. Brown, J.D., Robinson, W.H., Shepherd, F.R. and Dzoiba, S. in "Secondary Ion Mass Spectrometry SIMS IV" (Benninghoven, A., Okano, J., Shimizu, R. and Werner, H.W., eds.), Springer, Berlin, p. 296 (1984).
68. McIntyre, N.S., Fichter, D., Metson, J.B., Robinson, W.H. and Chauvin, W.J. Surf. Interface Anal. 7: 69 (1985).

69. Rehn, L.E., Danyluk, S., Wiedersich, H. Phys. Rev. Lett. 43: 1764 (1979).
70. Shikata, M. and Shimizu, R. Surf. Sc. 97: L363 (1980).
71. Butrymowicz, D.B., Manning, J.R. and Read, M.E. J. Phys. Chem. Ref. Data 5: 104 (1976).
72. Gossink, R.G., de Graffe, H.A.M. and Werner, H.W. J. Amer. Ceramic Soc. 62: 4 (1979).
73. Johnston, D.D., McIntyre, N.S., Chauvin, W.J., Lau, W.M., Nietering, K. and Schuetzle, D. in "Secondary Ion Mass Spectrometry SIMS V" (Benninghoven, A., Colton, R.J., Simons, D.S. and Werner, H.W., eds.), Springer, Berlin, p. 384 (1986).
74. Williams, F.L. and Nason, D. Surf. Sc. 45: 377 (1974).
75. Quinto, D.T., Sundaram, V.S. and Robertson, W.D. Surf. Sc. 28: 504 (1971).
76. Liao, Z.L., Tsaur, B.Y., Mayer, J.W. J. Vac. Sci. Technol. 16: 121 (1979).
77. Gillam, E. J. Phys. Chem. Sol. 11: 55 (1959).
78. van Oostrom, A. J. Vac. Sci. Technol. 13: 224 (1976).
79. Jacobi, K. and Ranke, W. J. Electron Spectrosc. Relat. Phenom. 8: 225 (1976).
80. Singer, I.L., Murday, J.S. and Cooper, L.R. J. Vac. Sci. Technol. 15: 725 (1978).
81. McGuire, G.E. Surf. Sc. 76: 130 (1978).
82. Arthur, J.R. and LePore, J.J. J. Vac. Sci. Technol. 14: 979 (1977).
83. Tagläuer, E. and Heiland, W. in "Proc. Symp. on Sputtering" (Varga, P., Betz, G. and Viehböck, F.P., eds.) Perchtoldsdorf, Vienna, p. 423 (1980).
84. Wittmaack, K. Nucl. Instrum. Meth. B2: 569 (1984).
85. Behrisch, R. in "Sputtering by Particle Bombardment II" (Behrisch, R., ed.), Springer, Berlin, p. 1 (1983).
86. Kelly, R. Surf. Sci. 90: 280 (1979).

87. Carter, G. and Colligon, J.S. "Ion Bombardment of Solids" Heinemann, London (1965).
88. Betz, G. and Nehner, G.K. in "Sputtering by Particle Bombardment II" (Behrisch, R., ed.), Springer, Berlin, p. 11 (1983).
89. Harrison, D.E., Kelly, P.W., Garrison, B.J. and Winograd, N. Surf. Sc. 76: 311 (1978).
90. Littmark, U. and Hofer, W.O. Nucl. Instrum. Methods 168: 329 (1980).
91. Sigmund, P. and Gras-Marti, A. Nucl. Instrum. Methods 168: 389 (1980).
92. Sigmund, P., Olivá, A. and Falcone, G. Nucl. Instrum. Meth. 194: 541 (1982).
93. Williams, P. Appl. Phys. Lett. 36: 758 (1980).
94. Wack, W. and Wittmaack, K. Surf. Interface Anal. 4: 230 (1982).
95. Lidzbarski, E. and Brown, J.D. in "Secondary Ion Mass Spectrometry SIMS V" (Benninghoven, A., Colton, R.J., Simons, D.S. and Werner, H.W., eds.), Springer, Berlin, p. 306 (1986).
96. Stark, J. Z. Elektrochem. 14: 752 (1908).
97. Sigmund, P. in "Sputtering by Particle Bombardment I" (Behrisch, R., ed.), Springer, Berlin, p. 9 (1981).
98. Sigmund, P. Phys. Rev. 184: 383 (1969).
99. Roth, J. in "Sputtering by Particle Bombardment II" (Behrisch, R., ed.), Springer, Berlin, p. 91 (1983).
100. Andersen, H.H. and Bay, H.L. in "Sputtering by Particle Bombardment I" (Behrisch, R., ed.), Springer, Berlin, p. 145 (1981).
101. Eckstein, W. and Biersack, J.P. Appl. Phys. A 37: 95 (1985).
102. Tsunoyama, K., Suzuki, T., Ohashi, Y. and Kishidaka, H. Surf. Interface Anal. 2: 212 (1980).
103. Mayer, J.W., Ericsson, L. and Davies, J.A. "Ion Implantation of Semiconductors" Academic Press, N.Y., p. 76 (1970).

104. Naguib, H.M. and Kelly, R. Rad. Eff. 25: 1 (1975).
105. Wittmaack, K. Nucl. Instrum. Meth. Phys. Res. B2: 674 (1984).
106. Klaus, N. J. Vac. Sci. Technol. 19: 201 (1981).
107. Higatsberger, J. and Klaus, N. Acta Physica Austriaca 41: 269 (1975).
108. Holland, R. and Blackmore, G.W. Surf. Interface Anal. 4: 174 (1982).
109. Deline, V.R., Katz, W., Evans Jr., C.A. and Williams, P. Appl. Phys. Lett. 33: 832 (1978).
110. Wittmaack, K. J. Appl. Phys. 52: 527 (1981).
111. Williams, P., Deline, V.R., Evans Jr., C.A. and Katz, W. J. Appl. Phys. 52: 530 (1981).
112. Wittmaack, K. Nucl. Instrum. Methods B2: 674 (1984).
113. Krauss, A.R. and Gruen, D.M. Surf. Sc. 90: 564 (1979).
114. Williams, P. Surf. Sc. 90: 588 (1979).
115. Andersen, C.A. and Hinthorne, J.R. Science 175: 853 (1972).
116. Slodzian, G. and Hennequin, J.F. Compt. Rend. (Paris) B263: 1246 (1966).
117. Williams, P. and Evans Jr., C.A. Surf. Sc. 78: 324 (1978).
118. Krohn, V. J. Appl. Phys. 33: 3523 (1962).
119. Tsong, I.S.-T. and Yusuf, N.A. Appl. Phys. Letters 33: 999 (1978).
120. Van der Weg, W.F. and Bierman, D.J. Physica 44: 206 (1969).
121. Thomas, G. and de Kluizenuaar Nucl. Instrum. Methods 132: 449 (1976).
122. Reuter, W. in "Secondary Ion Mass Spectrometry SIMS V" (Benninghoven, A., Colton, R.J., Simons, D.S. and Werner, H.W., eds.), Springer, Berlin, p. 94 (1986).

123. Blaise, G. and Nourtier, A. Surf. Sc. 90: 495 (1979).
124. Carter, G. and Colligon, J.S. "Ion Bombardment of Solids", Heinemann, London, p. 56 (1965).
125. Kaminsky, M. in "Quantitative Techniques in Secondary Ion Mass Spectrometry" (Sakaki, Y. and Evans Jr., C.A., eds.), Univ. of Hawaii, Honolulu, p. 12 (1975).
126. Gomer, R. Sol. State Phys. 20: 93 (1975).
127. Andersen, C.A. Int. J. Mass Spectrom. Ion Phys. 3: 413 (1970).
128. Hagstrum, H.D. in "Electron and Ion Spectroscopy of Solids" (Fiermans, L., Vennik, J. and Dekeyser, W., eds.), Plenum, London, p. 273 (1978).
129. Thomas, G.E. and De Kluizenaar, E.E. Nucl. Instrum. and Methods 132: 449 (1976).
130. Man, K. and Yu, M.L. in "Secondary Ion Mass Spectrometry SIMS V" (Benninghoven, A., Colton, R.J., Simons, D.S. and Werner, H.W., eds.), Springer, Berlin, p. 26 (1986).
131. Gnaser, H. Int. J. Mass Spectrom. Ion Processes 61: 81 (1984).
132. Sroubek, Z. Nucl. Instrum. Meth. 194: 533 (1982).
133. Krohn, V.E. in "Microbeam Analysis - 1981" (Geiss, R.H., ed.), San Francisco Press, San Francisco, p. 296 (1981).
134. Lang, N.D. in "Secondary Ion Mass Spectrometry SIMS V" (Benninghoven, A., Colton, R.J., Simons, D.S. and Werner, H.W., eds.), Springer, Berlin, p. 18 (1986).
135. Morgan, A.E. and Werner, H.W. Anal. Chem. 48: 699 (1976).
136. Harrison, D.E., Kelly, P.B., Garrison, B.J. and Winograd, N. Surf. Sc. 76: 311 (1978).
137. Knotek, M.L. Phys. Today, Sept.: 24 (1984).
138. Disko, M.M. Proc. of Materials Research Society, Paper 630 (1985).

139. Burns, M.S. in "Secondary Ion Mass Spectrometry SIMS V" (Benninghoven, A., Colton, R.J., Simons, D.S. and Werner, H.W., eds.), Springer, Berlin, p. 426 (1986).
140. Galuska, A.A. and Marquez, N. *ibid.*, p. 363.
141. Morgan, A.E. *Surf. Interface Anal.* 2: 123 (1980).
142. Morgan, A.E. and Clegg, J.B. *Spectrochimica Acta* 35B: 281 (1980).
143. Reuter, W. and Wittmaack, K. *Appl. Surf. Sc.* 5: 221 (1980).
144. Yu, M.L. and Reuter, W. *J. Appl. Phys.* 52: 1478 (1981).
145. Galuska, A.A. and Morrison, G.H. *Int. J. Mass Spectrom. Ion Proc.* 61: 59 (1984).
146. Pivin, J.C., Roques-Carnes, C. and Slodzian, G. *Int. J. Mass Spectrom. Ion Proc.* 26: 219 (1978).
147. Pivin, J.C., Roques-Carnes, C. and Slodzian, G. *J. Appl. Phys.* 51: 4158 (1980).
148. Slodzian, G. in "Secondary Ion Mass Spectrometry SIMS III" (Benninghoven, A., Giber, J., Laszlo, J., Riedel, M. and Werner, H.W., eds.), Springer, Berlin, p. 115 (1982).
149. Pivin, J.C. and Roques-Carnes, C. *J. Microsc. Spectrosc. Electron.* 7: 277 (1982).
150. Yu, M.L. and Reuter, W. *J. Appl. Phys.* 52: 1489 (1981).
151. Kamanov, G.V. "The Oxide Handbook" (Turnton, C.N. and Turton, T.I., eds. and trans.), Plenum, New York, (1973).
152. Taga, Y. in "Secondary Ion Mass Spectrometry SIMS V" (Benninghoven, A., Colton, R.J., Simons, D.S. and Werner, H.W., eds.), Springer, Berlin, p. 32 (1986).
153. Koval', A.G., Mel-nikov, V.N. and Bondar', S.A. *Sov. Phys. Tech. Phys.* 26: 83 (1981).
154. Meyer, Ch., Maier, M. and Bimberg, D. *J. Appl. Phys.* 54: 2672 (1983).
155. Galuska, A.A. and Morrison, G.H. *Anal. Chem.* 55: 2051 (1983).

156. Brewer, L. and Brackett, E. Chem. Rev. 61: 425 (1961).
157. Brown, J.D. and Vanderworst, W. Surf. Interface Anal. 7: 74 (1985).
158. Robinson, W.H. and Johnston, D.D. "IMS 3f Users Guide", Surface Science Western Report, University of Western Ontario, London, Canada (1985).
159. Colby, U.W. in "Practical Scanning Electron Microscopy" (Goldstein, J.I. and Yakowitz, H., eds.), Plenum Press, New York, p. 552 (1976).
160. Huber, A.M., Morillot, G. and Friederich, A. in "Secondary Ion Mass Spectrometry SIMS IV" (Benninghoven, A., Okano, J., Shimizu, R. and Werner, H.W., eds.), Springer, Berlin, p. 278 (1984).
161. Huber, A.M., Morillot, G. in "Secondary Ion Mass Spectrometry SIMS V" (Benninghoven, A., Colton, R.J., Simons, D.S. and Werner, H.W., eds.), Springer, Berlin, p. 353 (1986).
162. Gibbons, J.F., Johnson, W.S. and Mylroie, S.W. "Projected Range Statistics, Semiconductors and Related Materials", 2nd ed., Dowden, Hutchinson and Ross Inc., Stroudsburg, Penn. (1975).
163. F.R. Shepherd, private communication.
164. Winterbon, K.B. "Range-Energy data for keV ions in amorphous materials" AECL-3194, Atomic Energy of Canada Limited Report, Chalk River, Ont., Nov. (1968).
165. Winterbon, K.B., Sigmund, P. and Sanders, J.B. Mat. Fys. Medd. Vid. Selsk. 37, No. 14 (1970).
166. Weast, R.C. (ed.) "CRC Handbook of Chemistry and Physics", CRC Press Inc., 59 (1978).